CHARACTERIZATION OF RESPONSE SPECTRA FOR NEAR FIELD CONDITIONS BY EARTHQUAKE GROUND MOTION SIMULATION

by

Karin Şeşetyan

B.S., Civil Engineering, Boğaziçi University, 1994

M.S., Earthquake Engineering, Boğaziçi University, 1997

Submitted to Kandilli Observatory and
Earthquake Research Institute in partial fulfillment of
the requirements for the degree of
Doctor of Philosophy

Graduate Program in Earthquake Engineering
Boğaziçi University
2007

ACKNOWLEDGEMENTS

I would like to express my deepest gratitude to Professor Raul Madariaga and Professor Mustafa Erdik for their guidance through this research and also setting before me examples of deepest knowledge, cooperation and kindness. I am grateful to Professor Gülay Barbarosoğlu for all the effort she put in for the signature of the joint PhD agreement between Boğaziçi University and Université de Paris-Sud XI.

I thank Eser Durukal for simply everything. Her constant friendship, support and guidance have been invaluable in all those years that we spent in Kandilli Observatory. Mine Betül Demircioglu is encouragement itself. I thank her for acting as my personal motivator during my study, for sharing not only the office but also all the hard times. I would like to thank Susana Custodio for readily providing me the slip models of the Parkfield earthquake before they were published, Marco Frisenda for helping me with the program and Mario Chavez for all our discussions always focusing on the engineering aspect of simulation. I thank Gülüm Birgören for providing me help whenever I needed, and all my friends in the Department of Earthquake Engineering, especially Ufuk Hancilar, Cüneyt Tüzün and Gökçe Tönük. I also thank Ahmet Suat Gündüz for putting together and organizing the huge output set (including mine) of the Benchmark study.

This thesis study could not be realized without the support of the French Embassy in Turkey. I thank the "Service d'Action et de Coopération Culturelle" of the French Embassy in Turkey for providing joint PhD opportunities for Turkish students in France and awarding me with a joint PhD scholarship. This work was also supported by TUBITAK, under the project 103I050, which is gratefully acknowledged.

I am grateful to Professor Mustafa Aktar for his kind support and valuable suggestions. I would also like to thank all the members of the jury for their readiness to come together through their tight schedule and the administration of UPSXI for their helpfulness. Finally a huge "thank you" goes to my family and my relatives in France.

ABSTRACT

CHARACTERIZATION OF RESPONSE SPECTRA FOR NEAR FIELD CONDITIONS BY EARTHQUAKE GROUND MOTION SIMULATION

Strong ground motion estimation tools such as empirical ground motion prediction equations rely mostly on recorded data. Good quality strong motion data became available mostly in recent years and are still sparse for near field conditions. Strong ground motion records on the other hand contain them several characteristics such as source, path and especially local site effects. These features can sometimes be hardly differentiated when one is willing to study only one of them. As such, realistic simulation of the 3D wavefield generated by a fault rupture in a heterogeneous medium becomes critical for the study of strong ground motion. Particularly features such as intra-event and inter-event spatial and temporal variability of ground motion can be studied in detail. With increasing computational power and newly emerged methods such simulations become increasingly feasible. In this study I use kinematic simulation with 3D Staggered – Grid Finite Difference method to study the characteristics of near source effects of strong ground motion. I also aim to prove that kinematic simulation with 3D Staggered – Grid Finite Difference method (3DFD) is a useful tool to analyze and estimate the characteristics of long period strong ground motion. For this purpose first a simulation model has been set for the 2004 Mw=6.0 Parkfield earthquake. Making use of the available 3D crustal velocity structure of the region and several slip models of the earthquake over 40 near source recordings produced by the event have been simulated. Encouraged by the very good agreement between observed and simulated waveforms, 3DFD has been used for the characterization of directivity effects in the near source region. Eleven earthquakes covering a magnitude range from 6.0 to 7.4 have been modeled using one or more slip models for each of them. Eight of these events had a strike-slip mechanism whereas the remaining ones were dip-slip events. Resulting spatial distributions of fault parallel, fault normal and average response spectral accelerations at longer periods have been analyzed to

derive general formulations for the modification of the response spectral values found from earthquake hazard analysis to include near source directivity effects.

With recently emerging structural design methods, engineering studies concentrate more and more on the long period characteristics of strong ground motion. The present study validates kinematic simulation tools, particularly the 3DFD method used herein as a useful method for the simulation of low frequency strong ground motion in realistic earth media for engineering purposes.

ÖZET

FAY YAKIN SAHASINDA TEPKİ SPEKTRUMU ÖZELLİKLERİNİN KUVVETLİ YER HAREKETİ BENZEŞİMİ YÖNTEMİ KULLANILARAK BELİRLENMESİ

Deprem tehlikesi belirleme çalışmalarında kullanılan kuvvetli yer hareketi tahmin modelleri genellikle ampirik verilere dayanmaktadır. Güvenilir kuvvetli yer hareketi kayıt sayısı son yıllarda oldukça artmış olmakla beraber fay yakın sahasinda elde edilmiş kayıt sayısı sınırlı kalmıştır. Depremlerden elde edilen kayıtların bir dezavantajı ise bu kayıtların kaynak, yol ve özellikle yerel zemin koşulları etkilerinin tamamını yansıtması ve dolayısıyla bu özelliklerden herhangi birinin incelenmesinde gerekli ayrışımın bazı durumlarda mümkün olmamasıdır. Bu nedenle heterojen bir ortamda fay yırtılması sonucunda oluşacak üç boyutlu dalga yayınımının gerçekçi bir şekilde benzeşimi kuvvetli yer hareketi özelliklerinin, ve özelllikle deprem içi ve depremler arası düzlemsel değişkenliklerin belirlenmesi açısından çok önemlidir. Bu çalışmada üç boyutlu atlamalı ızgaralı sonlu farklar yöntemi ile kinematik benzeşim yapılarak yakın fay sahası koşullarında kuvvetli yer hareketlerinin özellikleri incelenmiştir. İkinci bir amaç ise üç boyutlu atlamalı ızgaralı sonlu farklar yönteminin (3DFD) uzun peryodlu yer harektinin özelliklerinin analiz ve tahmininde kullanılabilecek uygun bir yöntem olduğunun kanıtlanmasıdır. Bu amaçla öncelikle 2004 M_w = 6.0 Parkfield depremi için bir benzeşim modeli hazırlanmış ve bu depremden elde edilen 40'ın üzerindeki yakın saha kaydı başarılı bir şekilde simüle edilmiştir. Bu benzeşimden elde edilen olumlu sonuçlara dayanılarak 3DFD yöntemi ile yakın saha koşullarının özelliklerinin belirlenmesi amacıyla 6.0 – 7.4 magnitüd aralığında sekizi yanal atımlı ve üçü ters atımlı olmak üzere 11 deprem simüle edilmiştir. Elde edilen yüzey yer hareketleri faya paralel ve faya dik doğrultudaki bileşenler ve ilgili tepki spektrumları cinsinden değerlendirilmiş ve deprem tehlikesi analizinden elde edilen yer hareketlererinin yakin fay sahası etkileri açısından modifikasyonu için basit modeller önerilmiştir.

Depreme dayanıklı tasarım konusunda yeni geliştirilen ve özellikle spektral yer değiştirmelere dayanan yöntemler kuvvetli yer hareketinin uzun peryodlardaki özelliklerinin belirlenmesi konusunu gündeme getirmektedir. Bu çalışma, kinematik simülasyonun ve özellikle kullanılan 3DFD yönteminin mühendislik uygulamaları açısından gerekli olacak düşük frekanslı yer hareketlerinin elde dilmesi açısından uygun bir yöntem olduğunu ortaya koymaktadır.

TABLE OF CONTENTS

LIST OF FIGURES

LIST OF TABLES

LIST OF SYMBOLS / ABBREVIATIONS

a and b	Regression parameters of the Gutenberg-Richter magnitude recurrence relationship
$a(t)$	Ground acceleration time history at a station
Ai	Site amplification coefficient
c_1, c_2 and c_3	Period dependent coefficients
C_1	Horizontal rupture velocity
C_2	Vertical rupture velocity
c_o	Constant
c_n	Amplitude of the n^{th} harmonic of the Fourier series
$d(t)$	Ground displacement time history at a station
$\dot{D}$	Slip rate
$D(x,t)$	Slip vector across the fault
$\Delta\Sigma[D]$	Complex singular functional of D and its time and space derivatives.
dh	Grid spacing
$f(x)$	Force distribution of the source
$f_R(r)$	Probability density function for distance (r)
$f_M(m)$	Probability density function for magnitude (m)
$Fmax$	Maximum frequency
$G(x,t)$	Green's tensor
M	Magnitude
Mw	Moment magnitude
$\dot{m}$ (x)	Moment rate distribution of the source
N_a and N_v	Means of near-source factors
P	Probability of occurrence of at least on event,
P-wave	Compressional wave
R_{rup}	Closest distance to the rupture plane
s	Second

S_a	Maximum value of the structural acceleration response to a particular input motion
S_d	Maximum value of the structural displacement response to a particular input motion
Sv	Maximum value of the structural velocity response to a particular input motion
S-wave	Shear wave
T_{Dir}	Width of the largest velocity pulse
$T_d(r)$	Distance taper
$T_m(m)$	Magnitude taper
ΔT	Stress change
T_p	Predominant period of an earthquake ground motion recording
T_v	Pulse period
$U(x,t)$	Displacement vector field
$u(x,t)$	*S*implified form of a seismogram at an arbitrary position x
u_g	The ground displacement
$\dot{u}_g$	First time derivative of ground displacement
$\ddot{u}_g$	Second time derivative of ground displacement
u^+ and u^-	Displacements corresponding the points immediately above and below the fault
$v(t)$	Ground velocity time history at a station
$V(x,t)$	Particle velocity vector
V_p	Compressional wave velocity
V_r	Rupture velocity
V_s	Shear wave velocity
v_x, v_y and v_z	Velocity components
X and Y	Along strike and updip distance ratios
$x(t)$	A periodic function
x^+ and x^-	Points immediately above and below the fault
y	*R*esidual of the natural logarithm of the spectral acceleration or that of the duration or logarithm of the strike-normal to strike-parallel ratio at a given period

zsc	Source plane
α_1 *to* α_4 and *D*	Parameters to define the standard shape of fault normal to mean amplitude ratio
λ_m	Mean annual rate of exceedence of magnitude m
$\Gamma(t)$	Rupture zone spreading along the fault zone
$\Delta u(\xi,\tau)$	Slip on the fault
ϕ_n	The phase angle of the n^{th} harmonic of the Fourier series
$\lambda(x)$ and $\mu(x)$	Lamé's elastic constants
$\rho(x)$	Density of the elastic medium
$\sigma(x,t)$	*S*tress tensor
$\sigma_{ii}, \sigma_{xy}, \sigma_{zx}$ and σ_{zy}	Stress components
w_n	Natural frequency of the n^{th} harmonic of the Fourier series
θ and ϕ	Azimuth and zenith angles
1D	One dimensional
3D	Three dimonsional
3DFD	3D Staggered – Grid Finite Difference method
ARC	Arcelik station
BIE	Boundary Integral Equations
CFL	Courant – Friedrichs – Lewy parameter
CGS	California Geological Survey
CSMIP	California Strong Motion Instrumentation Program.
DSHA	Deterministic Seismic Hazard Assessment
DWNM	Discrete Wavenumber
FAS	Fourier Amplitude Spectrum
FD	Finite-Difference Method
FN	Fault Normal
FP	Fault Parallel
NEHRP	National Earthquake Hazards Reduction Program
NGA	Next Generation Attenuations
NS	North - South

PGA	Peak Ground Acceleration
PGD	Peak Ground Displacement
PGV	Peak Ground Velocity
PSHA	Probabilistic Seismic Hazard Assessment
SAF	San Andreas Fault
SDOF	Single Degree of Freedom
SKR	Sakarya station
SW	South -West
UBC	Uniform Building Code
USGS	United States Geological Survey.

1. INTRODUCTION

Principal goals of strong ground motion seismology are to improve the scientific understanding of physical processes that control strong shaking and to develop reliable estimates of seismic hazards to reduce loss of life and property in future earthquakes through improved resistance to earthquakes by both identification of high risk zones and earthquake resistant design and retrofit of structures. The tremendous growth of urban areas in seismically active regions, together with the tendency of the population to settle in or close to these urbanized areas augments the exposure to earthquake risk and consequently reliable estimates of the regional variation of the seismic hazard becomes crucial for the mitigation of the earthquake risk. Estimation of strong ground motion for engineering purposes begins with the regional assessment of the expected amplitudes of strong ground motion parameters that are critical in seismic design of an engineering structure. This is achieved through deterministic and/or probabilistic assessment of seismic hazard in a seismically active region. The next step is the identification of local factors that would cause the modification of the parameters determined in the previous step. These factors could be the effect of local site conditions, topographic and basin effects. These effects can either be assessed for a region or particularly at the location of the engineering project. Considering a rigorous seismic design effort for an engineering structure, the final step in terms of ground motion assessment would be the determination of a set of suitable strong ground motion time histories that would reflect all the expected earthquake source, path and site effects at the construction site. This set can either be obtained through a careful examination of the available recordings and/or by simulation of strong ground motion. Estimation of the expected ground motion at a particular area constitutes the intersection area of two disciplines, namely Geophysics and Earthquake Engineering, since without a thorough understanding of the causative effects of a fault rupture, the underlying processes and also the propagation and modification of seismic waves through the earth it is not possible to make a sound estimation. Whereas the physical understanding and mathematical representation of these processes have been a challenge for the geophysical community during the last century, statistical approaches based on observed data have been another tool for earthquake engineers to estimate the searched parameters where

uncertainties raised by both epistemic causes and also the aleatory nature of the earthquake processes.

Beginning with the 1992 Landers earthquake, increased number of near source recordings from recent earthquakes revealed that ground motions near the causative fault of an earthquake showed characteristics highly different than those located farther away. These effects were more pronounced in long period ground motions. As such, for long period structures such as bridges and tall buildings it would be important to include these near source effects in the associated probabilistic or deterministic seismic hazard computations. The identification of those differences and their formulation in a suitable way to be incorporated in seismic hazard assessment studies have been subject to a number of statistical studies, which will be covered in Chapter 4. Although their number increased by recent major earthquakes, obtaining good quality near fault recordings is still a challenge since it requires the installation of dense strong ground motion networks near fault zones where relatively large magnitude earthquake are highly expected. These recordings should also be obtained from different tectonic locations and cover a certain magnitude range to account for the uncertainties arising from the nature of the earthquake process As such, the aim of this thesis study has been to make use of the existing and well established deterministic simulation tools to understand the spatial variation of the ground motion parameters required for engineering purposes in the near source region and to derive formulations to incorporate these near source effects in seismic hazard assessment studies.

In this chapter, first a short description is given for the ground motion parameters that are of engineering interest and used in the study. Following that, I will dwell on the principles of seismic hazard analysis which constitutes the first step in the estimation of those parameters in a study area. The ground motions obtained from a basic seismic hazard analysis should be corrected for near source effects, local site conditions, topographic and basin effects if and when necessary. Assessment of local geological, topographic and basin effects are not considered in the thesis study. In the third section of the first chapter I will present a summary of previous studies on the characterization of near source effects, a subject which will also be elaborated in the Chapter 3. A brief review of the concepts and

methods related with low frequency simulation of strong ground motion will also be presented.

1.1. Seismic Ground Motion Parameters

Both time and frequency domain characteristics of the strong ground motion are used in engineering applications. Parameterization of these characteristics is a useful tool for their incorporation in further studies such as assessment of earthquake hazard or structural response to a particular seismic excitement. In the present section a short description of the seismic ground motion parameters that are used within the context of this thesis study will be given. Comprehensive descriptions can be found in Kramer (1996) and Stewart *et al.* (2001).

1.1.1. Time Domain Parameters

The most common representation of ground motion is a time history and the related most commonly used parameters are the peak values of ground displacement *d(t)*, velocity *v(t)* and acceleration *a(t)*, at a site caused by an earthquake excitation. They are denoted by PGD, PGV and PGA respectively. Peak values give the largest absolute amplitudes of the respective (mostly non-filtered but base-line corrected) time series:

$$PGD \equiv \max\left(\left|u_g\right|\right) \tag{1.1}$$

$$PGV \equiv \max\left(\left|v\right|\right) = \max\left(\left|\dot{u}_g\right|\right) \tag{1.2}$$

$$PGA \equiv \max\left(\left|a\right|\right) = \max\left(\left|\ddot{u}_g\right|\right) \tag{1.3}$$

where $u_g=d(t)$ is the ground displacement time history at a particular station. Peak values can be obtained for all three components of ground shaking, i.e. for the two orthogonal horizontal and the vertical components. The two horizontal components are in general given as components in NS and EW directions in recorded time histories, whereas in fault normal and fault parallel directions in simulated ones. Peak horizontal values can refer to the maximum peak value of the two horizontal components, their average (mean) value or

to the peak value of the resultant time series after taking the vector sum of both. In this work peak horizontal values refer to the geometric mean of the two horizontal components unless otherwise stated.

Acceleration time histories are associated with higher frequency range of the ground motion which are poorly represented in simulation studies. As such, in this work I will mostly concentrate on velocity and displacement time histories and peak amplitudes which are adequately covered in the frequency band of the deterministic simulation methods, as explained in the following sections.

1.1.2. Spectral Parameters

Fourier amplitude spectra and particularly response spectra are the two commonly used tools in earthquake engineering for the quantification and analysis of the ground motion in the frequency domain.

- Fourier Amplitude Spectra (FAS):

Using a Fourier series, a periodic function, *x(t)*, can be expressed as:

$$x(t) = c_0 + \sum_{n=1}^{\infty} c_n \cos(\omega_n t + \phi_n) \tag{1.4}$$

In this form, c_n and ϕ_n are the amplitude and the phase angle, respectively of the n^{th} harmonic of the Fourier series. The Fourier series provides a complete description of the ground motion in the frequency domain since the time history can be recaptured by the Inverse Fourier Transform. The Fourier Amplitude Spectrum (FAS) is a plot of the amplitude, c_n, versus frequency and is used to see how the amplitude of the motion is distributed with respect to frequency. FAS of acceleration records plotted in logarithmic scale exhibit a plateau over an intermediate frequency range. The lower bound of this plateau is the cut off frequency which is inversely proportional to the cube root of seismic moment (Brune, 1970). This indicates that large earthquakes produce greater low-frequency motions than the smaller ones. The predominant period, T_p, of an earthquake

ground motion recording is the period of vibration corresponding to the maximum value of its smoothed FAS, and provides a useful but rough representation of the frequency content.

- Response Spectra:

Response spectrum which is extensively used in earthquake engineering, describes the maximum linear (visco – elastic) response of a single degree of freedom system (SDOF) to a particular input motion as a function of its natural period of vibration and damping ratio. The response may be expressed in terms of acceleration, velocity or displacement. These spectral amplitudes can be used to define the earthquake load on a particular structure if a more specific time history analysis is not required. The maximum value of the structural response to a particular input motion depends only on the natural frequency and the damping ratio of the SDOF system. The maximum values of acceleration, velocity and displacement are referred to as spectral acceleration (S_a), spectral velocity (S_v) and spectral displacement (S_d) respectively. For linear, elastic SDOF systems, the spectral displacement, velocity and acceleration are approximately related to each other by the following expressions:

$$S_d = \max|u| \tag{1.5}$$

$$S_v = \max|\dot{u}| \approx \omega_0 S_d = PSV \tag{1.6}$$

$$S_a = \max|\ddot{u}| \approx \omega_0^2 S_d = \omega_0 PSV = PSA \tag{1.7}$$

where u and ω_0 are the displacement and natural frequency of the SDOF system. PSV and PSA are the pseudo spectral velocity and the pseudo spectral acceleration respectively. Although they are not the true maxima of the acceleration and velocity response they are very close and can approximately be assumed to be equal to S_v and S_a.

1.2. Basics of Seismic Hazard Assessment

Quantitative estimation of the expected level of shaking in terms of parameters that will be used in the earthquake resistant design of a structure is called a seismic hazard analysis. These estimations constitute the first and basic step in the determination of the so-

called design ground motions for the desired structural performance levels. Following steps would be incorporation of directivity and local site conditions, determination of compatible ground motion time histories either from existing databases or by simulation, site response analyses, and assessment of liquefaction and slope failure potentials due to ground shaking. Seismic hazard can be assessed either deterministically, i.e. for a particular earthquake scenario, or probabilistically, in which uncertainties in earthquake size, location and time of occurrence are considered to obtain probabilities of exceedence of ground motion levels in specified time intervals. Intensity, peak ground acceleration, velocity and displacement and the corresponding response spectral values are the most commonly considered engineering parameters in a seismic hazard study.

Identification of possible earthquake sources constitutes the first step in both deterministic and probabilistic earthquake hazard assessment studies. This is achieved through investigation of geologic evidence of faulting, since earthquakes are likely to occur in places that have been the locations of past events and that some evidence of their occurrence, such as relative displacements can be geologically observed. The term “fault activity” is used for a fault zone that is known to have generated earthquakes in the past to define its possibility that it will produce earthquakes in the future. For instance California Division of Mines and Geology defines an active fault as one that has produced surface displacement within Holocene time (approximately the past 10,000 years). For the design of critical structures such as nuclear power plants or LNG facilities more severe criteria can be used, since the identification of “active” or “capable” faults constitutes the main input in a hazard assessment. The rupture lengths and observed displacements on fault zones and geologic segmentation criteria can be used to estimate the earthquake magnitudes that can be generated by a specific fault. Compilation of the earthquake catalog (both historically evidenced and instrumentally recorded seismicity) of the region of interest is the second step in hazard assessment. With the information of earthquake sources and the associated seismicity, one can proceed with a deterministic seismic hazard assessment (DSHA) study.

The steps of DSHA are 1) identification of all possible sources and the associated earthquake potentials, 2) determination of the closest source to site distance for each source zone, 3) selection of the source zones and associated magnitudes that will control the

hazard at the site, i.e., that will produce the highest values of considered ground motion parameters and 4) computation of these ground motion parameters using empirical ground motion prediction equations.

Empirical ground motion prediction equations are used to define the ground motion expected at a site given an earthquake at a particular location in terms of its magnitude and distance to the site and some other variables such the fault type or the soil type at the site. Empirical ground motion prediction equations are developed based on the statistical treatment of peak amplitudes obtained from mostly recorded (and in some cases simulated) strong ground motion time histories and provide a statistical distribution of the expected ground motion values for given source, distance and site parameters with the median and the associated standard deviation.

The basics of the Probabilistic Seismic Hazard Assessment (PSHA) are set by Cornell (1968). Identification of seismic sources and associated seismicity are similar to DSHA. However probability density functions must be defined for the possible location of an earthquake within a zone and also for its earthquake magnitude generation pattern. Uniform distributions are usually used to define the location of an earthquake within a zone. A magnitude recurrence relationship has to be defined for each source zone to represent its magnitude generation potential. The so-called Gutenberg – Richter law (Gutenberg and Richter, 1944) is the most widely used magnitude recurrence relationship for a source zone. It is expressed as

$$\log \lambda_m = a - bm \tag{1.8}$$

where λ_m is the mean annual rate of exceedence of magnitude m, within that zone, a and b are the regression parameters. Several variations of the Gutenberg – Richter law, and also the characteristic earthquake distributions can be used. The choice of the recurrence law for a source zone depends on how well the characteristics of a fault are known.

Earthquakes are generally assumed to occur randomly within time. This assumption allows the use of simple probabilistic models such as the Poisson model which states that

$$P = 1 - e^{-\lambda_m t} \tag{1.9}$$

where P is the probability of occurrence of at least on event, t is the time interval of interest, and λ_m is the mean annual rate of exceedence of magnitude m. Time dependent models on the other hand, assume that the probability of occurrence of an earthquake within a zone increases with the time elapsed since the last event in that zone.

Combining all these ingredients the probability that a ground motion parameter Y at a particular location will exceed a particular level y is given by

$$P[Y > y] = \iint P[Y > y|m,r] f_M(m) f_R(r) dm dr \tag{1.10}$$

where $P[Y > y|m,r]$ is obtained from the empirical ground motion prediction equation and $f_M(m)$ and $f_R(r)$ are the probability density functions for magnitude (m) and distance (r) respectively.

1.3. Studies on Near Source Effects

Ground motion close to a ruptured fault can be significantly different from those further away. Within a distance of a few tens of kilometers from the fault rupture, ground motions are influenced by the rupture mechanism, the direction of rupture propagation relative to the site, locations of high and low slip zones, i.e. asperities or barriers within the rupture plane, and also resulting permanent displacements. These characteristics are called near source or directivity effects. The estimation of ground motions close to an active fault should account for these effects. Forward directivity occurs when rupture propagates towards a site with a slip also in the same direction. In this case energy is accumulated near the rupture front from each successive slip zone along the fault. The resulting wave form is a large amplitude velocity pulse with a short duration and polarized in fault normal direction. The pulse of motion is characterized by large amplitude in intermediate to long periods. If the rupture propagates away from a site, the arrival of seismic waves is distributed in time. The resulting ground motion is lower in amplitude and longer in duration. This condition is referred to as backward directivity. Large earthquakes also

cause permanent ground displacements in the near source region termed “fling step”. Fling step occurs in direction parallel to the slip. In strike-slip faulting directivity pulse occurs in fault normal component whereas the fling step is observed in fault parallel displacement. In dip-slip ruptures both the directivity pulse and the fling step occur in the fault normal component.

Somerville *et al.* (1997) conducted an analysis on the near source ground motion recordings available at that time and derived rules for the modification of both the fault normal and average horizontal spectral accelerations obtained from a routine hazard assessment study. These rules were considered in UBC (1997). Somerville *et al.* (1997) also provided relationships for the differentiation of ground motion duration in forward and backward directivity regions. Abrahamson (2000) applied distance and magnitude tapers to the model provided by Somerville *et al.* (1997) to make it applicable to a probabilistic seismic hazard analysis. He also made some modifications in the predictive equations of Somerville *et al.* (1997) using more recent data and simulation results. Somerville (1998), Alawi and Krawinkler (2000) and Rodriguez-Marek (2000) proposed relationships between logarithm of peak horizontal velocity, magnitude and logarithm of distance. The same authors also proposed relationships between the pulse period, T_v, and the earthquake magnitude, where T_v is the period of the largest cycle of motion..

Studies on the quantification of fling step (i.e. permanent ground displacements near the source) are scarcer. To have an idea on the amplitude of the fling step near a fault rupture, empirical equations for the estimation of maximum or average fault displacements with respect to magnitude, such as the well known Wells and Coppersmith (1994) relationships can be used.

Studies have also been conducted to characterize near source ground motions with low-frequency simulations. Aagaard and Heaton (2004) investigated the effect of rupture velocity in strike-slip ruptures while Aagaard et al (2004) investigated the effect on near source ground motions of dip and rake angles for dip-slip earthquakes. Recently, a comprehensive earthquake recording database was formed and offered to research groups for the development of new empirical ground motion prediction models called the Next Generation Attenuations (NGA) such as Boore and Atkinson (2006), Campbell and

Bozorgnia (2006) and Chiou and Youngs (2006). Recently Spudich and Chiou (2007, personal communication with P. Somerville) used this database to develop empirical equations that would reflect the effects of near-source directivity on average horizontal, strike-normal, and strike-parallel components of motion, and to propose alternatives for incorporating effects in ground motion mapping. The results of this study are not known to be published.

The aim of this thesis being the characterization near source effects based on strong ground motion simulation, some basic concepts and relevant applications of simulation remaining within the frame of low frequency simulation methods are summarized in Section 1.4.

1.4. Simulation of Strong Ground Motion

Simulation of strong ground motion finds its application in two different ways in seismology. First of them is what is called as the “inversion”, that is the modeling of source processes in an earthquake with the help of recorded strong ground motion data. The second is the estimation of the ground motion at any location by modeling the earthquake faulting process, the earth medium in a reasonable scale covering the source and the station and if possible the local site effects such as topography, basin structure and non-linear soil conditions near the station. This second type of modeling is widely used in engineering applications since a reasonable site specific estimate of both time and frequency domain characteristics of the strong ground motion is crucial for the design process of an engineering structure. Both kinematic and dynamic approaches can be used in source modeling. Kinematic simulation uses predetermined source parameters i.e. the slip on the fault is defined as a function of fault plane coordinates and of time. Rupture velocity and rise time can be taken as constant throughout the fault or variable if data is available. In dynamic models source parameters are determined from solution of dynamic equations where regional tectonic stresses and the friction law are predefined. In kinematic source models, the slip distribution over the fault plane as well as the space time evolution of it can be taken from “inversion” results of past earthquake data or can be found using dislocation models such as the Haskell model (Erdik and Durukal, 2002). In dynamic source models, shear dislocation or slip is the result of a stress drop in a tectonic region

(Madariaga, 1976; Kostrov and Das, 1989; Scholtz, 1989). The direction, time evolution and amount of slip over the fault plane are controlled by the surrounding forces in the region, as well as the material properties of the earth medium in the region.

The so-called dislocation model is the most useful and widely used kinematic description of an earthquake. In this model the earthquake is simulated as the kinematic spreading of a displacement discontinuity along a fault plane.

The force – dislocation equivalence theorem (Burridge and Knopoff, 1964) states that the displacement field due to shear dislocation on an infinitesimal surface element is the same as the one obtained by a double-couple applied at the element without any dislocation. With the help of this theorem it was possible to analytically express the displacement field through the earth medium, provided that the displacement discontinuity across the fault plane is known. The displacement field can be expressed as the space – time convolution of the source function with the so-called Green's function, which is the earth's response to a double-couple which represents the point source (e.g. Aki and Richards, 1980, p. 27). As such, it is possible to express the radiation from a dislocation model as a functional of the distribution of slip on the fault plane. The simplified form of a seismogram *u(x,t)* at an arbitrary position *x* is given in Equation 1.11 (Madariaga and Olsen, 2002).

$$u(x,t) = \int_0^t \int_{S_\xi} \Delta u(\xi,\tau) G(x-\xi, t-\tau) d\xi d\tau \tag{1.11}$$

where $\Delta u(\xi,\tau)$ is the slip on the fault and *G(x,t)* is the Green's tensor which can be computed using simple layered models of the earth medium or more complex numerical methods such as the Finite Difference method.

The so-called Haskell model was introduced by Haskell (1964) and since then it has been the most important dislocation model. In this model slip is characterized with a ramp type source – time function propagating unilaterally along a rectangular fault at a constant rupture velocity. Rise time and amount of final slip are constant throughout the fault. The complete seismic radiation for Haskell's model was computed by Madariaga (1978).

The slip history of the fault determined with a dislocation model can then be used to compute the stress history on the fault. The procedure was first proposed by Mikumo and Miyatake (1979). Olsen *et al.* (1997) for instance use this method in the three dimensional dynamic simulation of the 1992 Landers earthquake.

Two methods have been widely used in the modeling of three-dimensional wave propagation. These are the boundary integral equations (BIE) method and the finite-difference method (FD). The BIE method was pioneered by Das and Aki (1977) and later developed by various researchers. It is very successful in the modeling of earthquake recurrence and the transition from transient accelerated fault creep to fully dynamic rupture propagation. The BIE method can accommodate complex fault geometries but at its current state can only be used for homogeneous earth conditions. (Madariaga *et al.*, 1998). The FD method was introduced by Madariaga (1976) and Andrews (1976) for the study of seismic ruptures and developed by various authors. The FD method can be efficiently used in the study of rupture propagation in heterogeneous elastic media. The stagerred grid-velocity – stress formulation was developed by Madariaga (1976) to study dynamic rupture problems and is based on the discretization of the system described with a symmetric velocity – stress formulation of the 3D elastic wave equation. Olsen *et al.* (1995) and Olsen and Archuleta (1996) demonstrated the efficiency of the forth-order formulation of the velocity-stress method by computing wave propagation caused by a kinematically defined rupture in a large-scale 3D model.

Olsen (2000) uses finite-difference finite-fault simulations to estimate the three dimensional response of the Los Angeles basin to nine different earthquake scenarios. Amplification is quantified as the peak velocity obtained from the 3D simulation divided by that predicted using a regional one dimensional crustal model. The physical model is discretized with a grid spacing equivalent to 5 nodes per minimum shear wavelength of 2.5km, which limits the maximum resolved frequency to 0.5 Hz. The full model is discretized at 0.4 m. All scenarios are kinematically simulated using variable slip distributions, radially propagating outward with a constant rupture velocity. The rupture velocity is taken as 2.7 km/sc for the SAF scenarios and 3 km/s for all the other finite fault scenarios. The slip distributions are taken as the variations of the kinematic inversion results for the 1992 Landers and 1994 Northridge earthquakes. A triangular slip rate

function is used. The rise time is 3 s for the SAF ruptures, 0.2 s for the Whittier Narrows earthquake and 1 s for the remaining events. A staggered-grid finite difference scheme is used to solve the 3D elastic equations of motion. The accuracy is forth order in space and second order in time. The numerical implementation of the 3D scheme is described in Olsen (1994). The results of the simulations are used to construct site amplification maps for the Los Angeles basin. Later, a similar work was conducted within the context of the TeraShake project (Olsen *et al.*, 2006). A M 7.7 earthquake was simulated along the 199 km of the San Andreas fault between Cajon Creek north of Los Angeles and Bombay Beach on the shore of Salton Sea. The aim of the study was to compute the impact of such an earthquake on the densely populated sediment filled basins in Southern California and northern Mexico. The second phase of the TeraShake project was characterized by the incorporation of a dynamic rupture component.

Discrete wavenumber method, introduced by Bouchon and Aki (1977) is another method to simulate ground motions in a horizontally layered earth medium by accurately calculating the complete Green's functions with a minimum computational effort. The method introduces a spatial periodicity of sources to discretize the radiated wavefield, and relies on the Fourier transform in the complex frequency domain to calculate Green's functions. The method was later modified by Bouchon (2003) to incorporate extended sources. Although it is an efficient method requiring much less computing time and memory, the discrete wavenumber method can only be used for horizontally layered earth medium.

1.5. Outline of the Thesis

The aim of the present work is the characterization of near source ground motions based on low frequency simulation. For the purpose the 3D Finite Difference Simulation Code developed and installed in the Geology Laboratory of Ecole Normale Supérieure, Paris, is used. Another objective of the thesis is the verification, validation, and adaptation of the present code for its usage in various engineering applications. This is done in the following steps:

1. Verification of the code by comparison with other methods

2. Validation by checking against recorded data
3. Evaluation and formulation of the near field strong ground motion characteristics using simulated ground motion

The second chapter of the thesis presents the numerical method and some applications. First a brief history of the numerical method and the governing equations are covered. Second the simulation code is presented with the required input and the associated output files. The efficiency of the method in simulation of wave propagation in 3D earth medium is demonstrated for a Haskell type source with an example solved in both homogeneous and horizontally layered media, and also in a 3D basin structure. Third, results of the code are checked against the analytical solutions provided by Anderson and Luco (1983) and the results obtained by the discrete wavenumber method again for the simple case of a Haskell type source in a homogenous half space. The results of a benchmark study (Durukal *et al.*, 2006), on the comparison of the available low frequency simulation codes are also presented. The results are compared with other simulation codes for a rectangular fault in a horizontally layered half space. In this case the rupture initiates at the hypocenter and propagates radially along the fault.

The third chapter of the thesis deals with the validation of the results using recorded strong ground motion data. The 2004 Mw 6.0 Parkfield earthquake is chosen as the testbed of this section, as it provided the greatest number of near field accelerograms ever recorded for an earthquake. The moderate size of the rupture length and the proximity of the recording stations allowed for the modeling of a very dense grid. Various slip models obtained for the 2004 rupture have been incorporated in the model and the results were compared. The availability of a 3D velocity model for the Parkfield area has been another advantage for the simulation with the finite difference method. Comparison of the recorded data with the simulated time histories provided satisfactory results for the work to go on with more generic models aiming at the characterization of near source data.

The characteristics of near source ground motions as observed from recorded data, as well as studies conducted for the modeling of these characteristics are covered in the fourth chapter. Effects of rupture directivity on seismic hazard computed for a region and the

methodologies of deterministic and probabilistic seismic hazard assessment including near source effects are also presented.

The fifth chapter presents the simulation studies carried out for the characterization of near source motion. For this purpose, first the setup of the previously mentioned benchmark study is used to assess the effects of different kinematic rupture parameters, such as rupture velocity, slip amount, rise time and depth of asperity on stations in both forward and no directivity regions. Second various earthquakes possessing either strike-slip and dip-slip mechanisms within a reasonable magnitude range were simulated. In this connection available slip models are used and available rise time and rupture velocity data are incoporated. As for the earth structure, a simple horizontally layered velocity model was chosen and used in all the models in order to purely concentrate on the effects of rupture directivity and exclude the effects that would arise from the three dimensional heterogeneity of the crust. The resulting simulations correspond to time histories that would be recorded on a rock outcrop. As such, the local site effects that would result from heterogeneities in much smaller scales, such as the upper 100 m of the earth crust were not considered. The analysis of the obtained results for engineering purposes and discussions are covered in the last two sections of Chapter 5.

Chapter 6 provides a summary of studies conducted and results obtained within the context of this thesis.

2. THE NUMERICAL METHOD

Finite Difference has been established as a suitable tool to simulate wave propagation in heterogeneous media. Several applications of the method have been elaborated by various researchers (e.g. Miyatake, 1980; Olsen and Archuleta, 1996, Pitarka and Irikura, 1996). The staggered – grid finite – difference method used in the present study was first proposed by Madariaga (1976) where he considered the body-wave pulses radiated from a plane circular shear fault expanding at a constant rupture velocity until it stops in an infinite homogeneous, isotropic, elastic medium. The problem was numerically solved to determine the slip rate on the fault and then these fault slip rates were summed in appropriate directions around the source to obtain the pulse shape in those directions. The velocity – stress finite difference method was extended to heterogeneous medium by Virieux (1986) and brought to fourth order accuracy in space by Levander (1988). The efficiency of the method proposed by Levander (1988) was tested by Olsen *et al.* (1995) and Olsen and Archuleta (1996) in large scale kinematic simulations of wave propagation in Los Angeles area. Madariaga *et al.* (1998) extended the fourth-order staggered-grid finite-difference method to study dynamic faulting in three dimensions. In the first and second parts of this chapter the method will be summarized and small applications will be presented to demonstrate the effectiveness of the method in simulation of wave propagation in different types of earth structures. Comparisons of the method with other analytical and numerical methods are covered in the third and fourth sections of this chapter.

2.1. The Staggered – Grid Finite – Difference Method

A full description of the so-called "velocity-stress finite-difference staggered-grid method" is given in Madariaga *et al.* (1998). The main features of the wavefield generated by a source model in an elastic earth model are as follows:

The 3D elastic wave equation is given in Equation 2.1.

$$\rho \frac{\partial^2}{\partial t^2} U = \nabla \cdot \sigma \tag{2.1}$$

where *U(x,t)* is the displacement vector field, a function of both position *x* and time *t*, and ρ *(x)* is the density of the elastic medium. σ *(x,t)* is the stress tensor and is defined by Equation 2.2.

$$\sigma = \lambda \nabla \cdot UI + \mu \left[(\nabla U) + (\nabla U)^T \right] \tag{2.2}$$

where λ *(x)* and μ *(x)* are Lamé's elastic constants and *I* is the identity matrix. The system is transformed into a more symmetric velocity-stress formulation by Madariaga (1976), Virieux and Madariaga (1982) and Virieux (1986) as given in Equation 2.3.

$$\begin{aligned} \rho \frac{\partial}{\partial t} V &= \nabla \cdot \sigma + f \\ \frac{\partial}{\partial t} \sigma &= \lambda \nabla \cdot VI + \mu \left[(\nabla V) + (\nabla V)^T \right] + \dot{m} \end{aligned} \tag{2.3}$$

where *V(x,t)* is the particle velocity vector and *f(x)* and $\dot{m}$ *(x)* are the force and moment rate distributions of the source, respectively.

Slip boundary conditions on the fault are computed assuming a flat horizontal fault perpendicular to the *z* axis in the elastic medium. $\Gamma(t)$ is the rupture zone spreading along the fault zone. The main feature of a rupture zone is that at any point inside the rupture zone displacements are discontinuous. The slip vector across the fault, that is, the jump between the negative and positive sides of the fault is given in Equation 2.4.

$$D(x,t) = u^+(x^+,t) - u^-(x^-,t) \tag{2.4}$$

xhere x^+ and x^- indicate points immediately above and below the fault respectively. u^+ and u^- are the corresponding displacements. Slip is associated through the solution of the wave equation given in Equation 2.3 to a change in the traction across the fault. The

traction is defined by $T = \sigma \cdot e_z = \lfloor \sigma_{zx}, \sigma_{yz}, \sigma_{zz} \rfloor$ and is associated to the slip by Equation 2.5.

$$\Delta T(x,t) = \Delta\Sigma[D] \quad \text{for} \quad x \in \Gamma(t) \tag{2.5}$$

where $\Delta\Sigma[D]$ is a complex singular functional of D and its time and space derivatives. With the help of a numerical procedure in Finite Difference the stress change ΔT is computed based on the slip distribution D at earlier times.

In seismic source dynamics it is assumed that the traction across the fault is related to the slip at the same point through a friction law. The friction can either be taken as slip weakening or rate weakening or as a combination of them. In the slip weakening friction law slip is zero until the total stress reaches a peak value, which is the yield stress. Once the yield stress is reached, slip begins to increase from zero. At the same time friction starts to decrease linearly with the amount of slip and becomes zero when the characteristic slip distance is reached. For large values of slip, however, the slip rate becomes the dominant parameter. In Madariaga et al (1998) it is assumed that for large slip D, friction increases when slip rate $\dot{D}$ decreases. This type of friction is called rate weakening.

The numerical implementation of the method is such that the system given in Equation 2.3 is solved in three dimensions using a fourth order approximation to spatial derivatives and a second order approximation to temporal derivatives. This is the staggered grid finite difference method developed by Olsen (1994), which is an explicit implementation of the velocity – stress formulation given in Equation 2.3. The method is named as staggered – grid since in this method the 3D finite-difference grid is staggered both in time and space. A cubic element of the grid used in the modeling of a planar shear fault is given in Figure 2.1 (Madariaga *et al.*, 1998). On this cubic element, stresses and velocities are calculated in alternating time steps. At time $t_N = N\Delta t$, particle velocity v is calculated from the stress components obtained in the previous step. At the next half-time step $t_{N+1/2}$, the stress is updated using the velocities calculated at time t_N, resulting in stress and velocity field computed at alternate times. The grid is also staggered in space since stress and velocities are computed using centered fourth – order finite differences in spatial

calculations as shown in Figure 2.1. This condition necessitates careful treatment of the boundary conditions and symmetries about the fault.

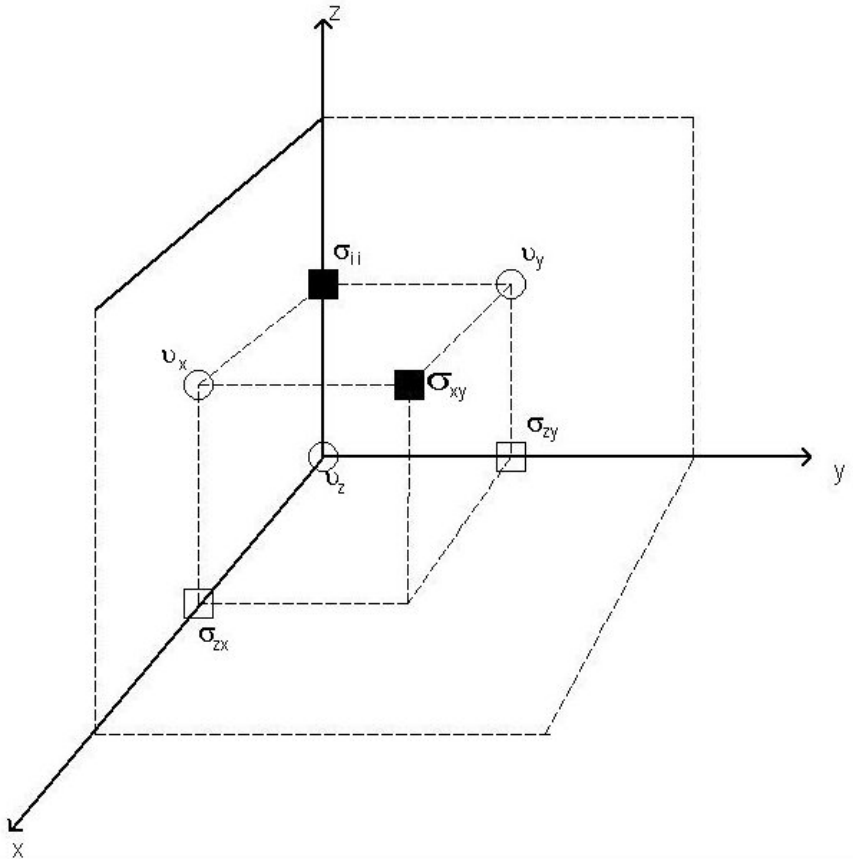

Figure 2.1. A cubic element of the 3D finite – difference grid used in the dynamic modeling of a planar shear fault (Madariaga *et al.*, 1998). σ and *v* represent the components of the stress tensor and particle velocity, respectively. The outer cube corresponds to the full cell, whereas the inner cube represents one eighth of it.

The wave equation (Equation 2.3) is solved with homogeneous initial conditions, i.e. initial velocities and stresses are all zero. All the waves propagating afterwards are generated by the fault. Since in the staggered – grid approach the stresses and velocities cannot be computed at the same grid points at thick fault zone extending one-half grid cell to each side of the fault axis is envisaged. The plane passing from the fault axis is called $z = zsc$ (Figure 2.2). In the shear fault case located in a homogeneous medium, v_x and v_y are antisymmetric and v_z is symmetric with respect to the plane $z = zsc$. Considering the stress components, σ_{zx} and σ_{zy} are symmetric while the normal stresses σ_{ii} and the shear stress

σ_{xy} are antisymmetric about the plane $z = zsc$. As it can be seen in Figure 2.1 and Figure 2.2, the antisymmetric velocity and stress components, v_x, v_y, σ_{ii} and σ_{xy} are computed at integer grid planes with respect to the fault plane ($zsc - 1$, zsc and $zsc + 1$) whereas the symmetric velocity and stress components v_z, σ_{zx} and σ_{zy} are computed at half integer planes, $zsc - ½$ and $zsc + ½$. To preserve the symmetry of the velocities and stresses the stress and velocity boundary conditions on the fault are applied differently. If the fault is slipping, the friction boundary conditions are imposed on the half integer planes $zsc - ½$ and $zsc + ½$. If the fault is locked, the velocity boundary conditions on the fault (that is $v_x = v_y = 0$) are applied on the fault plane zsc. The slip rate $\dot{D}$ between the walls of the fault is computed according to Equation 2.6.

$$\dot{D}(x, y, zsc) = v(x, y, zsc + \Delta z) - v(x, y, zsc - \Delta z) \tag{2.6}$$

Slip D is computed by numerical integration of the slip rate given in Equation 2.6.

For the kinematic model the source is implemented with the moment rate density, such that,

$$\dot{m} = \mu \dot{D} \tag{2.7}$$

where $\dot{D}$ is the slip rate on the fault (time derivative of Equation 2.4).

In fourth order simulations it is important that 4th order accuracy and symmetry are preserved so that in the 3DFD program the source moment tensor density is distributed over two lines of the grid situated on either side of the fault (Figure 2.2).

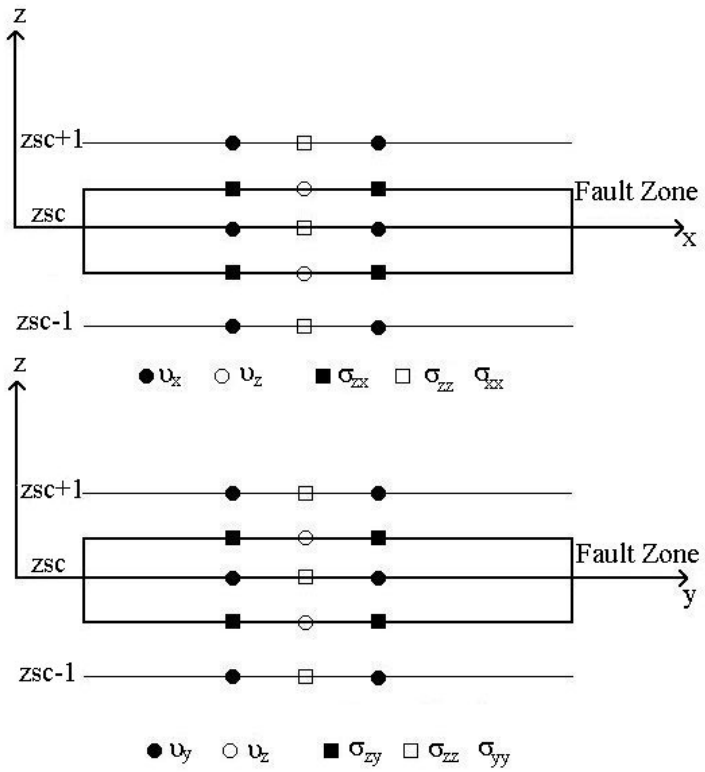

Figure 2.2. Vertical cross sections along *x* (top) and *y* (bottom) axes of the one grid thick fault zone (Madariaga *et al.*, 1998). The fault plane is set perpendicular to the *z* axis.

2.2. The Simulation Code Used in the Study – FD3D

The kinematic simulation code utilized in the present study was initially developed by Olsen (1994) in its scalar version. Appropriate boundary conditions were introduced by Madariaga *et al.* (1998). The code was completely rewritten and parallelized in 2002 – 2003 by Madariaga and Stoclet and subsequently modified by Frisenda and Madariaga in 2005 to incorporate various features such as finite source and variable slip. The code is written in FORTRAN 90 using MPI message passing interface. At the present stage it runs on the parallel processors installed in the Laboratory of Geology of Ecole Normale Supérieure in Paris.

2.2.1. The input and output files

The program needs three input files:

Input.dat: The file contains all the parameters necessary for simulation and storage of results. First the size of the cube and the number of processors that will be used in the analysis are specified. The dimension in vertical direction (z) is to be chosen such that if the number of processors to be used is "n", the cube can be divided into "n" horizontal layers of equal height. All other input data concerning the geometry of the cube, the time interval and the total duration of the analysis, as well as the stations for which the results will be stored are specified in this file. The program calculates the history of wave propagation at each point of the three dimensional grid. However as the storage of all this information is very difficult, it stores the ground motion only at time and grid intervals specified by the user. For instance if the time interval dt = 0.01s and time skip parameter ntskp = 50, ground motions at each node of the grid are stored every 0.5 s. The complete time history is stored only at the ground surface for stations with coordinates given in input.dat. The file also should contain information on the way the source will be incorporated in the model. The strike of the source is set parallel to x axis. Any dip angle can be specified. If the dip is 90º, the source is vertical and the second dimension of the source is set parallel to the z axis. The rake can be either 0 º or 90 º. That is at one time, only strike-slip or dip-slip dislocation can be accommodated by the program. The position of the rectangular source in the 3-D grid, the strike, the dip and the rake angles of the dislocation need to be specified in this file.

Structure.dat: The 3-D velocity structure (Vp, Vs and density) is defined in this binary file, which can be created by the little program makemodel.run for horizontally layered structures, or by makebasin.run for simple basin structures. Other than that any 3-D structure can be created in FORTRAN, with the condition that the structure is stored in binary format and in the order that will be read by the code.

The source: The program initially accommodated only Haskell type dislocation, in which a rupture initiated spontaneously at one end of the fault plane and propagated along the fault with constant rupture velocity and a constant amount of final slip. A trapezoidal source time function was considered. The file *source* contained the source time function created with the following parameters: rise time and total amount of slip reached at the end of the dislocation. Frisenda and Madariaga (2005) incorporated dislocation with a varying amount of slip at each node of the grid defining the finite fault. The rupture initiates at the

hypocenter and propagates radially with a constant rupture speed. The binary source file is generated by a small program that can be modified according to the needs of the user. In the study an exponential source-time function was used. The rise time at which each grid reaches its final amount of slip can be taken as constant throughout the fault or as a variable on each node. Rupture velocity, fault dimensions, location of the hypocenter, total source duration, rise time and amount of final slip at each node are the parameters required to define the source.

The program produces several output files. The velocity time histories v_x, v_y and v_z on the surface are stored at the time and grid intervals defined in the file *input.dat*. The files that correspond to directions *x*, *y* and *z* are named *SSX3Dmpiatt, SSY3Dmpiatt and SSZ3Dmpiatt* respectively. The velocity time histories on the vertical cross – sections *xz* and *yz* at the grid planes y = IYPOS and x = IXPOS, specified in the file *input.dat* are also stored. The files are named *SSX3Dmpixz, SSY3Dmpixz, SSZ3Dmpixz* and *SSX3Dmpiyz, SSY3Dmpiyz, SSZ3Dmpiyz* for v_x, v_y and v_z components in the *xz* and *yz* planes respectively. Snapshots of the wave propagation on the surface and also in the desired vertical cross – sections can be easily plotted with the help of these files. The complete velocity time histories v_x, v_y and v_z for the ground surface stations with coordinates also given in *input.dat* are saved in the files *sismox.dat*, *sismoy.dat* and *sismoz.dat* respectively. Data at these stations can be used for further detailed analyses of the waveforms.

2.2.2. Issues regarding the frequency resolution:

The frequency resolution is the main problem with the deterministic ground motion simulation methods. There are two imposing conditions on the choice of grid spacing “dh” and time interval “dt”. They are both related with the velocity structure. The first condition is that, in order to avoid numerical instabilities, the distance traveled by the wave with the highest velocity in one time interval should not be higher than a certain ratio of the grid spacing. This ratio is called the CFL (Courant – Friedrichs – Lewy) parameter (Courant *et al.*, 1928). In previous studies (i.e. Madariaga *et al.*, 1998) this ratio was taken as 0.43. In all the modeling works of the present study it is taken as 0.3. The grid spacing “dh” however is limited by the available computational power. The second condition is that, the frequency resolution of the simulation is governed by the number of nodes per minimum

shear wavelength used in the model. The frequency content of the slip model must be chosen so that the maximum frequency propagated by the grid has a wavelength that is longer than 8 grid steps. If higher frequencies are generated by the source they must be numerically damped in order to reduce spurious oscillations in the numerical simulations.

2.2.3. An example to be solved with FD3D

To demonstrate the computational power of the FD3D code, a simple example was designed. The simulation prism has dimensions of 65 km by 50 km by 20 km. The grid spacing is taken as 250 m, resulting in a grid of 260 * 200 * 80 nodes. The time interval is 0.01 s. A 30 km by 10 km strike slip fault is modeled with Haskell type dislocation and a trapezoidal source time function. The rise time is 2 s and the final amount of dislocation is 1m throughout the fault. The rupture propagates along the fault with a rupture velocity of 2.9 km/sec. The problem is solved for three different earth structures:

1. A homogeneous medium is modeled with P-wave and S-wave velocities of 6800 m/s and 3900 m/s respectively. The density of the medium is taken as 3300 kg/ m^3.
2. A horizontally layered earth structure is modeled with parameters given in Table 2.1.
3. A three dimensional basin structure is considered. The basin structure is taken similar to the one developed for the Marmara Sea in Turkey (Figure 2.3, Durukal *et al.*, 2007), but brought to half of its original size in every direction.

Table 2.1. The 1D earth model used in the example

DEPTH TO THE TOP OF LAYER (m)	Vp (m/s)	Vs (m/s)	DENSITY (kg/m^3)
0	3500	2200	2000
1000	5800	3400	2700
4000	6800	3900	3300

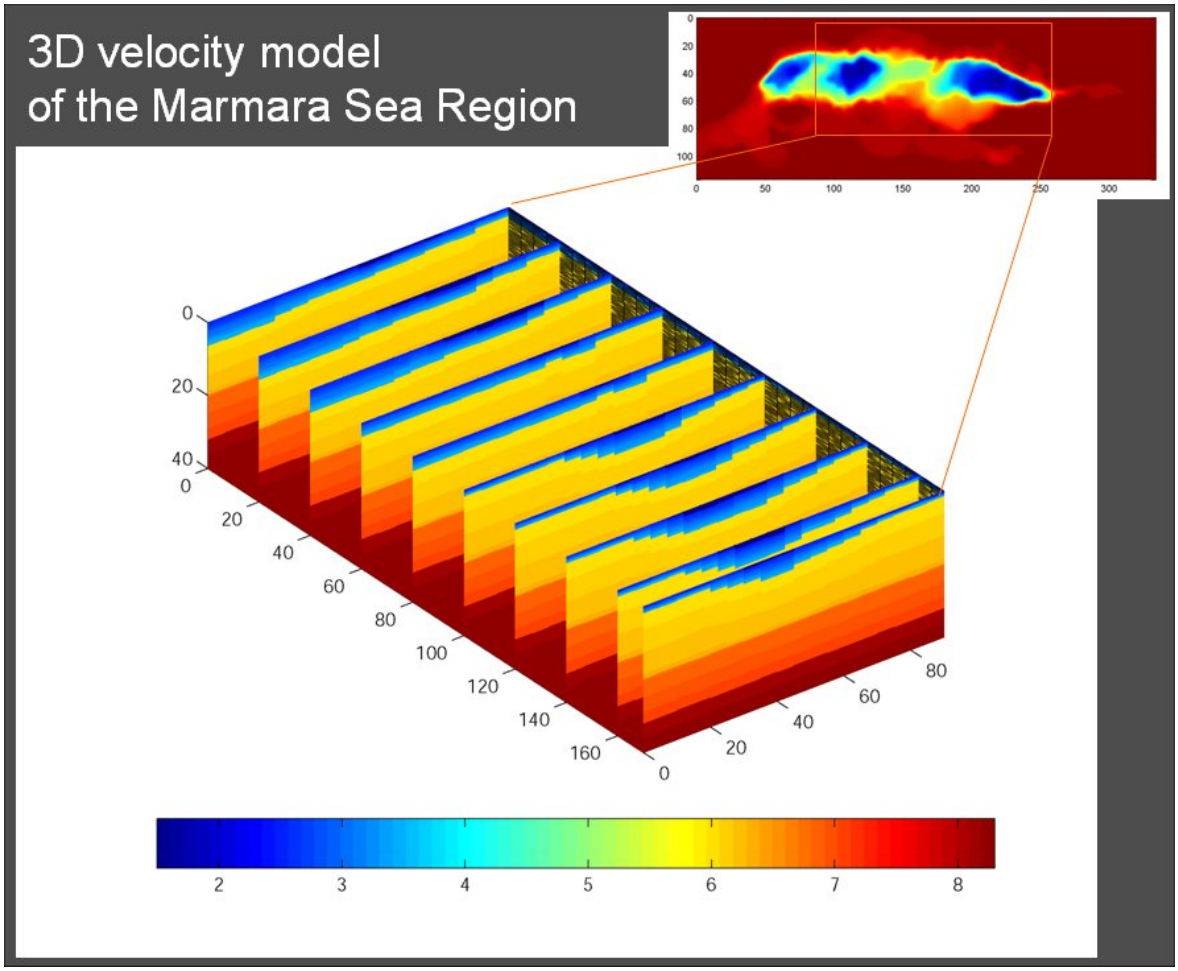

Figure 2.3. 3D P-wave velocity structure of the Marmara Basin (Durukal *et al.*, 2007)

Three planes were chosen to present the 3D wave field generated by the rupture of the strike-slip fault in each of the three earth models defined earlier. First fault parallel, fault normal and vertical velocities are plotted on the surface. Secondly, the same velocity components are plotted on a vertical plane parallel to the fault and thirdly, they are plotted on a vertical plane perpendicular to the fault. Figure 2.4 through Figure 2.6 present the wave propagation on those planes for the homogeneous earth model. Wave propagation for the horizontally layered model is given in Figure 2.7 through Figure 2.9. Figure 2.10 through Figure 2.12 represent the same triple for the 3D earth structure.

Time histories are computed for two stations shown on the first column of Figure 2.4, Figure 2.7 and Figure 2.10. The fault parallel, fault normal and vertical components of the velocity time histories low-pass filtered at 0.5 Hz and the associated Fourier Amplitude Spectra are presented in Figure 2.13 and Figure 2.14 for Stations 1 and 2 respectively.

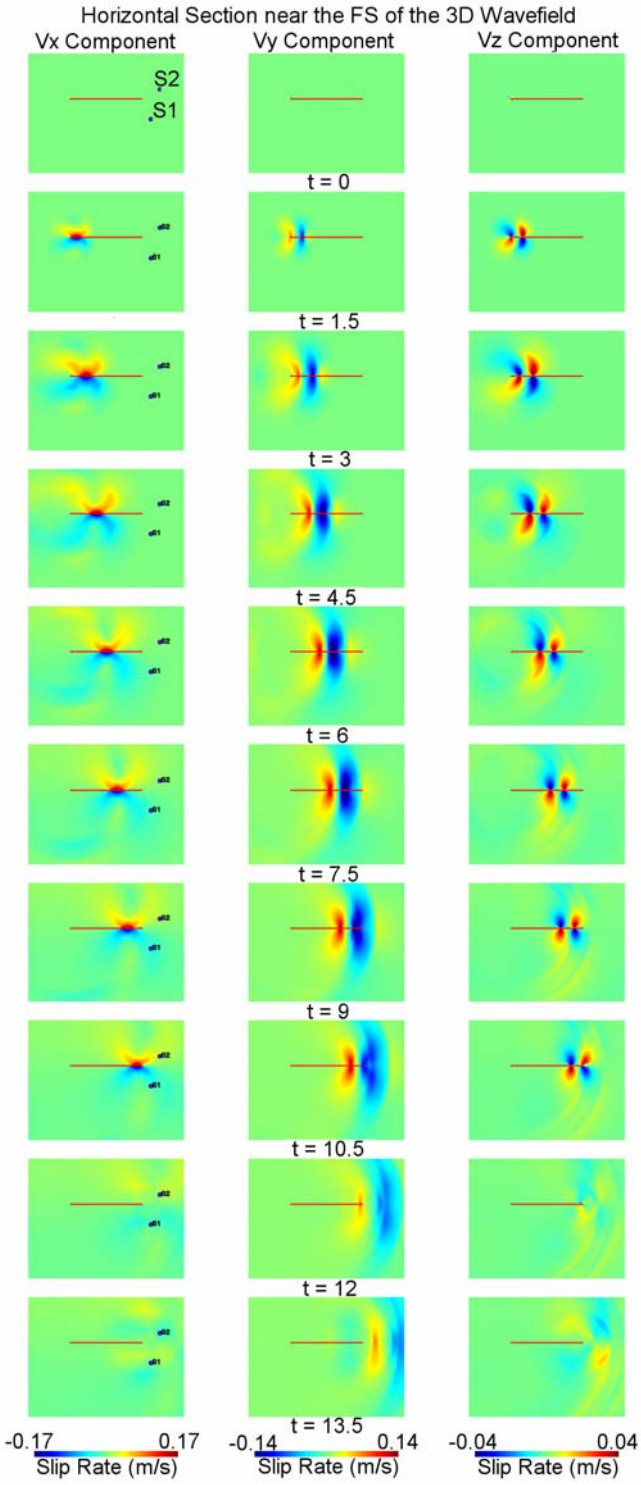

Figure 2.4. 3D wave propagation on the horizontal section near the free surface for the homogeneous earth model. The first, second and third columns present the propagation of the fault parallel, fault normal and vertical velocities respectively. The red line is the surface projection of the fault. S1 and S2 shown on the first column are the stations for which the time histories are provided.

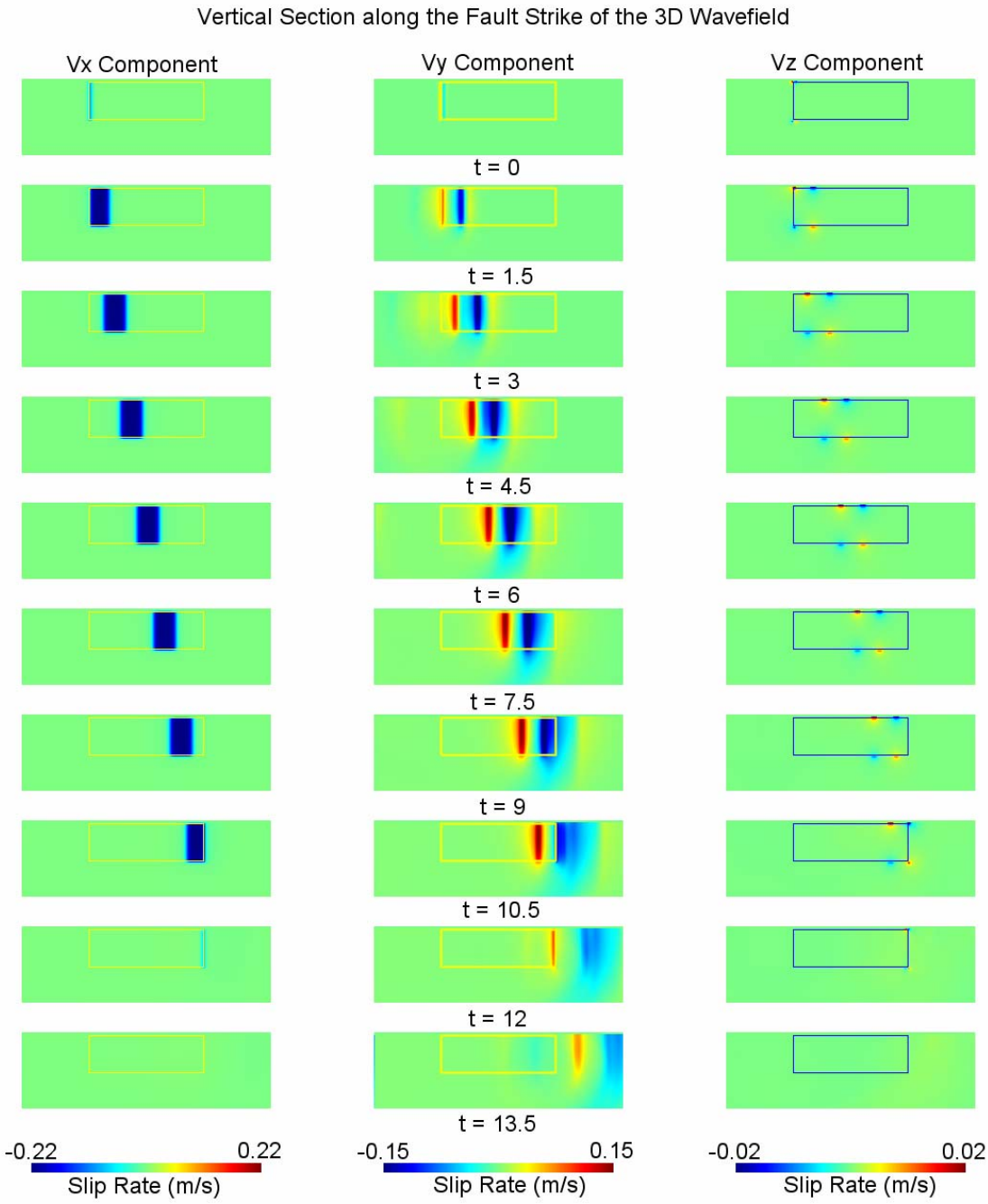

Figure 2.5. 3D wave propagation on a vertical plane parallel to the fault for the homogeneous earth model. The first, second and third columns present the propagation of the fault parallel, fault normal and vertical velocities respectively. The fault is presented by the rectangle.

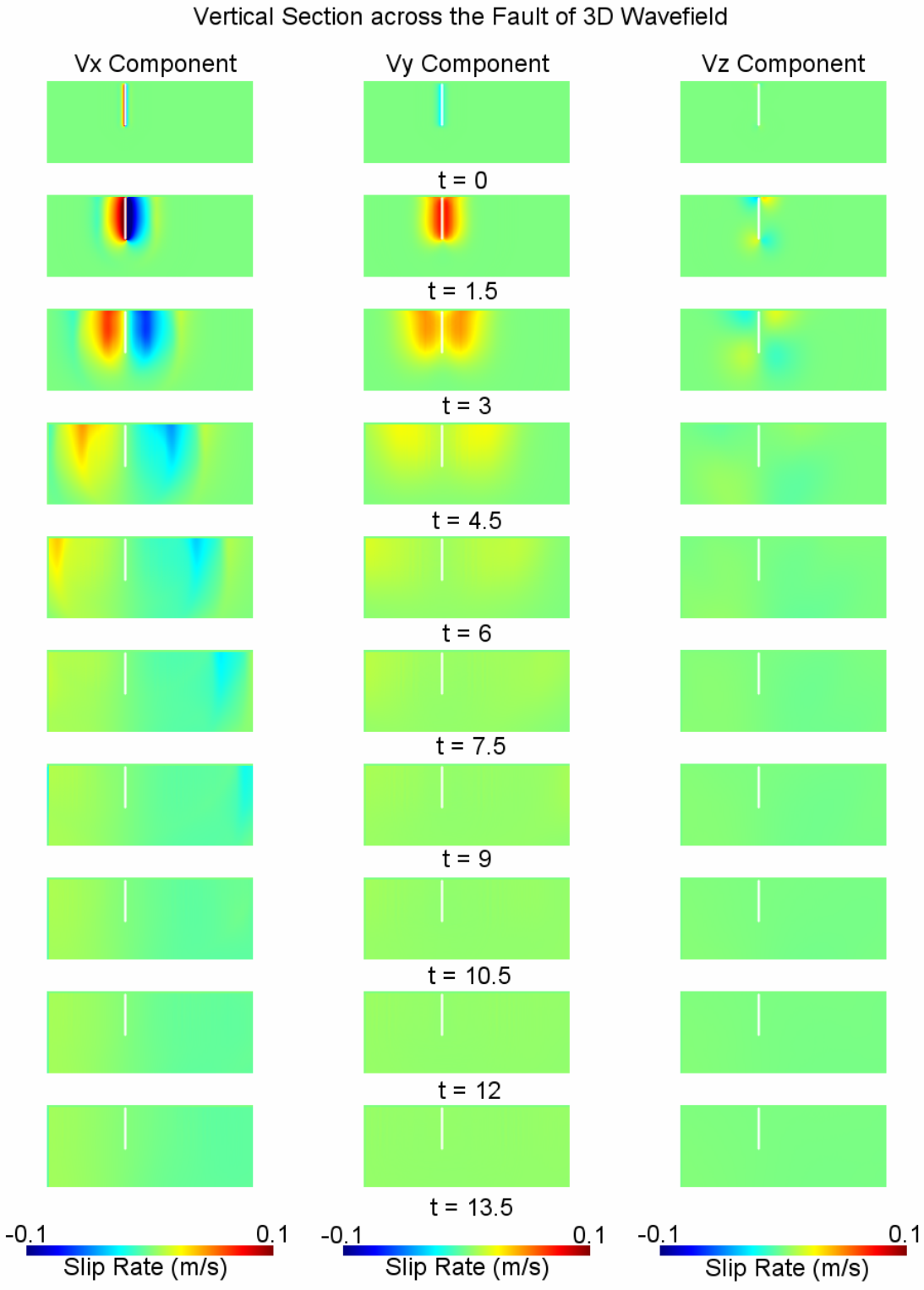

Figure 2.6. 3D wave propagation on a vertical plane perpendicular to the fault for the homogeneous earth model. The first, second and third columns present the propagation of the fault parallel, fault normal and vertical velocities respectively. The intersection of the fault with the representation plane is shown with the white line.

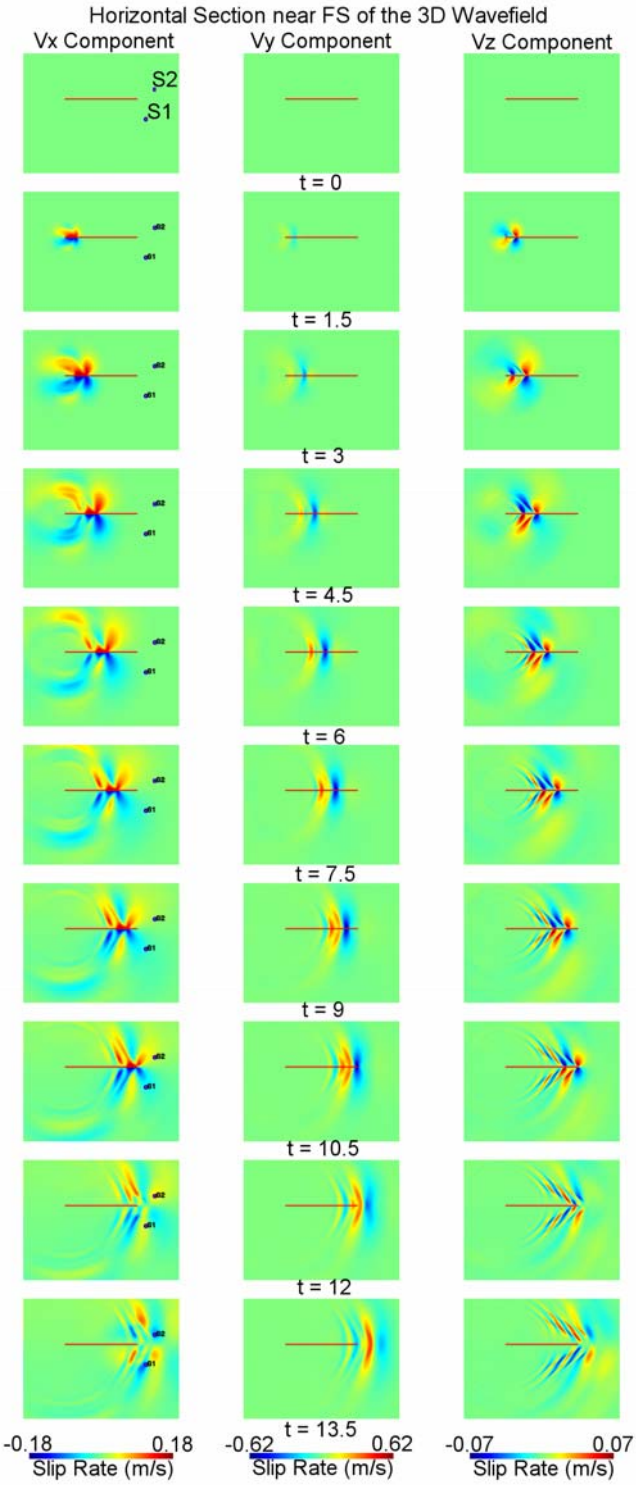

Figure 2.7. 3D wave propagation on the horizontal section near the free surface for the horizontally layered earth model. The first, second and third columns present the propagation of the fault parallel, fault normal and vertical velocities respectively. The red line is the surface projection of the fault. St1 and St2 shown on the first column are the stations for which the time histories are provided.

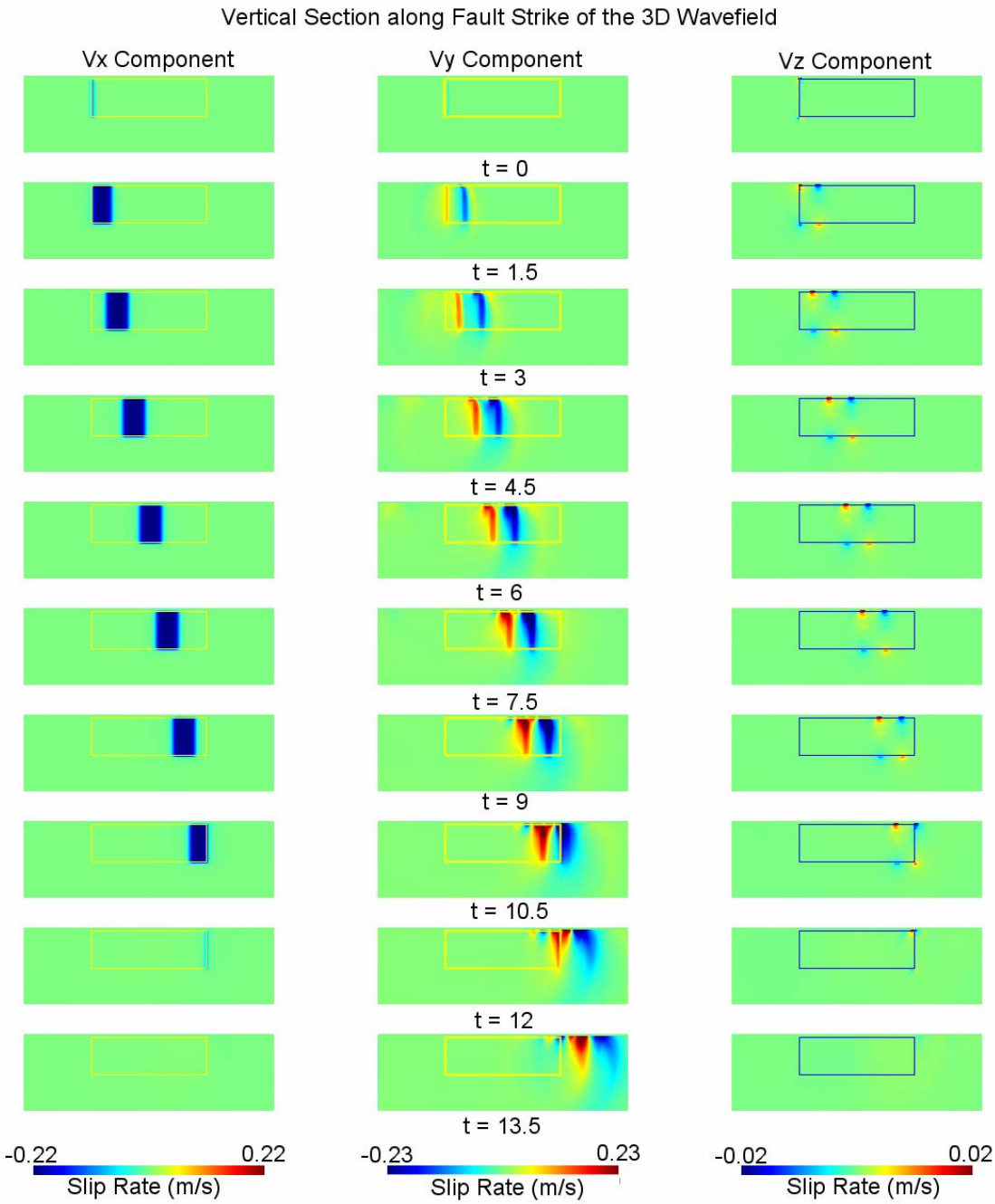

Figure 2.8. 3D wave propagation on a vertical plane parallel to the fault for the horizontally layered earth model. The first, second and third columns present the propagation of the fault parallel, fault normal and vertical velocities respectively. The fault is presented by the rectangle.

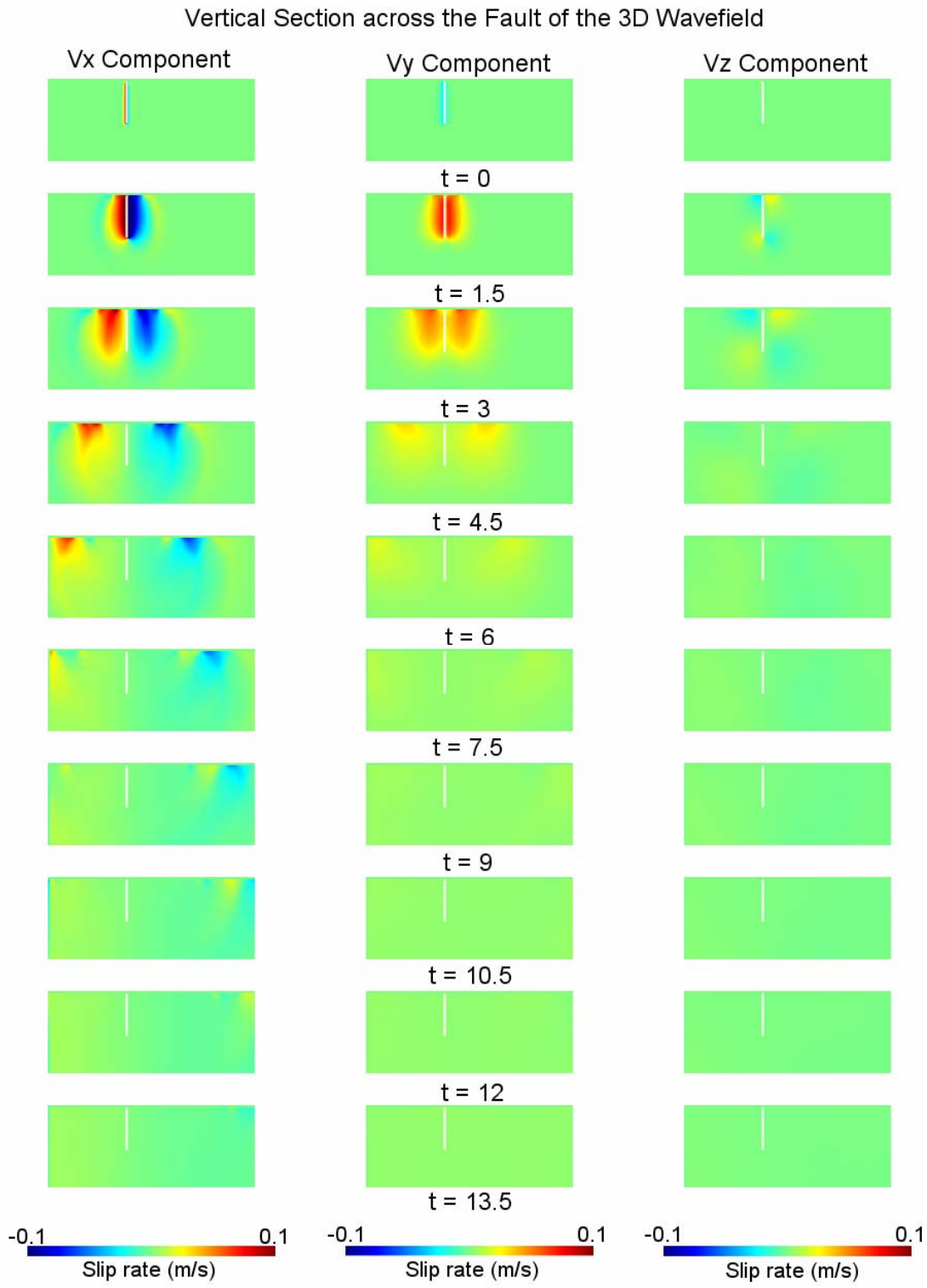

Figure 2.9. 3D wave propagation on a vertical plane perpendicular to the fault for the horizontally layered earth model. The first, second and third columns present the propagation of the fault parallel, fault normal and vertical velocities respectively. The intersection of the fault with the representation plane is shown with the white line.

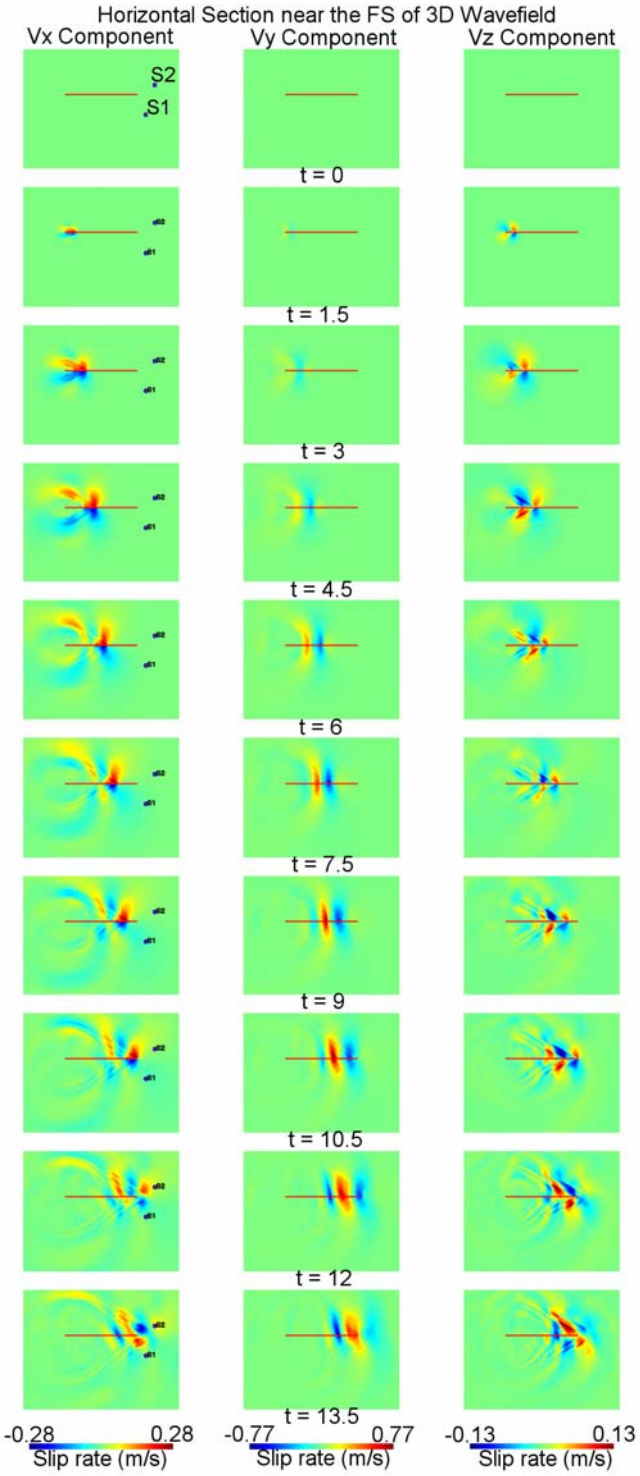

Figure 2.10. 3D wave propagation on the horizontal section near the free surface for the 3D earth model. The first, second and third columns present the propagation of the fault parallel, fault normal and vertical velocities respectively. The red line is the surface projection of the fault. St1 and St2 shown on the first column are the stations for which the time histories are provided.

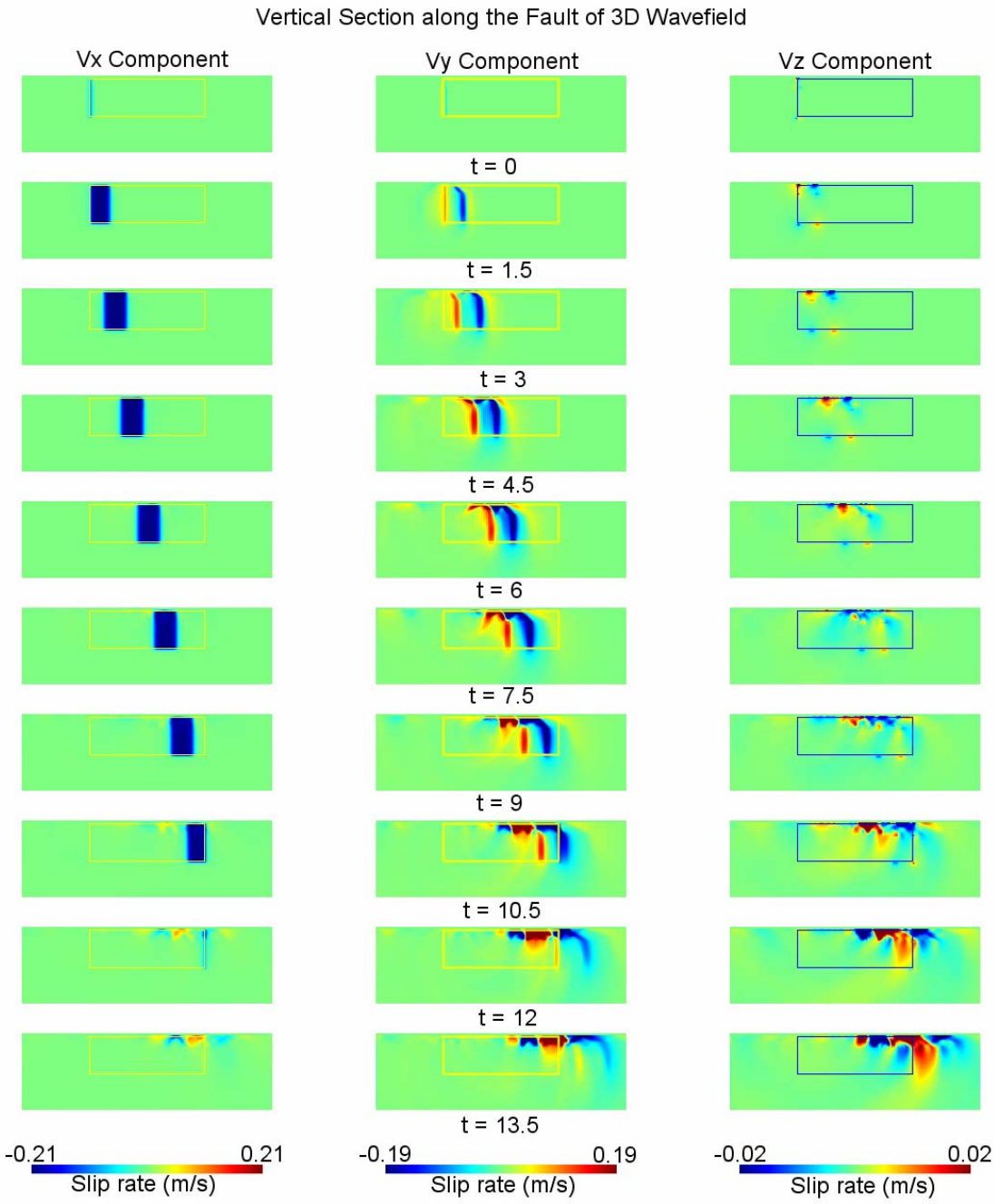

Figure 2.11. 3D wave propagation on a vertical plane parallel to the fault for the 3D earth model. The first, second and third columns present the propagation of the fault parallel, fault normal and vertical velocities respectively. The fault is presented by the rectangle.

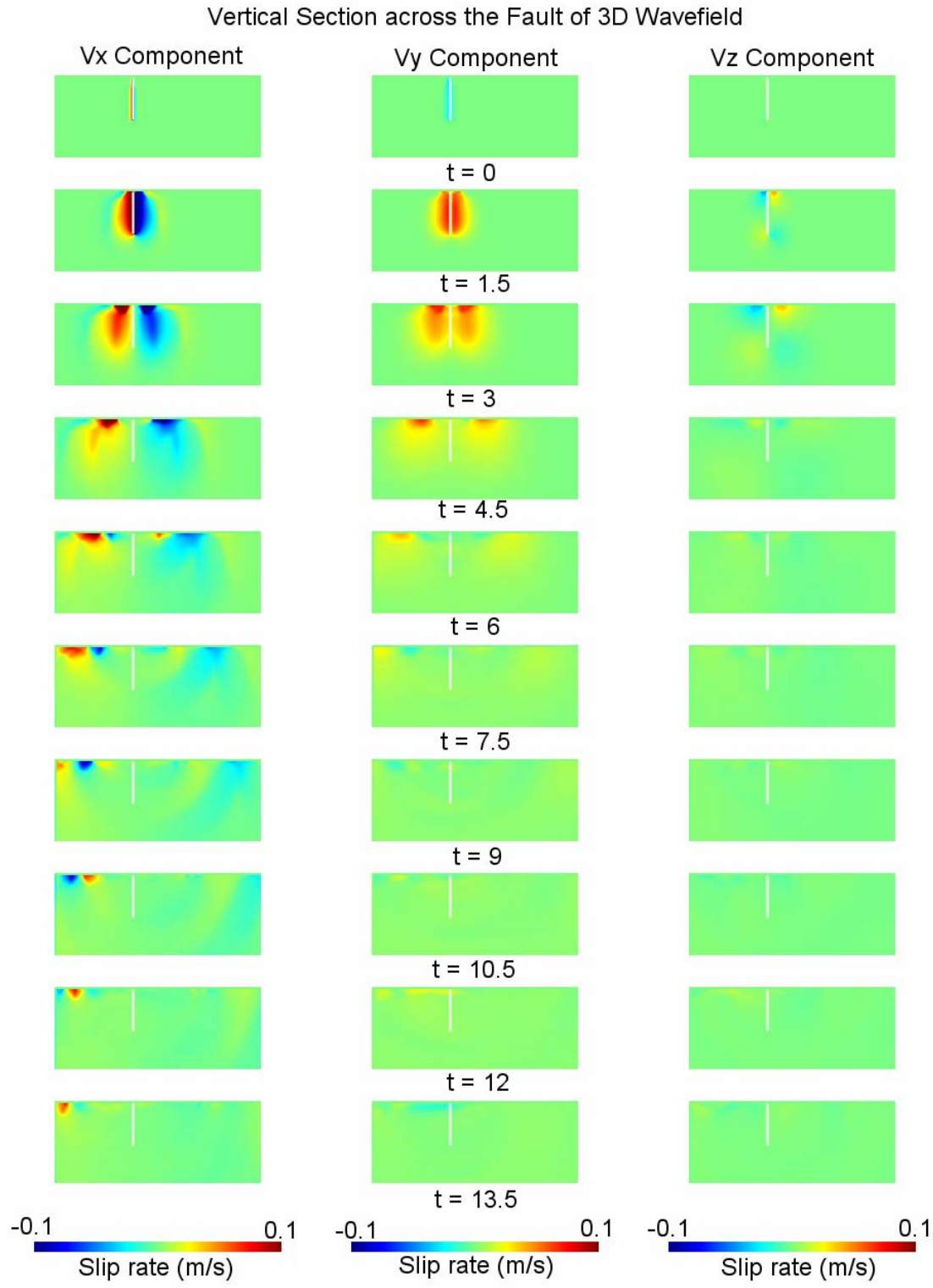

Figure 2.12. 3D wave propagation on a vertical plane perpendicular to the fault for the 3D earth model. The first, second and third columns present the propagation of the fault parallel, fault normal and vertical velocities respectively. The intersection of the fault with the representation plane is shown with the white line.

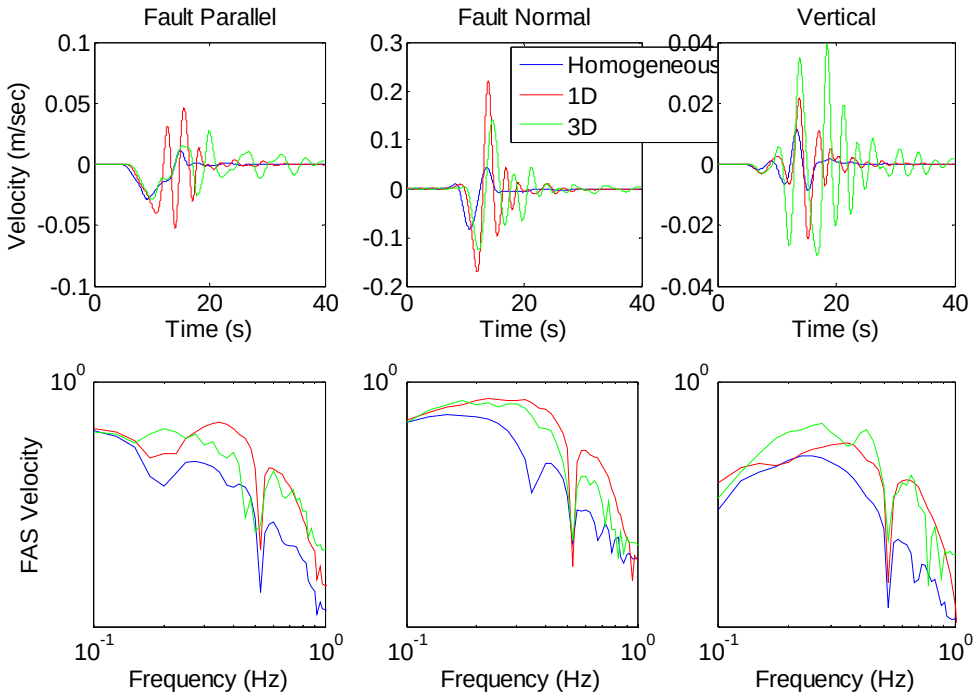

Figure 2.13. Velocity time histories simulated for Station 1 and the associated Fourier Amplitude Spectra

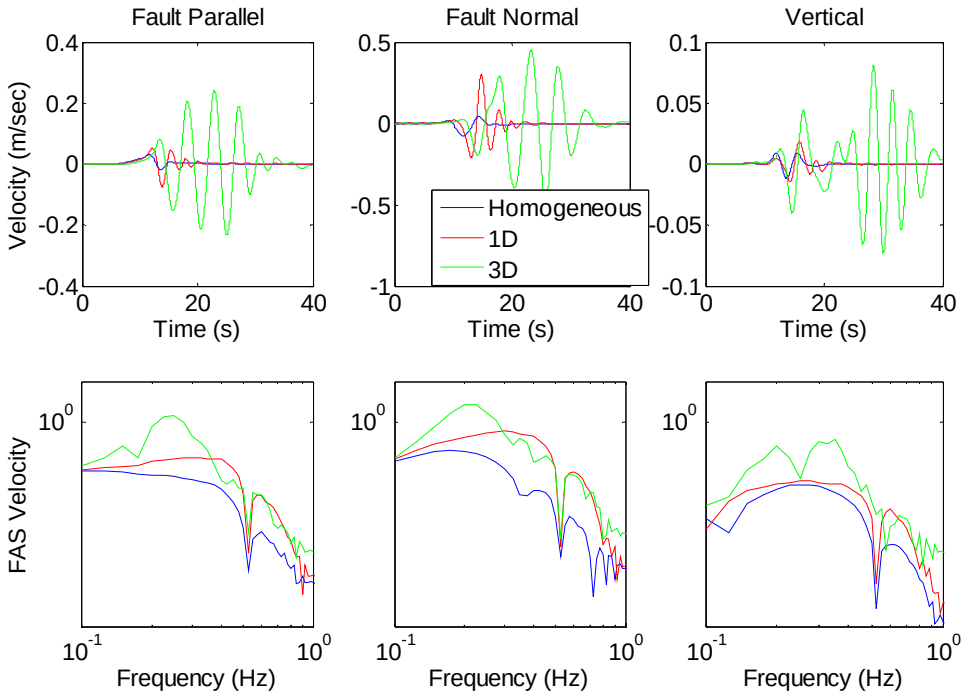

Figure 2.14. Velocity time histories simulated for Station 2 and the associated Fourier Amplitude Spectra

Comparing the simulations on Figure 2.4 for the homogeneous model and Figure 2.7 for the layered structure is very instructive. The surface wave field for the homogenous model is very simple, with the typical fault parallel fling and fault normal double pulses (red and blue zones). The wave field for the layered model shows clear evidence of shock waves, the plane wave fronts emanating at an angle from the rupture front in the V_x and V_z components. These waves appear because the rupture propagates at depth with a higher rupture speed (2900 m/s) than the shear wave speed in the shallow layer (2200 m/s). This figure is interesting because it shows that it is very easy to mistakenly think that ruptures are super-shear when observing them on the surface. The apparent super-shear shock waves only appear in the shallow layer as shown in the cross sections of Figure 2.8 and Figure 2.9.

Figure 2.10 to Figure 2.11 show many interesting features of the wave field produced by a simple source model when waves propagate inside a 3D basin. First the main features of the field on the surface are heavily distorted with strong amplification on one side of the fault (Figure 2.10). Second, the transverse pulse has now a more complex structure with three lobes near the end of the central panel. This means that if the basin is not taken into account in the interpretation of the simulations, it may be mistakenly concluded that the source time function changes sign. Lastly, as observed in the V_x and V_z component Rayleigh waves have been generated inside the basin by the interaction between the rupture front and the 3D velocity structure of the basin. The complexity of these Rayleigh waves is neatly observed in the cross-sections of Figure 2.11.

The seismograms in Figure 2.13 and Figure 2.14 show the effect of the basin on the seismograms of St1 and St2 respectively. St1 is located on relatively firm ground, whereas St2 is located directly on the basin. The large ringing waves that show on the 3D simulations are surface waves. As shown by TeraShake simulations of the Los Angeles basin, these waves are the most important sources of strong ground motion at intermediate frequencies of the order a fraction of a Hertz. In the Marmara Sea basin, they have characteristic frequencies of about 3 s. Further work will be needed to exploit these interesting results.

The program input files for the models presented in Section 2.2.3 are given in Appendix A.

2.3. Comparison of FD3D with Other Low Frequency Simulation Methods

In this section, simulations are carried out using simple models to test the validity of the results provided by the 3D Finite Difference code. For this purpose the analytical method of Luco and Anderson (1983) and the Discrete Wavenumber Method for an extended source of Bouchon (2003) are chosen. The parametric study provided in Anderson and Luco (1983, a and b) is taken as a base. Layouts as similar as possible to that one are modeled with the other two methods and the results are compared.

2.3.1. The Analytical Method of Luco and Anderson (1983)

In 1983, Luco and Anderson presented an analytical method to evaluate the transient response on the surface of an elastic half-space for a kinematic dislocation over an infinitely long fault of finite width and arbitrary dip. In three consecutive papers (Luco and Anderson, 1983; Anderson and Luco, 1983, a and b) the authors first derive a general integral representation for the displacement field on the surface of an elastic half-space for an arbitrary distribution of body forces, then for the general case of a slip dislocation over a plane region and for the particular case of a uniform slip dislocation. In the last two papers the authors utilize the obtained solution to study the characteristics of the near field ground motion for both vertical strike-slip faults and thrust faults with a given dip angle. The layout of the numerical example is provided in Figure 2.15. An 8 km deep vertical fault located at z_u = 2 km below the surface is considered. The slip function is described by a ramp with a finite duration of 2 s and a final dislocation amount of 1 m. The horizontal rupture velocity, C_1, is 3.184 km /s, whereas the vertical rupture velocity, C_2, is infinity, resulting in a vertical rupture front, similar to Haskell type dislocation. The P-wave and S-wave velocities of the homogeneous earth medium are taken as 6.0 km/s and 3.461 km/s respectively. The waveforms are obtained for stations located at 0.5 km, 1 km, 2 km, 5 km, 10 km and 20 km perpendicular to the fault. The resulting velocities and displacements are presented in Figure 2.16 and Figure 2.17 for strike-slip and dip-slip rupture cases respectively.

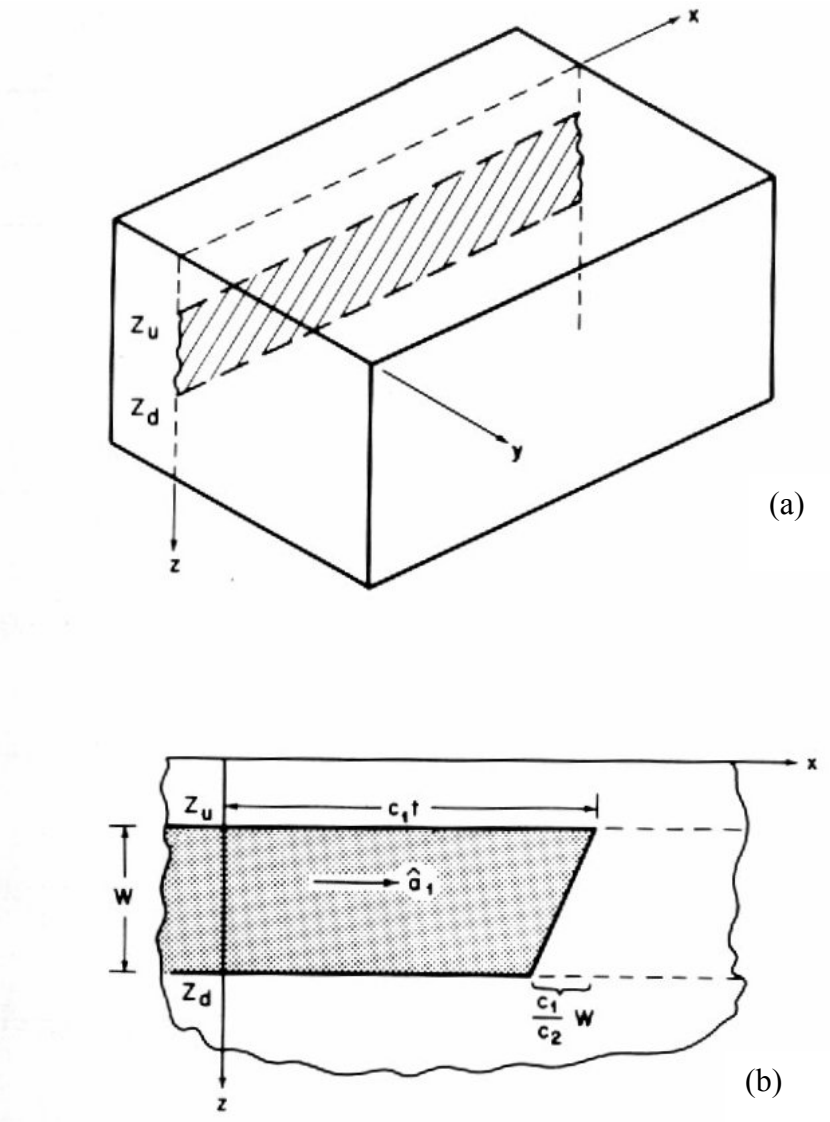

Figure 2.15. Description of the model (Anderson and Luco, 1983 a). (a) The plane shaded area is the vertical fault. Rupture occurs between z_u and z_d, and extends to $\pm\infty$ in the x direction. (b) Plan view of the plane containing the fault. The shaded area represents the part of the fault that has ruptured at time t. Slip on the fault is constant and is constrained to be horizontal.

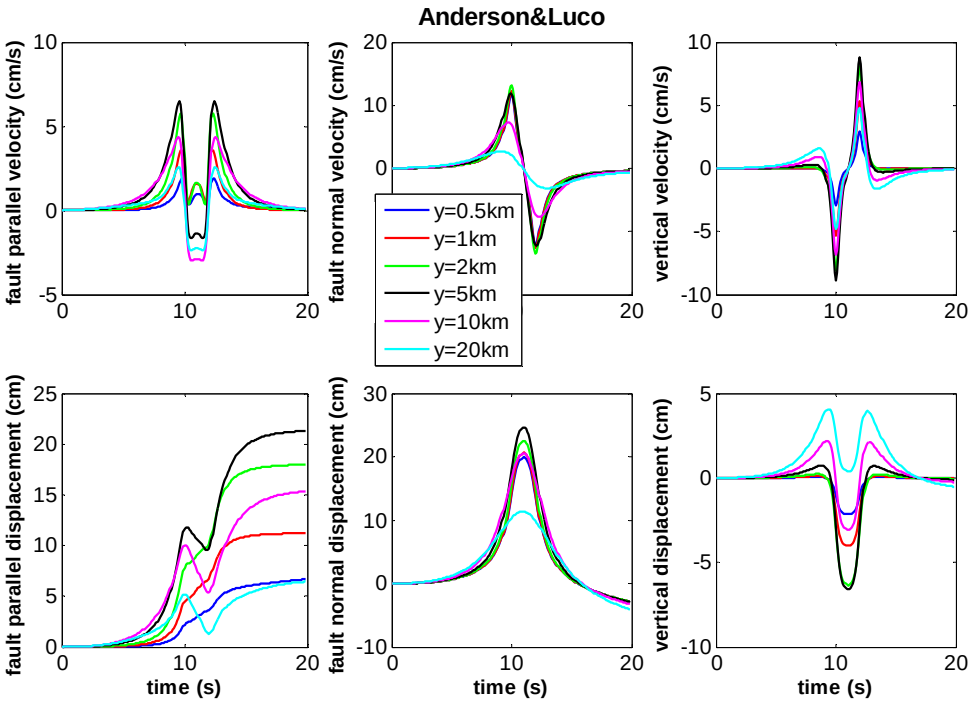

Figure 2.16. Velocities and displacements computed by Anderson and Luco (1983) method for strike-slip rupture

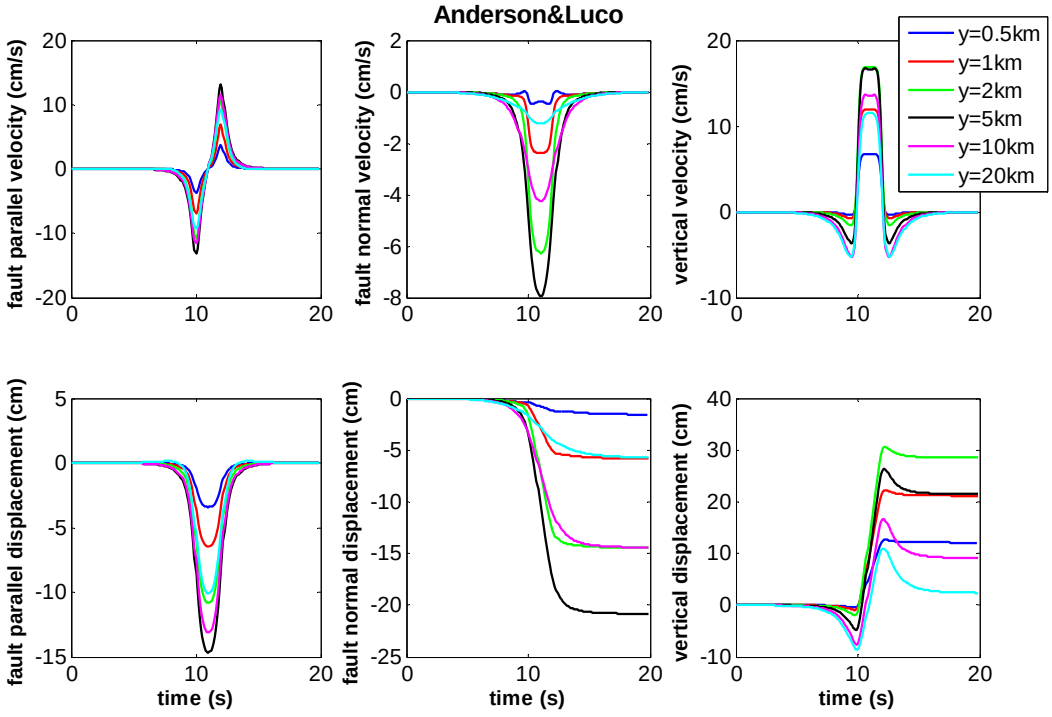

Figure 2.17. Velocities and displacements computed by Anderson and Luco (1983) method for dip-slip rupture

2.3.2. Solution with FD3D

The Haskell source version of the program FD3D was checked against the results provided by Anderson and Luco (1983, a and b). The simulation layout is given in Figure 2.18. The fault length is taken as 80 km to approximate the infinite fault considered by Luco and Anderson (1983). The velocity structure is the same as the one used in Section 2.3.1. . A grid spacing of 250 m and a time interval of 0.01 s are considered. The rupture is a Haskell type dislocation with a trapezoidal source time function and a rise time of 2 s. This corresponds to a ramp type dislocation smoothed at both ends. The final amount of displacement is 1 m throughout the rupture surface. The resulting velocities and displacements are presented in Figure 2.19 and Figure 2.20 for strike-slip and dip-slip ruptures cases respectively.

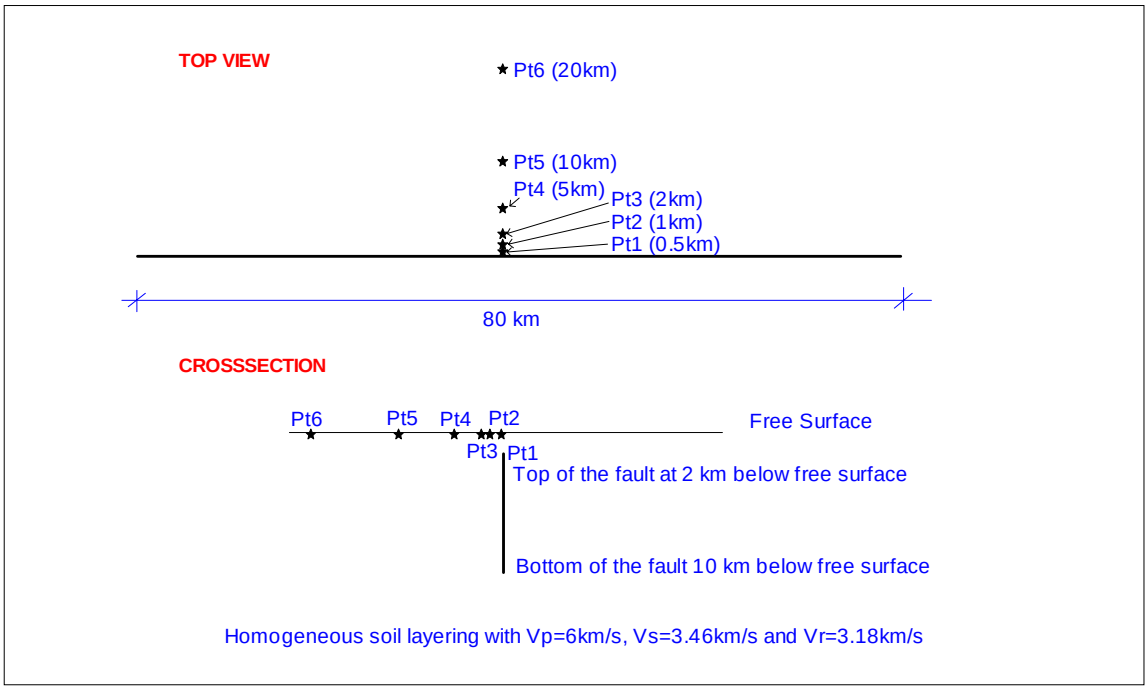

Figure 2.18. The simulation layout

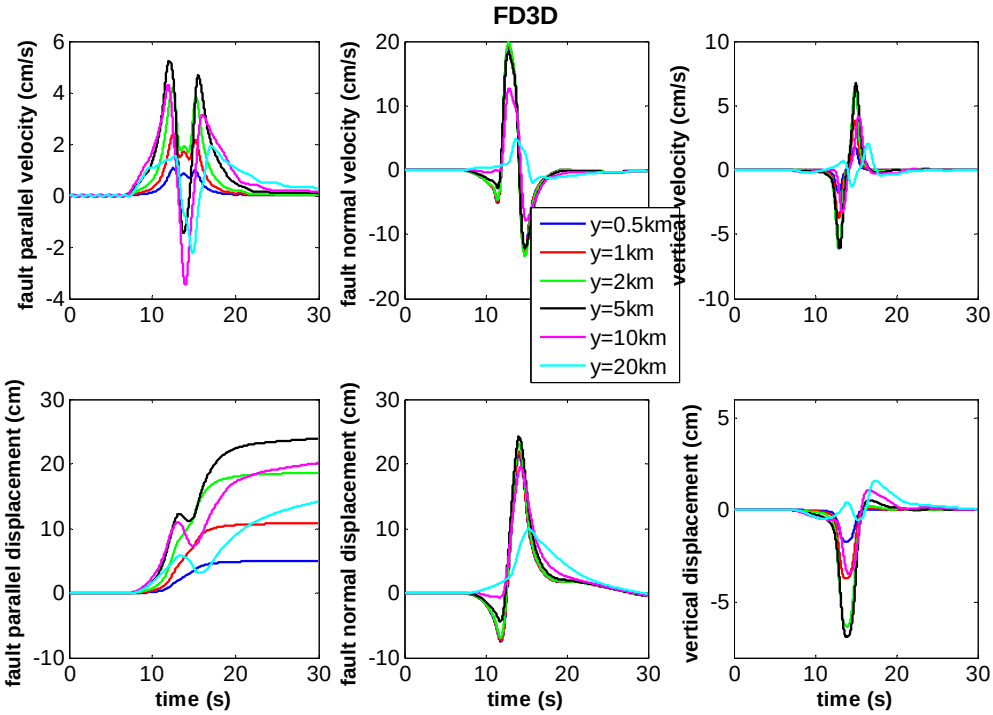

Figure 2.19. Velocities and displacements computed by FD3D for strike-slip rupture

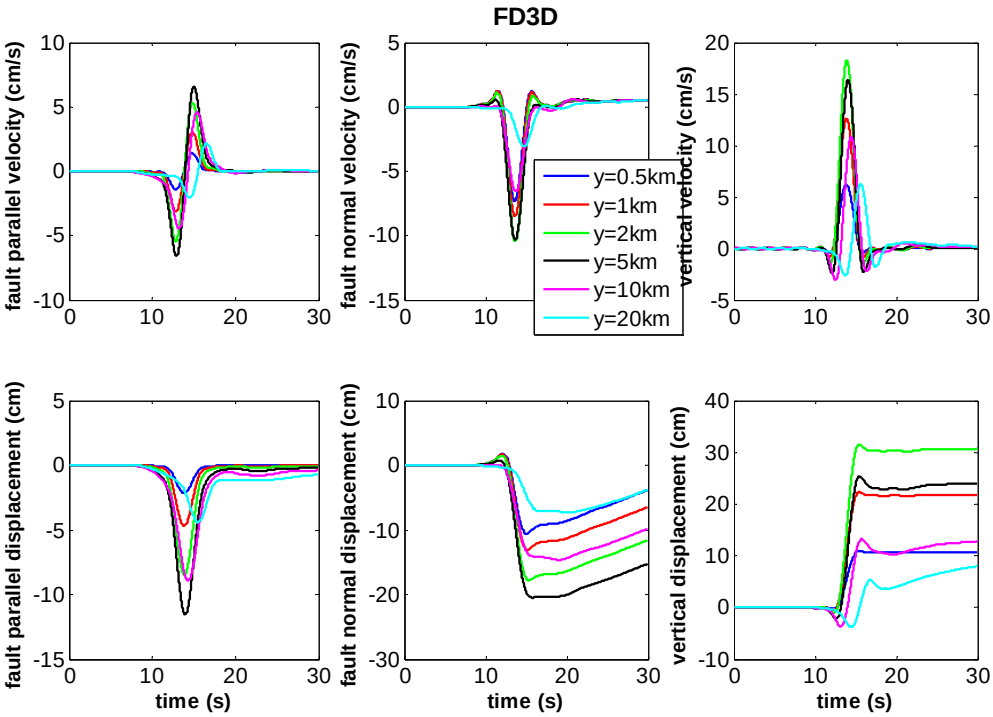

Figure 2.20. Velocities and displacements computed by FD3D for dip-slip rupture

2.3.3. Discrete Wavenumber Method

Bouchon (2003) presented a method to calculate the elastic radiation from an extended source using the discrete wave number method, where the source is represented by a superposition of elementary point sources. In the case of an earthquake, the fault is discretized into a two dimensional grid of double-couple point sources with a spacing smaller than the shortest wavelength considered. Slip amplitude and duration may vary at each point. The phase delay between each point source and the hypocenter is given by $e^{-i\omega t_r}$ where t_r is the time taken by the rupture front to propagate from the hypocenter to a particular point on the fault grid. Bouchon (2003) gives an application of this method where the ARC (Arcelik) and SKR (Sakarya) records of the 1999 Kocaeli earthquake are simulated.

For the Discrete Wavenumber simulations the following case is considered. The 80 km long fault plane is located between depths z_u = 2 km and z_d = 10 km and consists of 40 by 4 subfaults with dimensions of 2 km by 2 km. The hypocenter is located at 2 km depth. The rise time is taken as 2 s. The final amount of displacement is 1 m throughout the rupture surface. The resulting velocities and displacements are presented in Figure 2.21 and Figure 2.22 for strike-slip and dip-slip ruptures cases respectively.

The comparison of Fourier Amplitude Spectra of velocity time histories for the strike-slip rupture case are given in Figure 2.23 through Figure 2.25 for fault parallel, fault normal and vertical components respectively.

It should be noted that for the Discrete Wavenumber case, the rupture initiates at the hypocenter and propagates radially, whereas in the other two methods Haskell type dislocation is considered with rupture initiating along the vertical edge of the fault. When the fault normal velocities in Figure 2.20 and Figure 2.22 are compared, it can be observed that the total pulse duration in the DWNM is longer than FD3D. This would suggest the use of a lower cut-off frequency in the DWNM method.

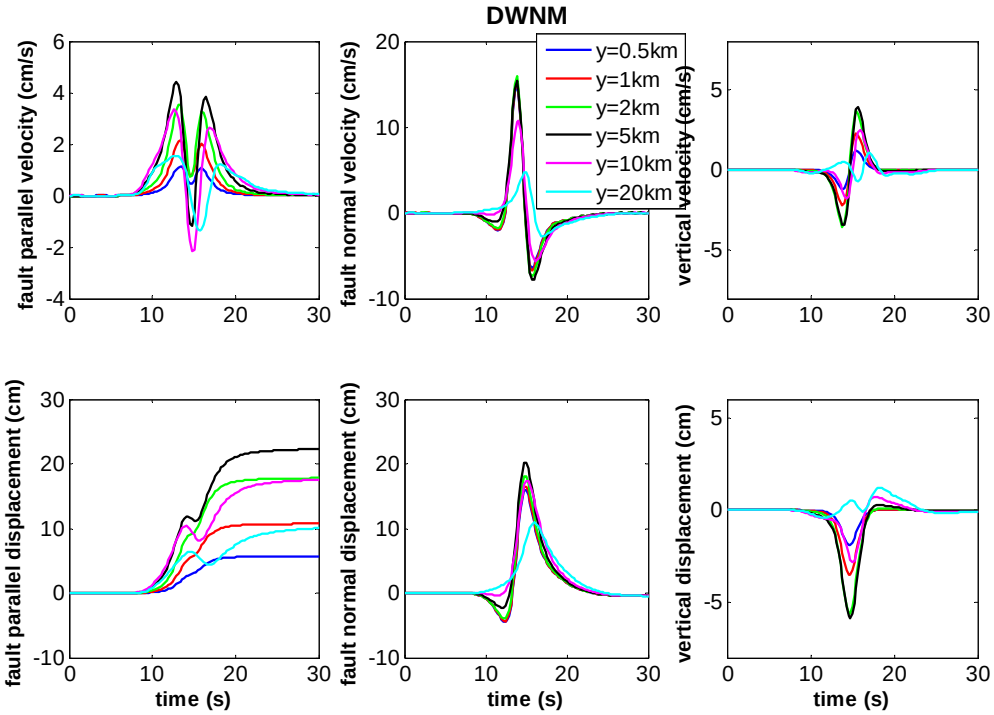

Figure 2.21. Velocities and displacements computed by DWNM for strike-slip rupture

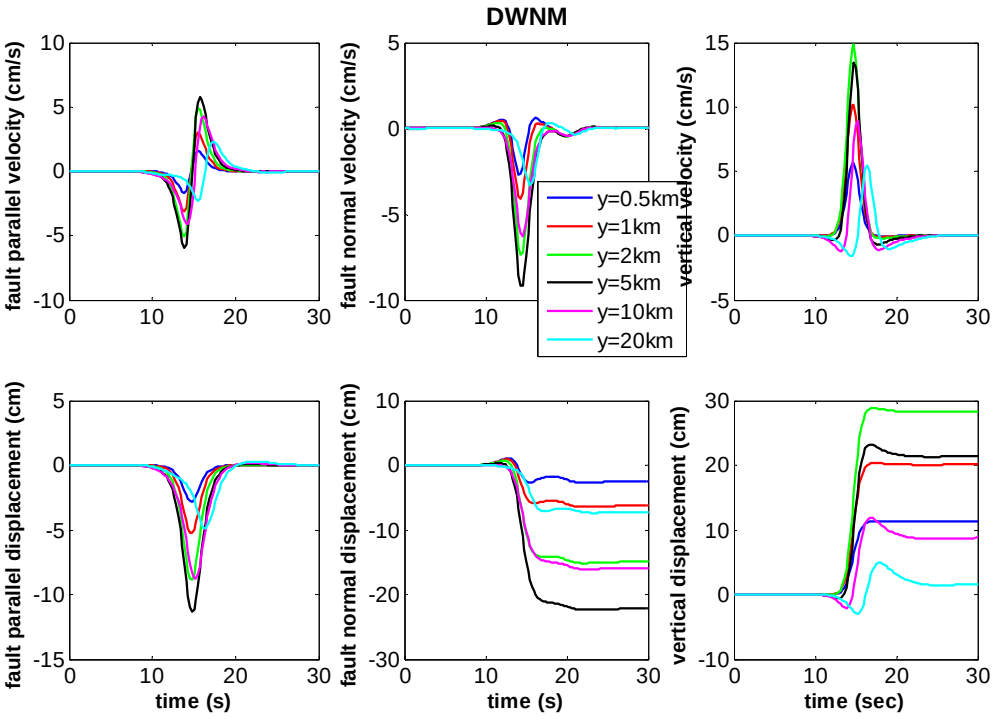

Figure 2.22. Velocities and displacements computed by DWNM for dip-slip rupture

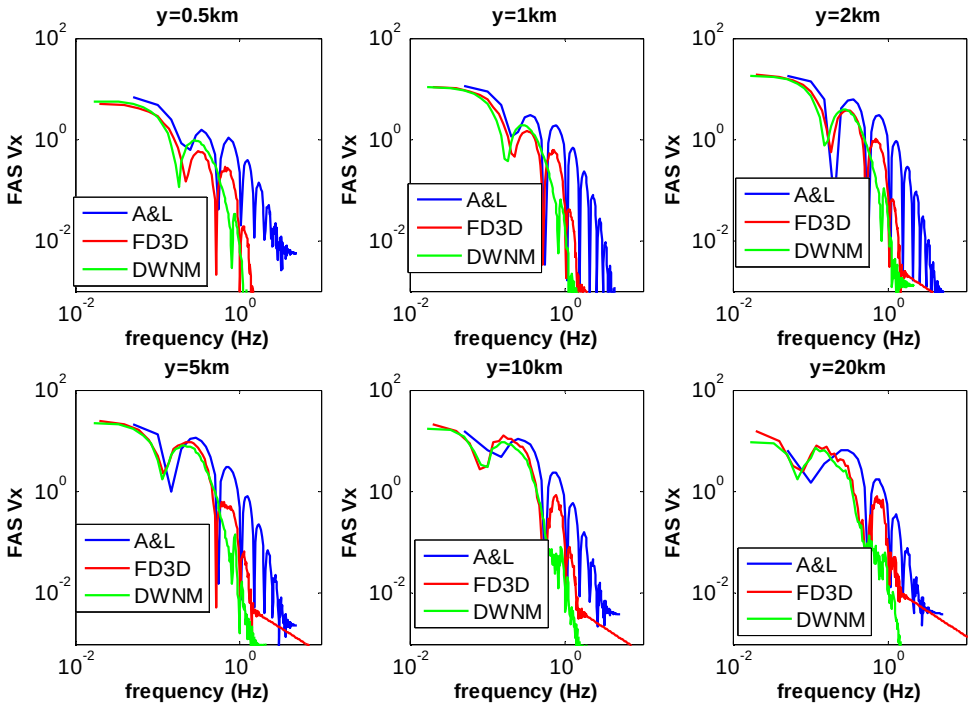

Figure 2.23. Comparison of Fourier Amplitude Spectra of fault parallel velocity time histories for the strike-slip rupture case

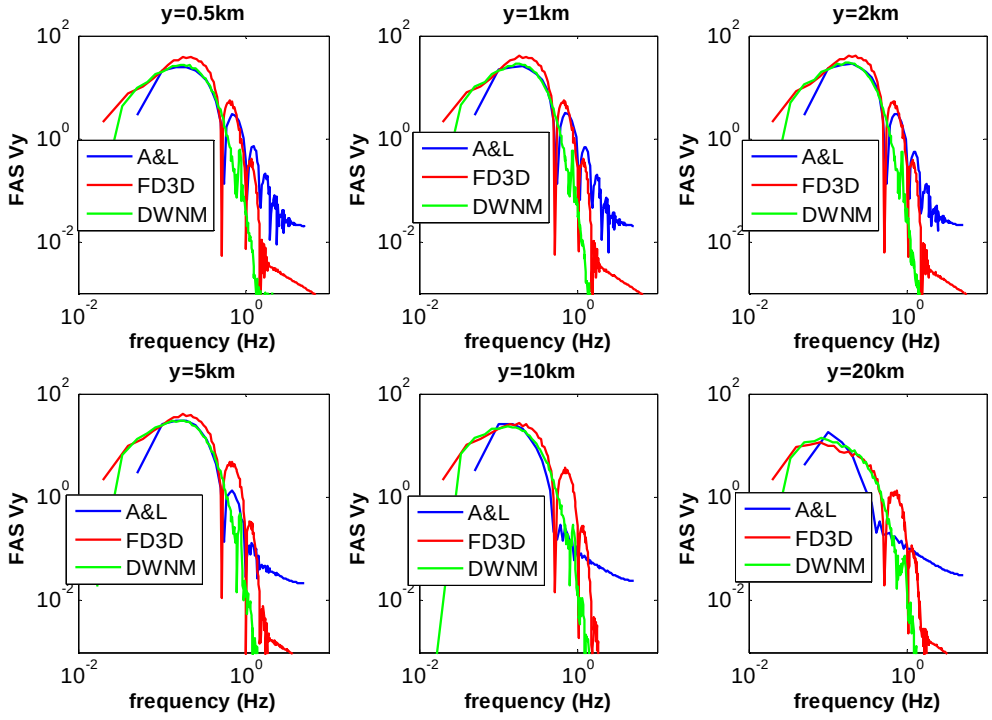

Figure 2.24. Comparison of Fourier Amplitude Spectra of fault normal velocity time histories for the strike-slip rupture case

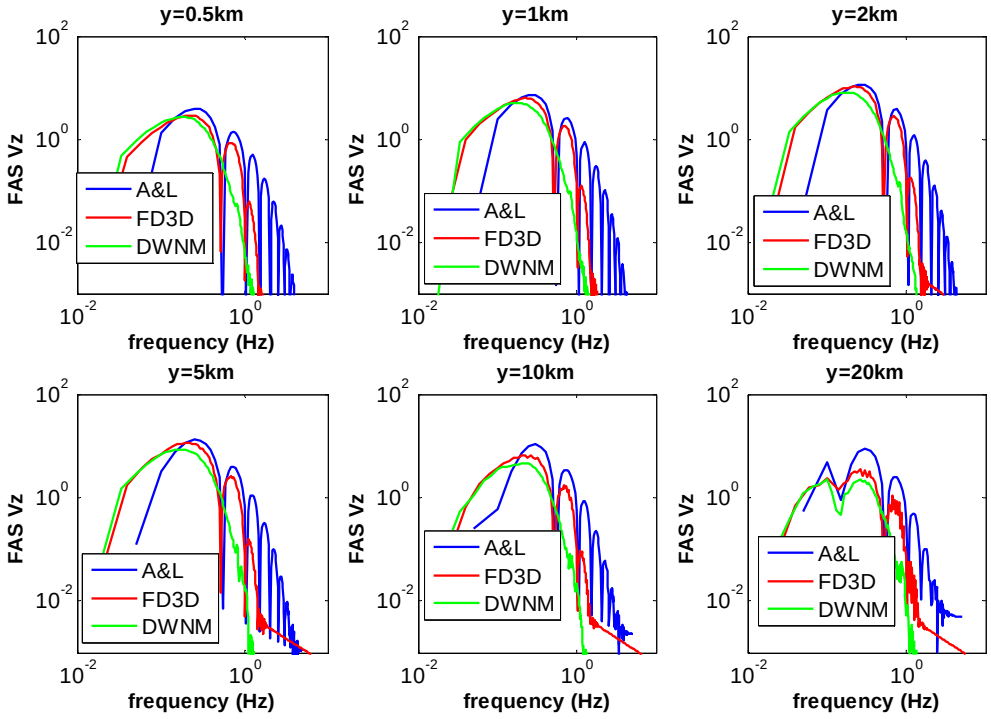

Figure 2.25. Comparison of Fourier Amplitude Spectra of vertical velocity time histories for the strike-slip rupture case

The motion caused by a finite fault with constant rupture velocity and slip, rupturing past a site can be interpreted as consisting of a starting phase, a phase associated with the passage of the rupture event, and a stopping phase. The radiation patterns of the starting and stopping phases are such that some components of the motion associated with these phases nearly vanish in the vicinity of the fault. As such, motions caused by the infinite-length fault dislocation model, considered in Anderson and Luco (1983) correspond to the rupture passage phase. The simulations by FD3D and DWNM are however obtained by a finite fault of 80 km length and include all the three phases of rupture passage. This difference is mainly observed in the observation point located 20 km away from the fault for which the fault cannot be considered as infinite. Another difference is that Anderson and Luco (1983) use either a step or a ramp dislocation function. The results for the ramp dislocation are used for the comparison. In FD3D however, a trapezoidal source time function is used, giving rise to a ramp dislocation curved in the rupture initiation and ending phases.

Considering the facts cited above, it can be concluded that all the three methods give comparable results in the waveforms, amplitudes and durations of the ground motion. Some differences are however observed in amplitudes and waveforms. Evaluation of the differences resulting from various simulation methods was the subject of a benchmark study conducted by Durukal *et al.* (2006) elaborated in the following section.

2.4. The Benchmark Study

Although most of the codes that are being used for ground motion simulation purposes rely on the same theoretical basis, variations in numerical implementation may result in simulated waveforms that differ from each other even if similar input parameters are used in the definition of the source, path and local soils. To understand the degree and extent of ground motion variability introduced by selected kinematic simulation codes, to check for cross-code variability, to check for inter-station variability introduced by different codes and to check the performance of available codes a parametric study for the source parameters was carried out by Durukal *et al.* (2005). The simulation layout consisted of 45 simulation points, a one-dimensional crustal model and a vertical fault plane (40 km by 20 m) with a strike-slip mechanism. The codes by Madariaga, Bouchon, Spudich, Wang and Irikura were included in the exercise. The simulation points were positioned at 1, 5, 15, 30 and 50 km distance to the fault with 9 observation points in each line. The simulation area covered 150 km x 50 km (Figure 2.26). The varied source parameters were slip, rise time, depth of asperity, rupture velocity and subfault size. The base case consisted of a homogeneous slip distribution of 1.5 m along the fault with a rise time of 2.0 s. The fault was located at 1km below the surface and a rupture velocity of 3.0 km/s was considered.

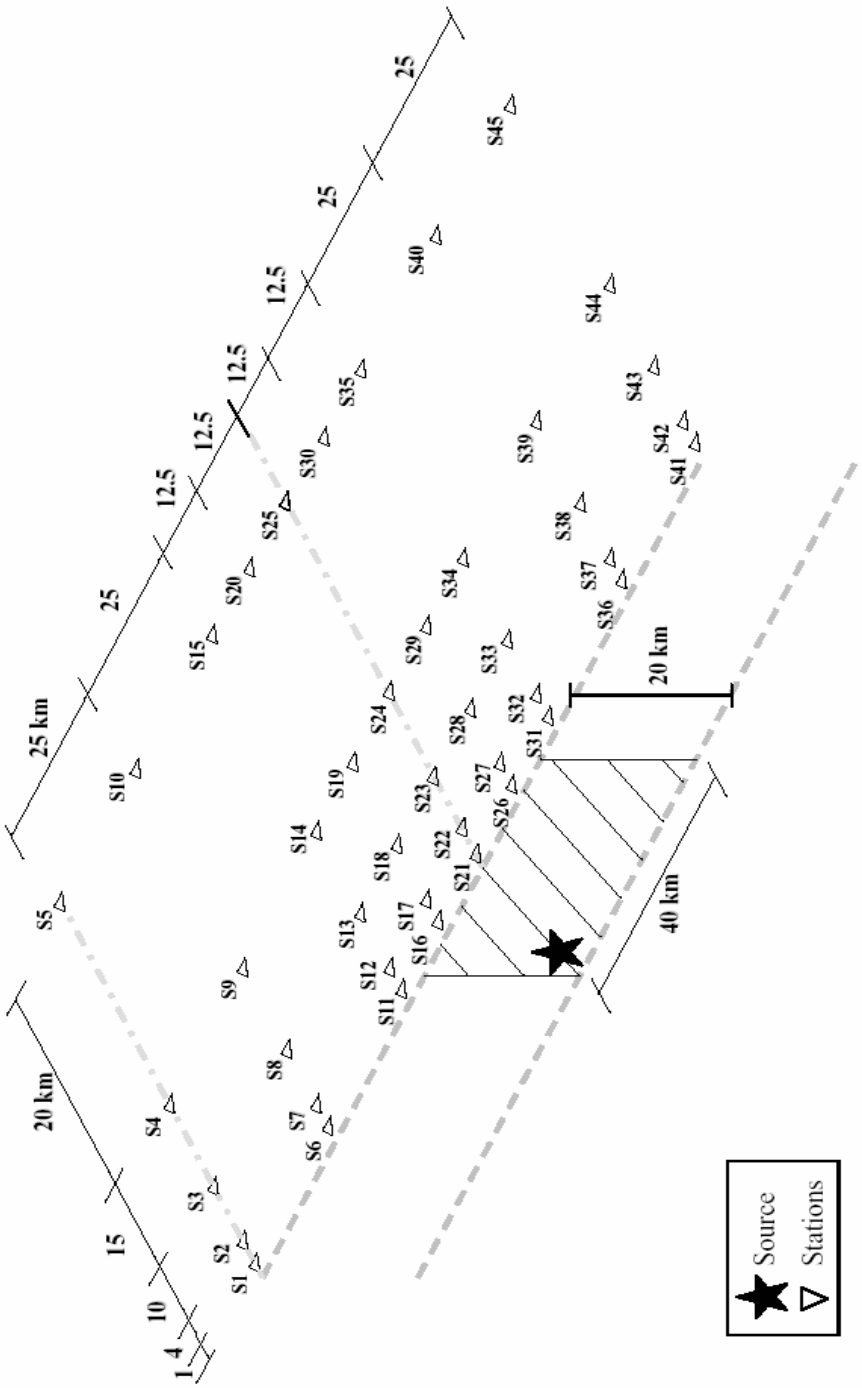

Figure 2.26. The simulation layout

A laterally homogeneous velocity structure based on Mindevalli and Mitchell (1989) was adopted (Table 2.2).

Table 2.2. The velocity structure

Depth (m)	V_p (km/s)	V_s (km/s)	Density (gr/cm^3)
0	1.7	1	1.7
500	3.5	2.2	2
4000	5.8	3.4	2.7
17000	6.2	3.6	2.8
32000	8	4.6	3.34

In the 3-D finite difference code a grid spacing of 250 m and time interval of 0.008 s were used. The dislocation was modeled such that it propagated circularly from the hypocenter with constant rupture velocity and an exponential source-time function to reach the final amount of slip. Corresponding program input files for the base case are given in Appendix A. The spatial distribution of peak ground velocity and displacements obtained for the base case with FD3D in both fault normal and fault parallel directions are presented in Figure 2.27.

A close examination of the spatial PGV and PGD distributions obtained by different methods revealed (e.g. Figure 2.28 and Figure 2.29) that the performance of the utilized codes were comparable at distances larger than about 15km from the fault. At distances smaller than 15km, a significant variation of displacements and velocities was evident for both displacements and velocities particularly in the fault normal direction. Figure 2.28 and Figure 2.30 depict the comparison of the time histories and the corresponding acceleration Fourier Amplitude Spectra obtained at Station 31 by different methods. The difference between codes observed in resulting velocities was particularly significant. This has very important implications for important engineering projects to be built in near-field conditions, where a reliable and realistic estimation of near-field ground motion becomes critical. One of the reasons of these differences could be the insufficient documentation about the codes. The frequency domain limitations and noise reduction procedures in particular, are sometimes not well documented. In the FD3D case, the two main limitations

were already described: CFL number controls the time step and the 8 grids per wavelength contained in the source is very penalising. If the latter is not implemented through a finite rise time, for instance, the simulation will produce highly dispersive wave fields. If the frequency limitations are unknown to the users the results could be considered good at frequencies not contained in the simulation.

Based on these observations, to prove the efficiency of a simulation method it became critical to carry out simulations that could be compared with real recordings. The 2004 Parkfield earthquake case constituted a perfect test bed as it generated a large number of recordings distributed in the near source area. As such, the present thesis study proceeded with the 3DFD simulation of the 2004 Parkfield earthquake. The subject is covered in Chapter 3.

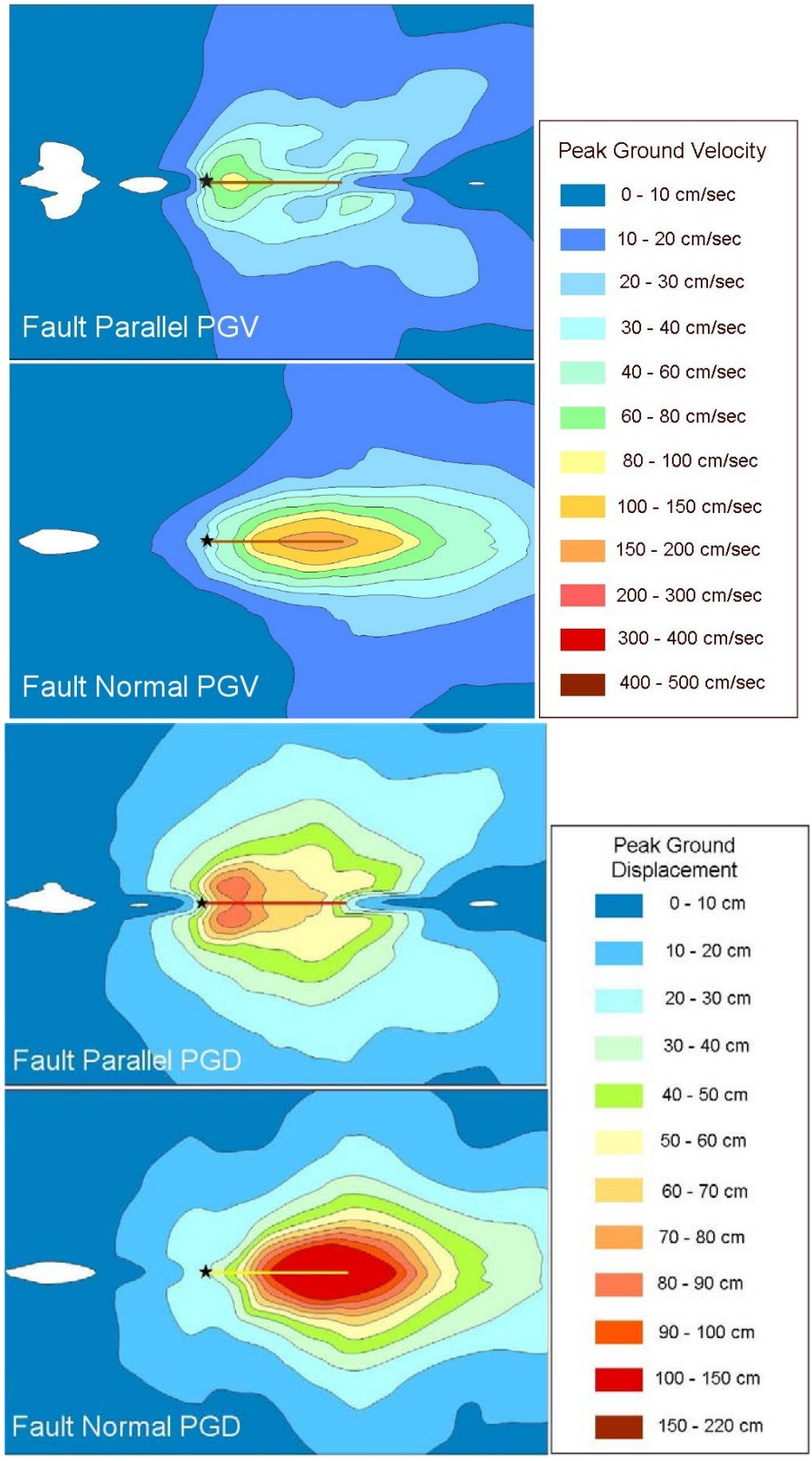

Figure 2.27. PGV and PGD distributions obtained by FD3D method for the base case of the benchmark study

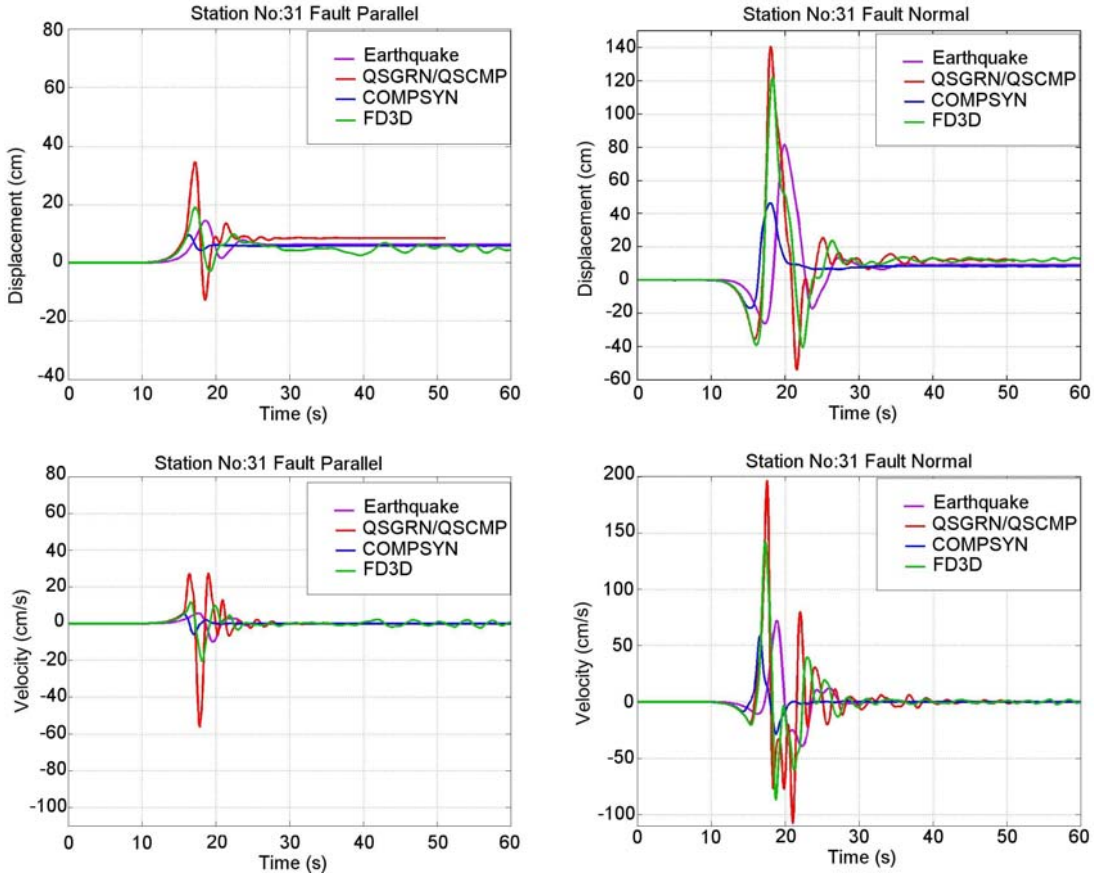

Figure 2.28. Time histories simulated by different codes for one of the stations located close the fault (Station 31)

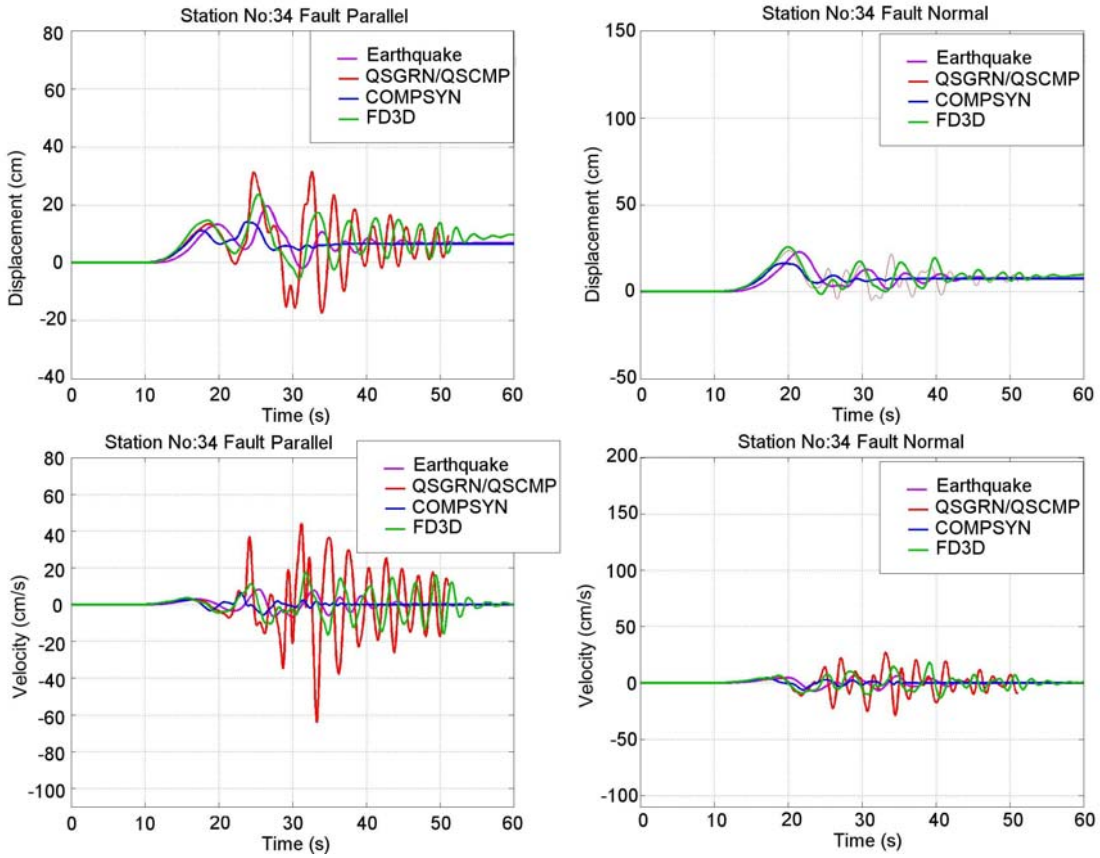

Figure 2.29. Time histories simulated by different codes for one of the stations located far from the fault (Station 34)

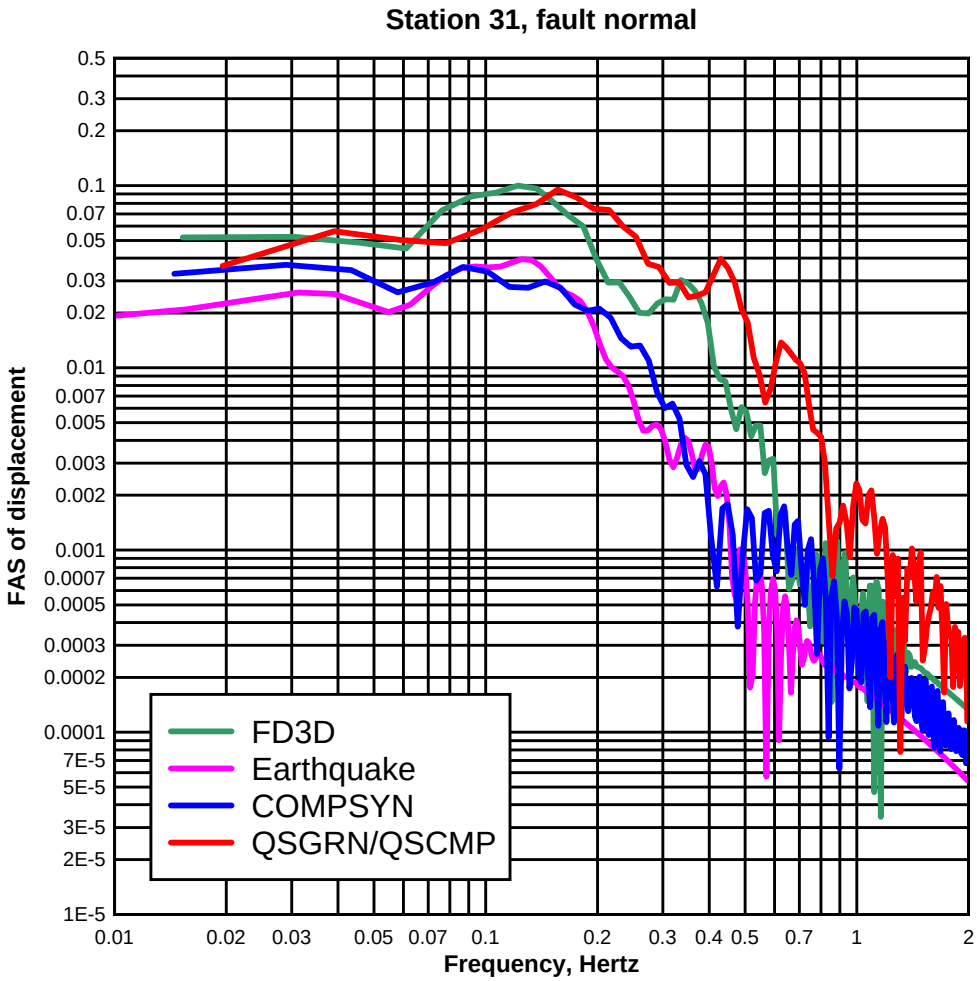

Figure 2.30. Comparison of the Fault Normal Displacement Fourier Amplitude Spectra for Station 31

3. KINEMATIC SIMULATION OF THE 2004 PARKFIELD EARTHQUAKE

The 2004 Parkfield, California earthquake provided a good case for testing the performance of the simulation code. The aim in this simulation study is to assess, given the kinematic rupture parameters and the crustal velocity structure, how well and realistically the code simulated the near field ground motions and also to understand the effects of changes in the different parameters utilized in the simulation process on the goodness of fit of simulated over recorded time histories.

3.1. The Earthquake

The Parkfield segment of the San Andreas Fault generated moderate size earthquakes in 1881, 1901, 1922, 1934 and 1966 that could be interpreted as characteristic earthquakes with a return period of approximately 20-30 years. Due to the expectancy of a characteristic earthquake on the same segment since 1990, the Parkfield area was densely instrumented by CSMIP (California Strong Motion Instrumentation Program) and USGS (United State of Geological Survey). The awaited earthquake occurred on September 2004 with a moment magnitude of 6.0. The hypocenter was 11 km SE of Parkfield, (Epicenter: 35.825 N, 120.374 W) at a depth of 8 km. Analyses conducted by USGS and UC Berkeley indicate that the event had a strike-slip mechanism, the strike and dip angles being 140° and 87°, respectively. Analysis of the aftershocks and rupture models indicate that the fault ruptured along the same section of the fault as that of the previous events in the similar magnitude Parkfield earthquake series. On the other hand, unlike the 1922, 1934, and 1966 shocks which ruptured from NW to SE, the 2004 earthquake initiated in the SE and ruptured to the NW.

The 2004 Parkfield earthquake produced the best near-field data ever recorded with 56 recordings within 20 km of rupture (Shakal *et al.*, 2005, Figure 3.1). The configuration of the array run by the California Geologial Survey (CGS) consists of a group of analog strong ground motion stations installed parallel to the fault called Fault Zone stations, complemented by three lines of stations, named the Cholame, Gold Hill and Vineyard

Canyon limbs, extending perpendicularly from the fault. In addition to these three limbs, the shorter Stone Corral limb extends to the east (McJunkin and Shakal, 1989). The strong motion data recorded by the CGS array is critically analyzed by Shakal *et al.* (2006). The Parkfield strong motion instrumentation also includes 12 high-resolution GEOS recorders installed by the US Geological Survey (USGS). The analysis results of these recordings are presented in Borcherdt *et al.* (2006).

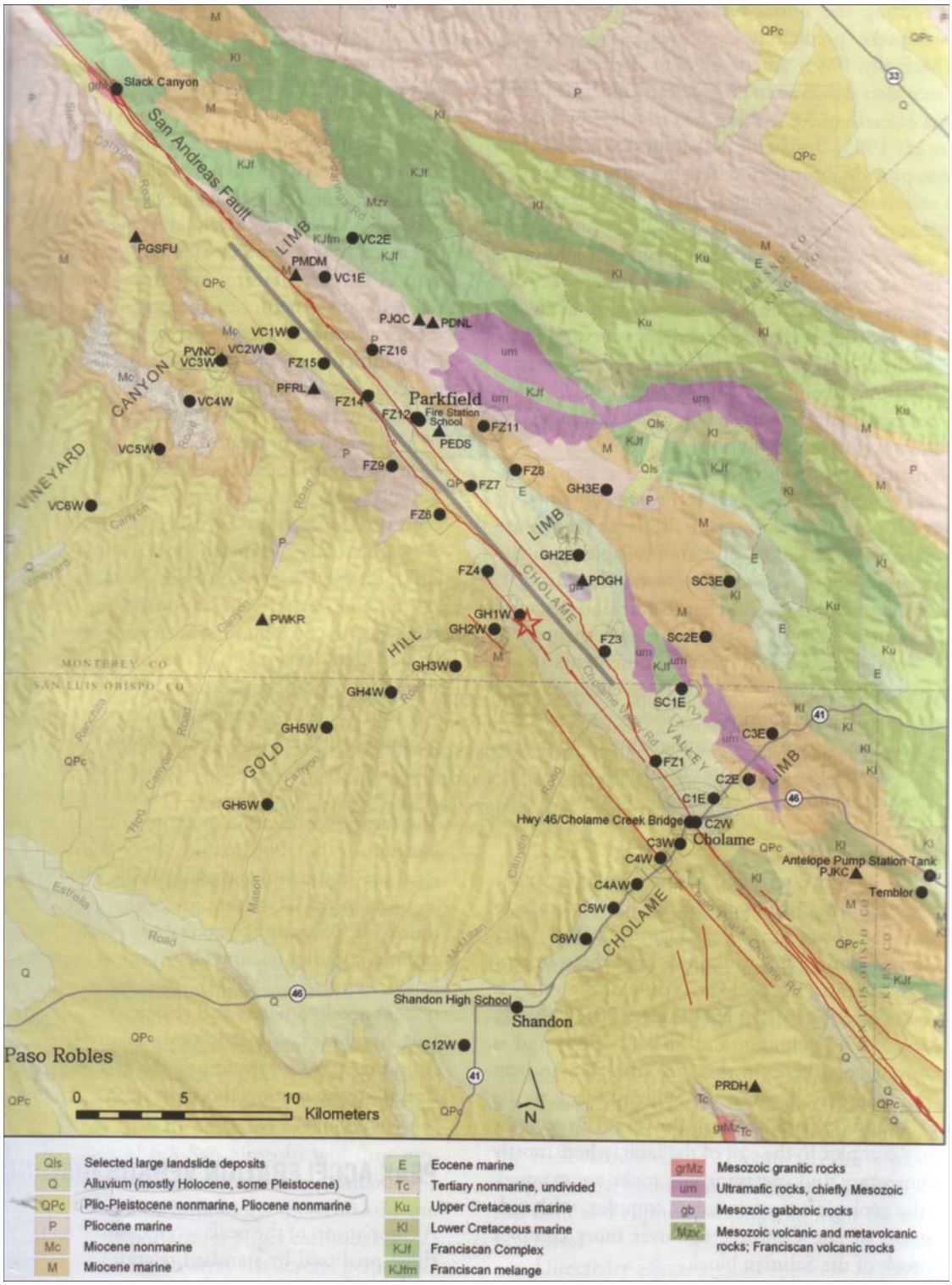

Figure 3.1. The 2004 Parkfield earthquake and the distribution of nearfield stations (Shakal *et al.*, 2005)

3.2. Modeling

The fourth order explicit finite difference code is used to compute ground motion in the vicinity of the fault with a crustal model of velocities and densities and a model of the slip distribution on the fault. The modeled region extends 55 km in NW – SE direction parallel to the fault and 33 km in NE – SW direction normal to the fault. The depth of the model is 18 km. A grid spacing of 100 m and a time step of 0.004 s are used. With a maximum P-wave velocity of 7000 m/s used in the modeling of the earth structure (as discussed in Section 3.2.5) the typical value of the CFL parameter is 0.28. The program generates the 3D velocity wave field for a rectangular prism of 550 x 330 x 180 nodes in fault parallel, fault normal and vertical directions respectively. Time histories are compared to real data obtained from 48 stations located around the fault (Figure 3.2). The study is conducted with the aim of assessing the effects of changes in slip models, source time functions and crustal velocity structures. The modal bias between the observed and simulated ground velocities as calculated by the ratio of the Fourier Amplitude Spectra (FAS) averaged over the 48 stations is used as an indicator of the goodness of fit. Ratios of Fourier Amplitude Spectra of the time histories of interest are frequently used in earthquake engineering since the frequency content of the ground motion is often related to the response of the earth and structures. H/V ratios to estimate the predominant period of the soils or spectral site amplification ratios can be cited among them. In this case the modal bias becomes a good indicator from an engineering point of view since it provides us information on the frequency range of the simulations. The modal bias is calculated as given in Equation 3.1

$$M = \frac{1}{n}\sum_{i=1}^{n}\frac{FAS(recorded)_i}{FAS(simulated)_i} \tag{3.1}$$

where n is the number of stations for which the data are compared. We estimate that with a grid size of a 100 m we can simulate seismic wave propagation for wavelength longer than 800 m, that is slightly less than 1 Hz for shear wave speeds of the order of 1000 m in the shallow layers of our models (Table 3.1 through Table 3.3).

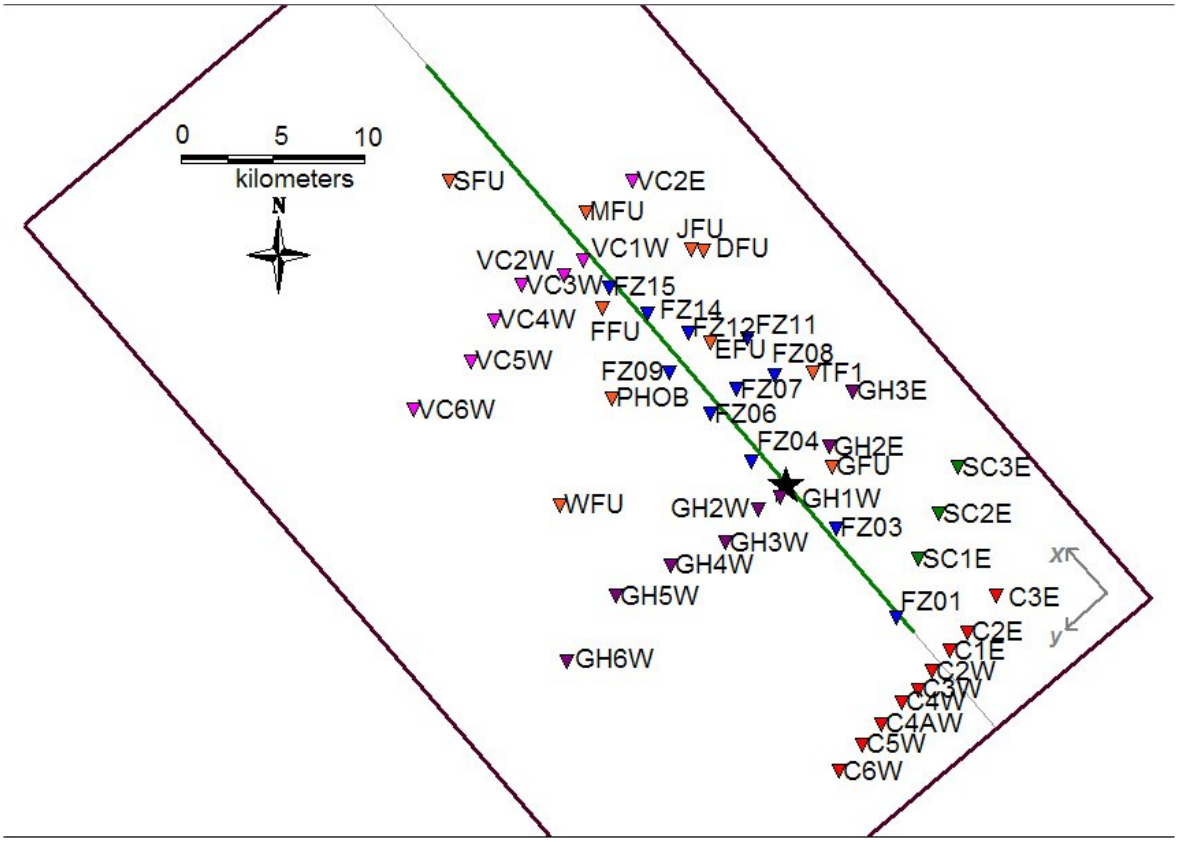

Figure 3.2. The layout of the stations and the position of the fault within the simulation grid. The fault is set parallel to the x axis of the simulation grid. The strike and dip angles the rupture are 140° and 87°, respectively. The green line represents the surface projection of the fault and the black star, the location of the epicenter. The stations labeled with C* form the Cholame array; SC*, the Stone Corral array; GH*, the Gold Hill array; FZ*, the fault zone array and VC*, the Vinyard Canyon array of CSMIP. Remaining ones are the stations run by USGS.

3.2.1. Slip Distribution

The analysis was conducted for three slip models proposed for the 2004 Parkfield earthquake. These were: the preliminary slip model developed by Ji (2004); the slip model of Ji *et al.* (2005) which was obtained from data of 14 strong motion and 13 GPS stations; the slip model of Liu *et al.* (2006) which was based on the kinematic inversion of recordings of 43 near field stations. All models are based on data low-pass filtered at 1 Hz. We found from our simulations that the preliminary model proposed by Ji (2004) fitted the observed data (as measured by the modal bias) less well than the other two. The

improvement was significant when the slip model of Ji *et al.* (2005) (Figure 3.4) was incorporated in our source model. The frequency content of the model of Liu *et al.* (2006) (Figure 3.5) seemed at first to remain below the results of Ji *et al.* (2005). However as the variation of different kinematic rupture parameters and also the local soil conditions as indicated in Liu *et al.* (2006) were included in the study, the match between the observed and the simulated velocity traces improved satisfactorily (Figure 3.6).

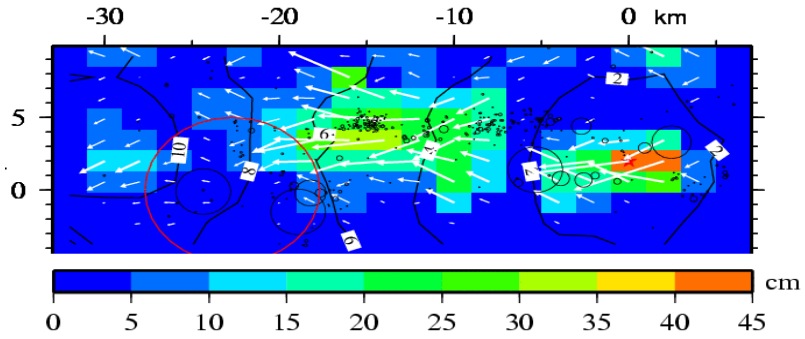

Figure 3.3. Slip model by Ji (2004)

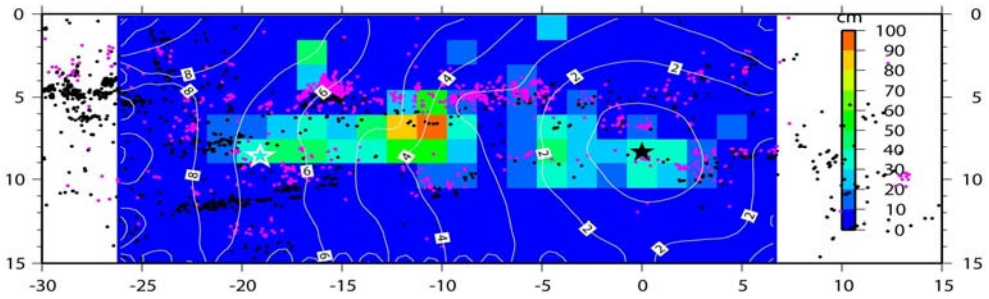

Figure 3.4. Slip model by Ji *et al.* (2005)

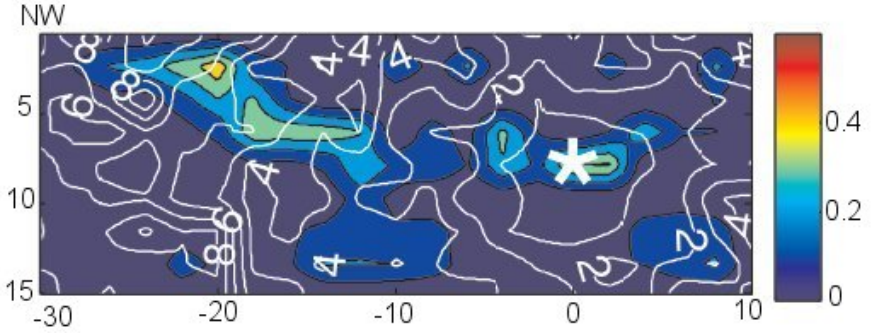

Figure 3.5. Slip model Liu *et al.* (2006)

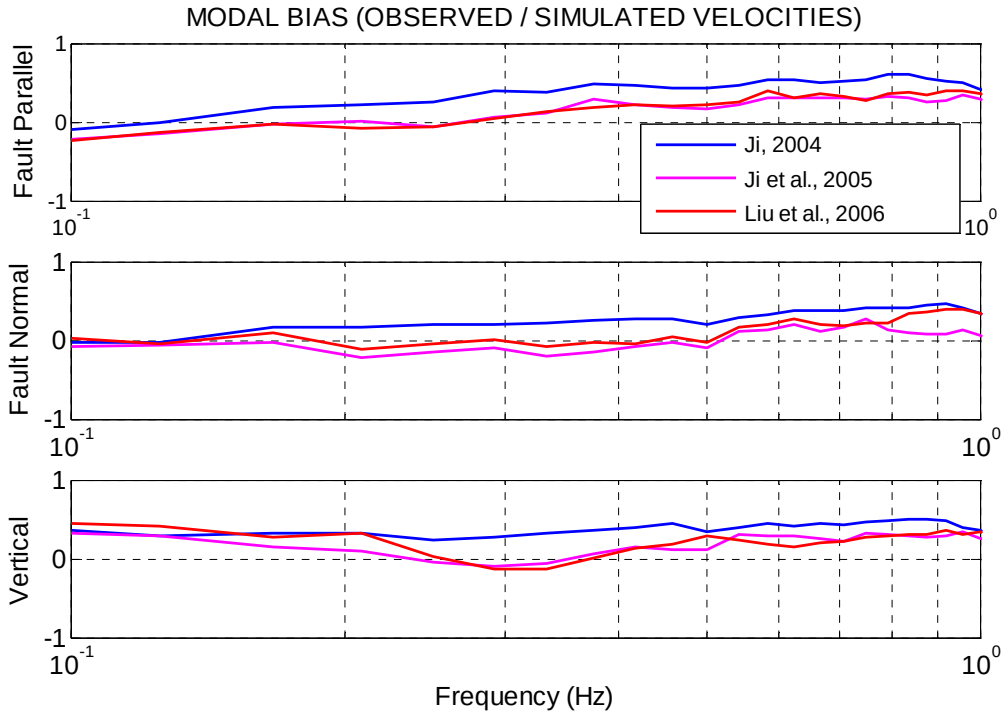

Figure 3.6. The modal bias obtained from various slip models

3.2.2. Effect of the Source Time Function

Trapezoidal and Gaussian type source time functions were used in the early stages of the finite fault simulations carried out with our finite difference simulation code. Later an exponentially decreasing source time function was adopted as in Figure 3.7, such that the concentration of the energy in the onset of the slip enhanced the frequency content of the simulations for frequencies above 0.4 Hz (Figure 3.8).

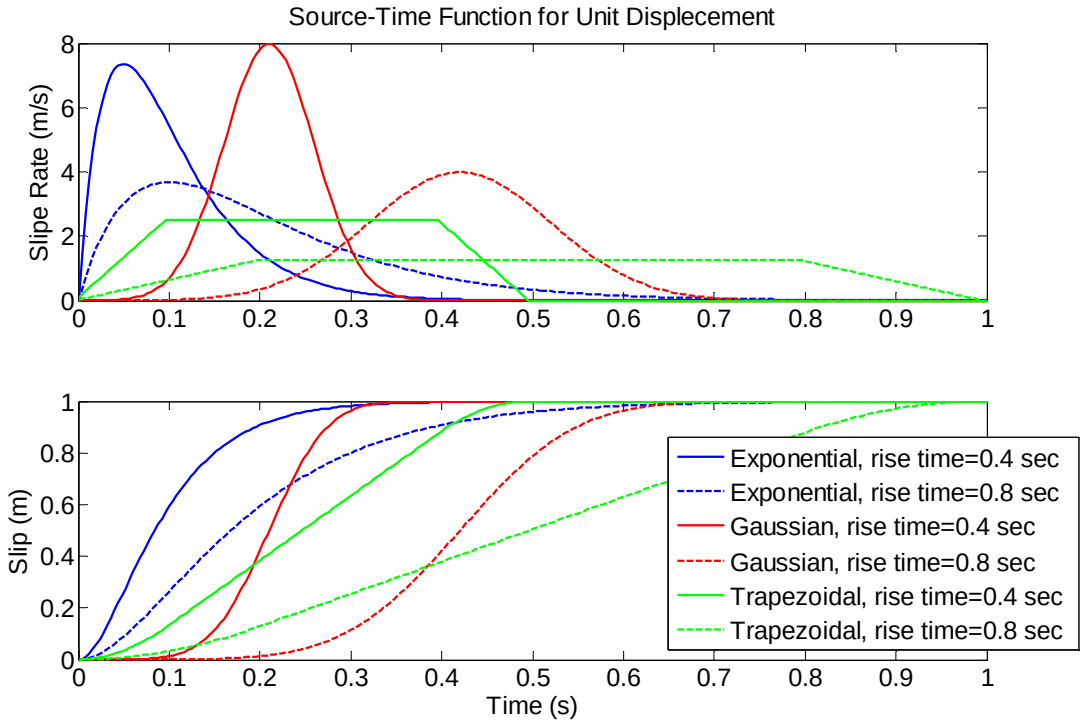

Figure 3.7. The source-time functions considered

3.2.3. Effect of Rise Time

Based on the model of Liu *et al.* (2006) and the exponential source time function, we tried several rise time values to understand its effect on the frequency content of the simulations. Two approaches have been used. The first one was to use a single rise time value for all the grids on the fault surface. The second was to use the rise time values given in the original slip model. The comparison of the modal bias thus obtained shows that while a very stable simulation of the wave field is obtained for constant rise time values above 0.8 s, some disturbance of the wavefield is observed for a rise time of 0.4 s. Nevertheless a lower modal bias is obtained for rise time = 0.4 s which is the lowest value that we have been able to use avoiding a noisy wavefield. The use of variable rise time did not ameliorate the results as the values ranged from 0.4 s to 4 s (Figure 3.9).

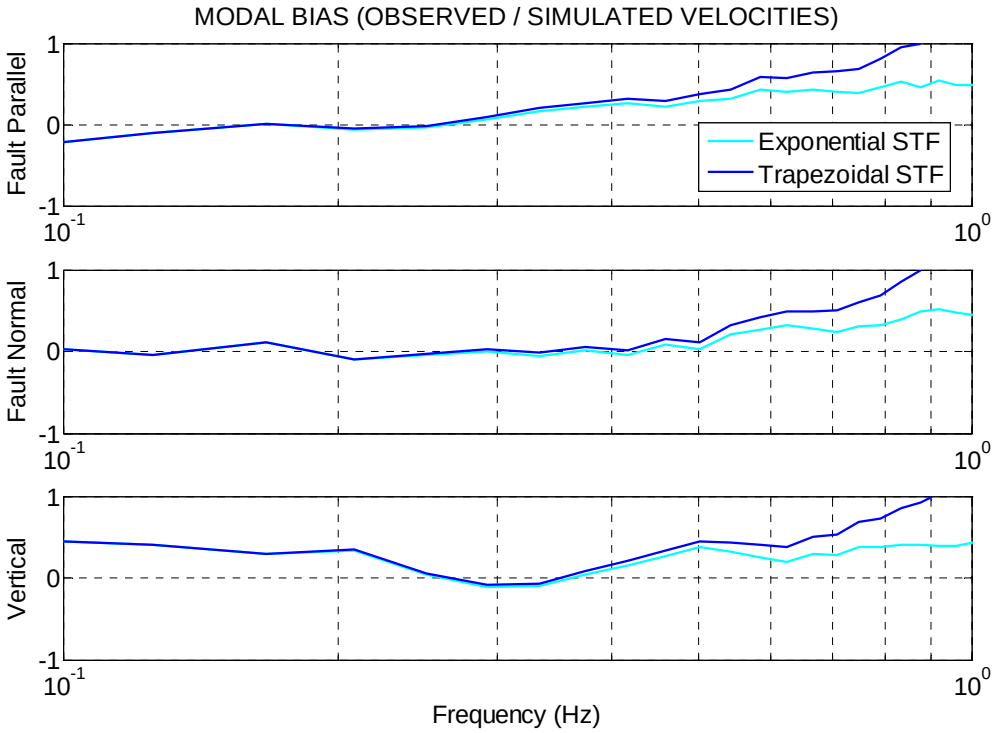

Figure 3.8. The modal bias obtained from various source-time functions

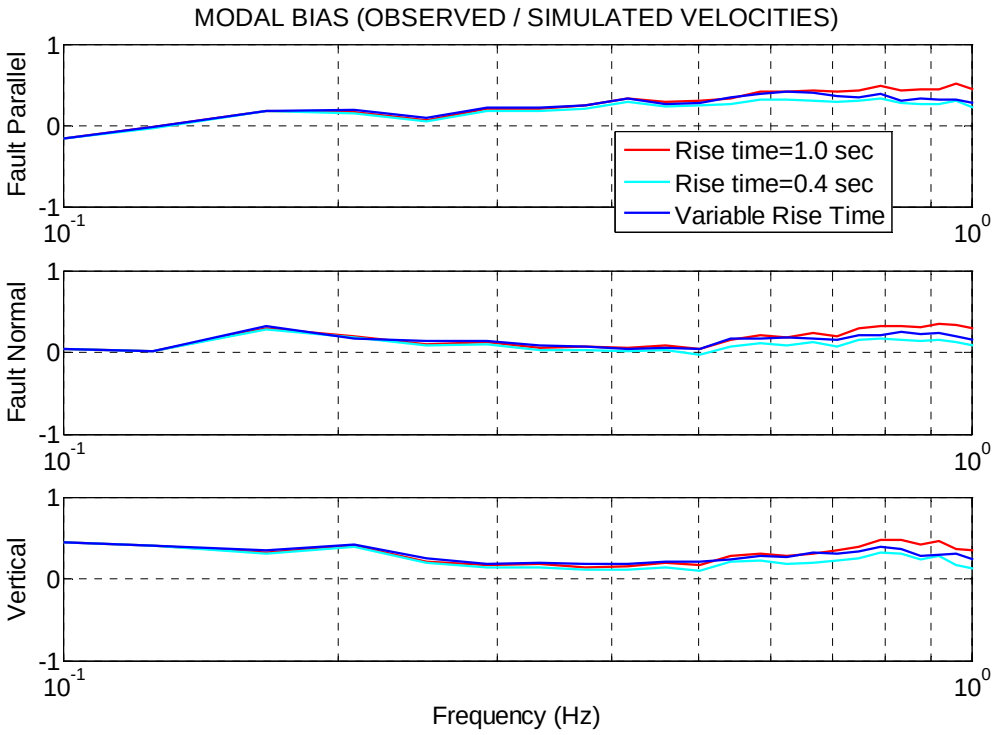

Figure 3.9. The modal bias obtained from various rise times

3.2.4. Effect of Rupture Velocity

The average rupture velocities in the individual slip models are incorporated in the study. However in Liu *et al.* (2006) two zones with clearly different average rupture velocities were indicated. The first zone was located around the hypocenter with an average rupture velocity of 2.8 km/s and in the second zone of higher slip near the surface having an average V_r of 3.3 km/s in the secondary region of large slip to the northwest of the hypocenter. These patches can be observed in Figure 3.5 where the white contours indicate the wavefront arrival times. As such, these zones are incorporated in the source model and the results are compared for different rise time values. The variable V_r approach with the lower rise time value increased the effectiveness of the simulation in higher frequencies (Figure 3.10).

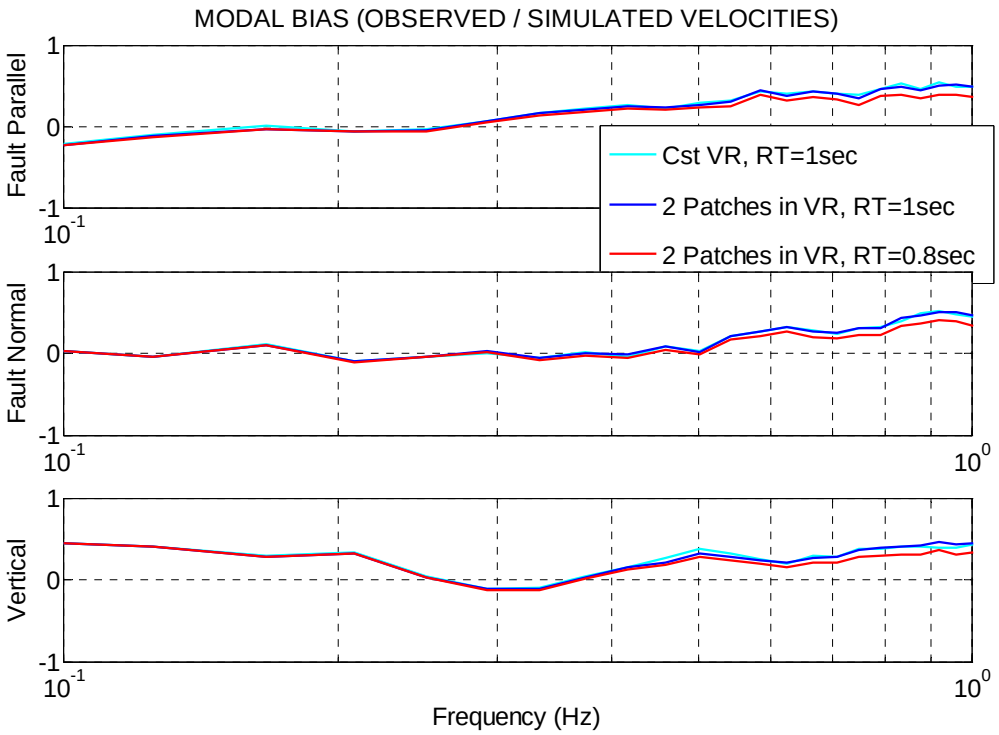

Figure 3.10. The modal bias obtained from various rupture velocities

3.2.5. Crustal Velocity Structure

The geologic structure in the Parkfield region is very complex east of the fault where mostly Mesozoic sedimentary and metamorphic rocks are exposed. The west of the fault,

less structurally deformed sedimentary deposits of middle to late Cenozoic age, cover older and more structurally complex Mesozoic terrain of the Salinian block (McJunkin and Shakal, 1989). The initial velocity structure used in the analysis was adopted from the velocity model provided by USGS. To be compatible with the grid size used in the 3D Finite Difference simulation and also with the frequency resolution aimed for (f_{max} = 1 Hz), the upper two layers in the velocity structure (V_s of 400 and 750 m/sec up to depths of 30 m and 250 m respectively) were omitted. Depending on the availability of information and also on the adaptability of the model to the inversion method used, different, but comparable crustal velocity models have been used in the derivation of the slip models for the 2004 Parkfield earthquake. Ji *et al.* (2005) and Liu *et al.* (2006) have used 1D velocity models differentiated for the SW and NE sides of the fault. Since then the 3D velocity model of Parkfield region became also available by Thurber *et al.* (2006). In the present study, the velocity structures used in individual studies are adopted but the results are also compared with those obtained using the 3D velocity structure. The 3D shear wave velocity and density models are obtained from the compressional wave model provided in Thurber *et al.* (2006) using the empirical conversion equations by Brocher (2005). The velocity structures used in the analysis are given in Table 3.1 through Table 3.3.

Table 3.1. Parkfield earth model (modified from USGS, used in the first simulations of Ji, 2004 and 2005), 5 layer model.

DEPTH TO THE TOP OF LAYER (m)	V_p (m/s)	V_s (m/s)	DENSITY (kg/m^3)
0	3200	1700	2200
1500	4940	2600	2400
2500	5450	2900	2500
4700	5880	3100	2700
9000	6800	3900	3000
12000	7000	4000	3200

Table 3.2. Velocity structure used in Ji (2005)

DEPTH TO THE TOP OF LAYER (m)	V_p (m/s)	V_s (m/s)	DENSITY (kg/m^3)
Southwest side			
0	2000	1150	2100
1000	3500	2000	2200
2000	4500	2600	2400
3000	5400	3200	2500
4000	5800	3350	2700
7000	6200	3600	2900
9000	6800	3900	3000
12000	7000	4000	3200
Northeast side			
0	2000	1150	2100
1000	3500	2000	2200
2000	4500	2600	2400
5000	5400	3200	2900
9000	6500	3750	3100
12000	7000	4000	3200

Table 3.3. Velocity structure used in Liu *et al.* (2006)

DEPTH TO THE TOP OF LAYER (m)	V_p (m/s)	V_s (m/s)	DENSITY (kg/m^3)
Southwest side			
0	1900	1000	2000
1000	3400	1700	2300
2000	4600	2400	2300
3000	5100	3100	2700
4000	5600	3600	2700
5400	6300	3600	2800
18700	6800	3900	2800
Northeast side			
0	2000	1100	2000
700	3800	2200	2300
1400	4300	2400	2300
2000	4800	2700	2300
3600	5300	3100	2500
7600	5800	3300	2700
14300	6200	3800	2800
20500	6800	3800	2800
24600	7000	4000	2800

The 3D seismic wavespeed structure of the wider Parkfield region was studied by Eberhart-Phillips and Michael (1993), which reported a strong velocity contrast across the San Andreas Fault, southwest side being faster. A primary exception of this structure is the 2004 Parkfield earthquake rupture zone where there exists a high velocity block in the northeast side of the fault. Based on the data generated by the aftershock activity of the 2004 Parkfield earthquake, increased computational power since previous studies and the development of the double-difference tomography method of Zhang and Thurber (2003), Thurber *et al.* (2006) developed a new compressional wavespeed model of the 2004 Parkfield earthquake rupture zone providing a clearer image of the high velocity zone

northeast of the fault. The inversion grid used in their study is presented in Figure 3.11. According to their conclusions this zone appears to be a separate body from the high Vp Salinian rocks on the southwest side of the San Andreas Fault. Further to the southeast, the high Vp body is separated from the fault zone which has an evident low velocity structure. A fault normal cross section of the P wave velocity structure at grid plane Y = -21 km (Figure 3.11) is presented in Figure 3.12. Fault parallel cross sections at X= -1 km (Southwest side) and X = 1 km (Northeast side) are presented in Figure 3.13 and Figure 3.14 respectively.

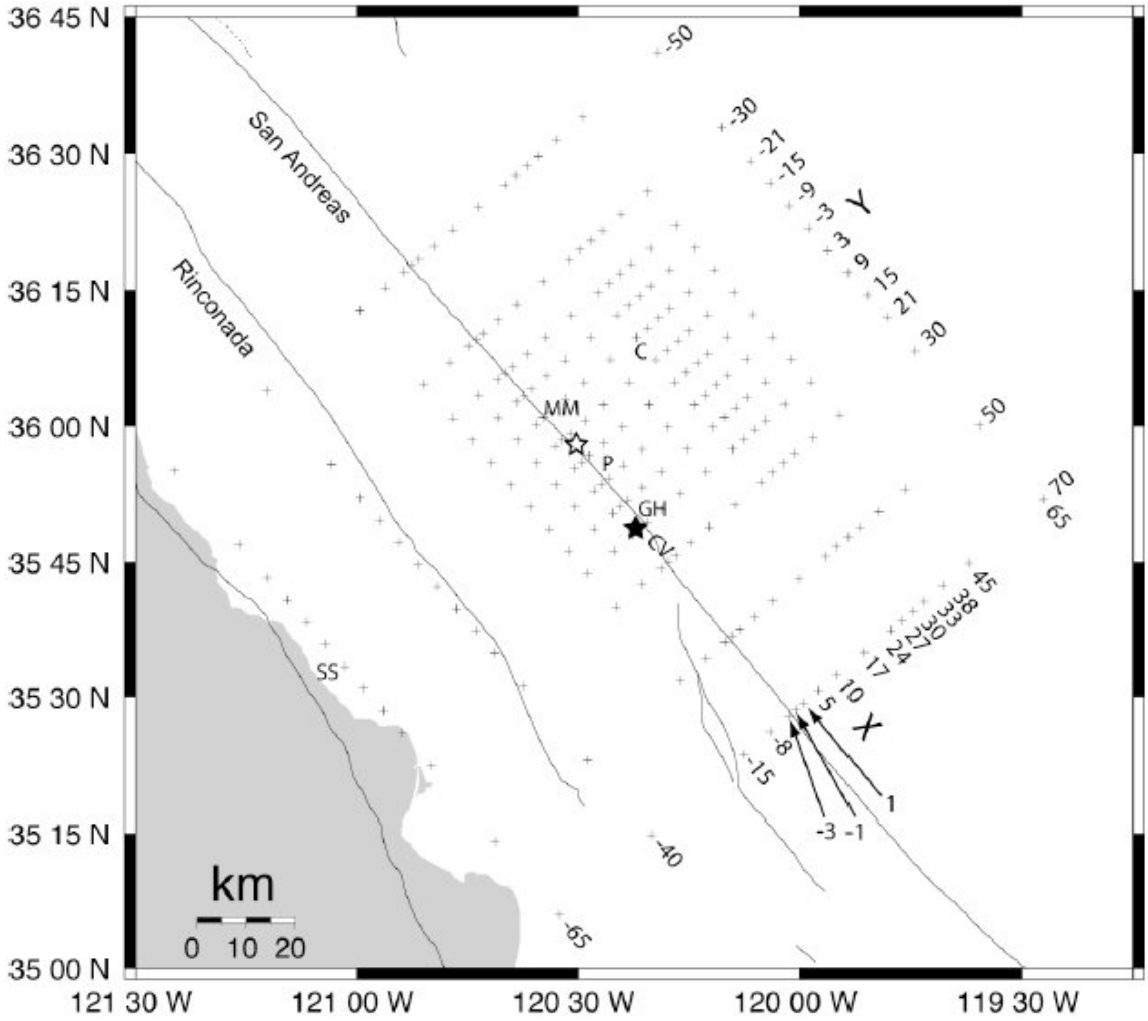

Figure 3.11. The inversion grid for the velocity structure of the 2004 Parkfield earthquake rupture zone by Thurber *et al.* (2006)

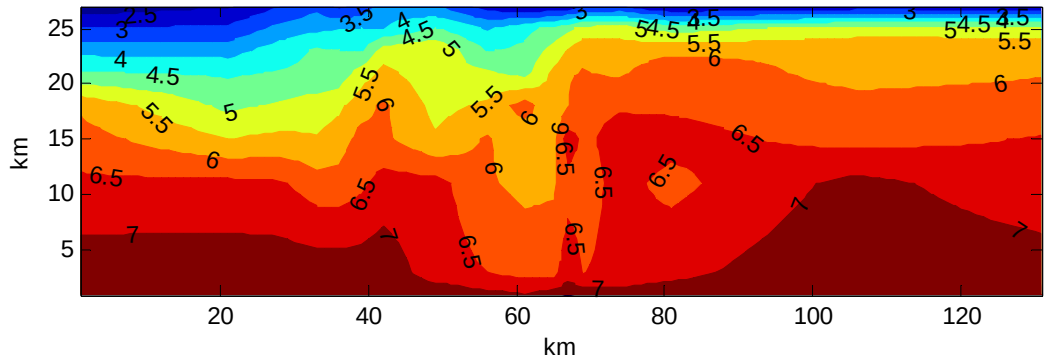

Figure 3.12. Fault normal cross section of the P wave velocity structure at Y = -21 km

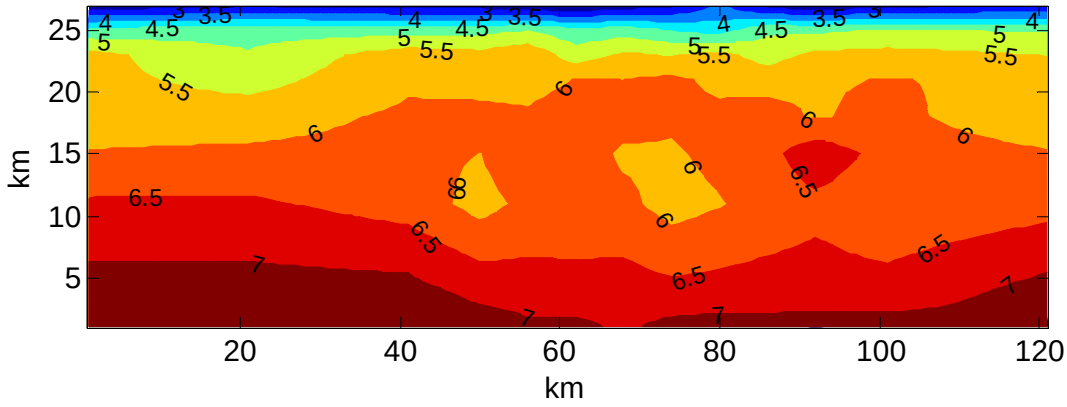

Figure 3.13. Fault parallel cross section of the P wave velocity structure at X = -1 km (Southwest side)

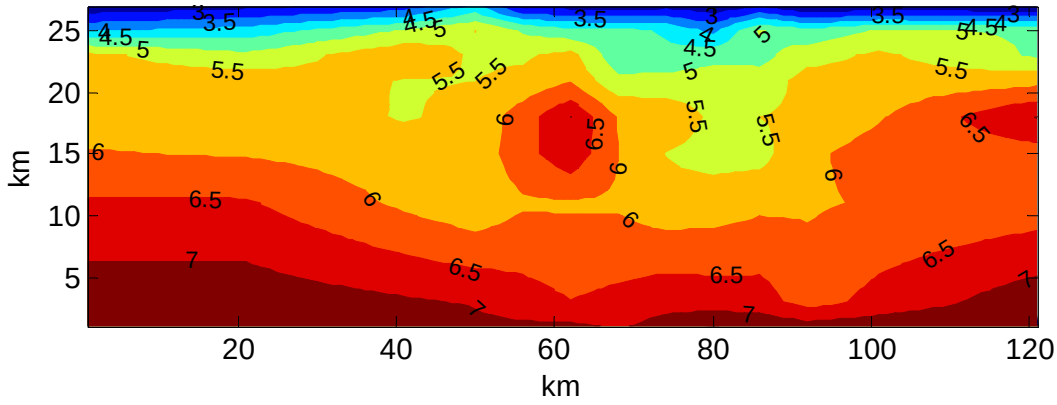

Figure 3.14. Fault parallel cross section of the P wave velocity structure at X = 1 km (Northeast side)

The 3D shear wave velocity and density models are obtained from the compressional wave model provided in Thurber *et al.* (2006) using the empirical conversion equations by Brocher (2005) as given in Equation 3.2 and Equation 3.3.

$$V_s = 0.7858 - 1.2344V_p + 0.7949V_p^{\,2} - 0.1238V_p^{\,3} + 0.0064V_p^{\,4} \tag{3.2}$$

where V_p and V_s are the compressional and shear wave velocities in km/s respectively.

$$\rho = 1.6612V_p - 0.4721V_p^2 + 0.0671V_p^3 - 0.0043V_p^4 + 0.000106V_p^5 \tag{3.3}$$

where ρ is the density in g/cm^3 and V_p is the compressional wave velocity in km/s.

As an approximation to site effects, Liu *et al.* (2006) use the data recorded by the Parkfield array during the 1983 M_w=6.5 Coalinga earthquake. Assuming the source is common to all stations, the deviation from a reference source spectrum is taken as a measure of the site effect. As such, constant coefficients of site amplification (Ai) are obtained for the frequency range of interest (0.16 to 1 Hz) and to remove the effect of local site conditions at the station level, the recorded data during the 2004 Parkfield earthquake are divided by these coefficients. When the same coefficients are used in the calculation of modal bias, for both the two sided 1D and the 3D velocity structures the bias has been significantly reduced (Figure 3.15).

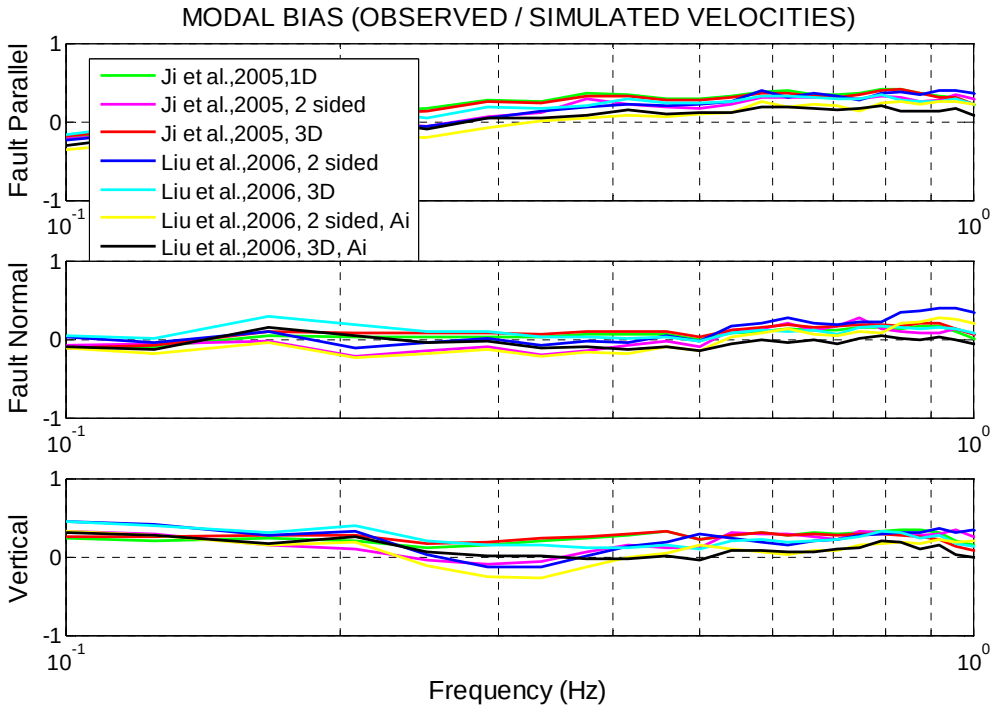

Figure 3.15. The effect of the velocity structure

The 3D wave field generated by the Parkfield 2004 rupture is illustrated in Figure 3.16 through Figure 3.18. The simulations correspond to the slip model of Liu *et al.* (2006), with a rise time of 1 s. The 3D crustal velocity structure of Thurber *et al.* (2006) is used. The effect of the velocity contrast between the northeast and southwest sides of the rupture is exhibited as the more rapidly moving rupture front in the lower side of the simulation grid in Figure 3.17. In Figure 3.17 we observe a brief shock wave trailing behind the rupture front. This is an effect of the low speeds of the 3D model near the surface. This shock wave also appears clearly in the transverse component (central panel) of the vertical cross sections shown in Figure 3.16 where the surface reflection clearly lags behind the direct wave generated by the rupture front.

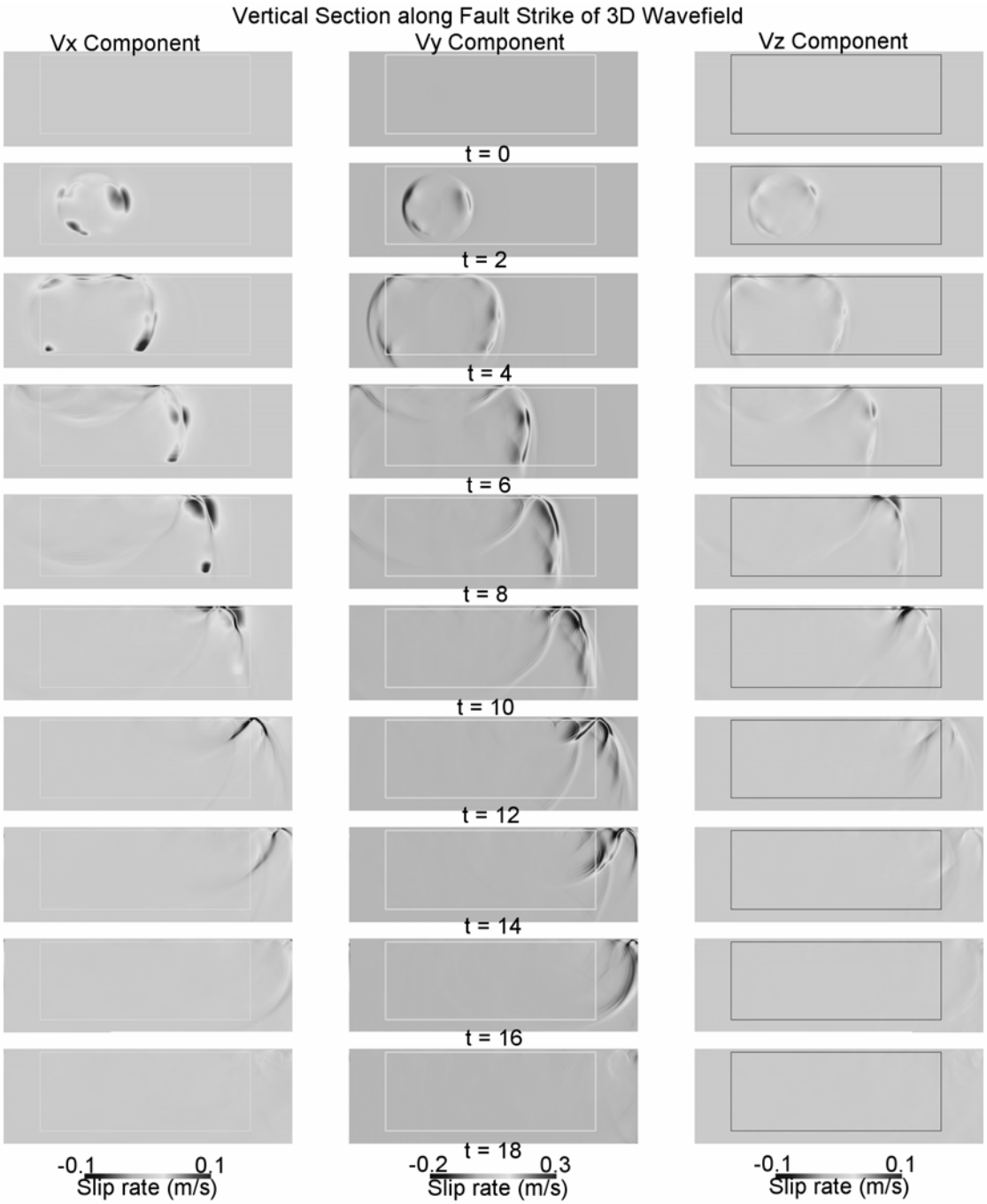

Figure 3.16. 3D wave propagation on a vertical plane parallel to the fault for the 3D earth model. The first, second and third columns present the propagation of the fault parallel, fault normal and vertical velocities respectively. The fault is presented by the rectangle.

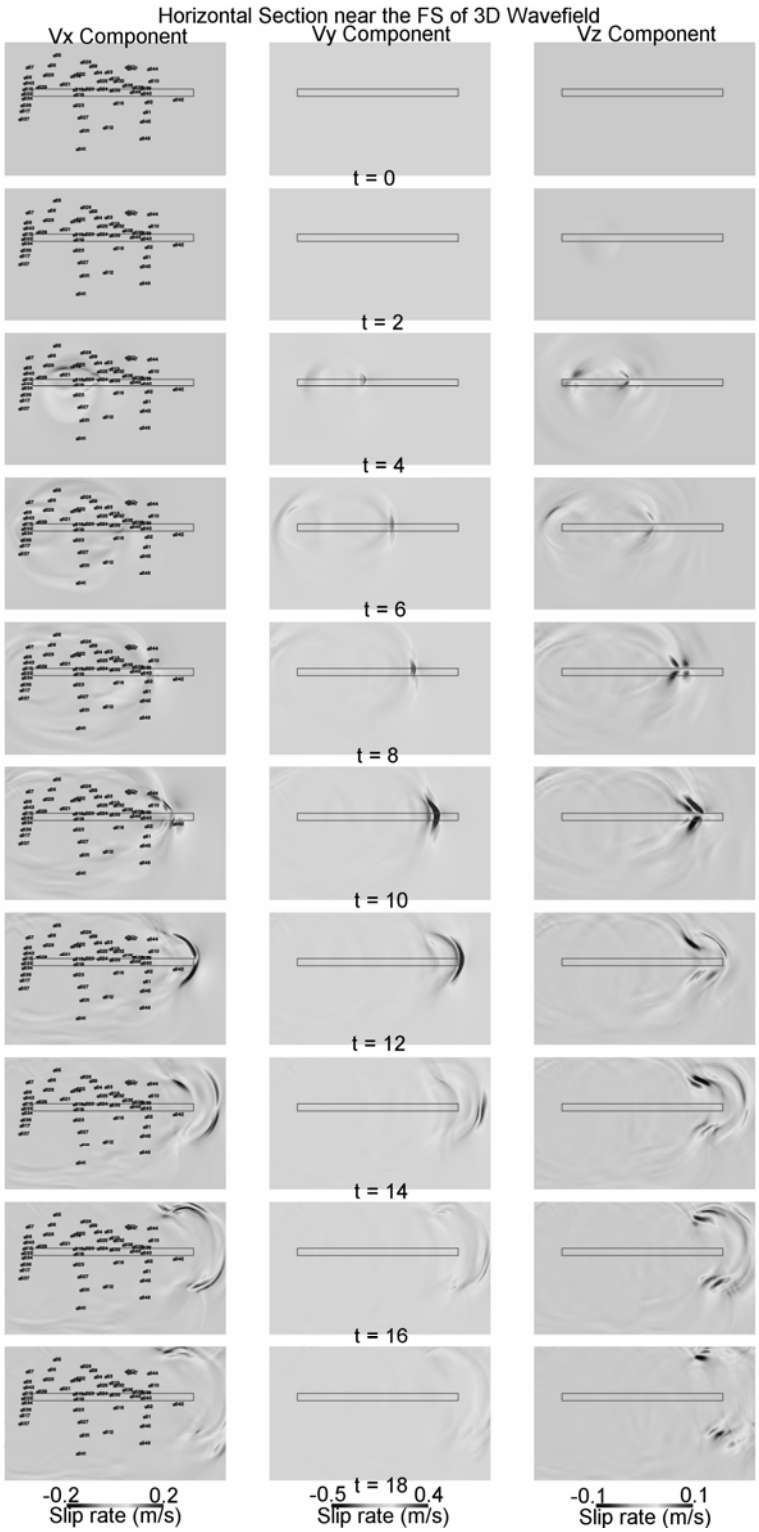

Figure 3.17. 3D wave propagation on the horizontal section near the free surface for the 3D earth model. The first, second and third columns present the propagation of the fault parallel, fault normal and vertical velocities respectively. The black rectangle is the surface projection of the fault. The upper left corner of each plot corresponds to the northeast corner of the simulation grid.

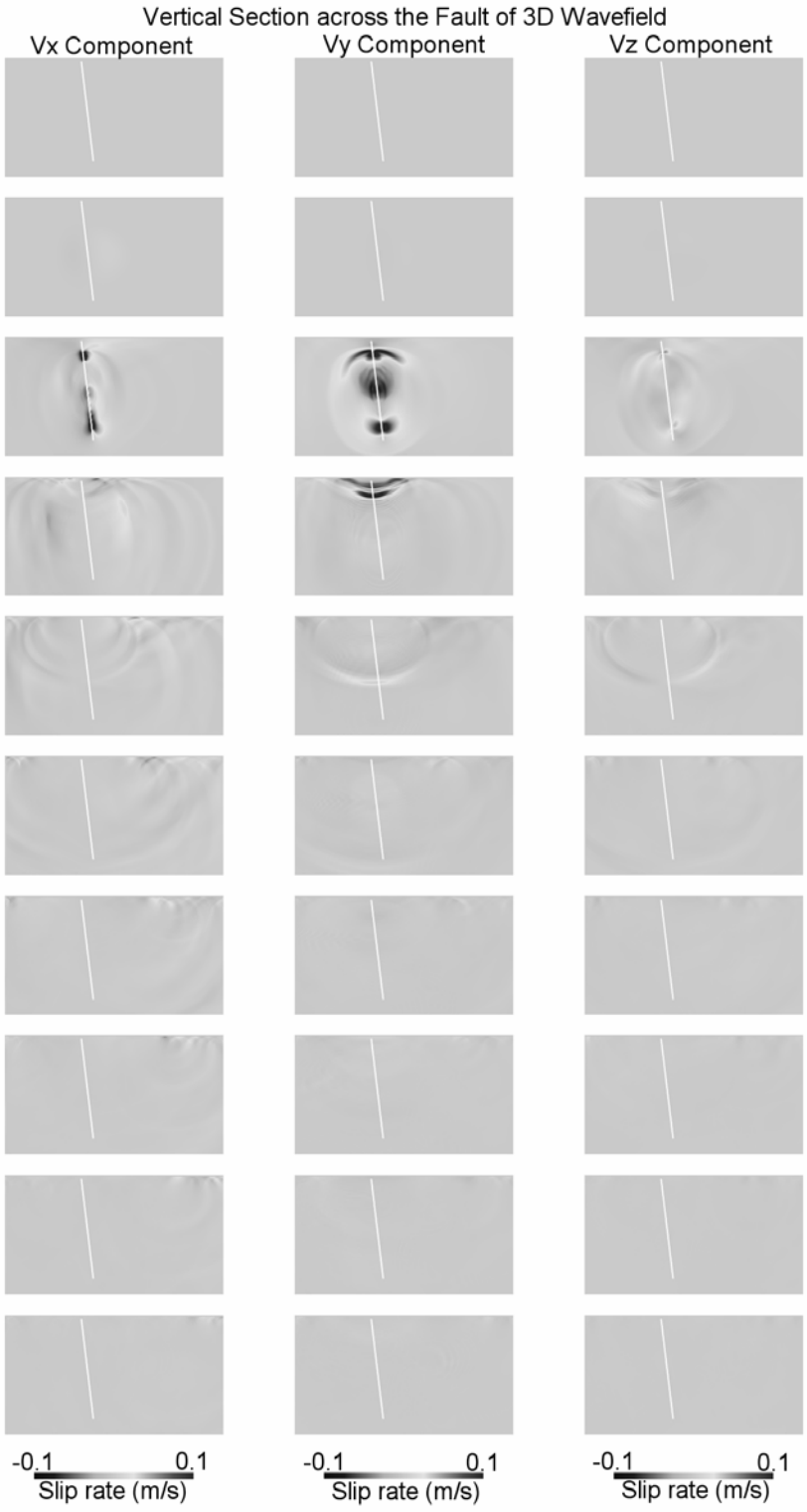

Figure 3.18. 3D wave propagation on a vertical plane perpendicular to the fault for the 3D earth model. The first, second and third columns present the propagation of the fault parallel, fault normal and vertical velocities respectively. The intersection of the fault with the representation plane is shown with the white line.

3.3. The simulated time histories

Array based comparison of the simulated and recorded velocity and displacement time histories and the corresponding Fourier amplitude spectra are presented in Figure 3.19 through Figure 3.38. The results obtained from the slip model of Liu *et al.* (2006) using the 3D velocity structure of the Parkfield region and also incorporating (when available) the site amplification factors given in Liu *et al.* (2006) are used for the comparison. All recorded and simulated time histories are low-pass filtered at 1Hz which is the maximum frequency that can be modeled with a grid of 100 m and a minimum shear wave speed of 1000 m. It should be noted that the fit in the vertical component of the ground motion is generally poorer than the horizontal components as Liu *et al.* (2006) assigned only 10 per cent weight to the vertical components of the recordings during the inversion process. Given that condition, the goodness of fit of the vertical components is also satisfactory except the Cholame array which lies in the backward directivity zone and the Fault Zone array which produced the worst overall results because of the waves trapped in the fault-zone.

The Gold Hill array (results in Figure 3.19 through Figure 3.21) is approximately perpendicular to the fault and passes through the epicenter. The ground motion recorded by this array is particularly sensitive to the initial part of the faulting and does not show directivity effects. Velocity and displacement amplitudes of this array in the fault parallel direction are larger than those in the fault normal direction. Fault parallel to fault normal response spectral ratios in the perpendicular plane passing through the epicenter obtained from the simulations are also consistent with this finding for various slip models.

The Vinyard Canyon array (results in Figure 3.22 through Figure 3.24) is also approximately perpendicular to the fault plane and is located at a 15 km distance from the epicenter in the forward directivity region close to the northern end of the rupture. The amplitudes in the fault normal direction are generally larger than those in the fault parallel direction and are all larger than those recorded and simulated in the Gold Hill array, a behavior observed in both recordings and simulations and which is consistent with the expected directivity effects. As in the Gold Hill array the goodness of fit of the station closest to the fault is less satisfactory than those in the mid distance range.

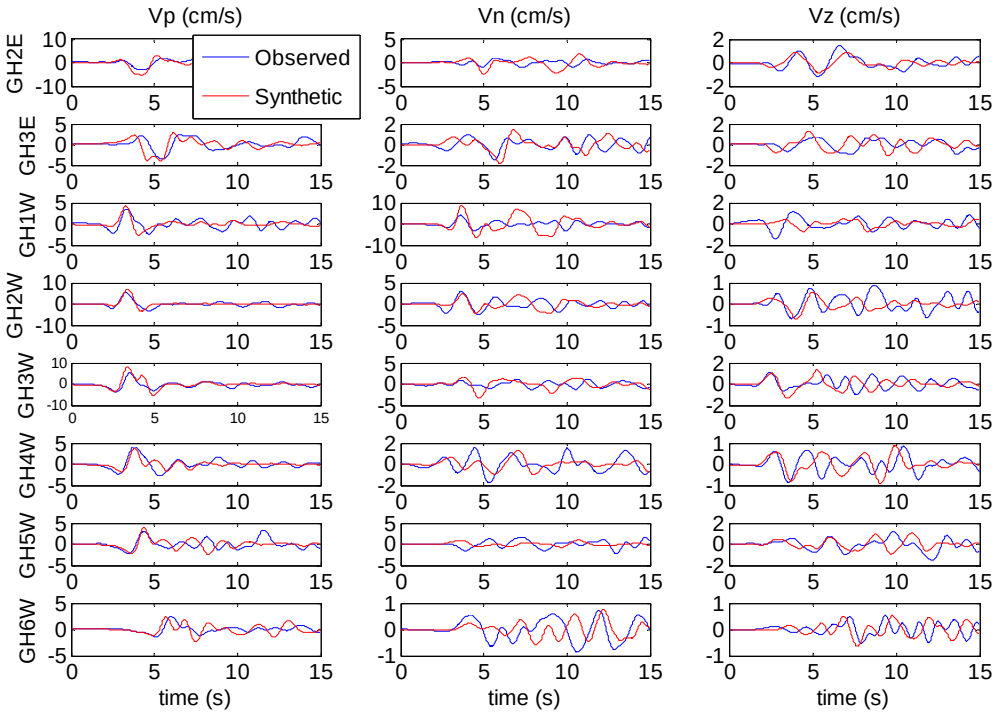

Figure 3.19. Goldhill array: observed and simulated velocity time histories

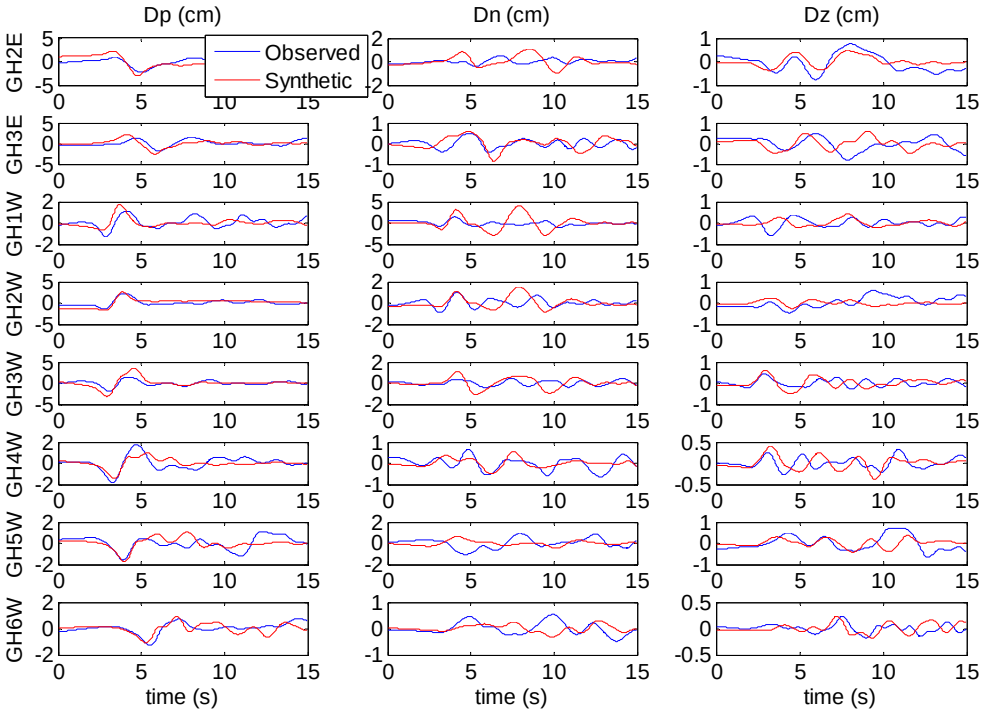

Figure 3.20. Goldhill array: observed and simulated displacement time histories

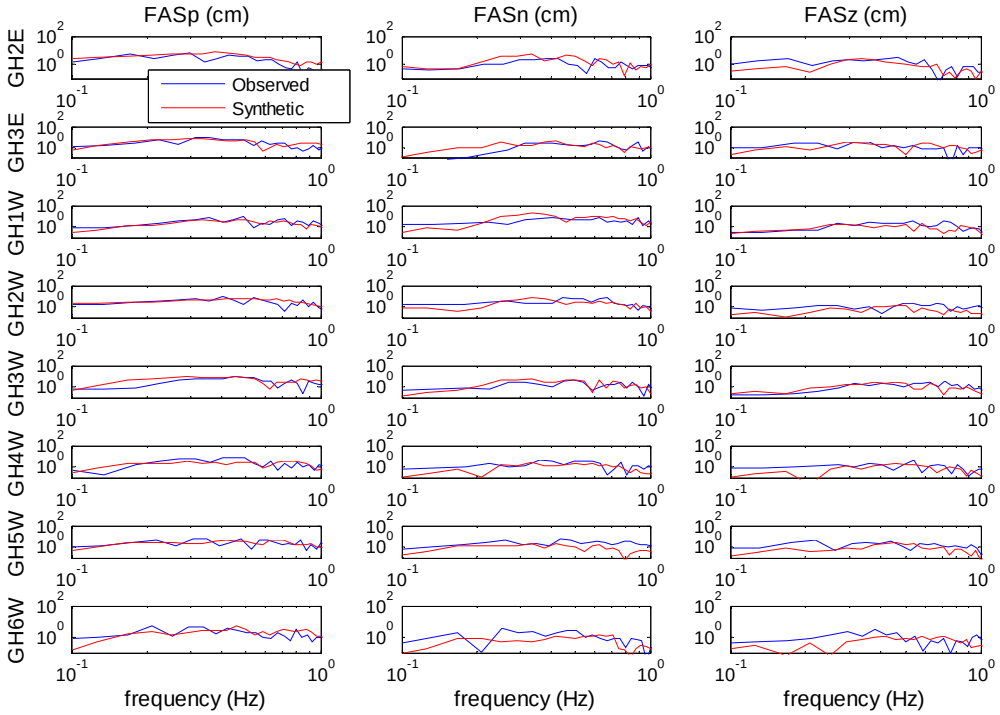

Figure 3.21. Goldhill array: Fourier amplitude spectra of the observed and simulated velocity time histories

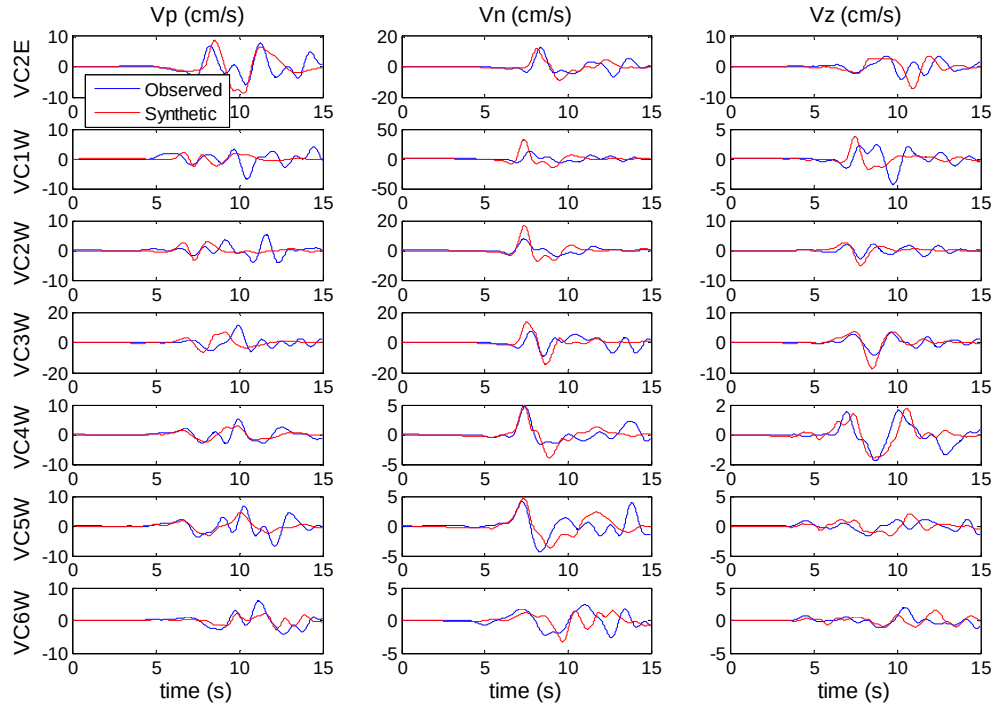

Figure 3.22. Vinyard Canyon array: observed and simulated velocity time histories

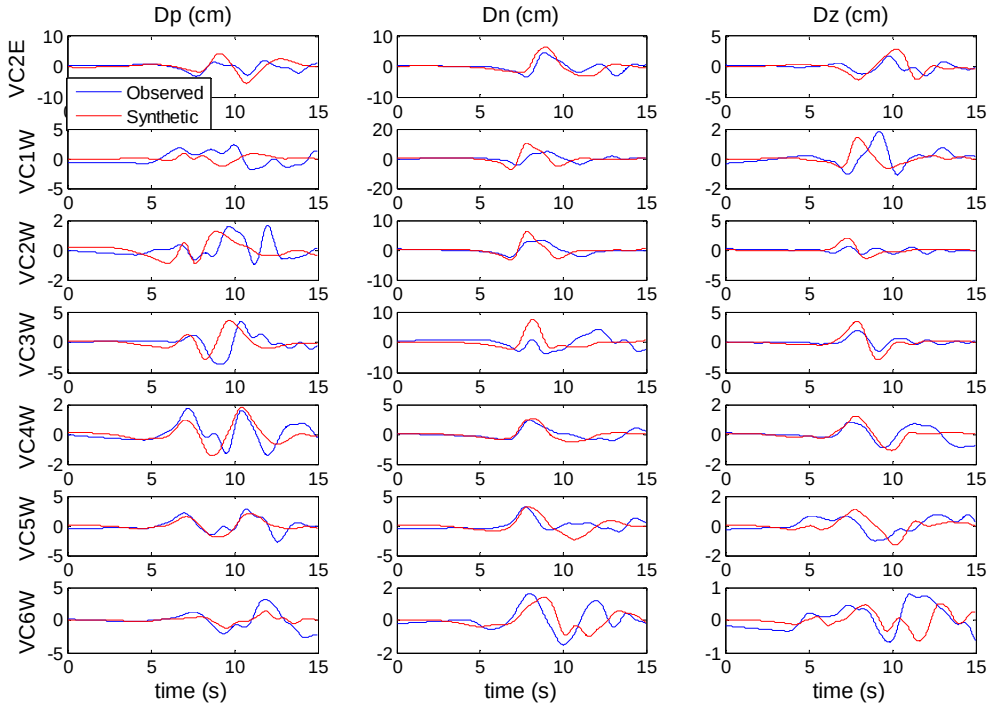

Figure 3.23. Vinyard Canyon array: observed and simulated displacement time histories

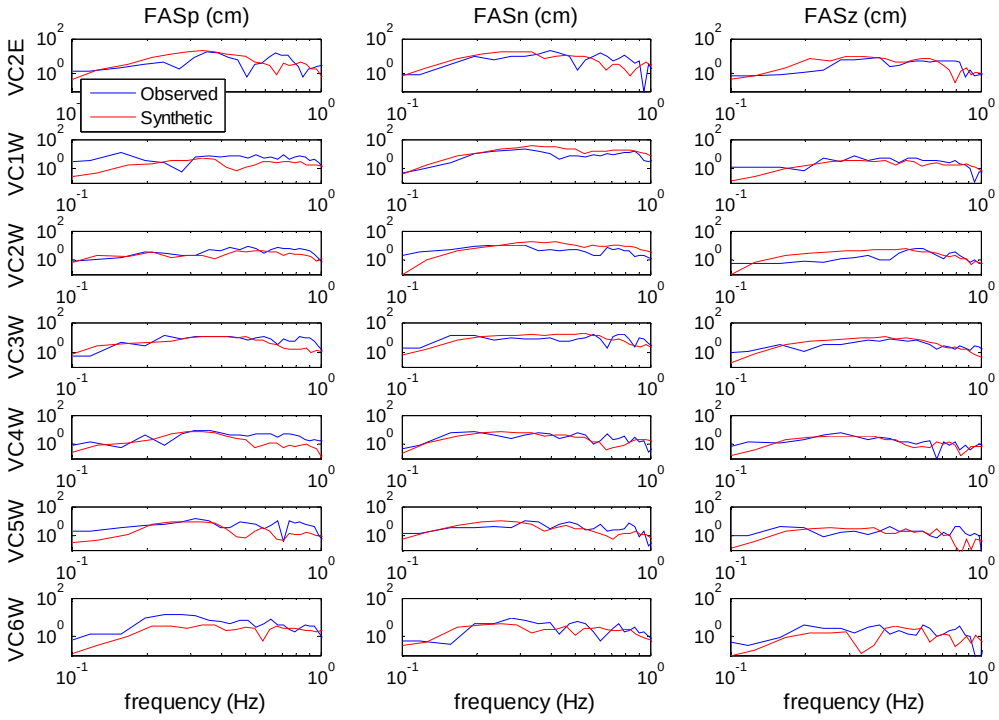

Figure 3.24. Vinyard Canyon array: Fourier amplitude spectra of the observed and simulated velocity time histories

The Stone Corral array (results in Figure 3.25 through Figure 3.27) consists of three instruments located in the northeast side of the fault close to the southwestern end of the rupture and at an angle slightly less than 90° with respect to the fault plane. The closest station is at a distance of about 3 km to the fault. The goodness of fit for this array is generally satisfactory for all components.

The Cholame array (results in Figure 3.28 through Figure 3.30) is also perpendicular to the fault close to the southeastern end of the rupture. Like the Vinyard Canyon array, the Cholame array also exhibits forward directivity characteristics with fault normal components larger than fault parallel components.

The Fault Zone array is formed with the aim of studying the variation of strong ground motion along the fault. As all stations along the Fault Zone array are located at very close distances to the fault, the goodness of fit of the simulated and recorded time histories are less satisfactory, the reason being that in the immediate vicinity of the fault, the records are dominated by the fault trapped waves. The same problem is also observed at the stations of the fault perpendicular arrays located at the immediate vicinity of the fault. However stations of the Fault Zone array which are located at a distance larger than a few kilometers to the rupture produced much favorable results.

The USGS array considered herein consist of nine instruments distributed in the near fault region. Among those stations the fit is particularly satisfactory at Station TF1, which is known to be located on rock and the recording not used in the inversion process by Liu *et al.* (2006).

From an overall examination of the stations' recorded and simulated time histories we can conclude that

- Goodness of fit is very sensitive to the slip model used. This means that there is a lot of information about slip distribution in the seismic records
- S- wave radiation from the fault plane in the forward directivity region dominates the goodness of fit of the simulations as the fault normal components are more satisfactorily simulated than the fault parallel components in that region where the

slip distribution from the entire rupture plane contributes to the ground motion. Fault parallel components are best simulated close to the epicentral region as evidenced by the simulations of the Gold Hill array which passes through the epicenter, since in that region radiation from only one asperity dominates the ground motion.

- Simulation is generally less satisfactory in the immediate vicinity of the fault where the fault-trapped waves dominate the ground motions.
- Simulation of the vertical components can be considered satisfactory given the fact that very low or even no weights were assigned to them during the inversion process.
- Improvement of the goodness of fit was achieved through modifications of various parameters such as slip model, source time function, rise time and crustal velocity structure. It should however be noted that the improvement is mostly achieved in the frequency range higher than 0.4 Hz. Below that level all models yielded comparable results.

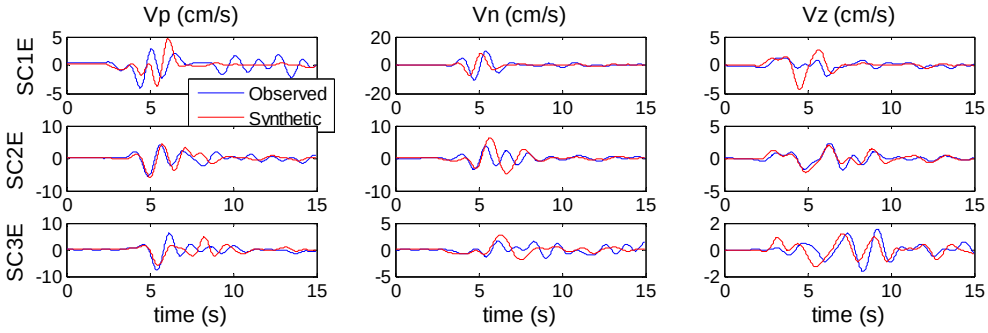

Figure 3.25. Stone Corral array: observed and simulated velocity time histories

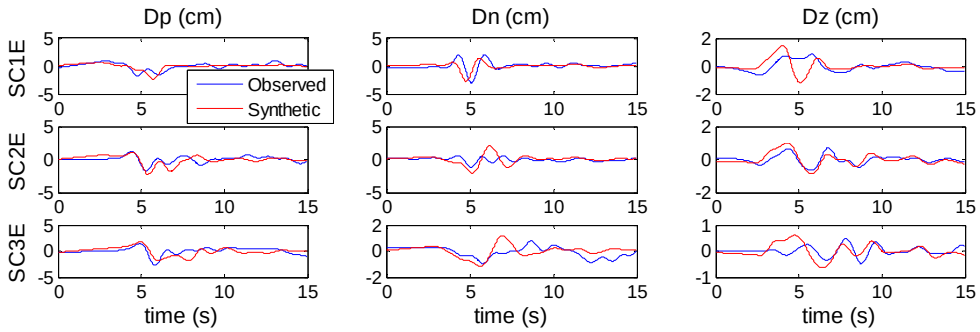

Figure 3.26. Stone Corral array: observed and simulated displacement time histories

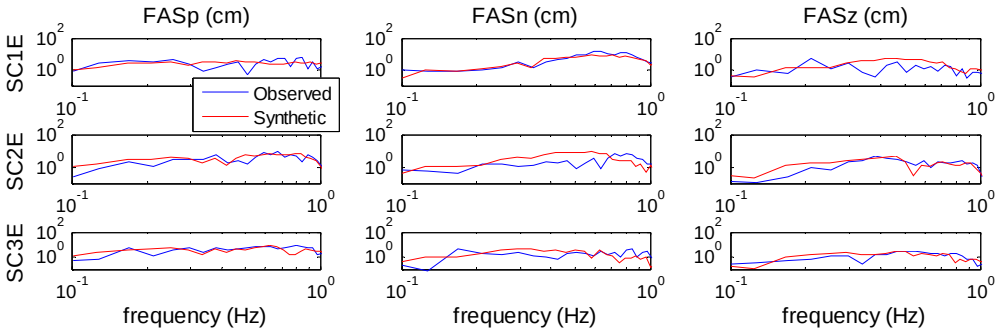

Figure 3.27. Stone Corral array: Fourier amplitude spectra of the observed and simulated displacement time histories

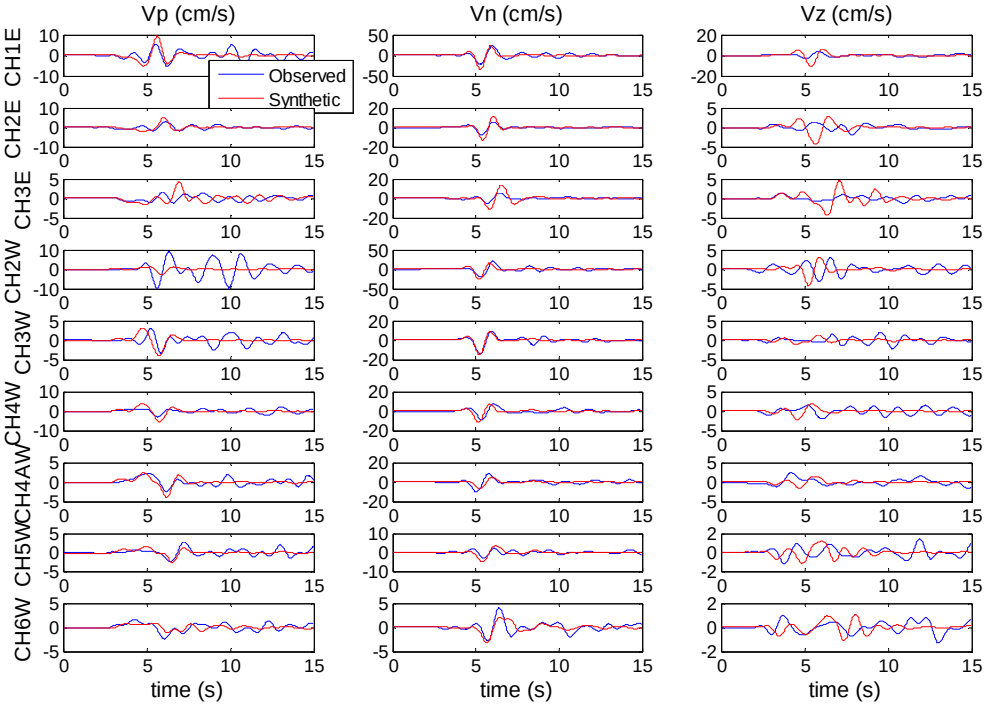

Figure 3.28. Cholame array: observed and simulated velocity time histories

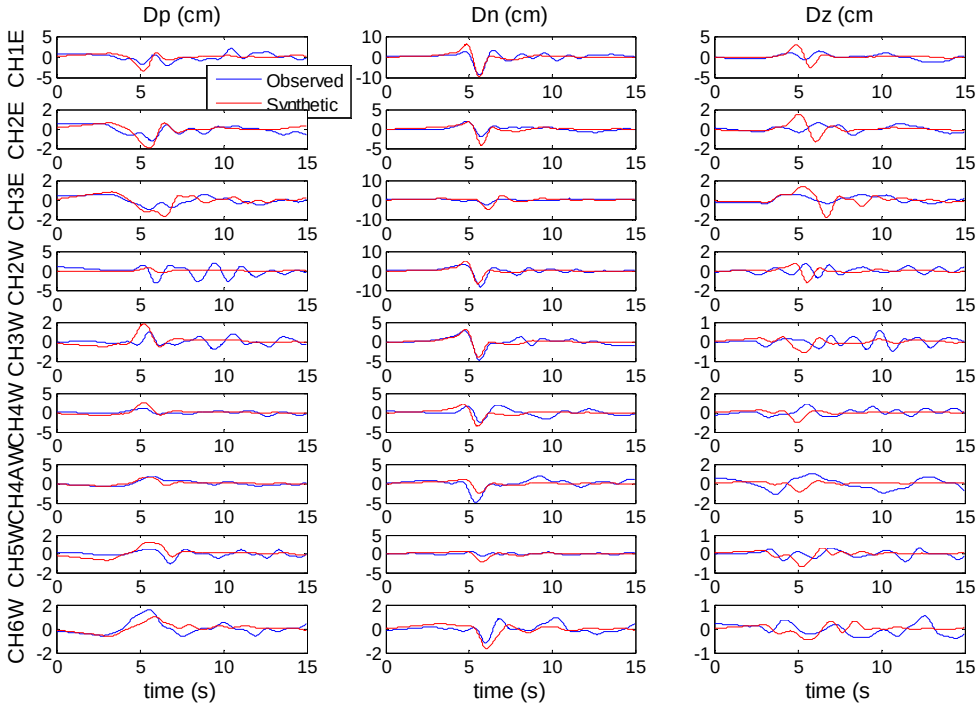

Figure 3.29. Cholame array: observed and simulated displacement time histories

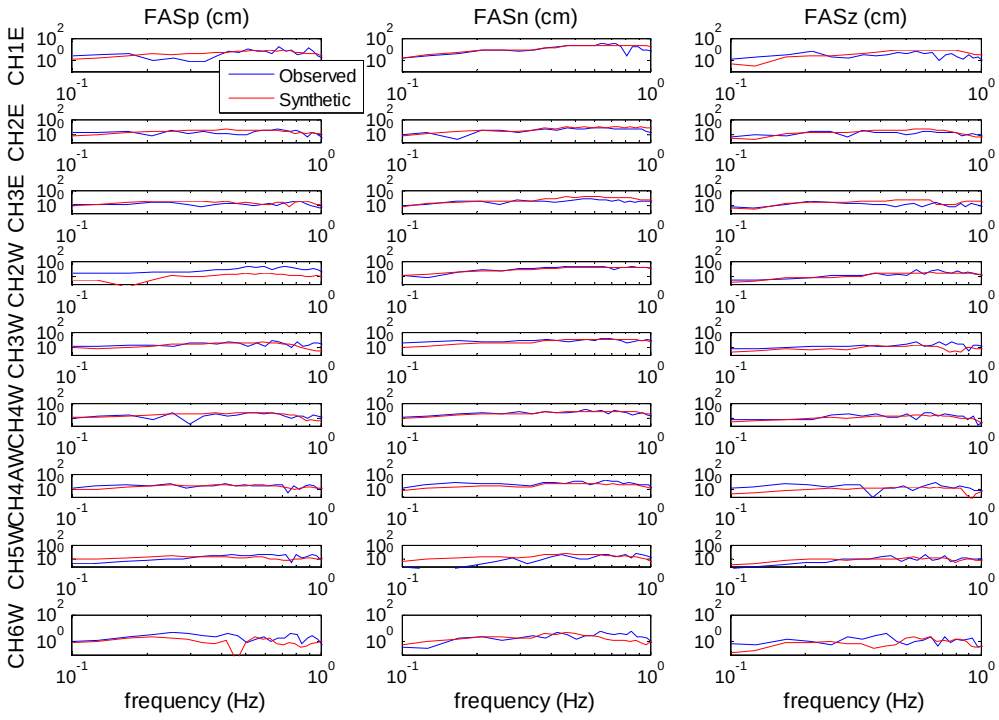

Figure 3.30. Cholame array: Fourier amplitude spectra of the observed and simulated displacement time histories

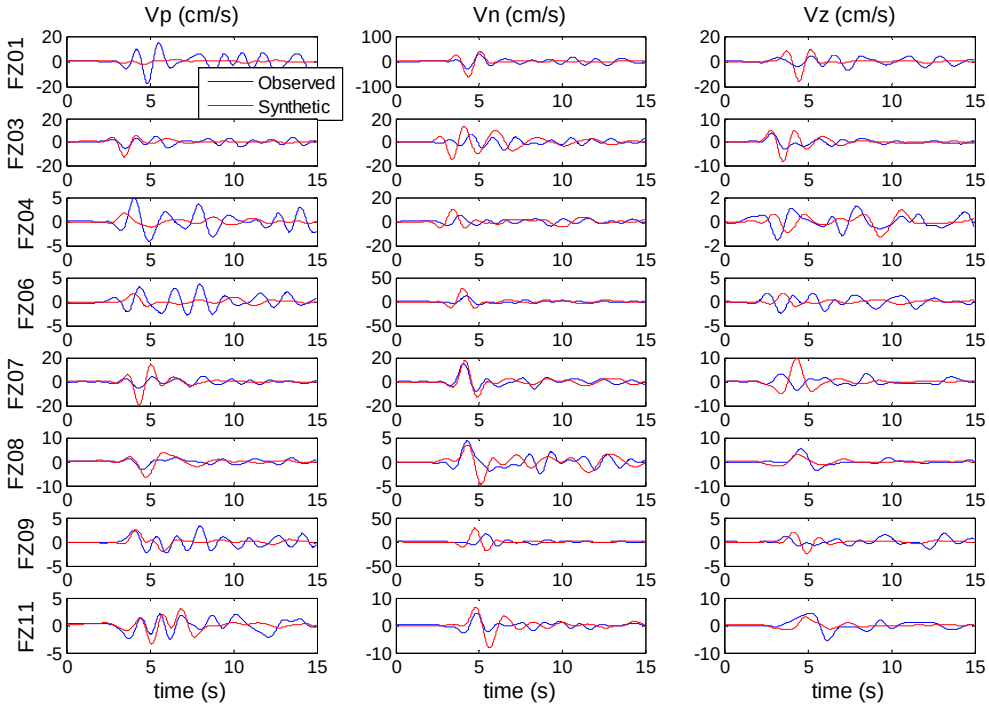

Figure 3.31. Fault Zone Array: observed and simulated velocity time histories

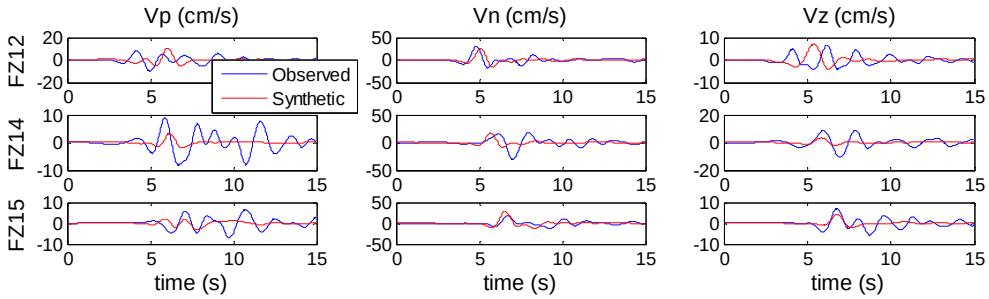

Figure 3.32. Fault Zone Array (cont): observed and simulated velocity time histories

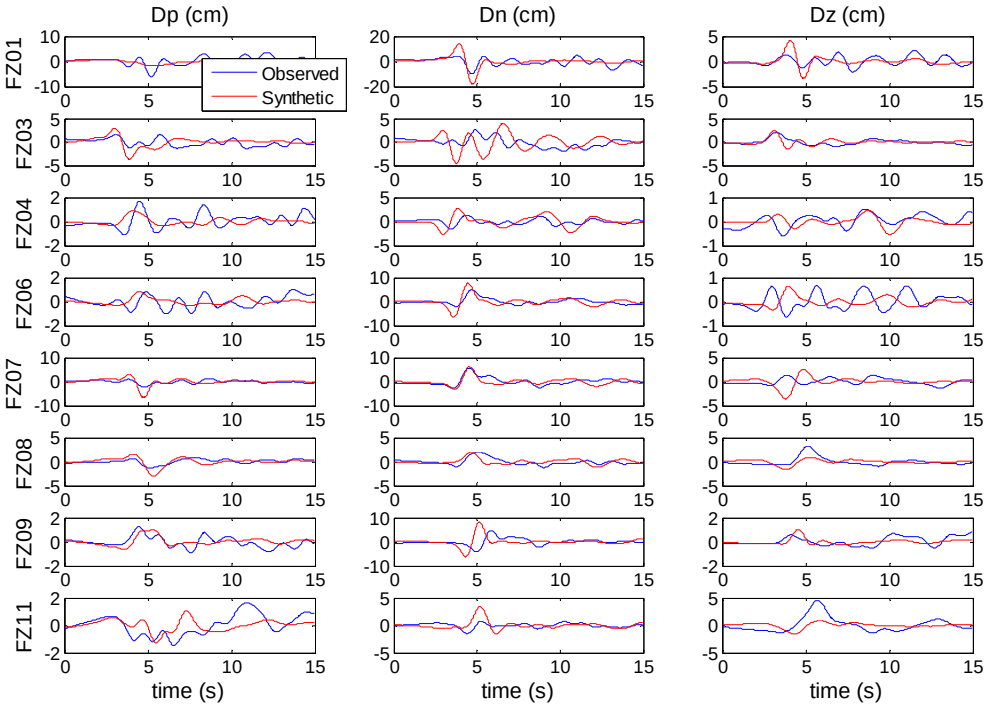

Figure 3.33. Fault Zone Array: observed and simulated displacement time histories

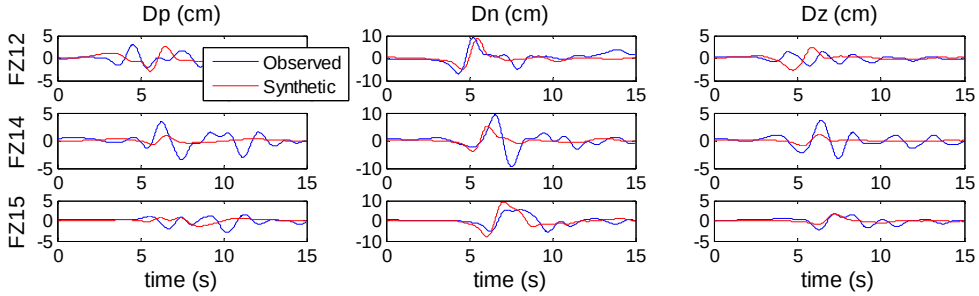

Figure 3.34. Fault Zone Array (cont): observed and simulated displacement time histories

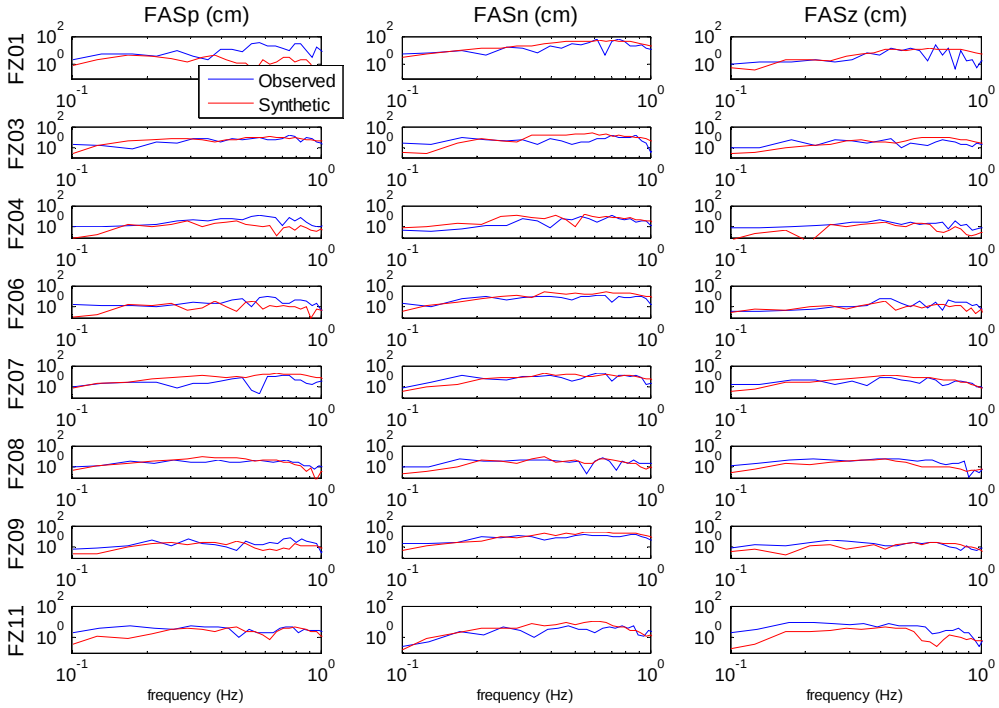

Figure 3.35. Fault Zone Array: Fourier amplitude spectra of the observed and simulated velocity time histories

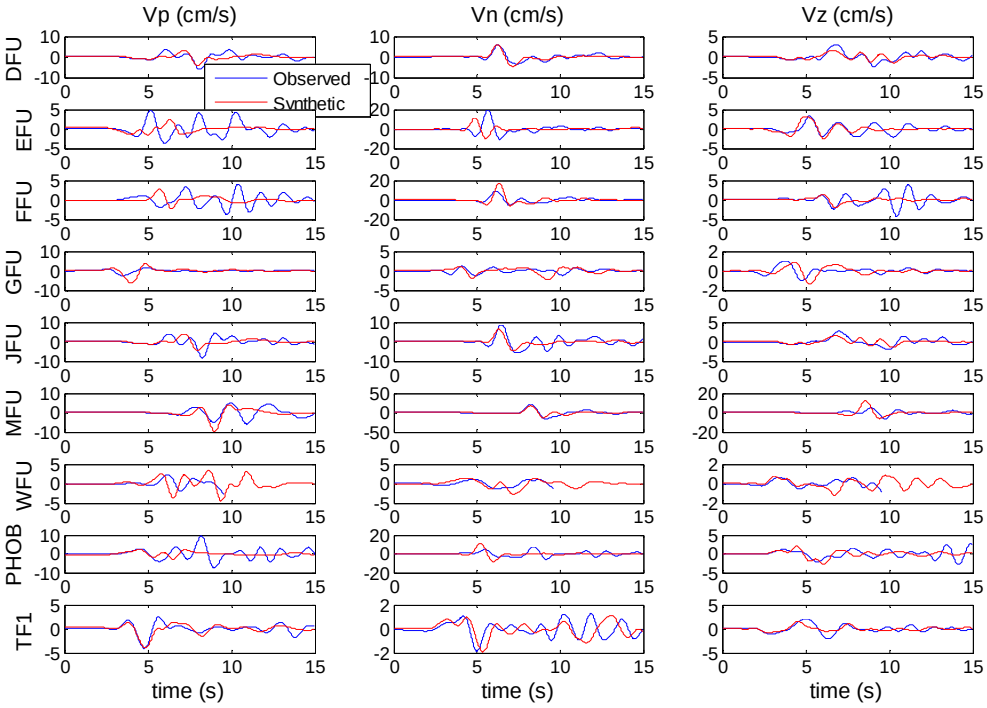

Figure 3.36. USGS stations: observed and simulated velocity time histories

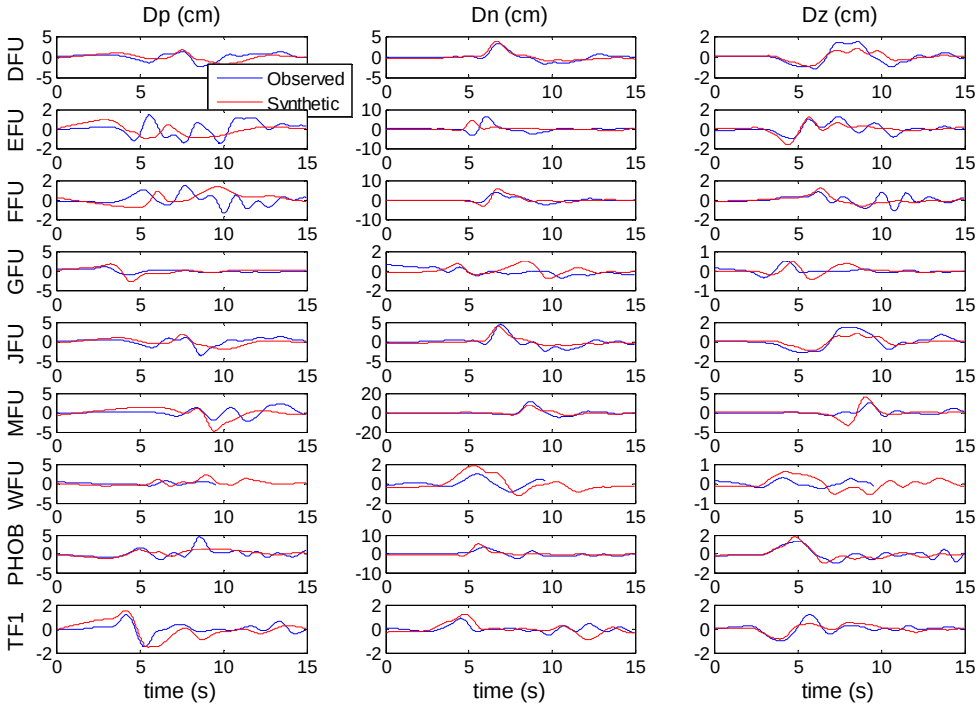

Figure 3.37. USGS stations: observed and simulated displacement time histories

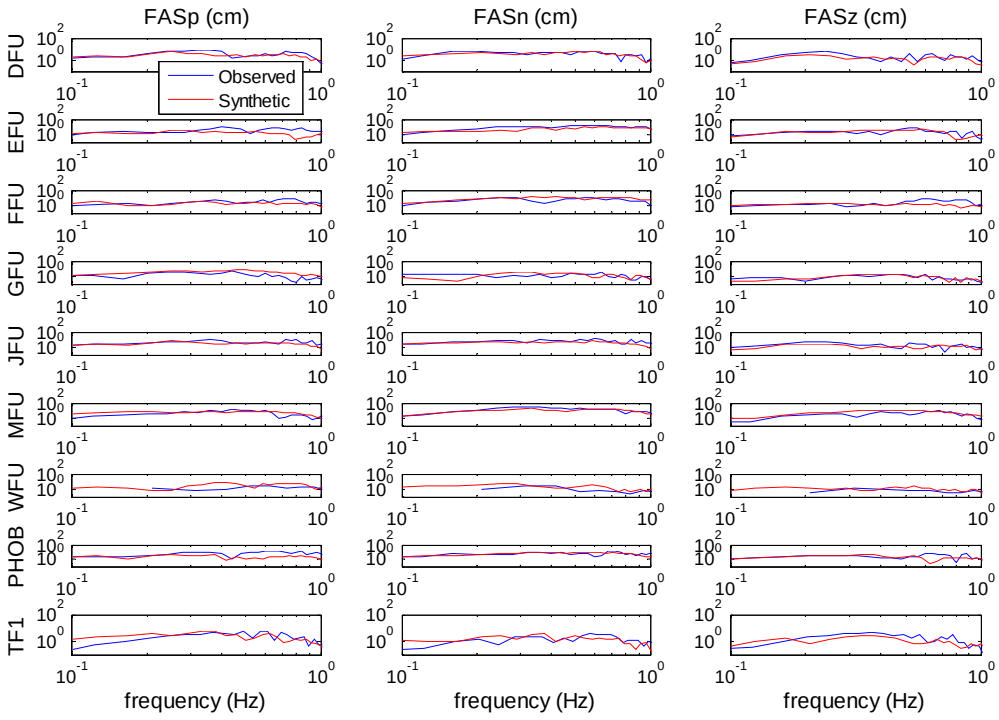

Figure 3.38. USGS stations: Fourier amplitude spectra of the observed and simulated velocity time histories

3.4. Evaluation of the simulations in the response spectral domain

The fit between acceleration response spectra corresponding to the observed and simulated time histories are also investigated. Figure 3.39 and Figure 3.40 represent the acceleration response spectra of the fault parallel and fault normal components of both simulated and recorded time histories of the Gold Hill and Vinyard Canyon arrays respectively. The results of both the Liu *et al.* (2006) and Ji (2005) slip models are shown. For the Gold Hill array which is located very close to the epicenter and one of the two largest asperities the response spectra are not much influenced by the variation in the slip models, whereas in the Vinyard Canyon array which is located in the forward directivity region, the response spectra exhibit a greater variance with respect to the slip model used and the fit of the recorded and simulated response spectra at particular stations change according to the slip model used.

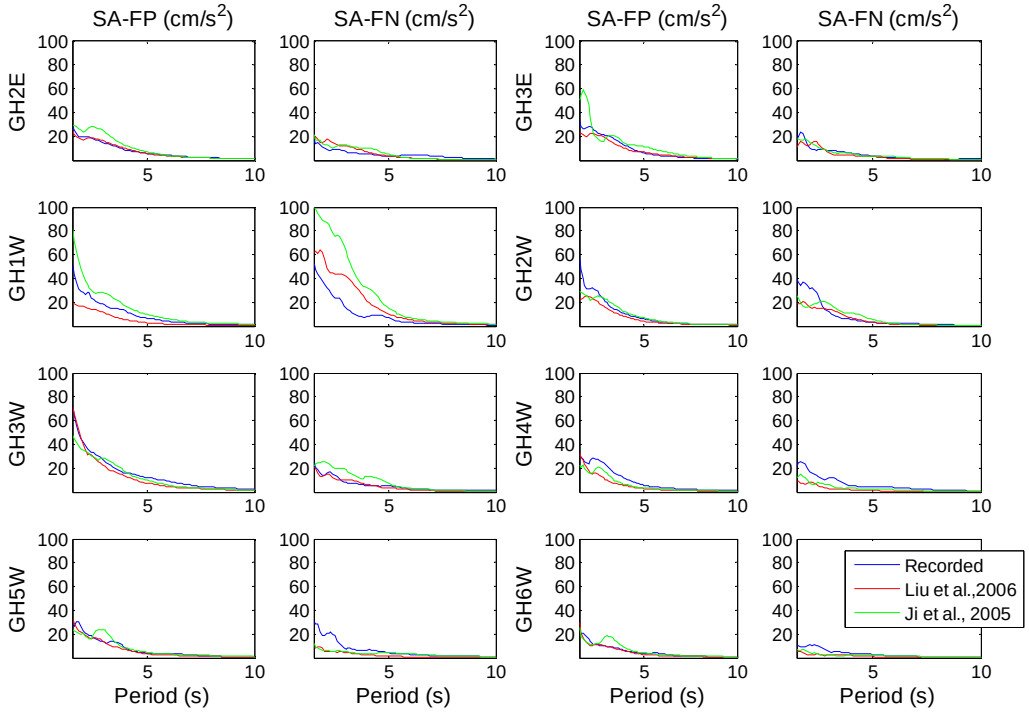

Figure 3.39. Acceleration response spectra of the observed and simulated time histories for the Gold Hill Array. The simulated time histories are low pass filtered at 1Hz, the recorded data are not filtered. The blue trace represents the response spectra of the recorded data, the red trace is the data simulated with the Liu *et al.* (2006) slip model, and the green trace is simulation result of the Ji (2005) slip model.

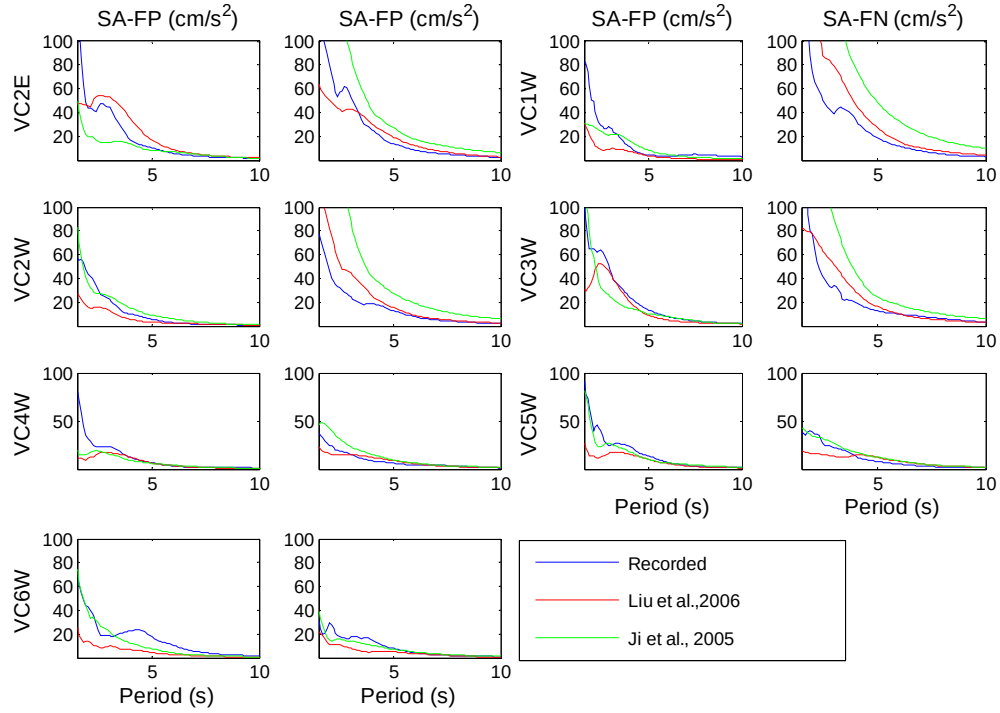

Figure 3.40. Acceleration response spectra of the observed and simulated time histories for the Vinyard Canyon Array. The simulated time histories are low pass filtered at 1 Hz, the recorded data are not filtered. The legend is the same as in Figure 3.39.

3.5. Distribution of Engineering Parameters

The main objective of the study being the use of the 3D Finite Difference code for engineering applications the ground surface distribution of some engineering parameters obtained from the simulation are investigated to see whether the results would be suitable for the analysis of the spatial variability of ground motion. The distributions of fault normal and fault parallel PGV, PGD and Response Spectral Accelerations at T=2.0 s obtained for the Liu et al. (2006) slip model are presented in Figure 3.41 through Figure 3.43. The results obtained so far indicate that a kinematic model in a realistic propagation medium gives results that can be used for many engineering applications. An outstanding feature of the simulations is that at high frequencies fault normal components near the edge of fault segments dominate the velocity and acceleration fields. Fault parallel component is reduced by the nodal plane that coincides with fault. The difference in the orientation of rupture propagation is clearly observed in the engineering parameters like PGV and PGD. The spatial distribution of peak values such as PGV, PGD and spectral amplitudes can be

used to study the low frequency range spatial variability of ground motion caused by various features of the earth crust such as attenuation, basin effects and topography as well as the rupture parameters such as slip distribution and rupture velocity. The simulated time histories and the associated response spectra can also be used in the assessment of design parameters for especially long period structures such as bridges or base isolated buildings. 3D Finite Difference simulations can also be used in connection with the spectral displacement based seismic design concepts recently emerging in earthquake engineering (e.g. Priestley *et al.*, 2007).

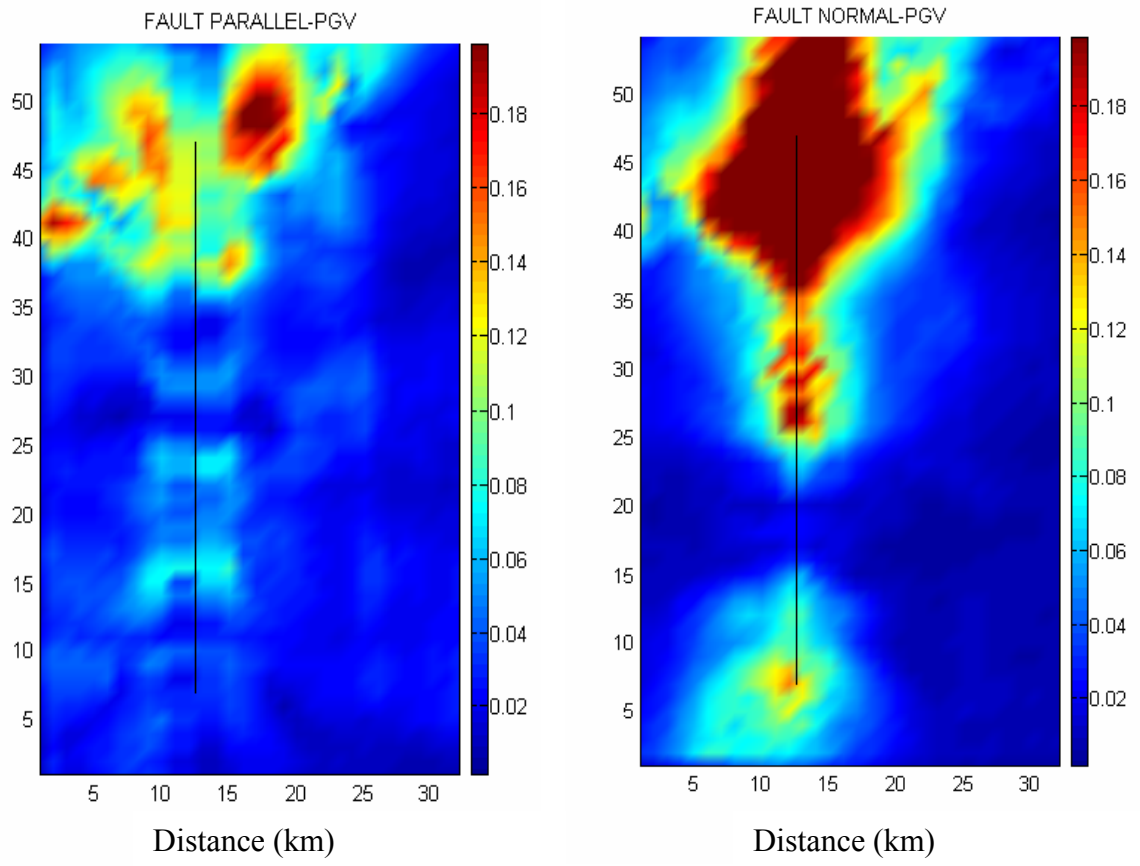

Figure 3.41. The distribution of fault parallel and fault normal peak ground velocities (m/s)

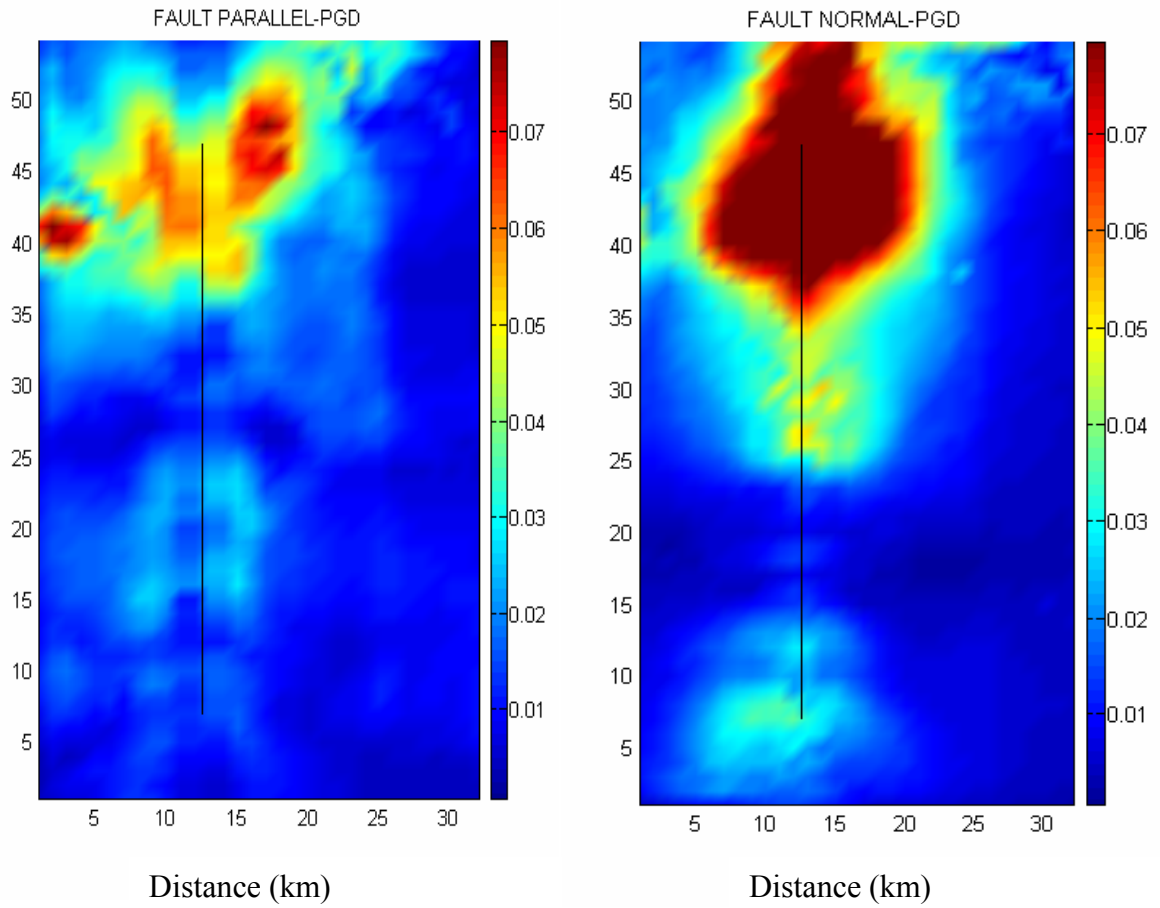

Figure 3.42. The distribution of fault parallel and fault normal peak ground displacements (m)

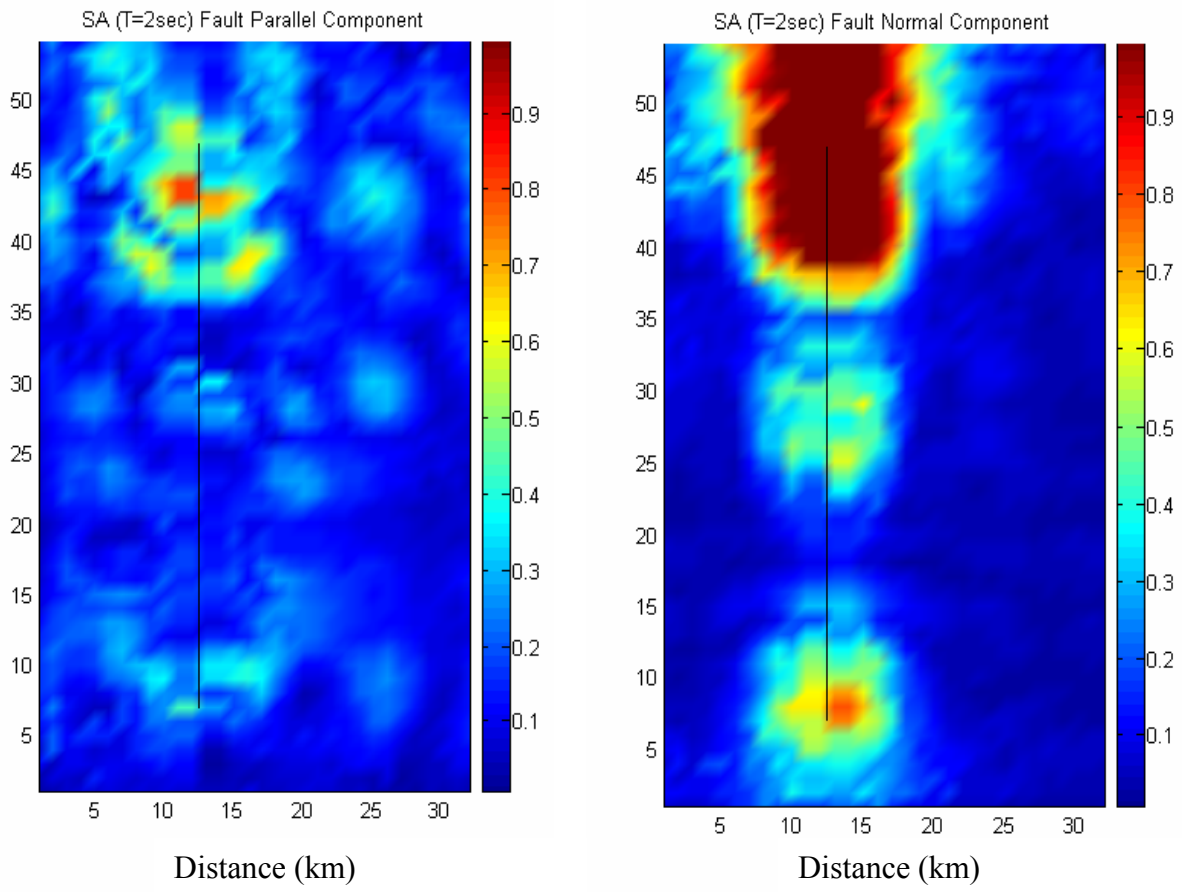

Figure 3.43. The distribution of fault parallel and fault normal spectral accelerations (m/s^2) for T=2.0 s

4. NEAR SOURCE GROUND MOTION

The ground motion recorded at a receiver set far enough from a rupturing fault would have characteristics highly different than the one that would be recorded at the vicinity of the fault. For a station in the far field the radiation of seismic waves from the rupture appears to originate form a single point and concepts such as receiver distance, radiation pattern, P and S wave arrival times can be more easily defined. If the station is located close to the source, the rupture can no longer be approximated as a single point. Instead, it is sensed as a heterogeneous slip over a surface or a volume and the recording is affected by the slip distribution, the location of the hypocenter, the rupturing direction and velocity. In that case it is more difficult to define those concepts and ground motion at two points equally distant from the fault may have characteristics highly different from each other according to their azimuth with respect to rupture propagation direction (Archuleta and Hartzell, 1981). Rupture generally proceeds along a fault surface as a series of small dislocations. In the case of a station that lies on the same axis with the fault and towards which a strike-slip rupture is propagating, the accumulation of the effects of the small dislocations along the fault causes azimuthal differences and the fault normal ground motion is characterized by a velocity pulse of large amplitude which carries almost all the energy of the rupture. This is called the forward directivity effect. At a station where the rupture propagates away, the effect of the series of dislocations is distributed in time resulting in long duration motions with low amplitude. This is called the backward directivity effect. In the case of a dip-slip rupture forward directivity conditions are observed up-dip from the hypocenter and at sites located along the surface exposure of the fault (Somerville *et al.*, 1997). Some examples of recent strong ground motion recordings exhibiting forward directivity effects in strike-slip faulting are given in Figure 4.1 through Figure 4.3. Figure 4.4 illustrates forward directivity effects from a dip-slip rupture.

Previous studies on the characterization of near source effects on the strong ground motion parameters relevant to a seismic hazard assessment study are discussed in the following sections.

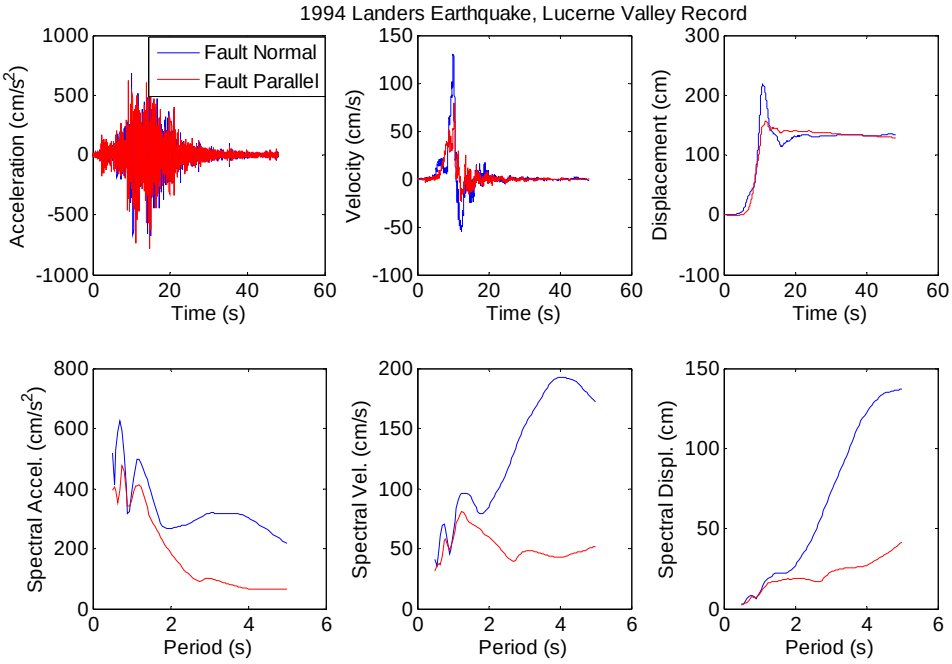

Figure 4.1. Fault normal and fault parallel acceleration, velocity and displacement time histories recorded at Lucerne Valley station during the 1992 Landers earthquake and the associated response spectra

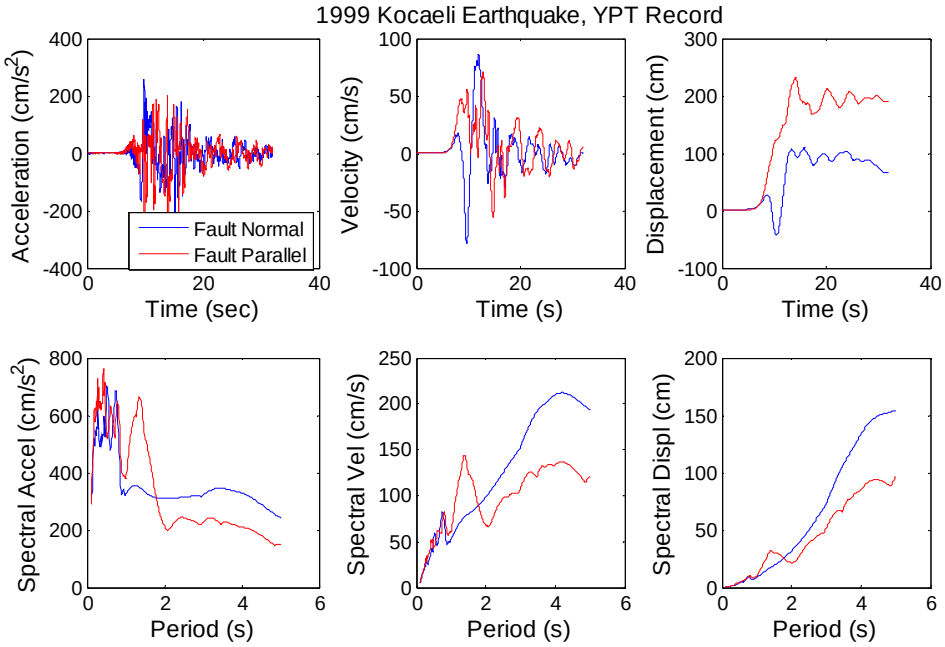

Figure 4.2. Fault normal and fault parallel acceleration, velocity and displacement time histories recorded at YPT station during the 1999 Kocaeli earthquake and the associated response spectra

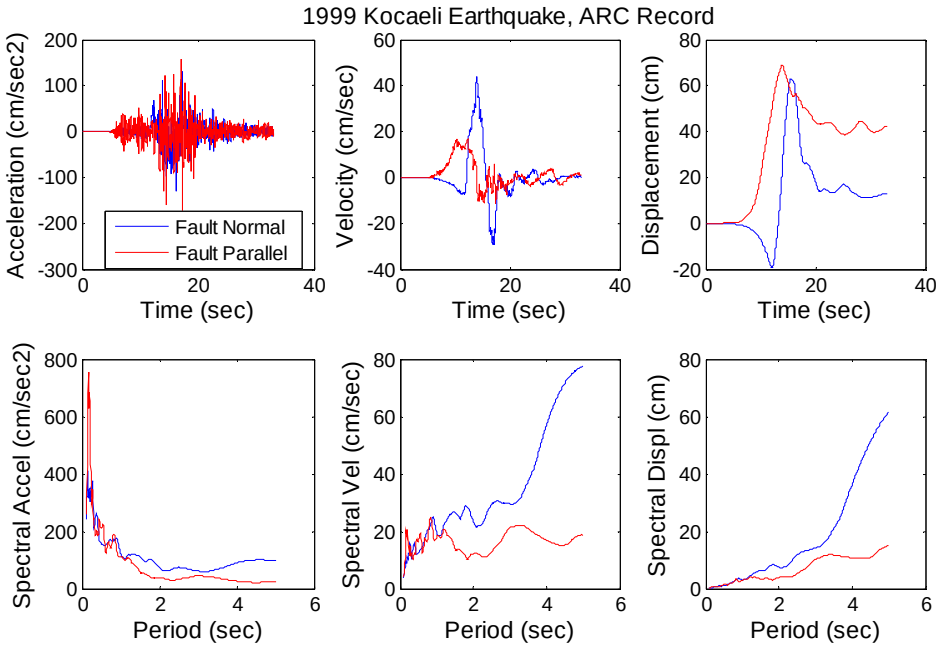

Figure 4.3. Fault normal and fault parallel acceleration, velocity and displacement time histories recorded at ARC station during the 1999 Kocaeli earthquake and the associated response spectra

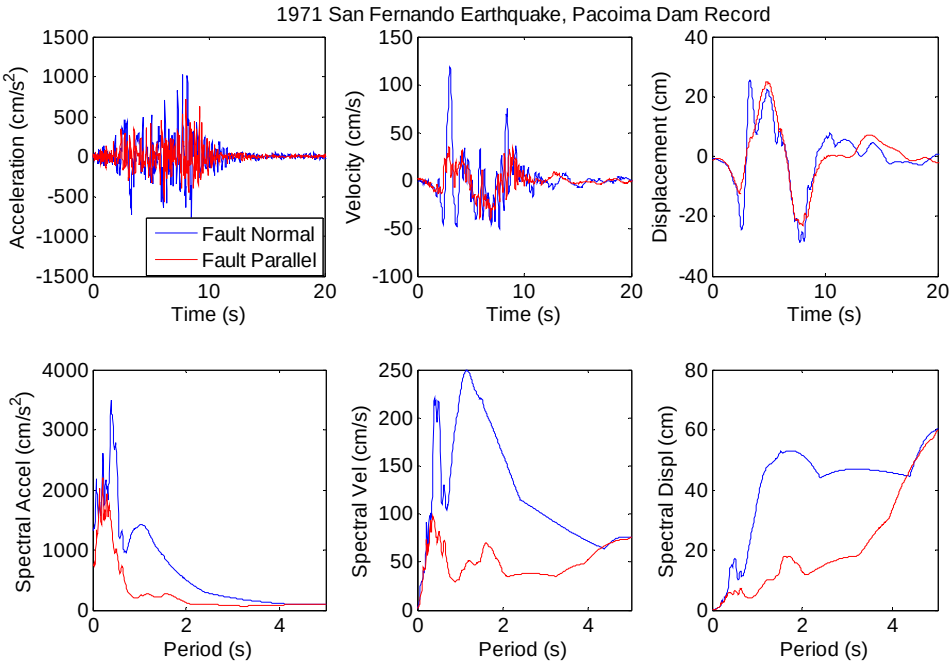

Figure 4.4. Fault normal and fault parallel acceleration, velocity and displacement time histories recorded at Pacoima Dam station during the 1971 San Fernando earthquake and the associated response spectra

4.1. Modification of Empirical Strong Ground Motion Prediction Equations

Based on the analysis of near fault strong ground motion data Somerville et al. (1997) proposed modifications to empirical ground motion prediction equations to account for the effects of rupture directivity on strong motion amplitudes and durations. The ground motion parameters considered were the average horizontal response spectral acceleration, the average duration of the two horizontal acceleration time histories and the ratio of strike-normal to strike-parallel spectral acceleration. Two parameters were chosen to define the spatial variation of the directivity effects. These were the fraction of the fault rupture lying between the hypocenter and the site and the angle between the fault plane and the path from the hypocenter to the site. These two parameters define the conditions which produce forward and backward directivity effects, the rupture front propagating towards the site and the alignment of the slip direction with the site producing forward directivity with a large displacement pulse normal to the site, whereas rupture propagating away from a site causing backward directivity effects with longer durations and low amplitudes in longer periods. The study points out that the ratio of strike normal to strike parallel motions is primarily a function of the radiation pattern of the earthquake. As such, regardless of the amplitudes, large ratios of strike-normal to strike-parallel motions are observed both in forward and backward directivity regions. The strike-normal to strike parallel ratio is mainly controlled by the angle and less controlled by the length and width ratios.

4.1.1. Spatial Variation in Average Horizontal Response Spectra

Somerville *et al.* (1997) use the residuals between the recorded average horizontal spectral acceleration and that calculated from the empirical ground motion prediction equations of Abrahamson and Silva (1997a) as inputs into a regression analysis and examine the dependence of these residuals on the angles and distance ratios. The proposed modification equations do not include magnitude and distance as parameters since it is assumed that the magnitude and distance dependence of the ground motion at a particular site is already accounted for by use of a basic empirical ground motion prediction equation such as Abrahamson and Silva (1997a). The forms are as follows:

$$y = C_1 + C_2 X \cos\theta \quad \text{for strike-slip faulting with } M_w > 6 \tag{4.1}$$

$$y = C_1 + C_2 Y \cos\phi \text{ for dip-slip faulting with } M_w > 6.5 \quad (4.2)$$

where y is the residual of the natural logarithm of the spectral acceleration at a given period, X and Y are along strike and updip distance ratios, θ and ϕ are azimuth and zenith angles and C_1 and C_2 are period dependent coefficients. The average horizontal spectral accelerations accounting for directivity effects can later be calculated as given in Equation 4.3.

$$\ln[SA_{dir}(M,r,x,\theta,T)] = \ln[SA(M,r,T)] + y(x,\theta,T) \quad (4.3)$$

where $\ln[SA(M,r,T)]$ is the spectral acceleration obtained from an empirical ground motion prediction equation. The spatial distribution of spectral acceleration modification factors (as the exponential of y) for a 50 km long strike-slip fault rupture with the epicenter located at 10 km from the fault end for periods of 1.0, 2.0 and 3.0 s are given in Figure 4.5.

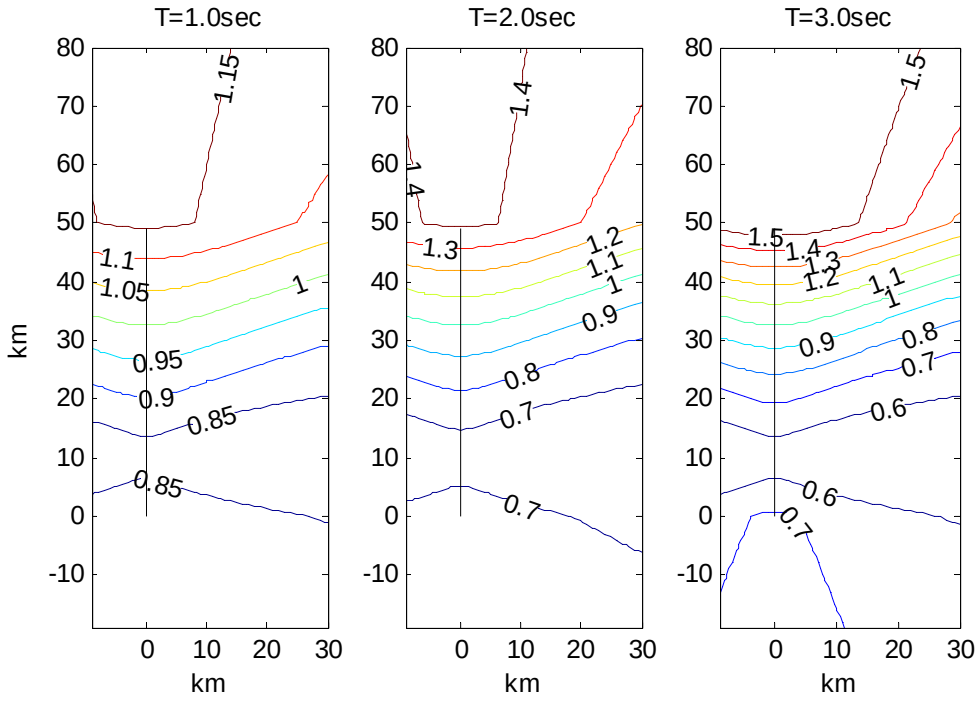

Figure 4.5. The spectral acceleration factors for a 50 km long strike-slip fault rupture with the epicenter located at 10 km from the lower end of the fault for periods of 1.0, 2.0 and 3.0 s as given in Somerville *et al.* (1997)

4.1.2. Spatial Variation in Strong Motion Duration

Somerville *et al.* (1997) use the residuals between the recorded duration and those calculated from the empirical model of Abrahamson and Silva (1997b) as inputs into a regression analysis and examine the dependence of these residuals on the angles and distance ratios. As the magnitude and distance dependence of Abrahamson and Silva (1997b) model is retained the proposed modification equations do not include magnitude and distance as parameters. The forms are as follows:

$$y = C_1 + C_2 X \cos\theta \quad \text{for strike-slip faulting with } M_w > 6.5 \tag{4.4}$$

$$y = C_1 + C_2 Y \cos\phi \quad \text{for dip-slip faulting with } M_w > 6.5 \tag{4.5}$$

where y is the residual of the natural logarithm of the duration at a given period, X and Y are along strike and up-dip distance ratios, θ and ϕ are azimuth and zenith angles and C_1 and C_2 are period dependent coefficients. As at longer distances for strike-slip earthquakes path effects such as the trapping of SH waves in sedimentary basins combine with source effects, a distance cut-off of 20 km is used in the development of the directivity function for duration. The spatial distribution of spectral acceleration modification factors (as the exponential of y) for a 50 km long strike-slip fault rupture with various epicentral locations along the fault are given in Figure 4.6. These factors of duration range between about 1.5 for $X\cos\theta = 0$ i.e. for minimum directivity conditions and 0.5 for $X\cos\theta = 1$ i.e. for maximum directivity conditions in strike-slip faulting.

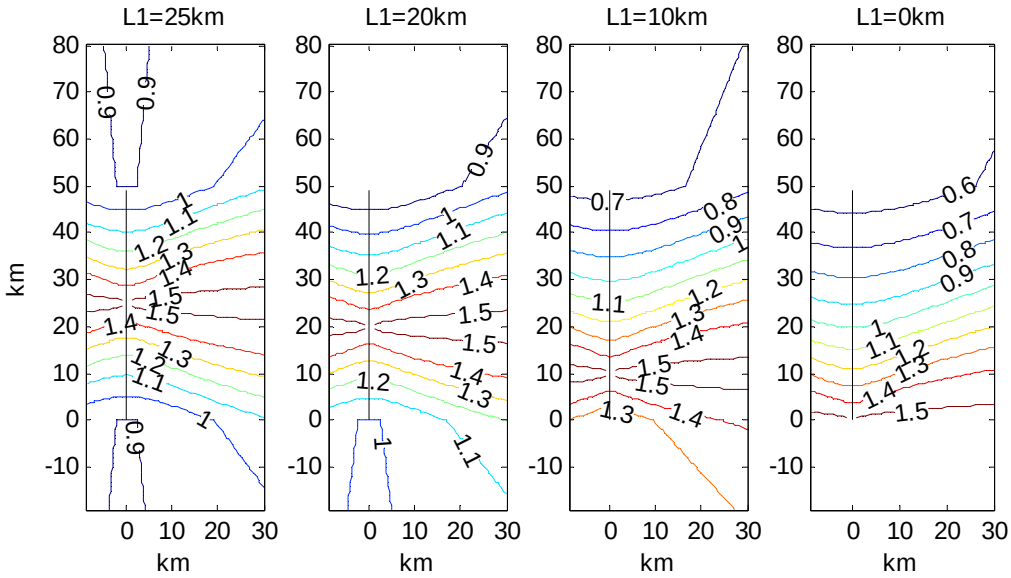

Figure 4.6. The duration factors for a 50 km long strike-slip fault rupture for epicenters located at various positions along the fault as given in Somerville *et al.* (1997)

4.1.3. Spatial Variation in the Ratio of Strike Normal to Average Motions

The ratio of the strike normal to average horizontal motion corresponds to the square root of the strike-normal to strike-parallel ratio. Somerville et al (1995) proposed the following form to express the dependence of the strike-normal to strike-parallel ratio on magnitude and fault distance.

$$y = C_1 + C_2 \ln\left(r_{rup} + 1\right) + C_3\left(M_w - 6\right) \text{ for } M_w > 6 \tag{4.6}$$

where y is the natural logarithm of the strike-normal to strike-parallel ratio for a given period, r_{rup} is the rupture distance in km, M_w is the moment magnitude and C_1 through C_3 are the period dependent regression coefficients.

Somerville et al (1997) added the effect of the azimuth and zenith angles θ and ϕ to this model. The effect of the distance ratio terms X and Y were found to be not significant and thus dropped. The resulting equation had the following form:

$$y = \cos 2\xi\left[C_1 + C_2 \ln\left(r_{rup} + 1\right) + C_3\left(M_w - 6\right)\right] \text{ for } M_w > 6,\ \zeta < 45° \tag{4.7}$$

where ζ is θ for strike-slip faulting and ϕ for dip-slip faulting. Other parameters are as defined above. y is 0 for $\zeta \geq 45°$. The spatial distribution of ratio of fault normal spectral acceleration to the average horizontal spectral acceleration for a 50 km long strike-slip fault rupture with the epicenter located at 10 km from the fault end for periods of 1.0, 2.0 and 3.0 s. is given in Figure 4.7.

The period dependent coefficients for the modification of average spectral acceleration, duration and the computation of fault normal component of the spectral acceleration as given in Somerville *et al.* (1997) are presented in Appendix B.

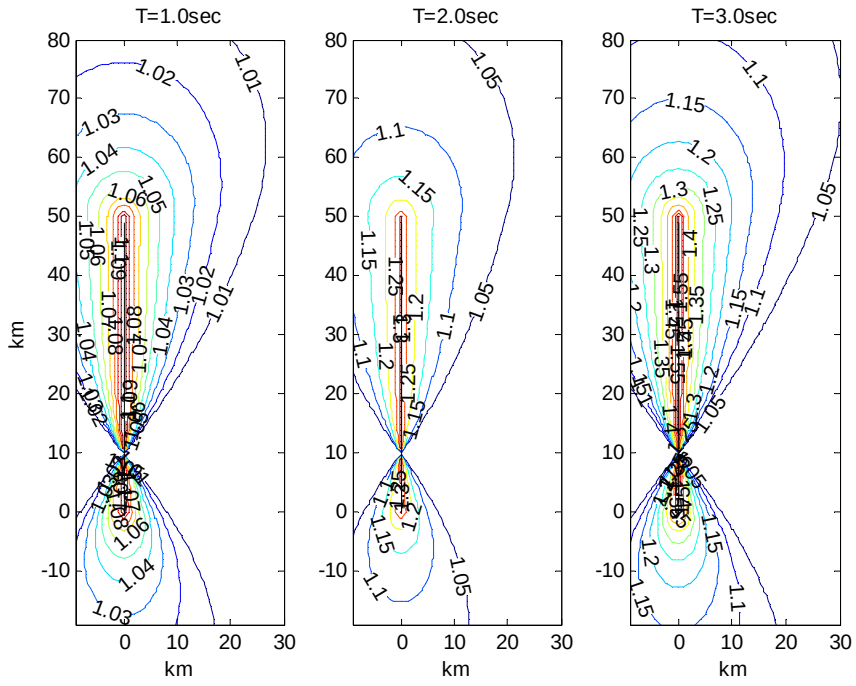

Figure 4.7. Fault normal to average horizontal spectral acceleration ratio for a 50 km long strike-slip fault rupture with the epicenter located at 10 km from the lower end of the fault for periods of 1.0, 2.0 and 3.0 s as given in Somerville *et al.* (1997)

4.2. Magnitude Scaling of Near Fault Directivity Pulse

Based on near field recordings of recent major earthquakes Somerville 2003 developed a model to estimate the period of the fault normal velocity pulse that would be observed in the forward directivity region. From a close observation of near fault recordings of buried rupture (M_w 6.7 – 7.0) and large surface rupture (M_w 7.2 – 7.6)

earthquakes the study points out that the spectral accelerations obtained from the former group exhibit large amplitudes in the intermediate period range (0.5 – 2.5 s) whereas those obtained for the second group have lower amplitudes in that range but larger ones in the longer periods (> 3 s). These observations reveal that spectral amplitudes do not increase monotonically at all amplitudes but are related to the narrowband character of the forward directivity pulse whose period is related to source parameters such as rise time and fault dimensions. As these parameters generally increase with increasing magnitude, Somerville (2003) links the period of the velocity pulse with magnitude as given in Equation 4.8 and Equation 4.9 for rock and soil sites respectively.

$$\log_{10} T_{Dir} = -3.17 + 0.5M_w \tag{4.8}$$

$$\log_{10} T_{Dir} = -2.02 + 0.346M_w \tag{4.9}$$

The resulting curves are illustrated in Figure 4.8. The curves for rock and soil sites intersect at magnitude M_w=7.4. The relationship for the soil sites gives lower values than that of the rock sites beyond that point. It is expected however that it will follow the shape of the rock sites for M_w > 7.4.

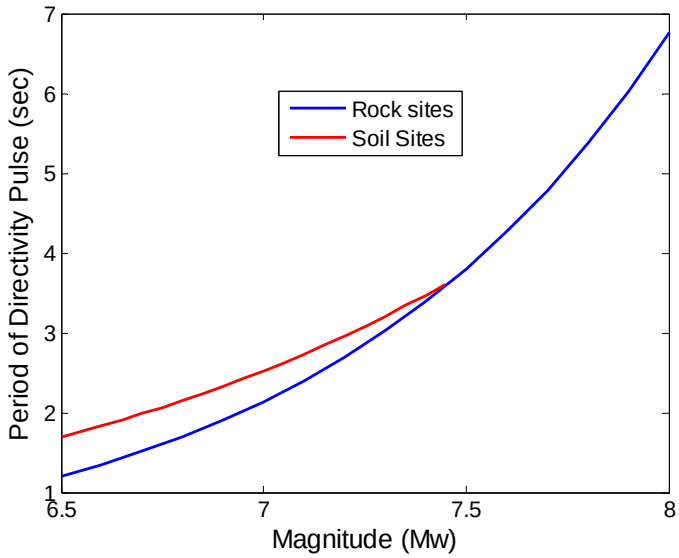

Figure 4.8. The period of directivity pulse (Somerville, 2003)

4.3. Incorporation of Rupture Directivity in Probabilistic Seismic Hazard Analysis

The 1997 Uniform Building Code (UBC, 1997) accounted for the near fault effects by means of near-source factors, N_a and N_v applied to the low-period (acceleration dominated) and intermediate period (velocity dominated) parts of the acceleration response spectrum respectively. The near source factors are specified for distances less than 15 m and for three different fault types (Table 4.1 through Table 4.3). These factors can be used to modify the mean horizontal spectral acceleration obtained from a seismic hazard study but do not address the larger fault-normal component.

Abrahamson (2000) modified the equational form given by Somerville *et al.* (1997) in order to make it applicable to probabilistic seismic hazard analysis. First a distance dependent taper function (Equation 4.10) was added to the model to reduce the effect to zero for distances larger than 60 km. A magnitude taper as given in Equation 4.11 was also added to reduce the effect to zero for magnitudes less than 6.0.

$$\begin{aligned} T_d(r) &= 1 && \text{for } r < 30 \text{ km} \\ &= 1-(r-30)/30 && \text{for } 30 \text{ km} \le r \le 60 \text{ km} \\ &= 0 && \text{for } r > 60 \text{ km} \end{aligned} \tag{4.10}$$

$$\begin{aligned} T_m(m) &= 1 && \text{for } m = 6.5 \\ &= 1-(m-6.5)/0.5 && \text{for } 6 = r \le 6.5 \\ &= 0 && \text{for } m < 6 \end{aligned} \tag{4.11}$$

The average horizontal spectral accelerations accounting for directivity effects can later be calculated as given in Equation 4.12.

$$\ln\left[SA_{dir}(M,r,x,\theta,T)\right] = \ln\left[SA(M,r,T)\right] + y(x,\theta,T)T_d(r)T_m(m) \tag{4.12}$$

where $\ln\left[SA(M,r,T)\right]$ is the spectral acceleration obtained from an empirical ground motion prediction equation. The spatial distribution of spectral acceleration modification factors (as the exponential of y) for a 50 km long strike-slip fault rupture with the epicenter

located at 10 km from the fault end and magnitude > 6.5 for periods of 1.0, 2.0 and 3.0 s. are given in Figure 4.9.

Table 4.1. Short period near source factors from the 1997 Uniform Building Code (N_a)

Seismic Source Type	Closest Distance to Known Seismic Source		
	≤ 2km	5 km	≥ 10km
A	1.5	1.2	1.0
B	1.3	1.0	1.0
C	1.0	1.0	1.0

Table 4.2. Intermediate period near source factors from the 1997 Uniform Building Code (N_v)

Seismic Source Type	Closest Distance to Known Seismic Source			
	≤ 2km	5 km	10km	≥ 15km
A	2.0	1.6	1.2	1.0
B	1.6	1.2	1.0	1.0
C	1.0	1.0	1.0	1.0

Table 4.3. Description of seismic source types

Seismic Source Type	Description	Seismic Source Definition	
		Maximum Moment Magnitude, M_w	Slip rate, s (mm/yr)
A	Faults that are capable of producing large magnitude events ant that have a high rate of seismic activity	$M_w \geq 7.0$	$s \geq 5$
B	All faults other than types A and C	$6.5 \leq M_w < 7.0$	$2 \leq s < 5$
C	Faults that are not capable of producing large magnitude events ant that have a relatively low rate of seismic activity	$M_w < 6.5$	$s < 2$

There are several ways to incorporate directivity effects in a seismic hazard assessment study. In both deterministic and probabilistic hazard assessment approaches, spectral accelerations at discrete periods greater than 0.6 obtained from the hazard study can be modified using the average response spectrum coefficients given in Somerville *et al.* (1997). Based on NEHRP (1997) provisions spectral accelerations at periods of 0.2 s (short period) and 1.0 s (intermediate period) obtained from the hazard assessment study can be used to construct the "Uniform Hazard Spectrum" for a specific site. In that case, the Uniform Hazard Spectrum can be corrected for directivity effects using the N_a and N_v coefficients of UBC (1997) given in Table 4.1 and Table 4.2 respectively. The directivity corrected spectral accelerations obtained from the two methods sited above represent the average horizontal spectral values (average of fault normal and fault parallel components) including the near source effects.

Abrahamson (2000) proposed a methodology to incorporate near source effects directly in probabilistic hazard assessment. In this method the location of the hypocenter on the rupture area is included as an additional source of aleatory variability. In standard probabilistic hazard calculations probability density functions are specified for the earthquake magnitude, rupture width, rupture area, location of the center of rupture along strike and location of the center of rupture down dip and the probability that the ground motion at a specific location exceeds a predefined value is calculated by integrating all these probability density functions over their possible ranges (Section 1.2). To account for the directivity effect an additional probability density function for the location of the hypocenter on the fault is added. Then the modification is incorporated with the help of Equation 4.12. Abrahamson (2000) assumed uniform distribution for the location of the hypocenter.

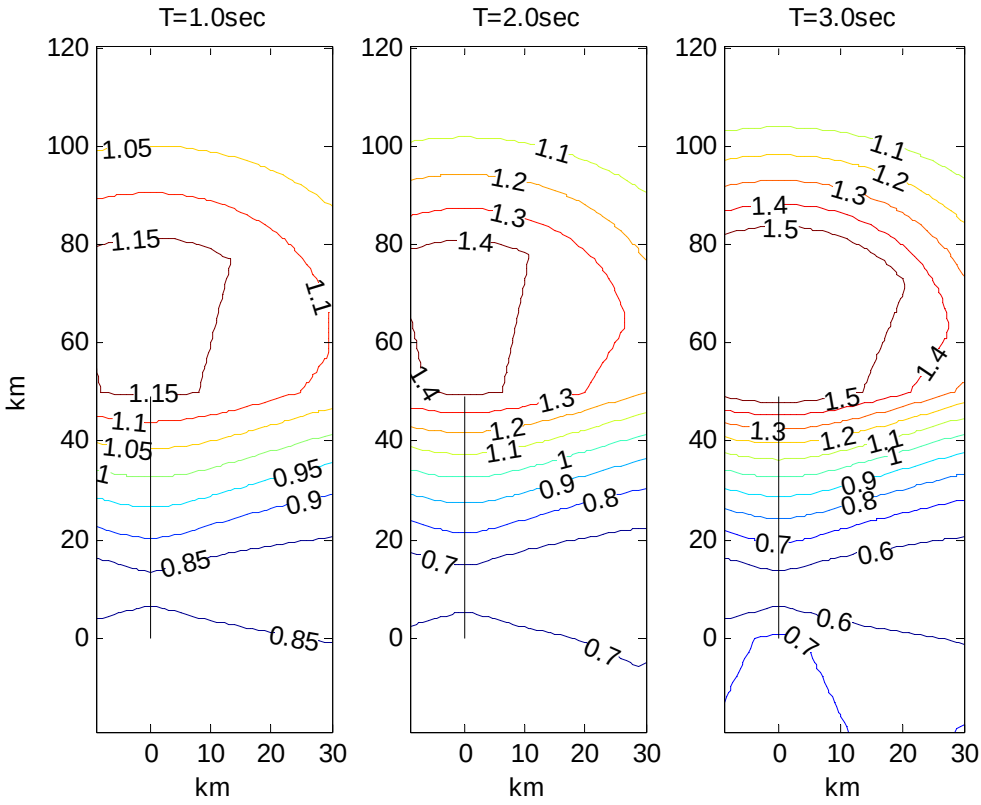

Figure 4.9. The spectral acceleration factors for a 50 km long strike-slip fault rupture with the epicenter located at 10 km from the lower end of the fault for periods of 1.0, 2.0 and 3.0 s as given in Abrahamson (2000)

5. MODELING OF RUPTURE DIRECTIVITY FOR INCORPORATION IN SEISMIC HAZARD ANALYSIS

Two approaches have been used to model rupture directivity effects. First a parametric study was conducted to study the effects of various rupture parameters on the peak ground and spectral amplitudes generated by a uniform slip on a finite fault. Two stations at equal fault distance, but one located near the epicenter and the other in the forward directivity region have been selected to study the spatial variability of various ground motion amplitudes.

Secondly, based on available slip models of recent earthquakes simulations have been conducted to assess the directivity effects generated by more realistic source parameter distributions. The resulting spectral acceleration and displacement distributions have been analyzed in terms of fault normal to geometric mean of the two horizontal components obtained from simulations as well as simulated over empirical average (based on empirical ground motion prediction equations without directivity) amplitudes to assess the near source effects based on magnitude, distance and period of vibration.

5.1. A Parametric Study

As mentioned in Section 2.4. Durukal *et al.* (2005) conducted a benchmark study to evaluate the differences in strong ground motion simulations arising from the usage of different methods. The same layout and the parametric set-up were used to conduct a parametric study in order to evaluate the effects of various simulation parameters in near fault ground motions. The varied source parameters were slip, rise time, depth of asperity, rupture velocity and subfault size (Table 5.1). The green shaded cells in Table 5.1 are identical and represent the base case. The parameter subfault size which is used to discretize the slip on the fault is not a variable parameter in FD3D, since in FD3D the fault s discretized at the same grid spacing as the whole simulation cube, and is therefore excluded from the present analysis.

Table 5.1. The parametric study model parameters

Model Number	Fixed Parameters	Parameter Varied	Parameter Value and Model Id.		
1	Rise Time= 2.0 s V_r = 3.0 km/s Depth of fault = 1km	Slip	1.0 m (1a)	1.5 m (1b)	2.0 (1c)
2	Rise Time = 2.0 s Slip = 1.5 m Depth of fault = 1 km	Rupture Velocity (V_r)	2.7 km/s (2a)	3.0 km/s (2b)	3.4 km/s (2c)
3	Slip = 1.5 m V_r = 3.0 km/s Depth of fault = 1 km	Rise Time	1.5 s (3a)	2 s (3b)	2.5 s (3c)
4	Rise Time= 2.0 s V_r = 3.0 km/s Slip= 1.5 m	Depth of asperity	0 km (4a)	1 km (4b)	

In the 3-D finite difference code a grid spacing of 250 m and time interval of 0.008 s were used. The dislocation was modeled such that it propagated circularly from the hypocenter with constant rupture velocity and an exponential source-time function to reach the final amount of slip. All resulting time histories were low-pass filtered at 1.0 Hz. The peak fault normal and fault parallel velocity and displacement distributions obtained for the base case were presented in Figure 2.27. In the present section the fluctuations in the ground motions with respect to source parameter changes are investigated. Table 5.2 provides the maximum values of fault normal, fault parallel and mean horizontal velocities and displacements for each scenario observed at stations S17 and S31 as well as maxima of all stations representing the maximum ground surface amplitudes. Stations S17 and S31 are located at a distance of 5 km to the fault, the first one being close to the hypocenter and the second one in the forward directivity region (Figure 2.26). The differences in the ground motions obtained for each group of scenario will also be discussed with respect to the time histories observed at these two stations.

Table 5.2. Maximum velocities and displacements at S17 and S31 and on the ground surface for each scenario

Scenario	Direction	Max. Horizontal Velocity			Max. Horizontal Displacement		
		S17 (m/s)	S31 (m/s)	All Stations (m/s)	S17 (m)	S31 (m)	All Stations (m)
1a	FN	0.32	0.95	1.19	0.20	0.81	0.91
	FP	0.45	0.14	0.56	0.57	0.13	0.57
1b	FN	0.48	1.42	1.79	0.30	1.22	1.36
	FP	0.68	0.21	0.84	0.85	0.19	0.85
1c	FN	0.64	1.90	2.38	0.40	1.62	1.81
	FP	0.90	0.27	1.11	1.13	0.25	1.13
2a	FN	0.38	0.83	1.21	0.26	1.01	1.17
	FP	0.49	0.19	0.81	0.76	0.17	0.76
2c	FN	0.57	2.25	2.25	0.30	1.69	1.69
	FP	0.97	0.26	0.96	0.97	0.22	0.97
3a	FN	0.51	1.53	1.97	0.31	1.42	1.26
	FP	0.71	0.22	0.94	0.86	0.87	0.20
3c	FN	0.40	1.21	1.48	0.27	1.11	1.22
	FP	0.61	0.17	0.67	0.80	0.18	0.80
4a	FN	0.48	1.40	1.91	0.31	1.20	1.37
	FP	0.68	0.21	1.33	0.86	0.20	1.20

Maximum fault normal velocities and displacements are observed at station S26, which is located in the forward directivity region, close to the right end of the fault, towards which the rupture is propagating. On the other hand, maximum fault parallel amplitudes are observed at station 16, which is the closest station to the epicenter. The fault distances of S16 and S26 are both 1km (Figure 2.26). Stations S17 and S31 being also equally distant to the fault exhibit similar directivity effects such that the fault normal amplitudes at S31 are much larger than its fault parallel amplitudes as well as the amplitudes in both directions of S17. S17 has fault parallel amplitudes larger than fault normal ones but this difference is not pronounced.

The differences caused by various rupture parameters are analyzed through comparison of time histories at stations S17 and S31 for the different scenarios. Figure 5.1 and Figure 5.2 represent the differences caused by slip amplitudes (Scenarios 1a, 1b and 1c). It can be observed that for a homogeneous rupture case, the increase in the velocity and displacement amplitudes and permanent displacements at both stations are directly proportional to the increase in the amount of slip. The changes caused by the usage of

different rupture velocity values are shown in Figure 5.3 and Figure 5.4 for velocities and displacements respectively. For S31 which is located in the forward directivity region both amplitudes and duration are strongly affected by the rupture velocity, as a rupture front approaching with a faster velocity towards the site causes a faster accumulation of energy resulting in a much narrower velocity pulse with higher amplitude in the fault normal direction.

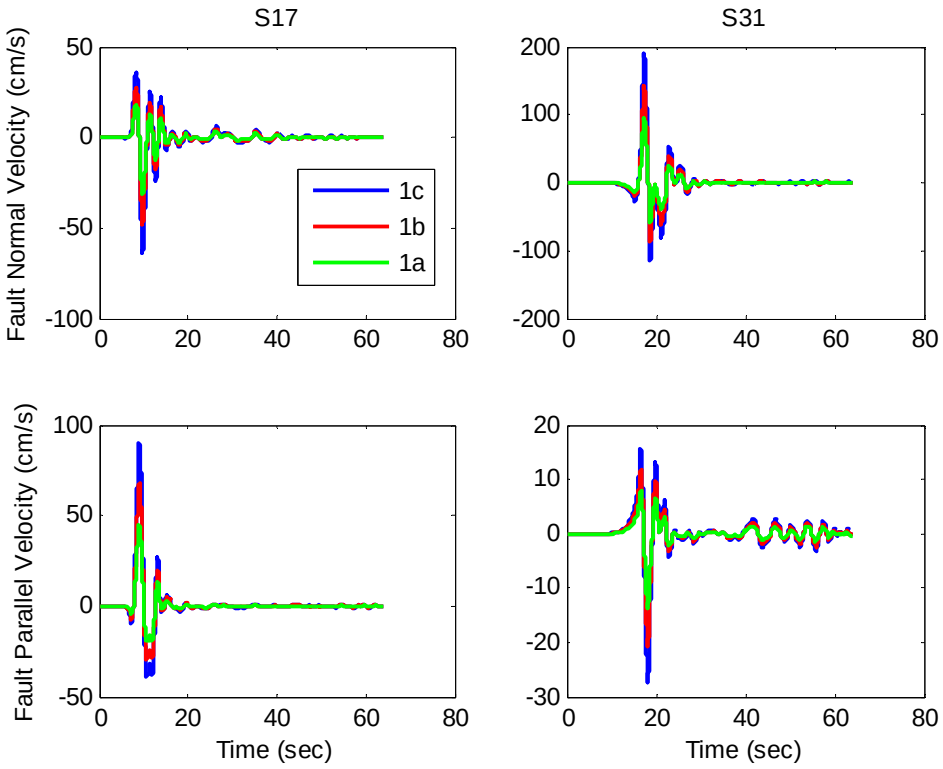

Figure 5.1. Comparison of horizontal velocity time histories at sites S17 and S31 for the three slip amounts (case 1a: 1 m, case 1b: 1.5 m, case 1c: 2 m)

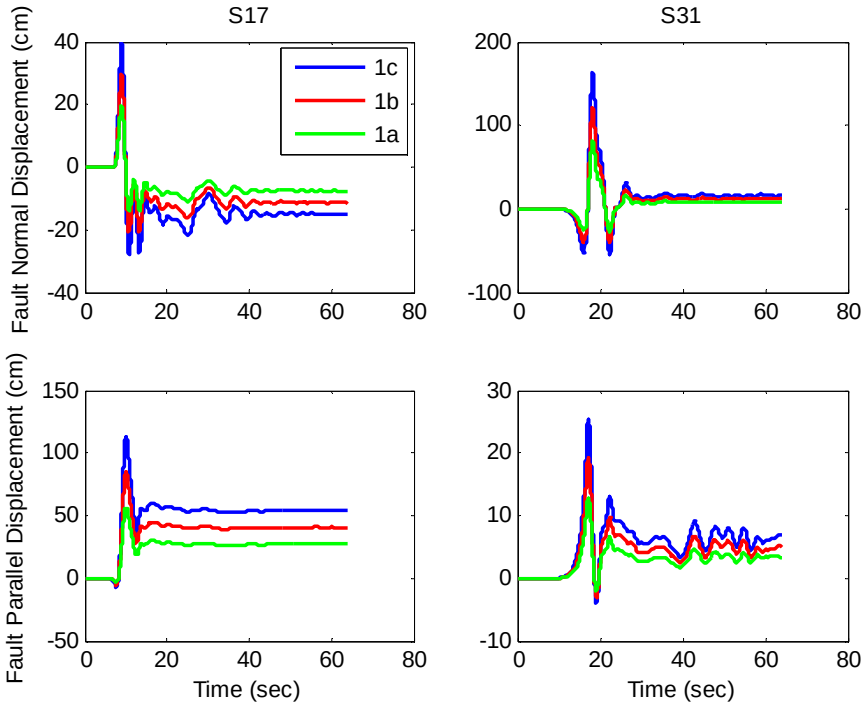

Figure 5.2. Comparison of horizontal displacement time histories at sites S17 and S31 for the three slip amounts (case 1a: 1 m, case 1b: 1.5 m, case 1c: 2 m)

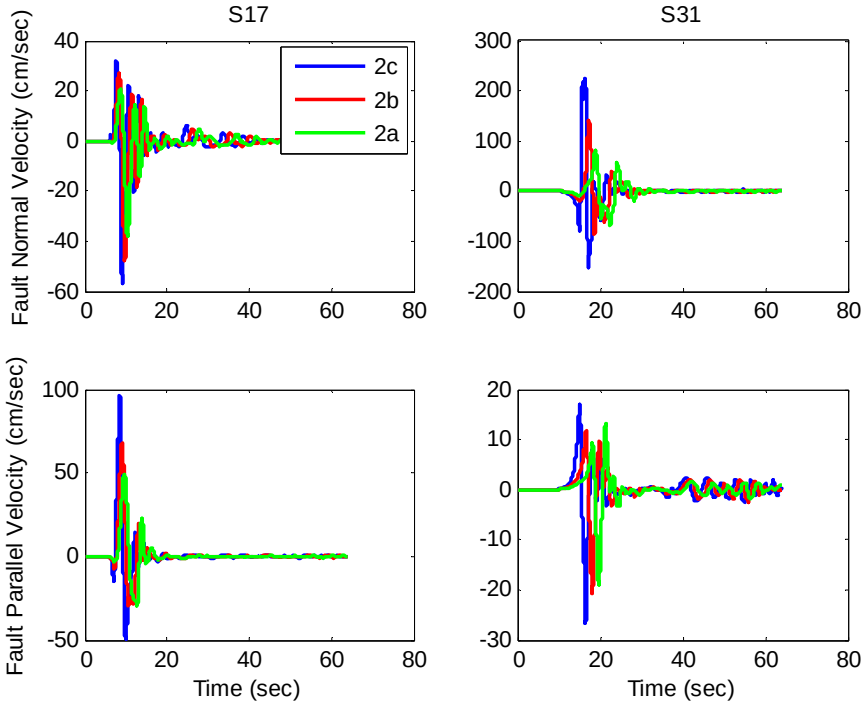

Figure 5.3. Comparison of horizontal velocity time histories at sites S17 and S31 for the three rupture velocities (case 2a: 2.7 km/s, case 2b: 3.0 km/s, case 2c: 3.4 km/s)

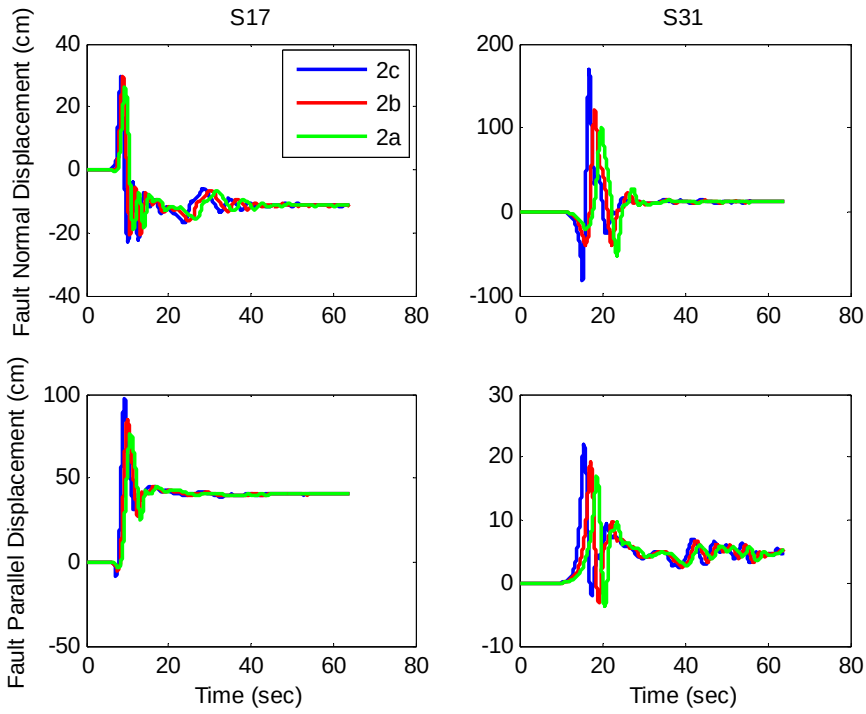

Figure 5.4. Comparison of horizontal displacent time histories at sites S17 and S31 for the three rupture velocities (case 2a: 2.7 km/s, case 2b: 3.0 km/s, case 2c: 3.4 km/s)

The changes in the ground motions caused by a change in the rise time considered in the simulations are presented in Figure 5.5 and Figure 5.6. Changes in the rise time have an effect similar to that of slip amplitude, which exhibits itself as a change on the velocity and displacement amplitudes but at a much lower scale. No changes are introduced at stations in the forward and no directivity regions in terms of differences in fault normal and fault parallel components. The depth of asperity on the other hand causes changes in especially in the fault parallel component of S17, which is located at 90° azimuth with respect to the fault plane and is consequently more influenced by the depth of the rupture surface. The response spectral accelerations at 5 per cent damping ratio computed for the scenarios 2a, 2b and 2c are presented in Figure 5.9. The effect in the forward directivity region of the change in rupture velocity is also clearly observed in the response spectral ordinates computed for S31.

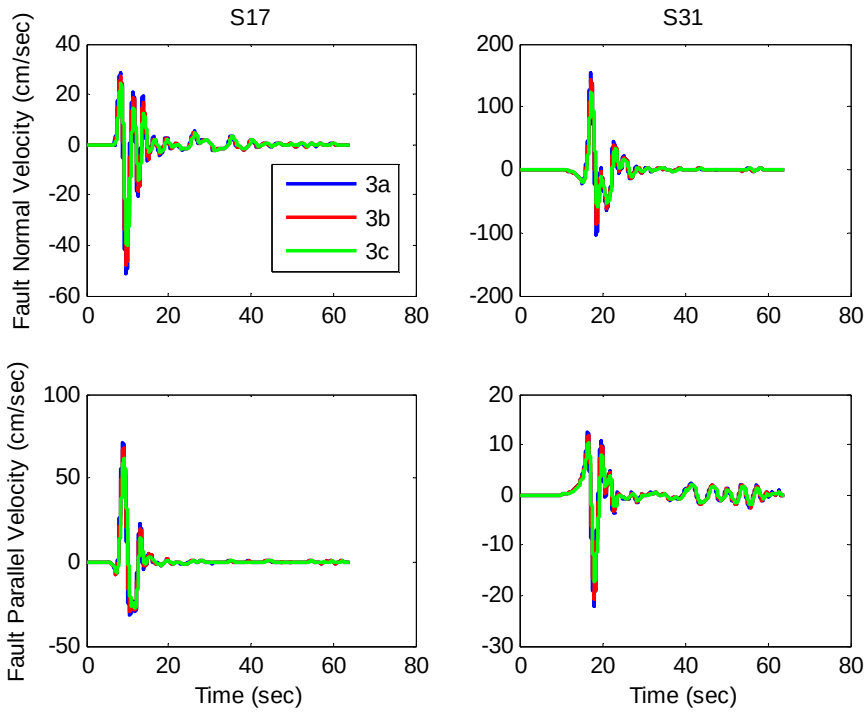

Figure 5.5. Comparison of horizontal velocity time histories at sites S17 and S31 for the three rise times (case 3a: 1.5 s, case 3b: 2.0 s, case 3c: 2.5 s)

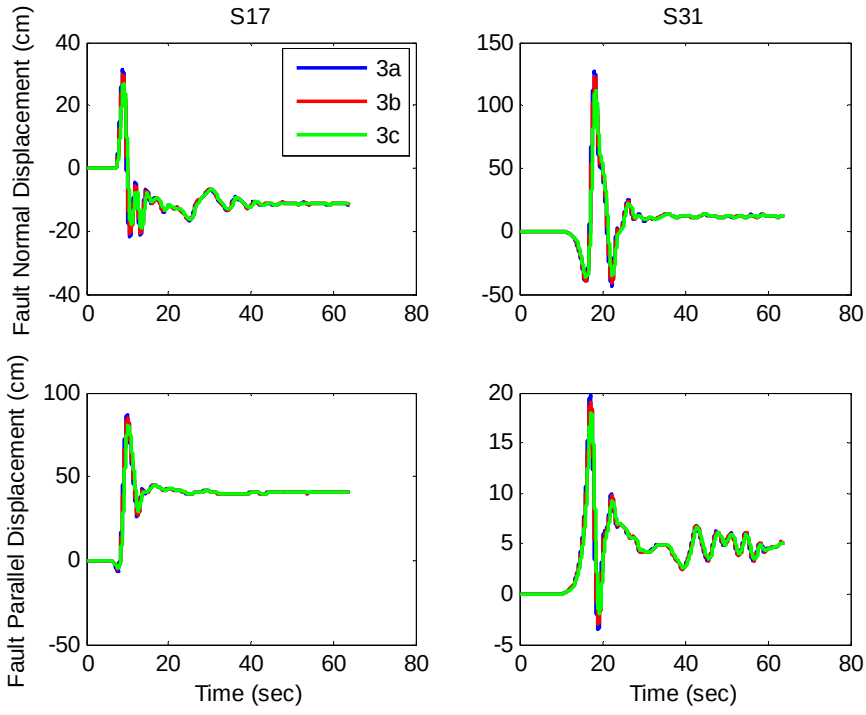

Figure 5.6. Comparison of horizontal displacement time histories at sites S17 and S31 for the three rise times (case 3a: 1.5 s, case 3b: 2.0 s, case 3c: 2.5 s)

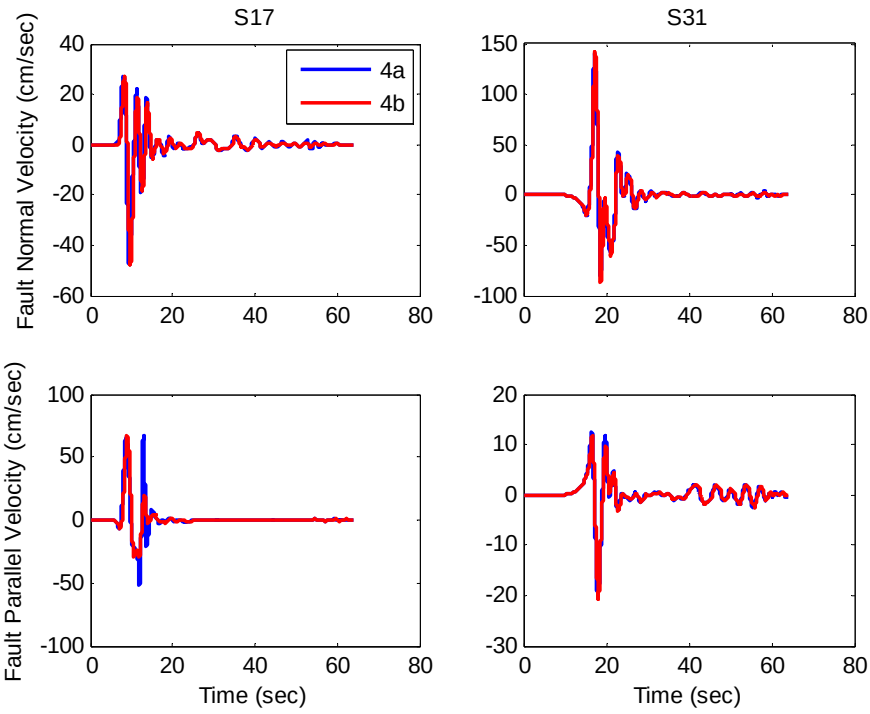

Figure 5.7. Comparison of horizontal velocity time histories at sites S17 and S31 for the two fault depths (case 4a: 0 km, case 4b: 1 km)

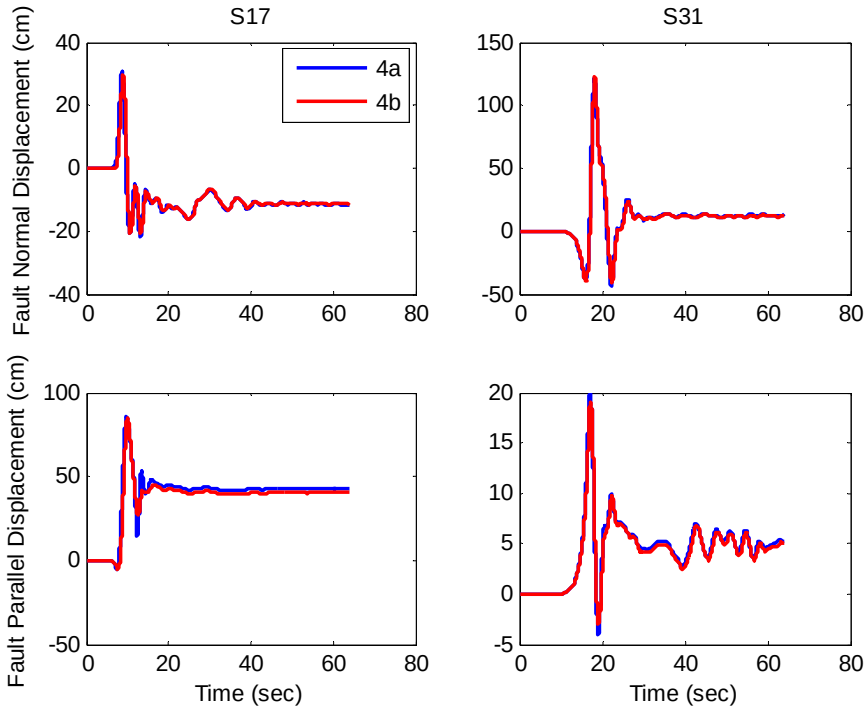

Figure 5.8. Comparison of horizontal displacement time histories at sites S17 and S31 for the two fault depths (case 4a: 0 km, case 4b: 1 km)

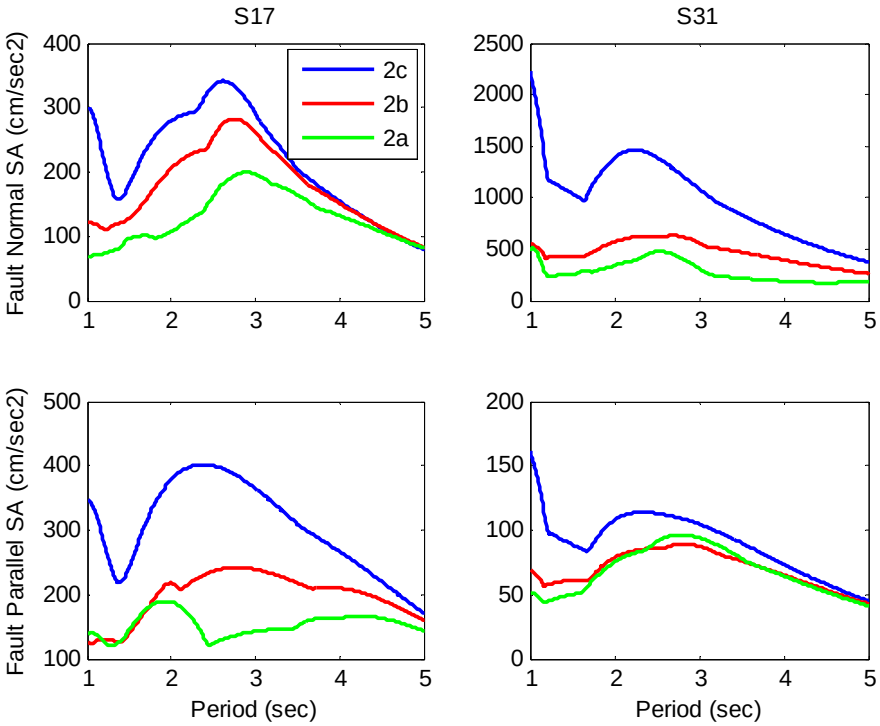

Figure 5.9. Comparison of response spectral accelerations at sites S17 and S31 for the three rupture velocities (case 2a: 2.7 km/s, case 2b: 3.0 km/s, case 2c: 3.4 km/s)

The ground surface distributions of 5 per cent damped spectral accelerations at discrete periods corresponding to fault normal and fault parallel time histories obtained from Case 1b are presented in Figure 5.10 and Figure 5.11 respectively. Figure 5.12 represents the distribution of mean spectral accelerations calculated as the geometric mean of two horizontal components. The directivity effects can be easily visualized in Figure 5.13 and Figure 5.14 where the spatial distribution of the fault normal to mean and fault parallel to mean spectral accelerations are shown respectively. This type of ground surface distributions has also been used in the next section where ground motions have been modeled with realistic slip models.

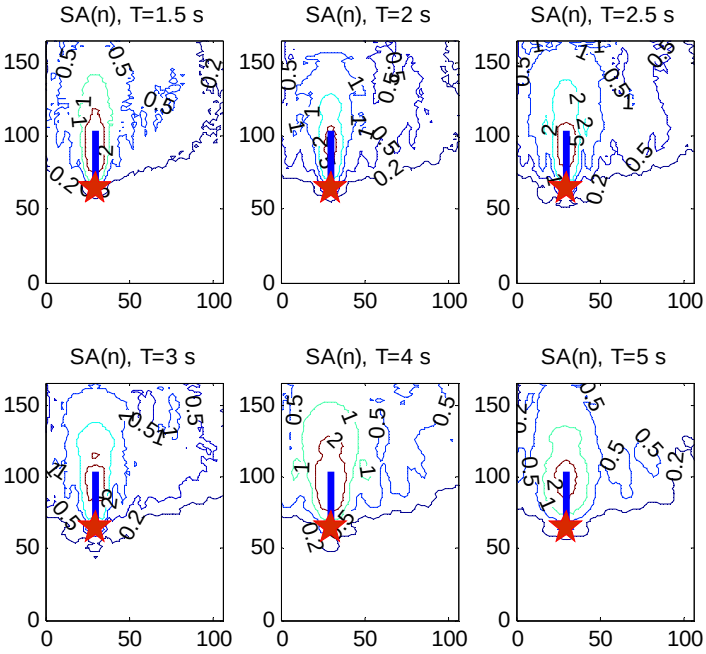

Figure 5.10. Distribution of fault normal spectral accelerations (m/s) obtained from the base case (case 1b)

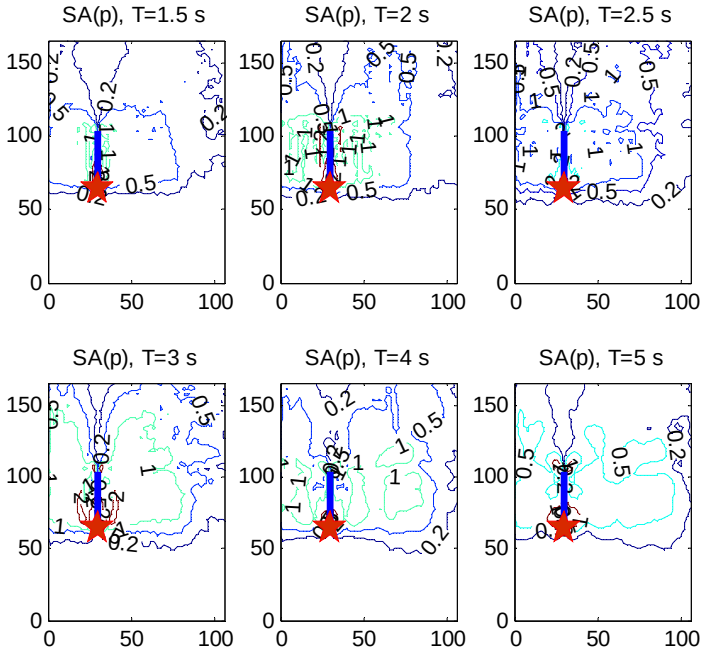

Figure 5.11. Distribution of fault parallel spectral accelerations (m/s) obtained from the base case (case 1b)

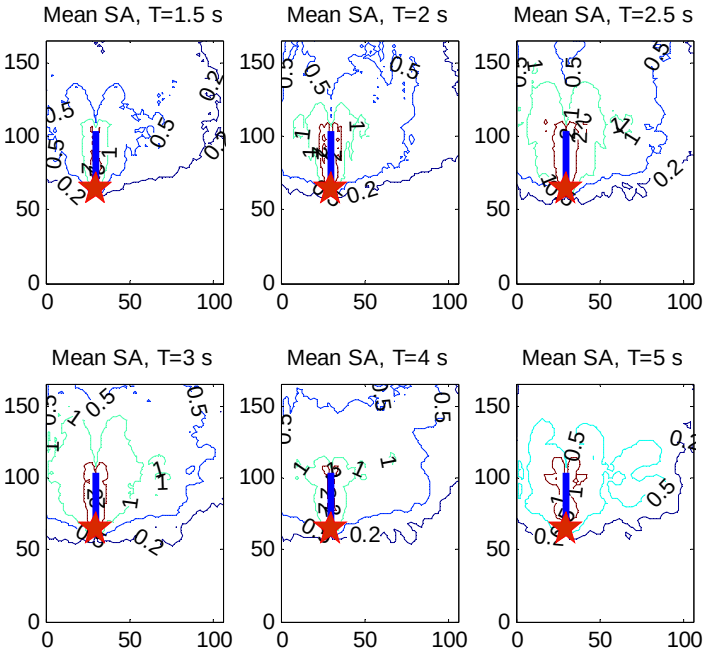

Figure 5.12. Distribution of mean spectral accelerations (m/s) obtained from the base case (case 1b)

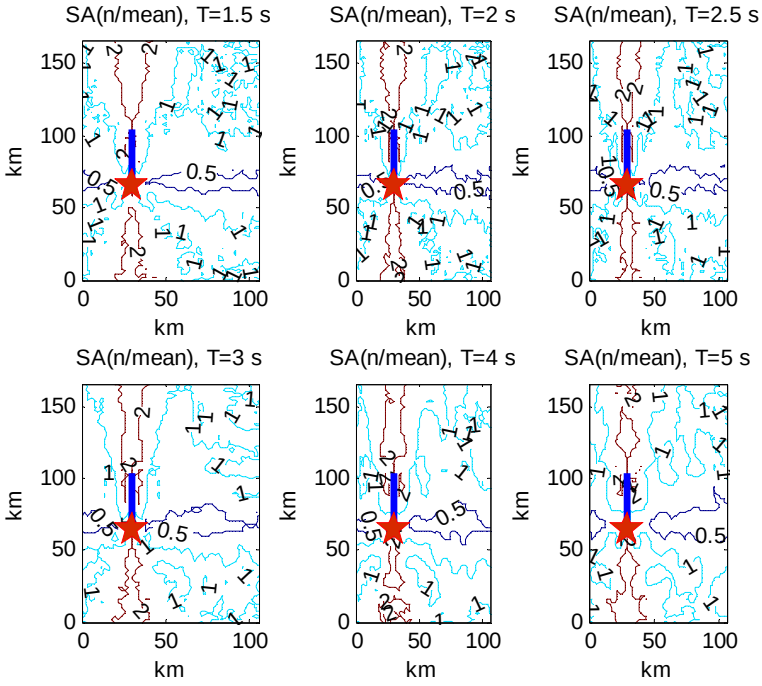

Figure 5.13. Distribution of the ratio of fault normal to mean spectral accelerations obtained from the base case (case 1b)

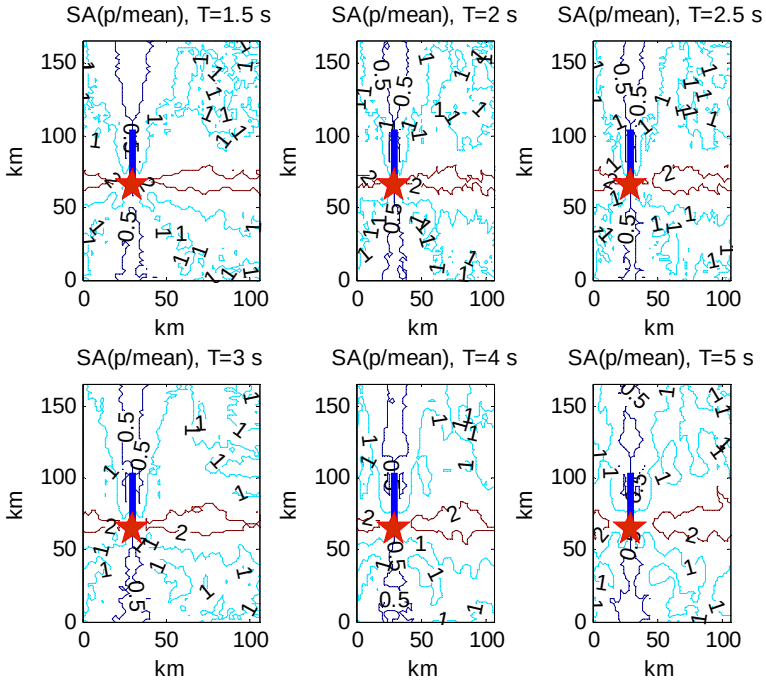

Figure 5.14. Distribution of the ratio of fault parallel to mean spectral accelerations obtained from the base case (case 1b)

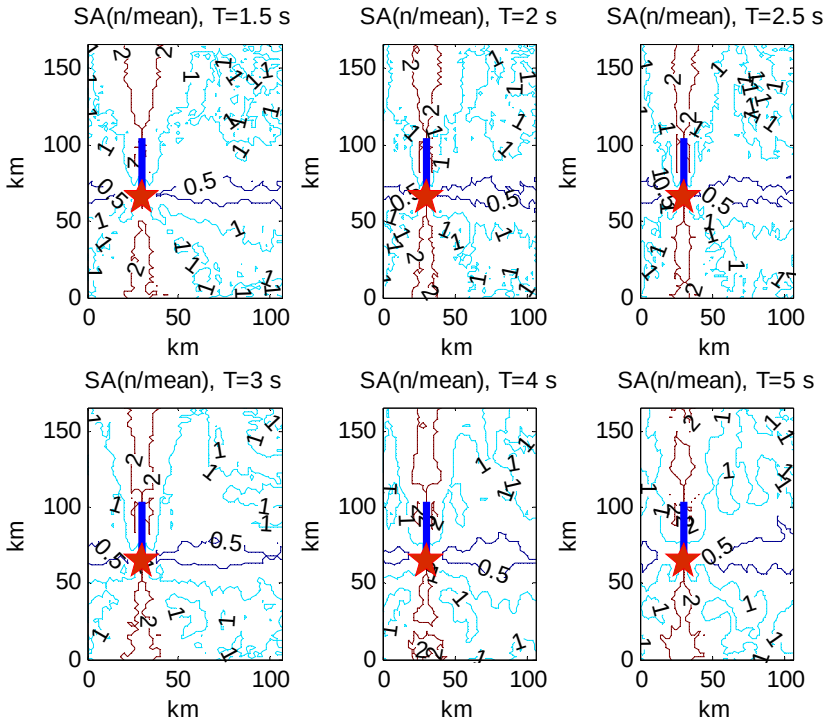

Figure 5.15. Distribution of the ratio of fault normal to mean spectral accelerations obtained from case 1c

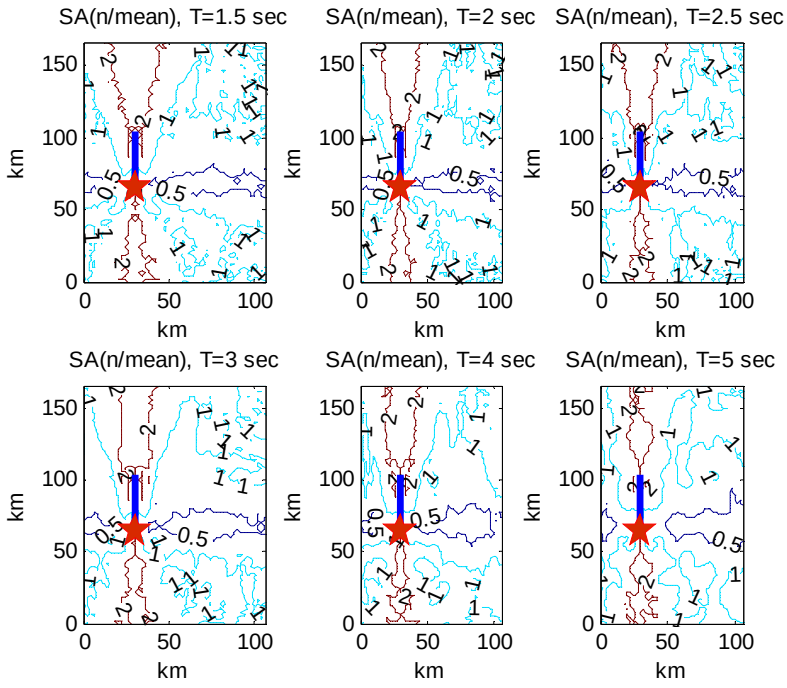

Figure 5.16. Distribution of the ratio of fault normal to mean spectral accelerations obtained from case 2c

5.2. Modeling of Near Source Ground Motion Based on Slip Distribution Models of Earthquakes

All of the four rupture source parameters considered in Section 5.1 influence at least one component of the near source ground motion. The slip amplitude and rupture velocity, above all, have a considerable effect on the ground motions and the corresponding response spectra. The effect of these source parameters are investigated through a parametric study. In the case of real earthquakes however, these source parameters are not constant. They have both inter-event and intra-event variability and to attack this variability a number of recent strike-slip and dip-slip earthquakes have been modeled using the available slip distribution models. The resulting surface distributions of spectral accelerations are suitable to derive generalized forms of response spectra for near field directivity effects for structural periods larger than 1.5 s.

A large number of finite source slip models for past earthquakes are available in the literature. The Database of Finite Source Rupture Models

(http://www.seismo.ethz.ch/srcmod) provides over 152 slip models compiled for 80 earthquakes within the magnitude range of 4.1 to 8.9. A number of slip models have been selected from this database to model the variability of near source ground motions as realistically as possible. The selection of the slip models were based on several criteria:

- Magnitude $M_w \geq 6.0$,
- Pure strike-slip or pure dip – slip events were chosen whenever possible,
- Rupture dimensions should be within the modeling limits with the available computational power without losing the spatial resolution (maximum grid spacing of 200 m) ,
- The frequency resolution of the slip models should be within the limits of $0 \leq f_{max} \leq 1$ Hz or higher whenever possible,
- The grid spacing of the slip models should be suitable for modeling with a spatial resolution of 100 m for events of intermediate magnitude range and 200 m for large earthquakes.

The list of earthquakes and the corresponding slip models selected using these criteria are given in Table 5.3 and Table 5.4 for strike-slip and dip-slip earthquakes respectively. The horizontally layered velocity structure used in the benchmark study was also adopted in the modeling of these earthquakes. Topographical and/or basin effects were not considered in order to concentrate only on the effects of rupture directivity. The original dip angles were adopted for all the events, however for the strike-slip events, simulations were also carried out for the vertical fault case. This however did not introduce much difference in the results obtained since dip angles of the strike-slip events were at most 10° off from the vertical.

Table 5.3. The events with a strike-slip mechanism simulated and used in the modeling of the directivity effects

Event	Slip model	Associated moment magnitude	Fault dimensions	Grid spacing used in modeling	Frequency range of the slip model
Imprerial Valley 1979	Archuleta (1984)	6.5	35 km * 13 km	100 m	Fmax: 1 Hz
Imprerial Valley 1979	Zeng and Anderson (2000)	6.5	42 km * 10 km	100 m	Fmax: 2 Hz
Morgan Hill 1984	Beroza and Spudich (1988)	6.25	30.5 km * 11 km	100 m	0.2 – 4 Hz
Superstition Hillls 1987	Wald *et al.*, 1990	6.51	20 km * 11 km	100 m	0.1 – 3 Hz
Landers 1992	Zeng and Anderson (2000)	7.2	77 km * 15 km	200 m	0.1 – 1 Hz
Kobe 1995	Sekiguchi *et al.* (1996)	6.96	63.5 km * 20.5 km	200 m	Fmax: 1 Hz
Kobe 1995	Zeng and Anderson (2000)	6.91	60 km * 20 km	200 m	Fmax: 1 Hz
Kocaeli 1999	Yagi and Kikuchi. (2000)	7.4	93.6 km * 21.6 km	200 m	0.01-0.8 Hz
Tottori 2000	Sekiguchi *et al.*, 2003	6.79	34 km * 17.6 km	100 m	0.1 – 1 Hz
Parkfield, 2004	Ji et al, 2005	6.0	38 km * 15 km	100 m	Fmax: 1 Hz
Parkfield, 2004	Liu *et al.*, 2006	6.0	40 km * 15.2 km	100 m	Fmax: 1 Hz

Table 5.4. The events with a reverse mechanism simulated and used in the modeling of the directivity effects

Event	Slip model	Associated moment magnitude	Fault dimensions and dip angle	Grid spacing used in modeling	Frequency range of the slip model
Tabas 1978	Hartzell and Mendoza (1991)	7.09	95 km * 45 km, 25°	200 m	0.2 – 2 Hz
Nahanni 1985	Hartzell *et al.* (1994)	6.77	48 km * 21.2 km, 40°	200 m	0.2 – 3 Hz
Northridge 1994	Hartzell *et al.* (1996)	6.68	20 km * 24.9 km, 25°	100 m	0.1 – 1 Hz

- **1979 Mw=6.5 Imperial Valley Earthquake**

Two slip models have been used to model the 1979 Imperial Valley earthquake. These were:

1. The slip model of Archuleta (1984), with horizontal and vertical grid spacing of 2.5 km and 1 km respectively (Figure 5.17). The model also included rise time and arrival time information for each node. However only the rise time data was adopted together with an average rupture velocity of 2800 m/s.
2. The slip model of Zeng and Anderson (2000). The grid spacing of the model was 0.5 km in both directions (Figure 5.18). A rupture velocity of 2500 m/s and rise time of 0.8 s. were adopted.

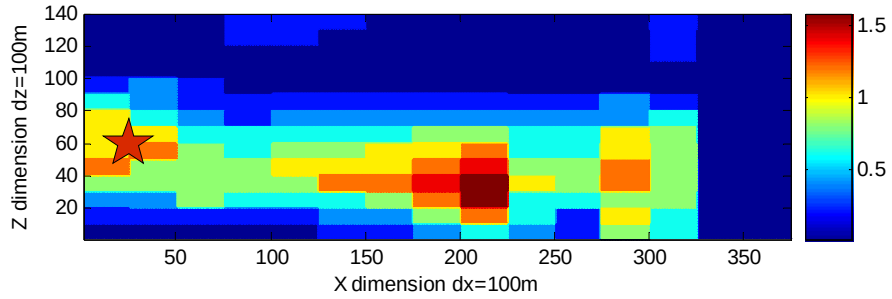

Figure 5.17. The slip model of Archuleta (1984). Slip amplitudes are given in meters. The red star represents the hypocenter.

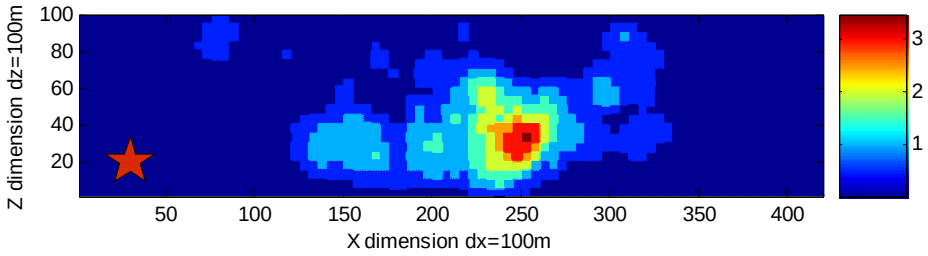

Figure 5.18. The slip model of Zeng and Anderson (2000). Slip amplitudes are given in meters. The red star represents the hypocenter.

- **1984 Mw=6.2 Morgan Hill earthquake**

The slip model of Beroza and Spudich(1988) was adopted to model this event. The horizontal and vertical grid spacings were 0.5 km and 1 km respectively (Figure 5.19). The rupture velocity adopted for this model was 2700 m/s and the rise time 0.4 s.

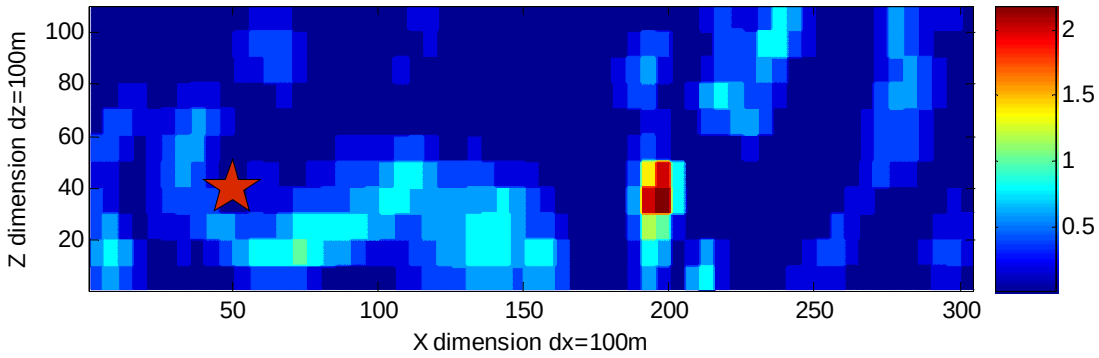

Figure 5.19. The slip model of Beroza and Spudich (1988). Slip amplitudes are given in meters. The red star represents the hypocenter.

- **1984 Mw=6.6 Superstition Hills earthquake**

The slip model of Wald *et al.* (1988) was adopted to model this event. The horizontal and vertical grid spacings were 1 km and 1.15 km respectively (Figure 5.19). The rupture velocity adopted for this model was 2400 m/s and the rise time 2 s.

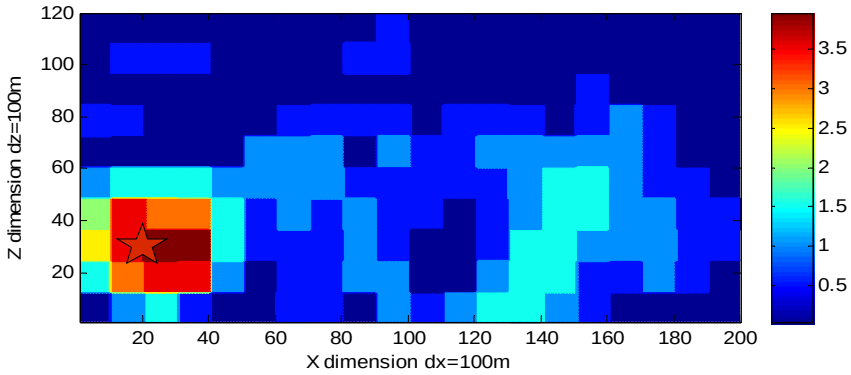

Figure 5.20. The slip model of Wald *et al.* (1990). Slip amplitudes are given in meters. The red star represents the hypocenter.

- **1992 Mw=7.3 Landers earthquake**

Several slip models exist for this earthquake. The slip model of Zeng and Anderson (2000) was selected to model the event due to frequency limits of the other models. The grid spacing was 0.5 km in both directions (Figure 5.21). Rupture velocity and rise time were not specified in the model. As such, a rupture velocity of 2800 m/s and a rise time of 2 s were adopted.

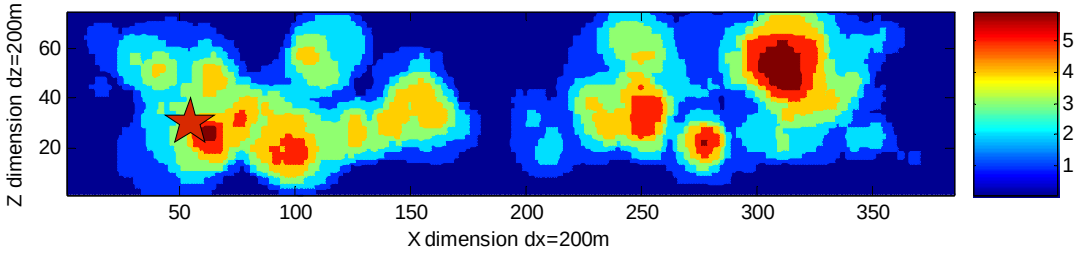

Figure 5.21. The slip model of Zeng and Anderson (2000). Slip amplitudes are given in meters. The red star represents the hypocenter.

- **1995 M_w=6.9 Kobe earthquake**

Two slip models have been used to model the earthquake. These were:

1.The slip model of Sekiguchi *et al.* (1996), with both horizontal and vertical grid spacings of 2.05 km which was approximated to 2 km (Figure 5.22). A rupture velocity of 3100 m/s and rise time of 2 s. were adopted.

2. The slip model of Zeng and Anderson (2000). The grid spacing of the model was 0.5 km in both directions (Figure 5.23). A rupture velocity of 3000 m/s and rise time of 2 s. were adopted.

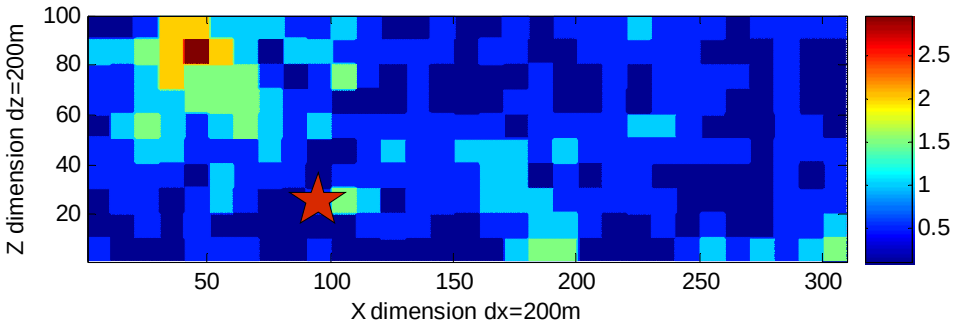

Figure 5.22. The slip model of Sekiguchi *et al.* (1996). Slip amplitudes are given in meters. The red star represents the hypocenter.

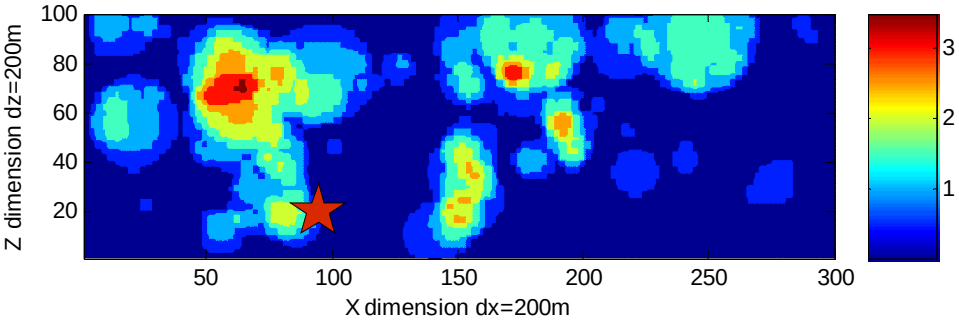

Figure 5.23. The slip model of Zeng and Anderson (2000). Slip amplitudes are given in meters. The red star represents the hypocenter.

- **1999 M_w= 7.6 Kocaeli earthquake**

Several slip models also exist for this event. However the rupture dimensions of only Yagi and Kikuchi (2000) could be incorporated in the simulation grid without an increase in the grid spacing used. The grid spacing of the rupture model was 3.6 km in both directions (Figure 5.24). A rupture velocity of 3000 m/s and a rise time of 2 s were adopted.

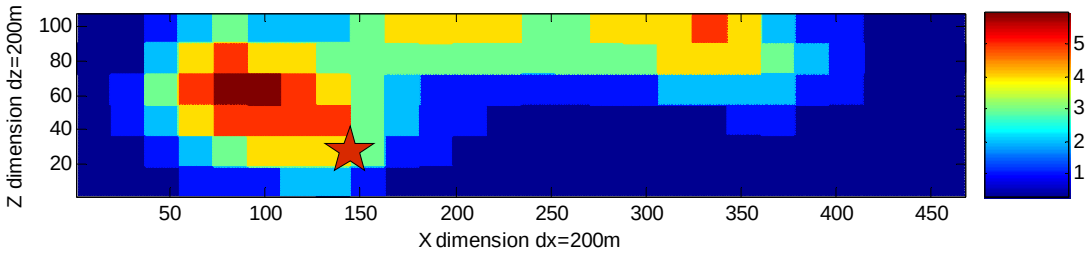

Figure 5.24. The slip model of Yagi and Kikuchi (2000). Slip amplitudes are given in meters. The red star represents the hypocenter.

- **2000 Mw=6.7 Tottori earthquake**

The slip model of Sekiguchi *et al.* (2003) was used to model this event. The horizontal and vertical grid spacings of the model were 2 km and 2.2 km respectively (Figure 5.25). The rupture velocity was 1800 m/s and the rise time 0.4 s.

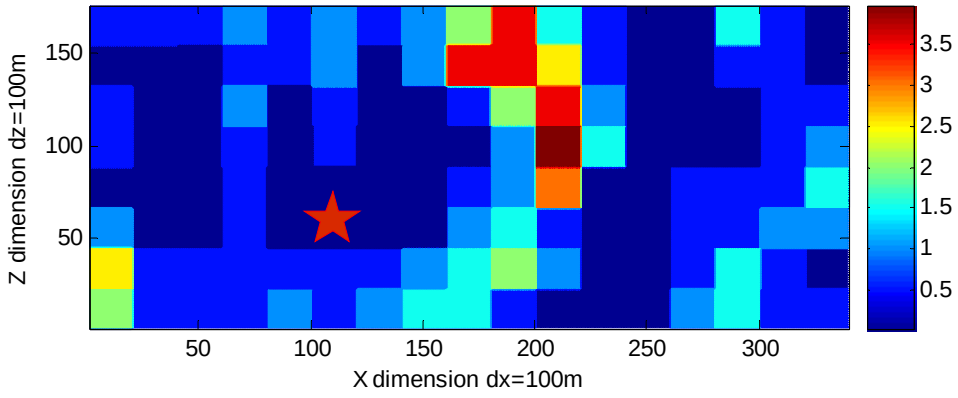

Figure 5.25. The slip model of Sekiguchi *et al.* (2003). Slip amplitudes are given in meters. The red star represents the hypocenter.

- **2004 Mw=6.0 Parkfield earthquake**

The slip models of Liu *et al.* (2006) and Ji *et al.* (2005) were selected to model the event. The horizontal and vertical grid spacings of the Liu *et al.* (2006) model were 1.8 km and 2.0 km respectively (Figure 5.26). The rupture velocity was taken as 2.8 km / sec and the rise time was variable as given in the model. The horizontal and vertical grid spacing of the Ji *et al.* (2005) model was 1.5 km Figure 5.27). The rupture velocity was taken as 2.85 km / sec and the rise time was 0.8 s.

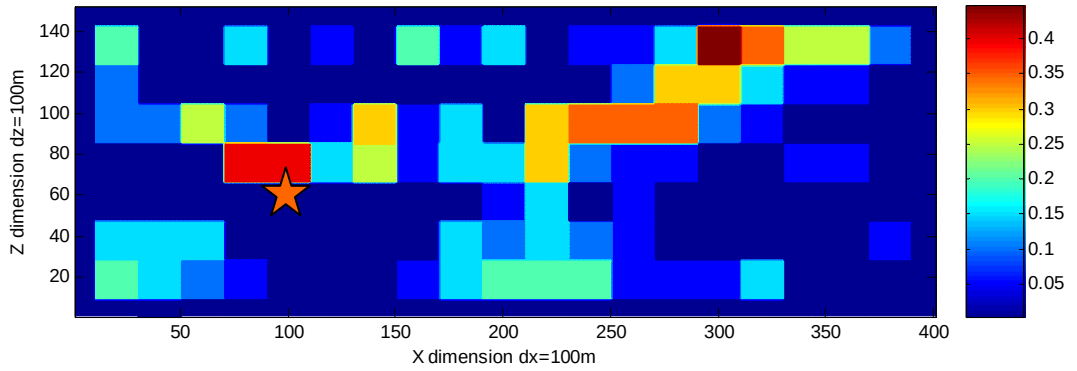

Figure 5.26. The slip model of Liu *et al.* (2006). Slip amplitudes are given in meters. The red star represents the hypocenter.

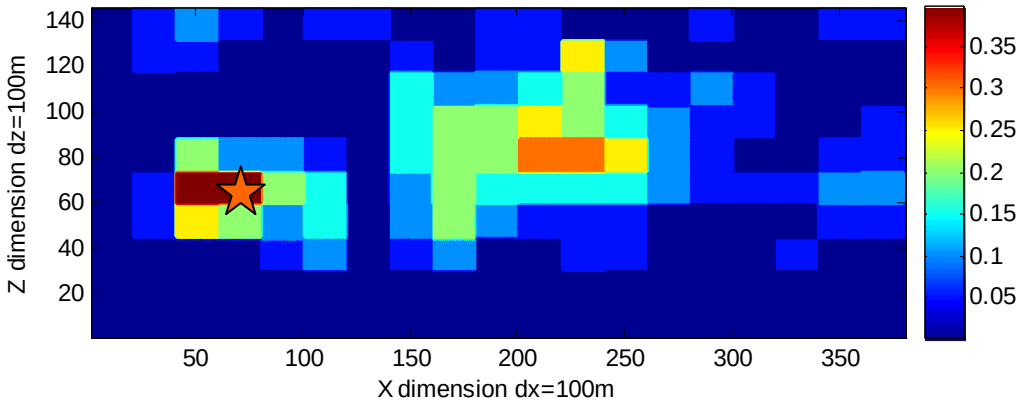

Figure 5.27. The slip model of Ji *et al.* (2005). Slip amplitudes are given in meters. The red star represents the hypocenter.

- **1978 Mw=7.1 Tabas earthquake**

The slip model of Hartzell and Mendoza (1991) was used to model this dip-slip earthquake (Figure 5.28). The horizontal and vertical grid spacing of the slip model was 4.5 km. The dip angle of the fault plane was 25°. An average rupture velocity of 2500 m/s and a rise time of 0.8 sec was used in the model.

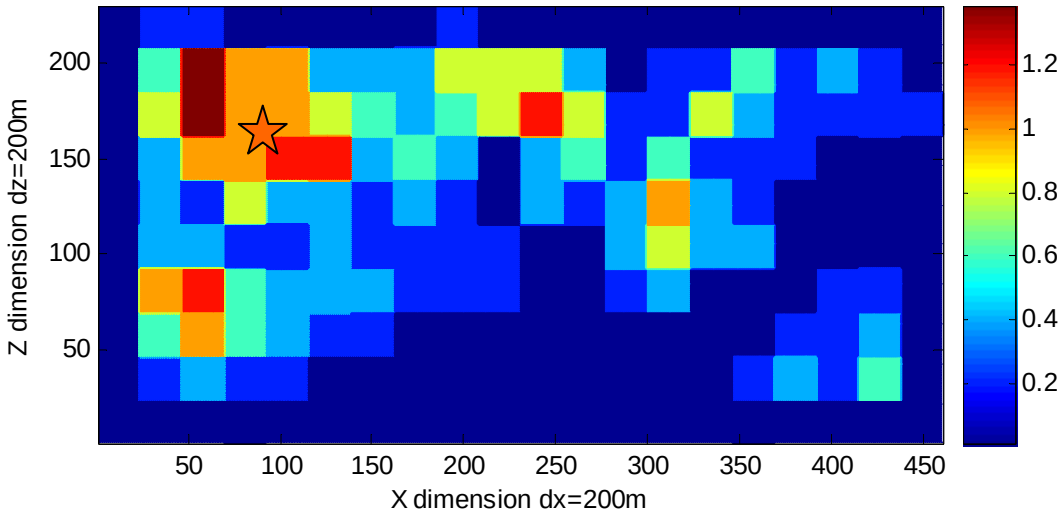

Figure 5.28. The slip model of Hartzell and Mendoza (1991). Slip amplitudes are given in meters. The red star represents the hypocenter.

- **1985 Mw=6.8 Nahanni Eathquake**

The slip model of Hartzell *et al.* (1994) was used to model the second one of the two Nahanni earthquakes (Figure 5.29). The horizontal and vertical grid spacings of the slip model were 2.66 km and 2.36 km repectively. The dip angle of the fault plane was 25°. An average rupture velocity of 2800 m/s and a rise time of 0.8 sec was used in the model.

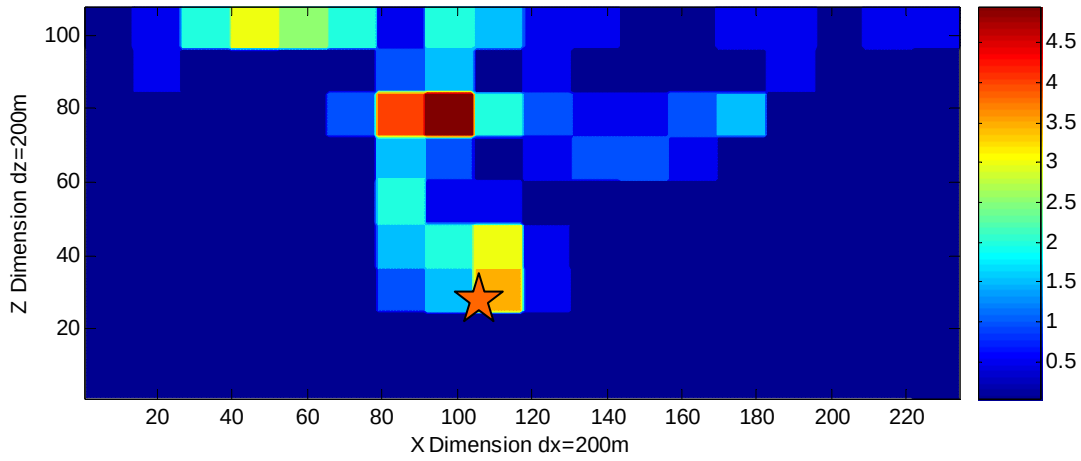

Figure 5.29. The slip model of Hartzell *et al.* (1994). Slip amplitudes are given in meters. The red star represents the hypocenter.

- **1994 Mw=6.7 Northridge earthquake**

The slip model of Hartzell *et al.* (1996) with horizontal and vertical grid spacings of 1.43 km and 1.73 km was used to model the event (Figure 5.30). The dip angle was 40°. The average rupture velocity was taken as 2800 m/s.

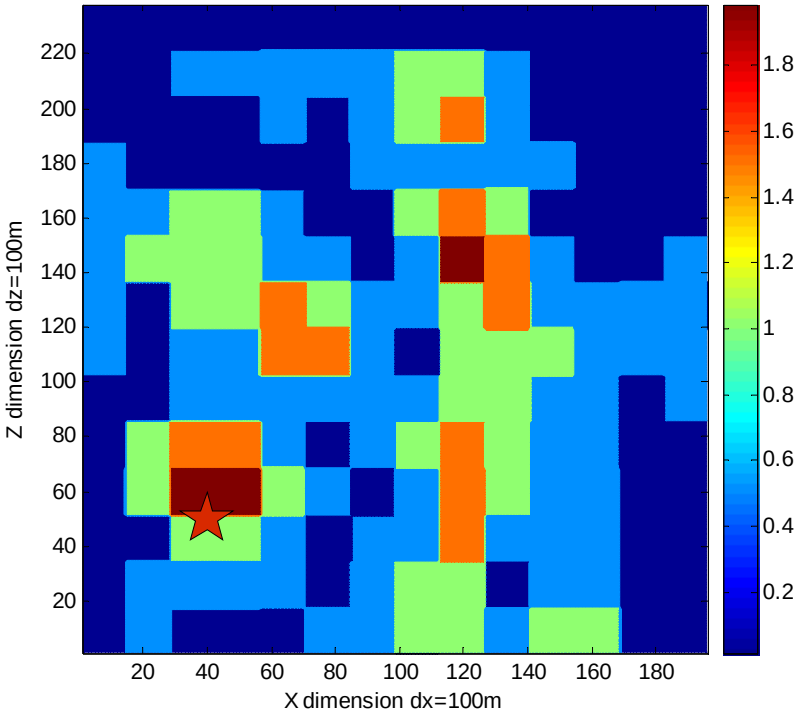

Figure 5.30. The slip model of Hartzell *et al.* (1996). Slip amplitudes are given in meters. The red star represents the hypocenter.

Following the examples set by previous researchers, the results of the simulations were analyzed in terms of two variables. The first one was the ratio of the fault normal 5 per cent damped spectral acceleration to mean 5 per cent damped spectral acceleration at each node of a grid with 1 km spacing for moderate events and 2 km spacing for large events at discrete periods of 1.5 s, 2 s, 2.5 s, 3 s, 4 s and 5 s. The spatial distributions of the ratios thus obtained are given in Figure 5.31 to Figure 5.41 for the 11 strike-slip rupture models and in Figure 5.42 through Figure 5.44 for t he dip-slip rupture models sited above.

Secondly, the mean horizontal spectral amplitudes obtained from the simulations were compared with response spectral accelerations obtained from empirical ground

motion prediction equations. The spectral amplitudes obtained from the empirical ground motion prediction equations represented the mean hazard parameter obtained for the case without directivity. The empirical spectral acceleration prediction relationship of Boore and Atkinson (2006) and the spectral displacement prediction relationship of Akkar and Bommer (2006) were chosen for this purpose. 5 per cent damped spectral accelerations corresponding to periods of 1.5, 2, 3, 4 and 5 sec and 5 per cent damped spectral displacements corresponding to 1.5, 2, 2.5, 3 and 4 sec of natural periods of vibration were considered. As the magnitude and fault type are the only source related parameters used in the empirical ground motion prediction equations and the attenuation through the earth strata are modeled based only on empirical data, simulated and empirical distribution of the ground motion have in fact no common parameters. As such, large discrepancies might be expected between simulated and empirical ground motion prediction based ground motions. However the simulation results in the epicentral region remained in all cases between ± 2σ range of the corresponding empirical values. The ratios of the 5 per cent damped mean spectral accelerations obtained from simulations to Boore and Atkinson (2006) prediction equation based spectral accelerations are presented in Figure 5.45 through Figure 5.54 for the eight strike-slip events considered in the study.

Ratios of mean 5 per cent damped spectral displacements obtained from simulations to spectral displacements based on Akkar and Bommer (2007) ground motion prediction equations are presented in Figure 5.55 through Figure 5.63. The equational forms and regression coefficients of Boore and Atkinson (2006) and Akkar and Bommer (2007) empirical ground motion prediction equations are given in Appendix B.

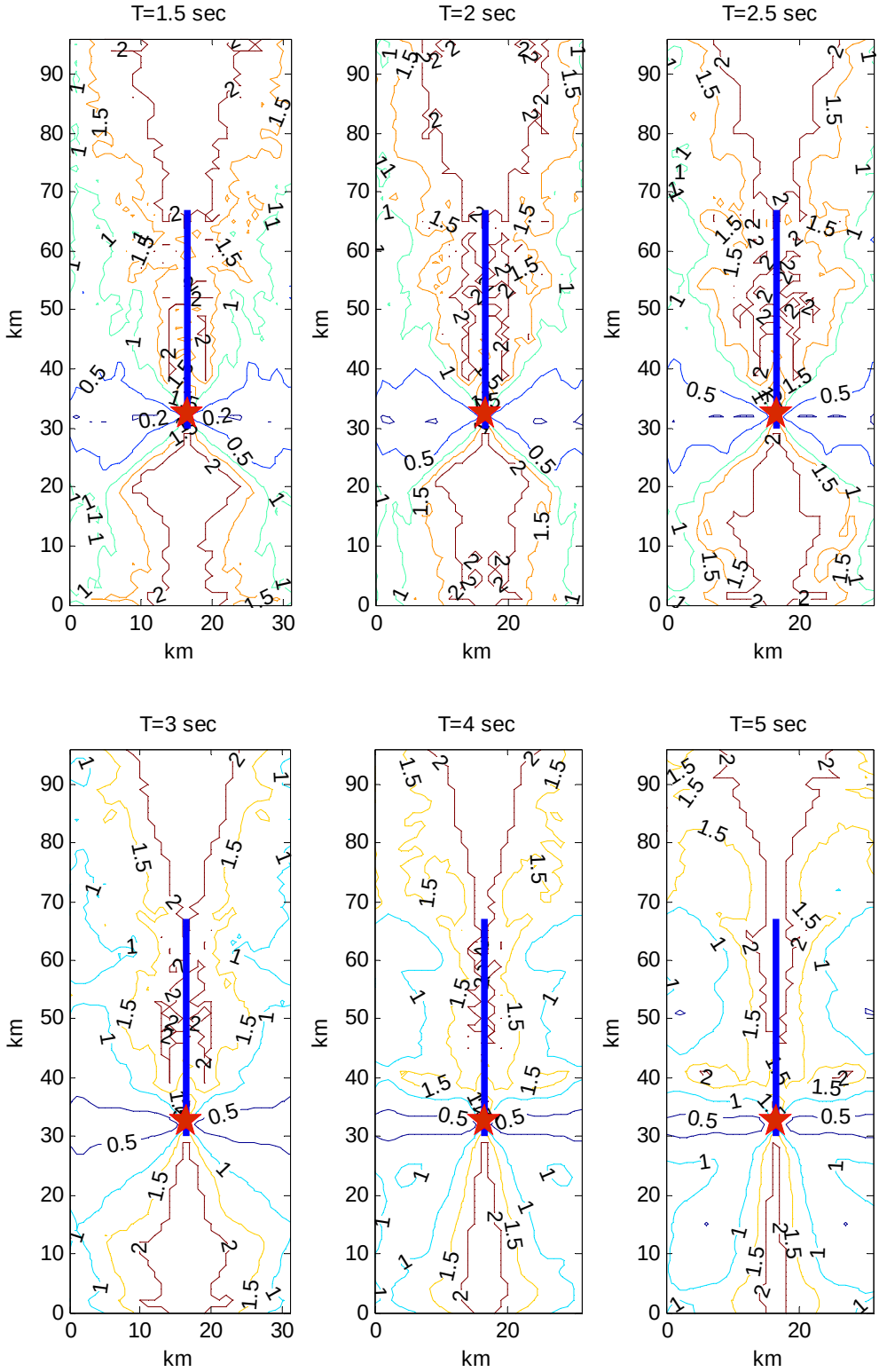

Figure 5.31. Ratio of fault normal to mean spectral accelerations obtained for the 1979 Imperial Valley earthquake (slip model of Archuleta, 1984). The blue line represents the surface projection of the fault and the red star is the epicenter.

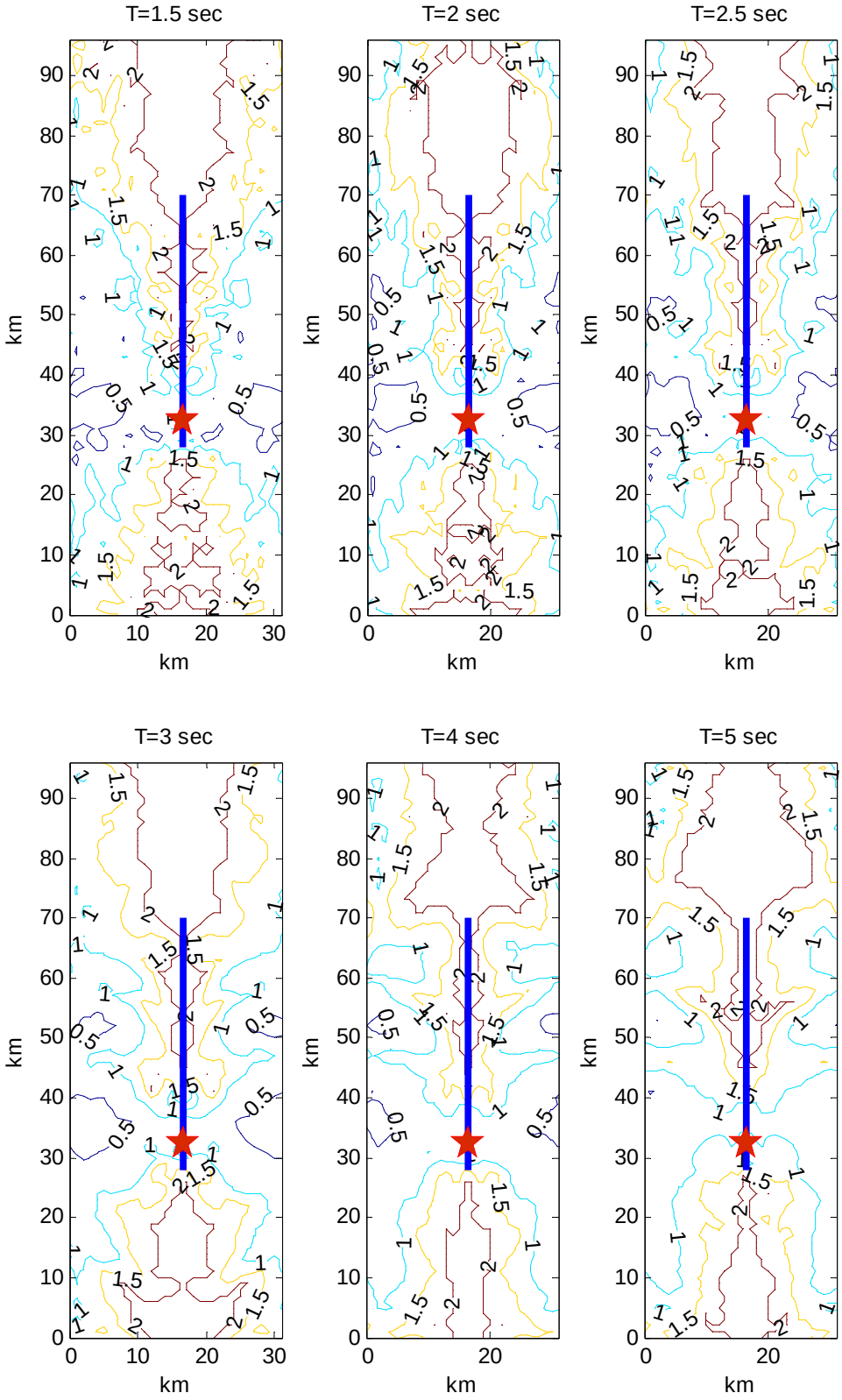

Figure 5.32. Ratio of fault normal to mean spectral accelerations obtained for the 1979 Imperial Valley earthquake (slip model of Zeng and Anderson, 2000). The blue line represents the surface projection of the fault and the red star is the epicenter.

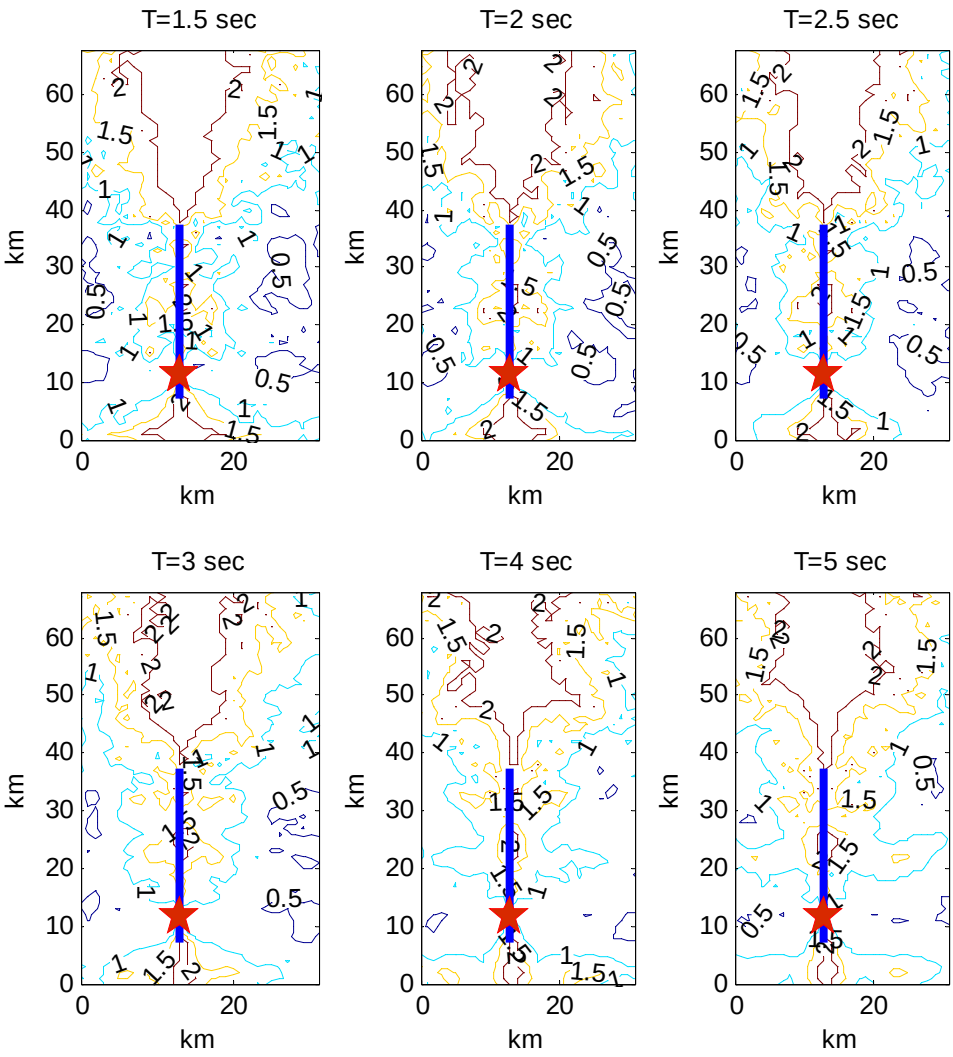

Figure 5.33. Ratio of fault normal to mean spectral accelerations obtained for the 1984 Morgan Hill earthquake (slip model of Beroza and Spudich, 1988). The blue line represents the surface projection of the fault and the red star is the epicenter.

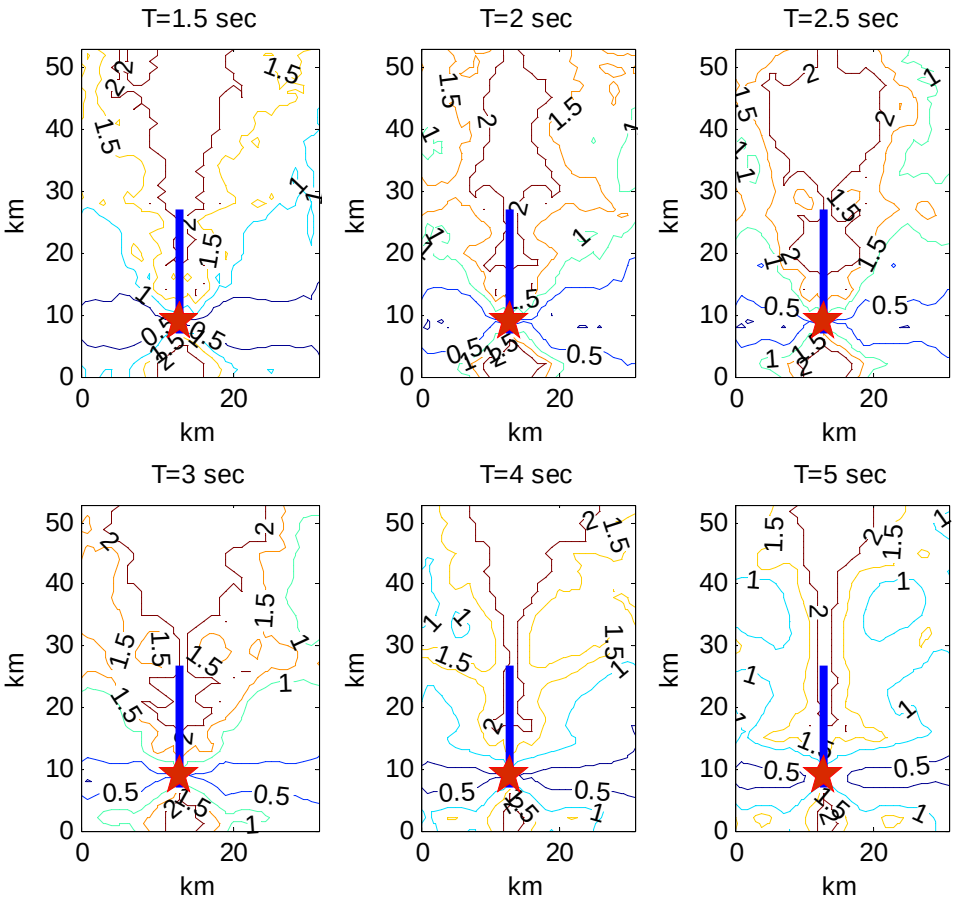

Figure 5.34. Ratio of fault normal to mean spectral accelerations obtained for the 1987 Superstition Hills earthquake (slip model of Wald et al, 1990). The blue line represents the surface projection of the fault and the red star is the epicenter.

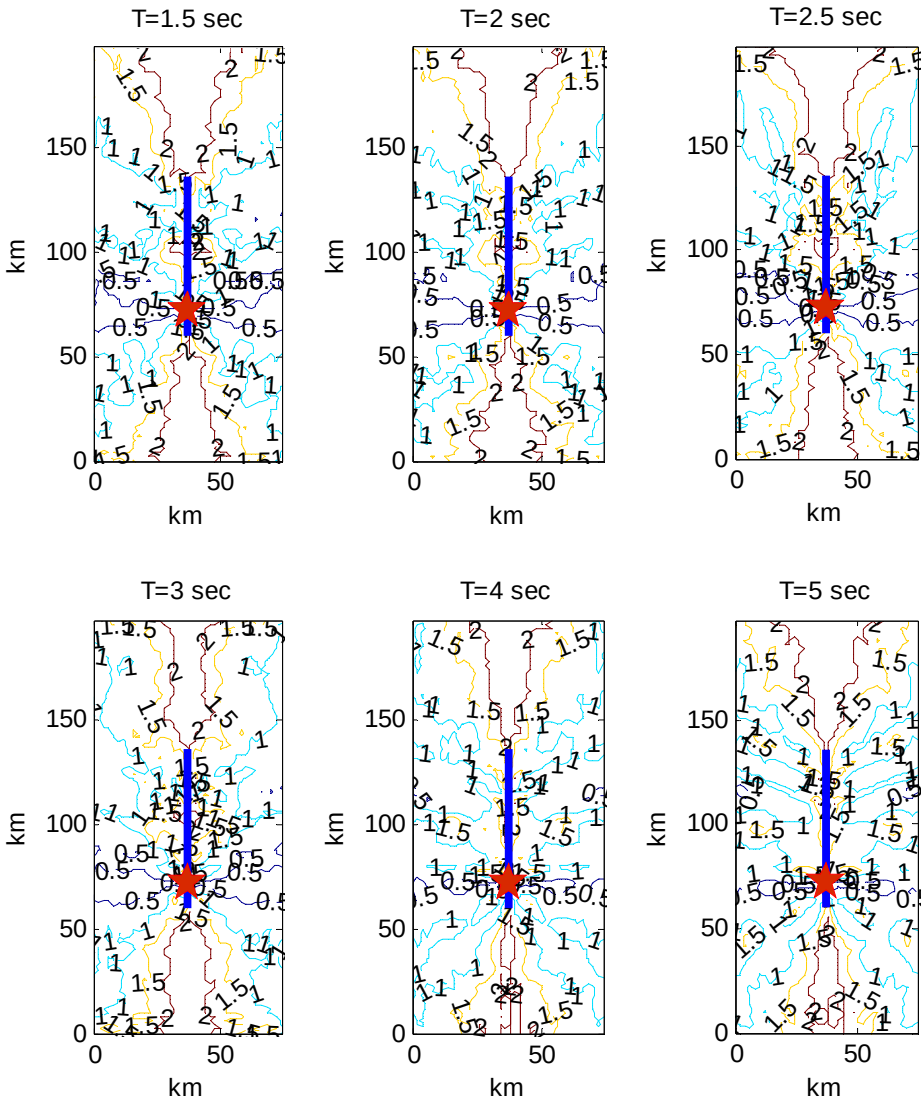

Figure 5.35. Ratio of fault normal to mean spectral accelerations obtained for the 1992 Landers earthquake (slip model of Zeng and Anderson , 2000). The blue line represents the surface projection of the fault and the red star is the epicenter.

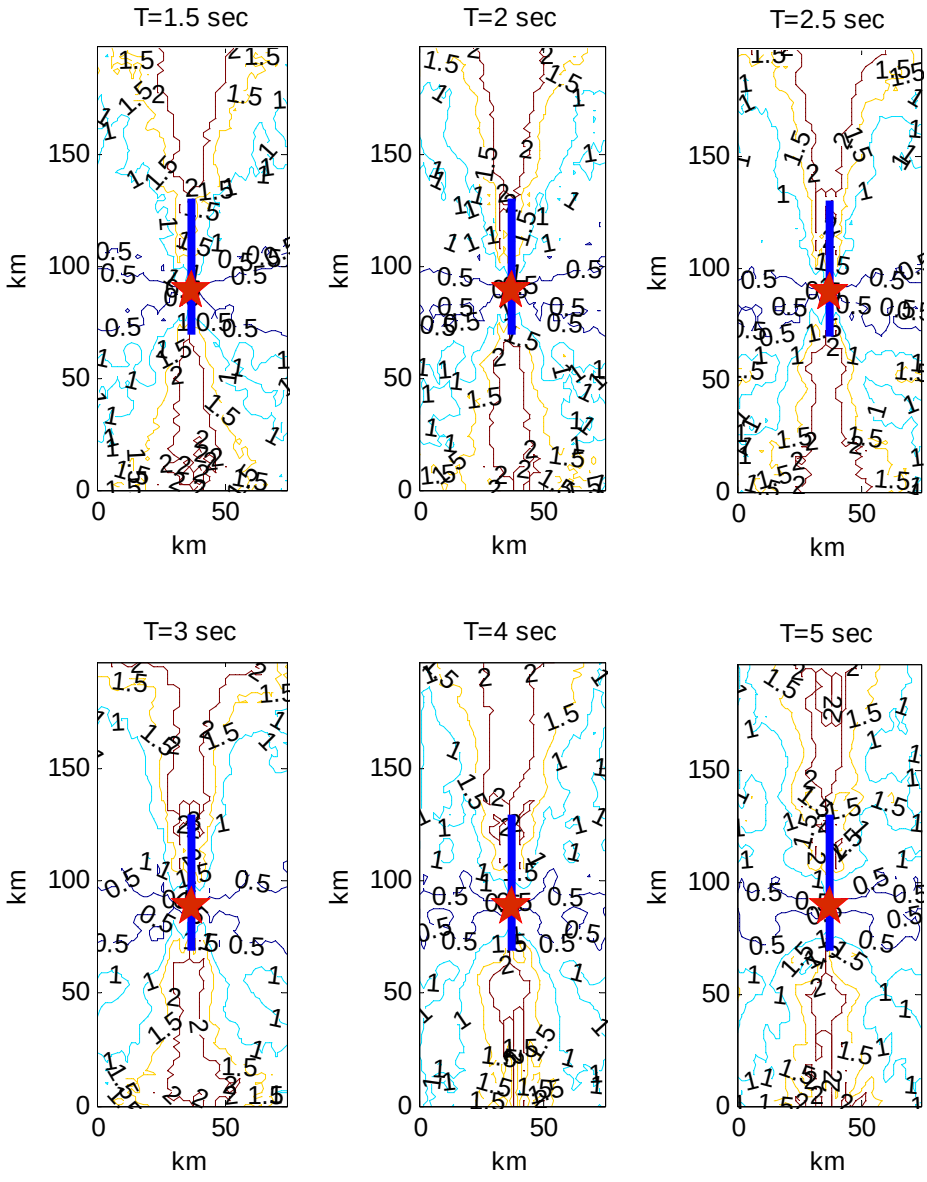

Figure 5.36. Ratio of fault normal to mean spectral accelerations obtained for the 1995 Kobe earthquake (slip model of Sekiguchi *et al.*, 1996). The blue line represents the surface projection of the fault and the red star is the epicenter.

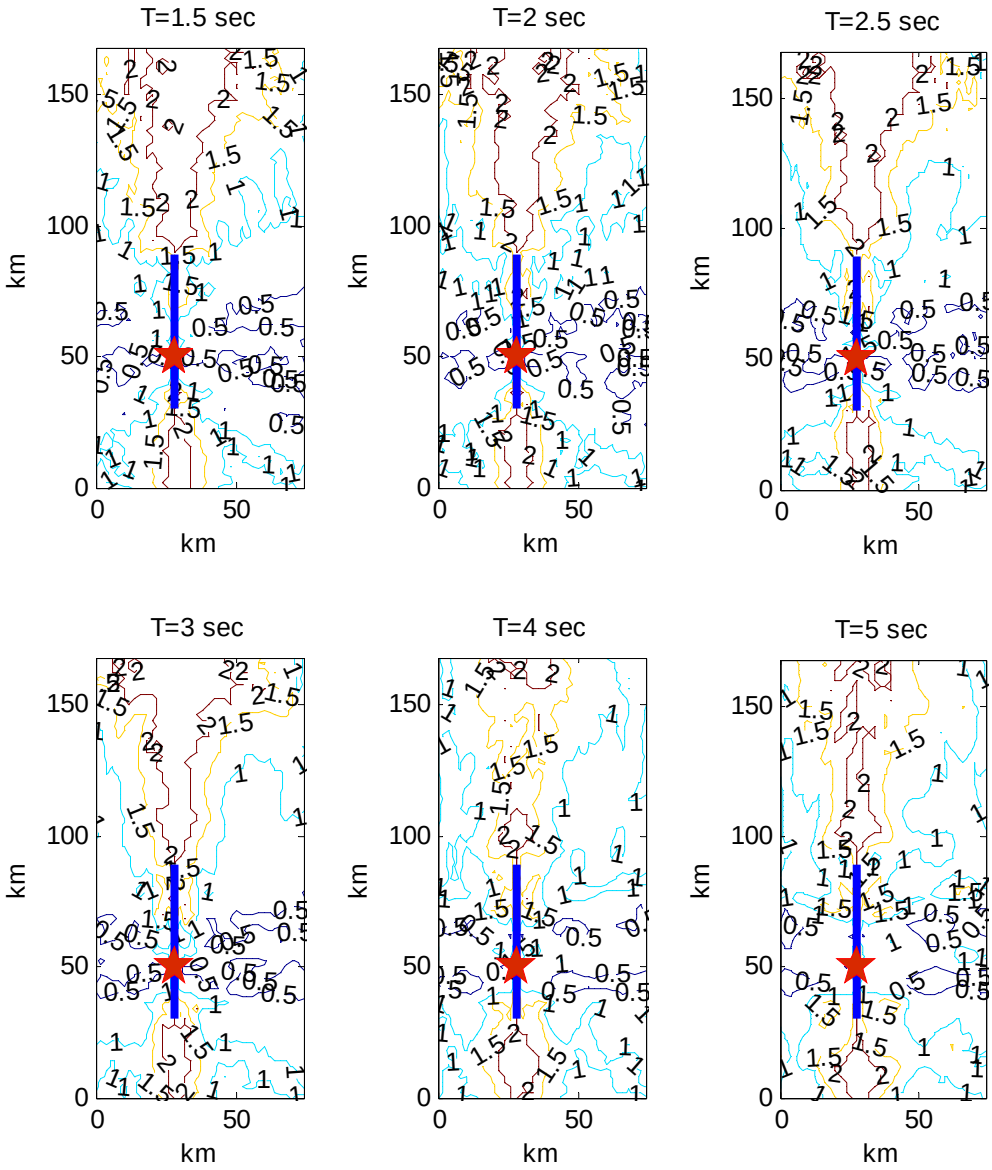

Figure 5.37. Ratio of fault normal to mean spectral accelerations obtained for the 1995 Kobe earthquake (slip model of Zeng and Anderson, 2000). The blue line represents the surface projection of the fault and the red star is the epicenter.

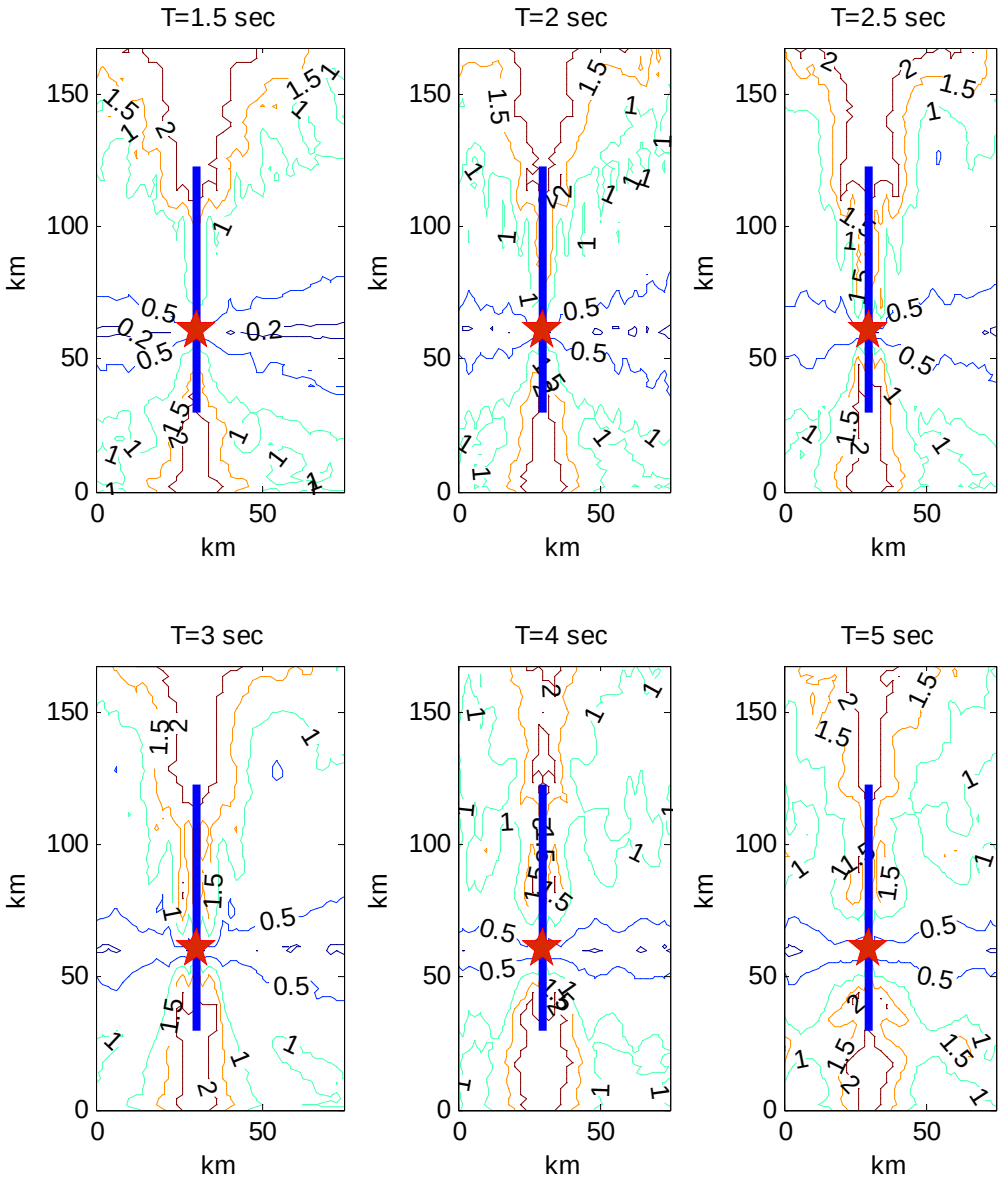

Figure 5.38. Ratio of fault normal to mean spectral accelerations obtained for the 1999 Kocaeli earthquake (slip model of Yagi and Kikuchi, 2000). The blue line represents the surface projection of the fault and the red star is the epicenter.

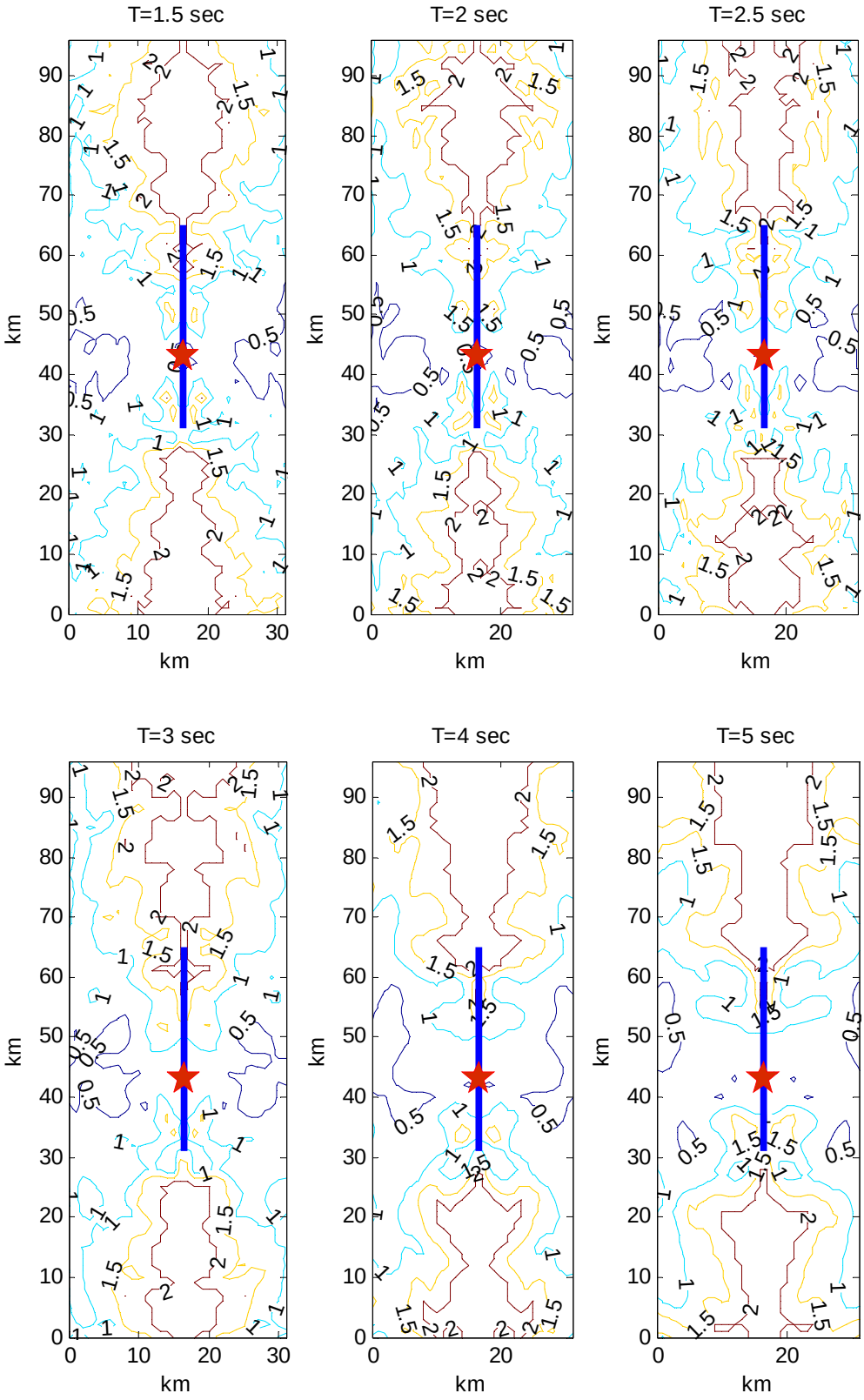

Figure 5.39. Ratio of fault normal to mean spectral accelerations obtained for the 2000 Tottori earthquake (slip model of Sekiguchi *et al.*, 2003). The blue line represents the surface projection of the fault and the red star is the epicenter.

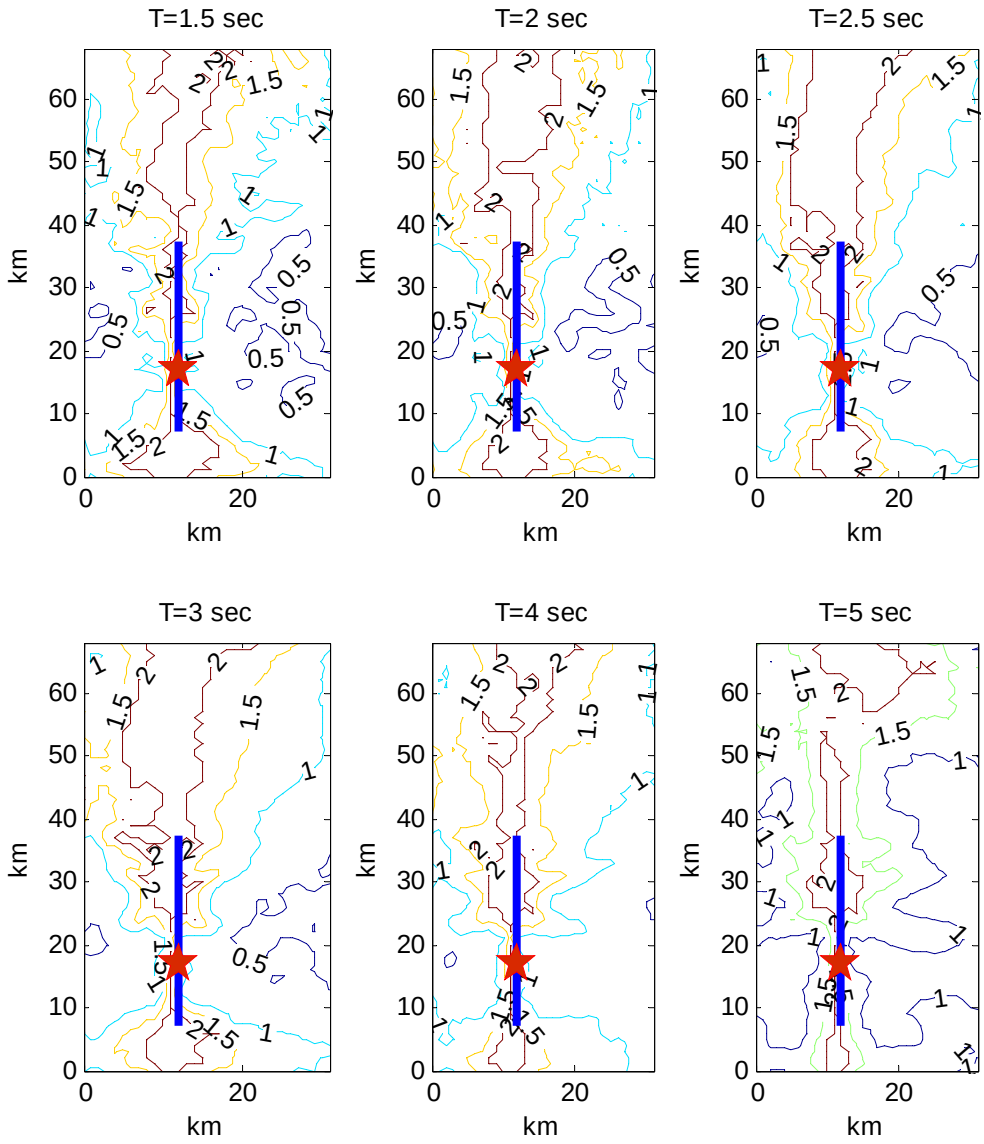

Figure 5.40. Ratio of fault normal to mean spectral accelerations obtained for the 2004 Parkfiield earthquake (slip model of Ji *et al.*, 2005). The blue line represents the surface projection of the fault and the red star is the epicenter.

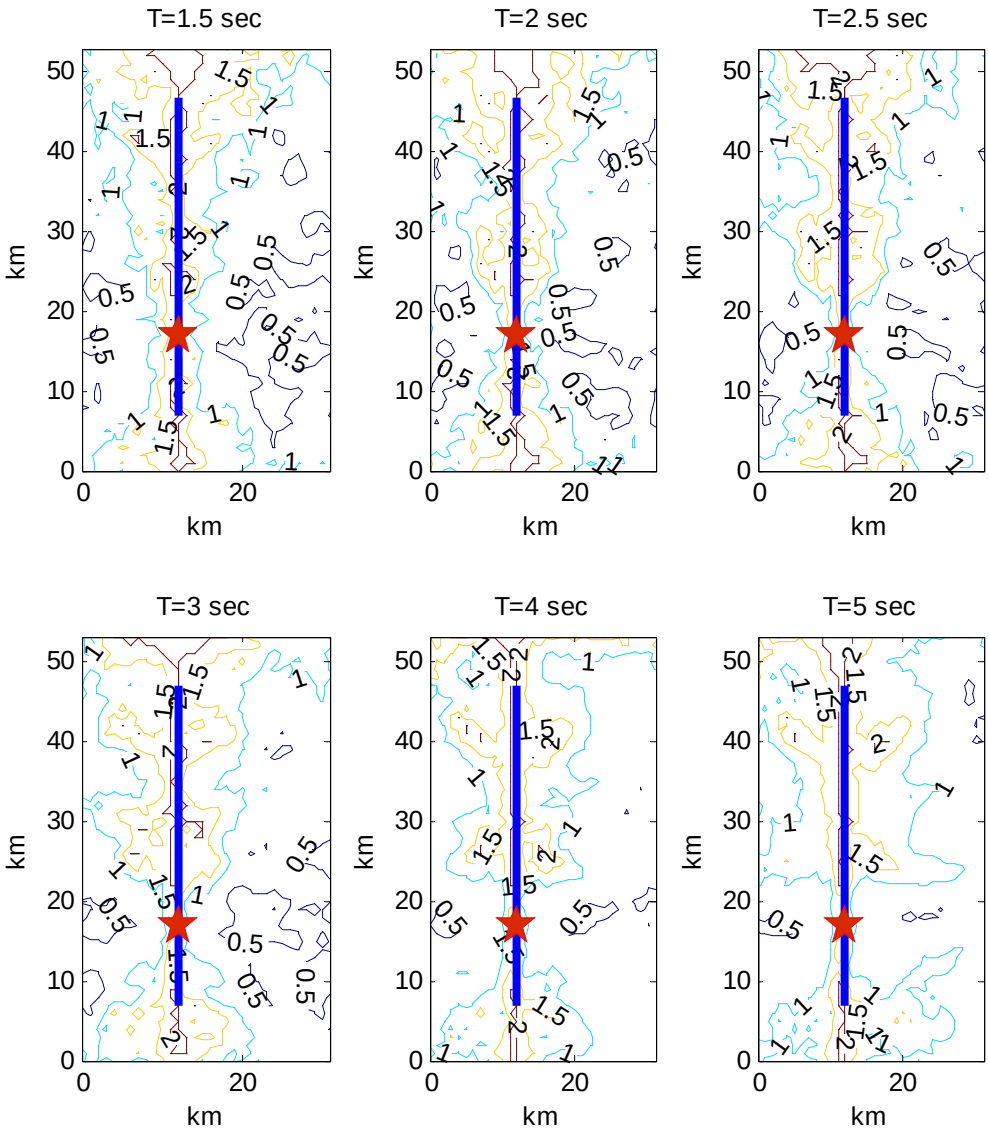

Figure 5.41. Ratio of fault normal to mean spectral accelerations obtained for the 2004 Parkfiield earthquake (slip model of Liu *et al.*, 2006). The blue line represents the surface projection of the fault and the red star is the epicenter.

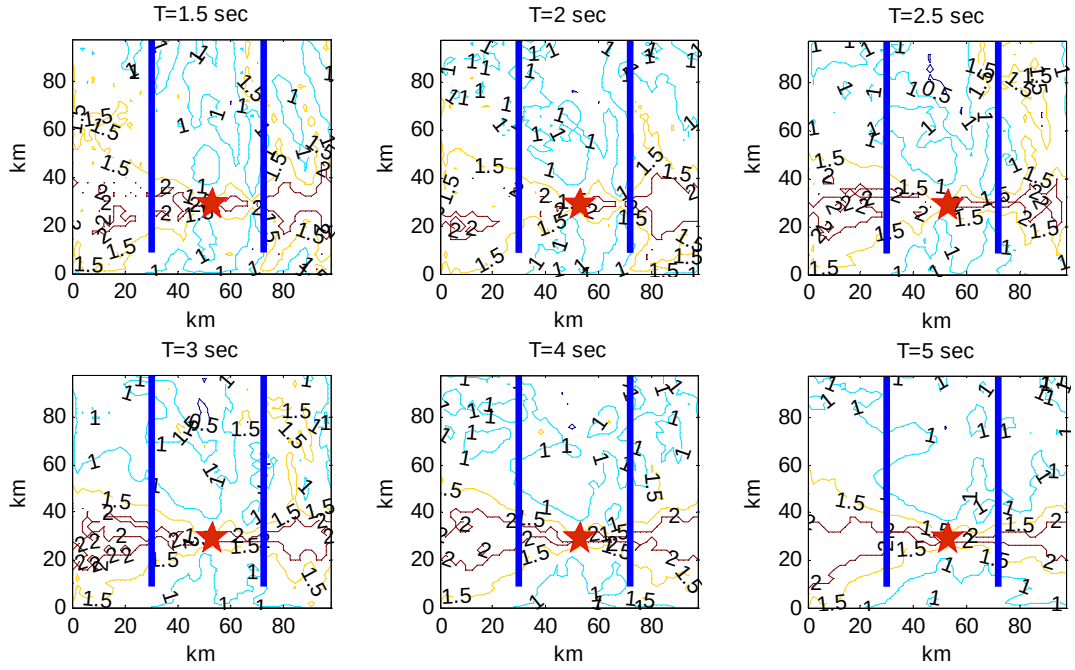

Figure 5.42. Ratio of fault normal to mean spectral accelerations obtained for the 1978 Tabas earthquake (slip model of Hartzell and Mendoza, 1991)

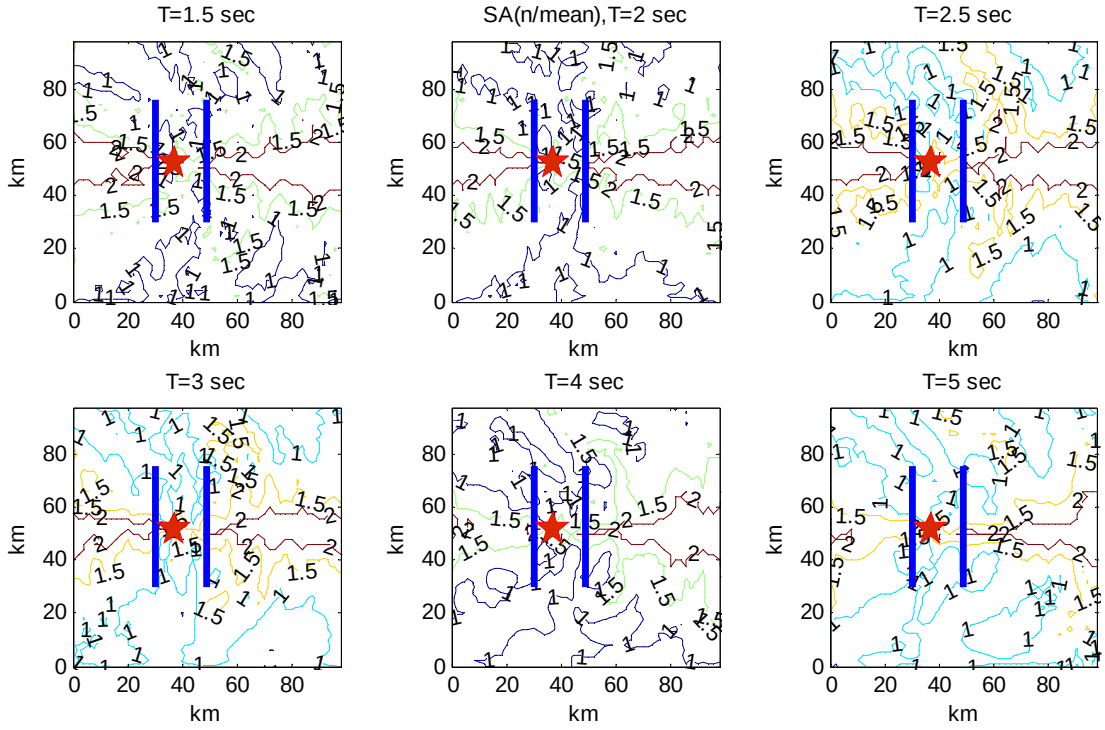

Figure 5.43. Ratio of fault normal to mean spectral accelerations obtained for the 1992 Nahanni earthquake (slip model of Hartzell *et al.*, 1994)

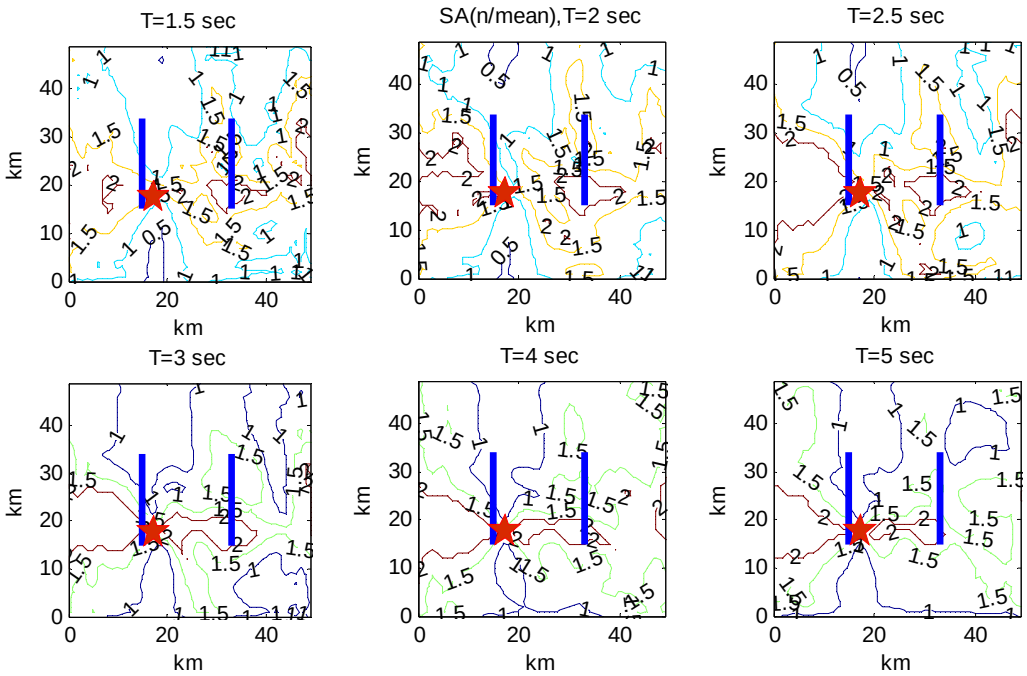

Figure 5.44. Ratio of fault normal to mean spectral accelerations obtained for the 1994 Northridge earthquake (slip model of Hartzell *et al.*, 1996)

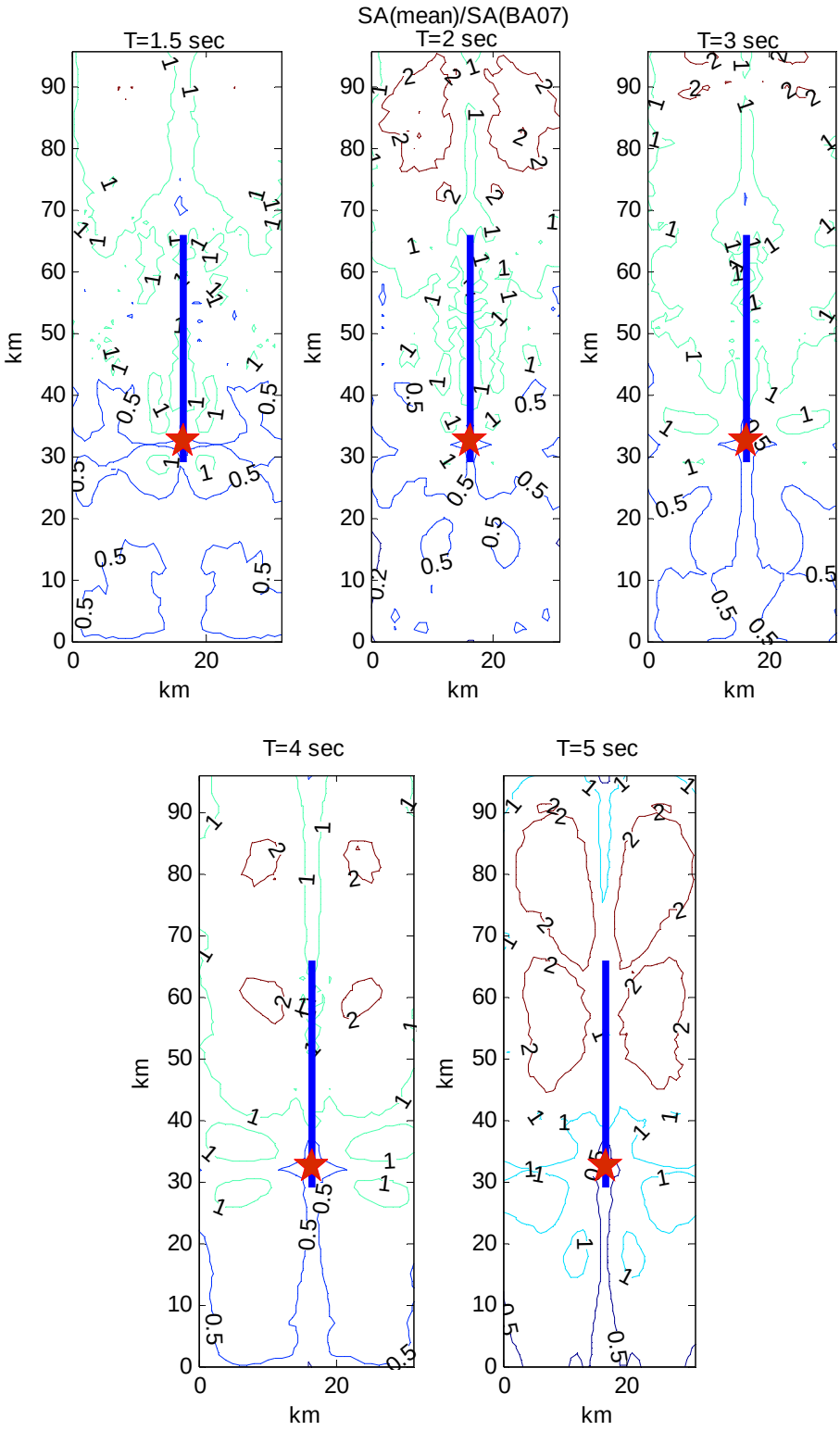

Figure 5.45. Simulated spectral accelerations over median (σ = 0) spectral accelerations obtained from the Boore and Atkinson (2006) empirical prediction equation for the 1979 Imperial Valley earthquake. Slip model of Archuleta (1984).

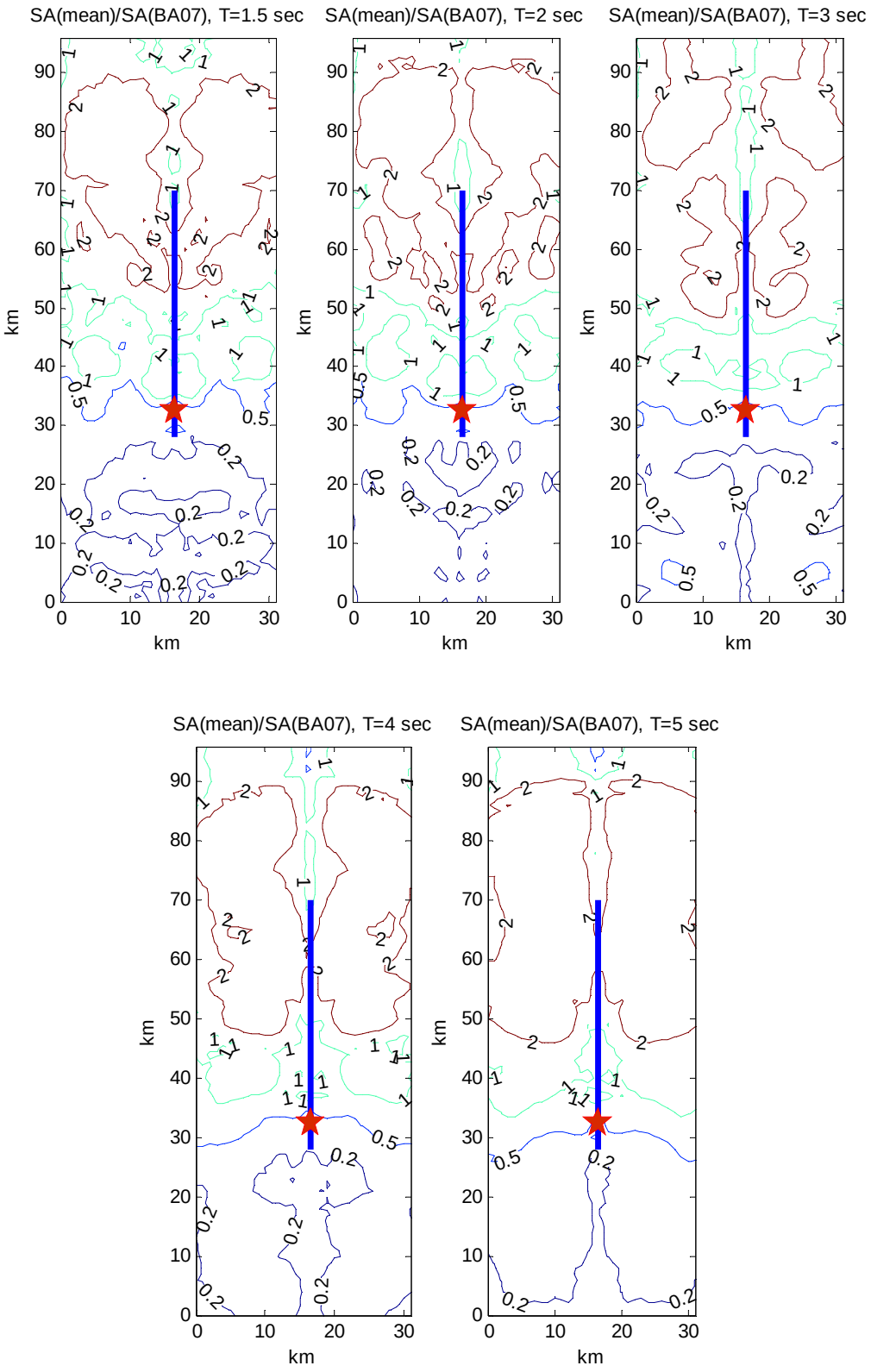

Figure 5.46. Simulated spectral accelerations over median ($\sigma = 0$) spectral accelerations obtained from the Boore and Atkinson (2006) empirical prediction equation for the 1979 Imperial Valley earthquake. Slip model of Zeng and Anderson (2000).

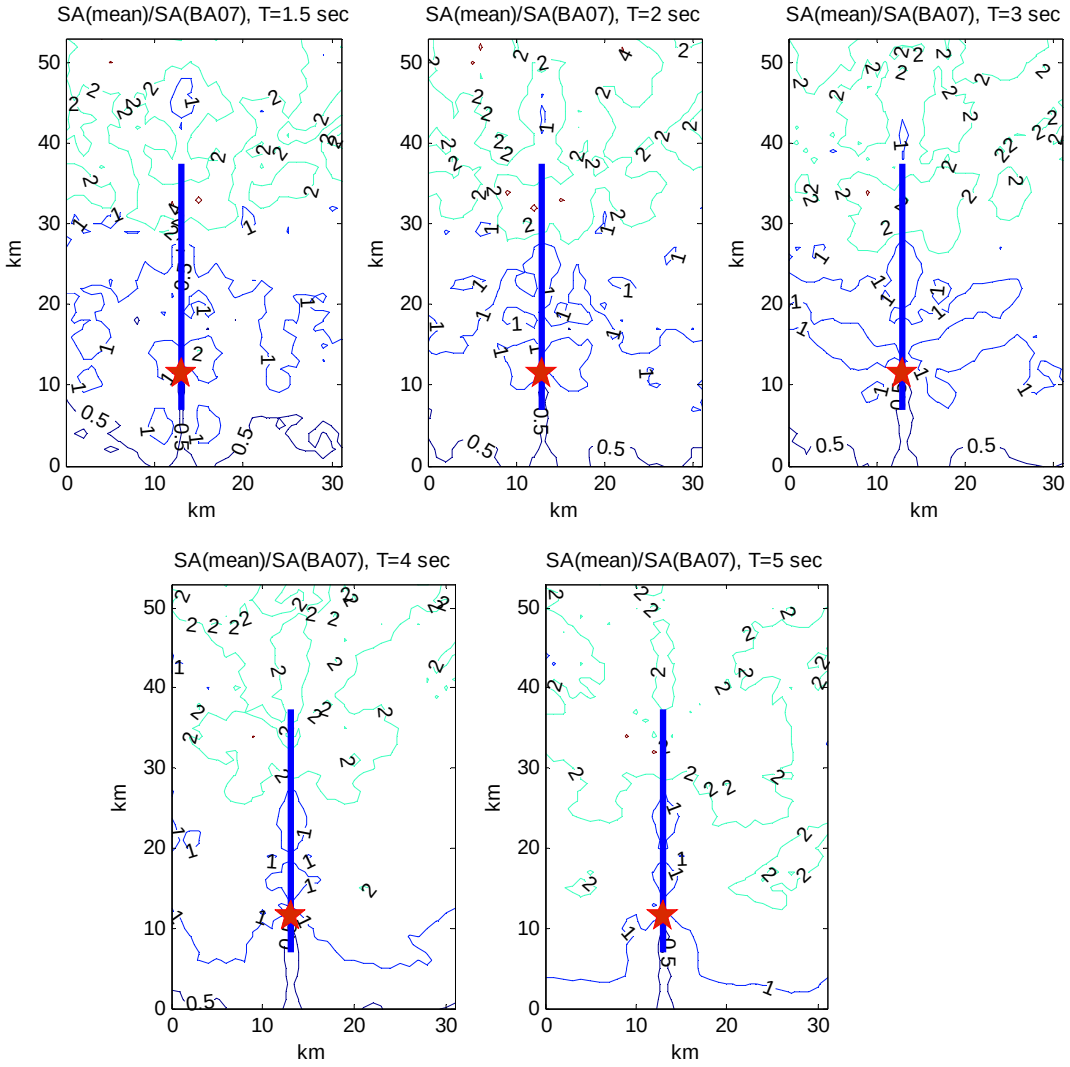

Figure 5.47. Simulated spectral accelerations over median ($\sigma = 0$) spectral accelerations obtained from the Boore and Atkinson (2006) empirical prediction equation for the 1984 Morgan Hill earthquake. Slip model of Beroza and Spudich (1988).

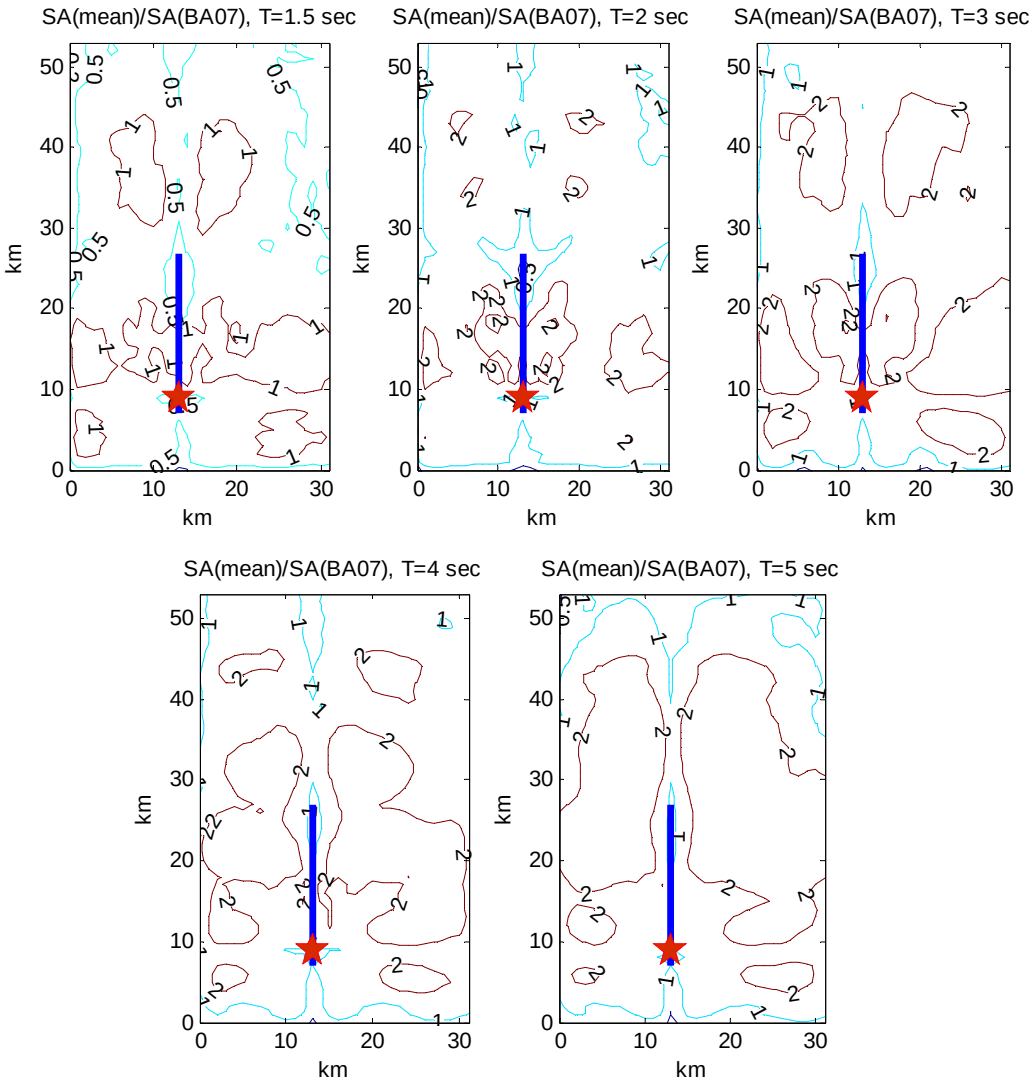

Figure 5.48. Simulated spectral accelerations over ($\sigma = 0.5$) spectral accelerations obtained from the Boore and Atkinson (2006) empirical prediction equation for the 1987 Supersition Hills earthquake. Slip model of Wald *et al.* (1990).

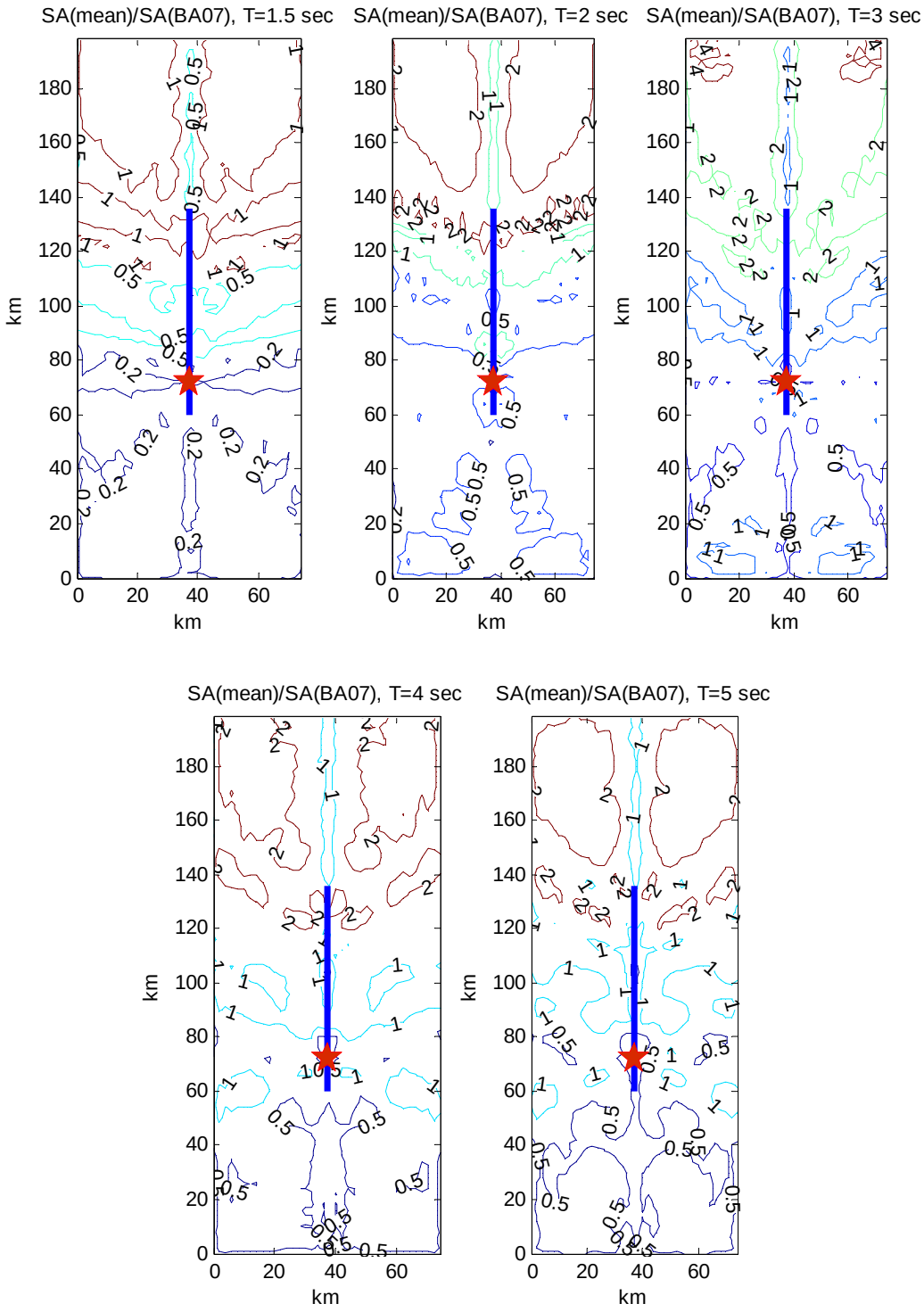

Figure 5.49. Simulated spectral accelerations over (σ = 1) spectral accelerations obtained from the Boore and Atkinson (2006) empirical prediction equation for the 1992 Landers earthquake. Slip model of Zeng and Anderson (2000).

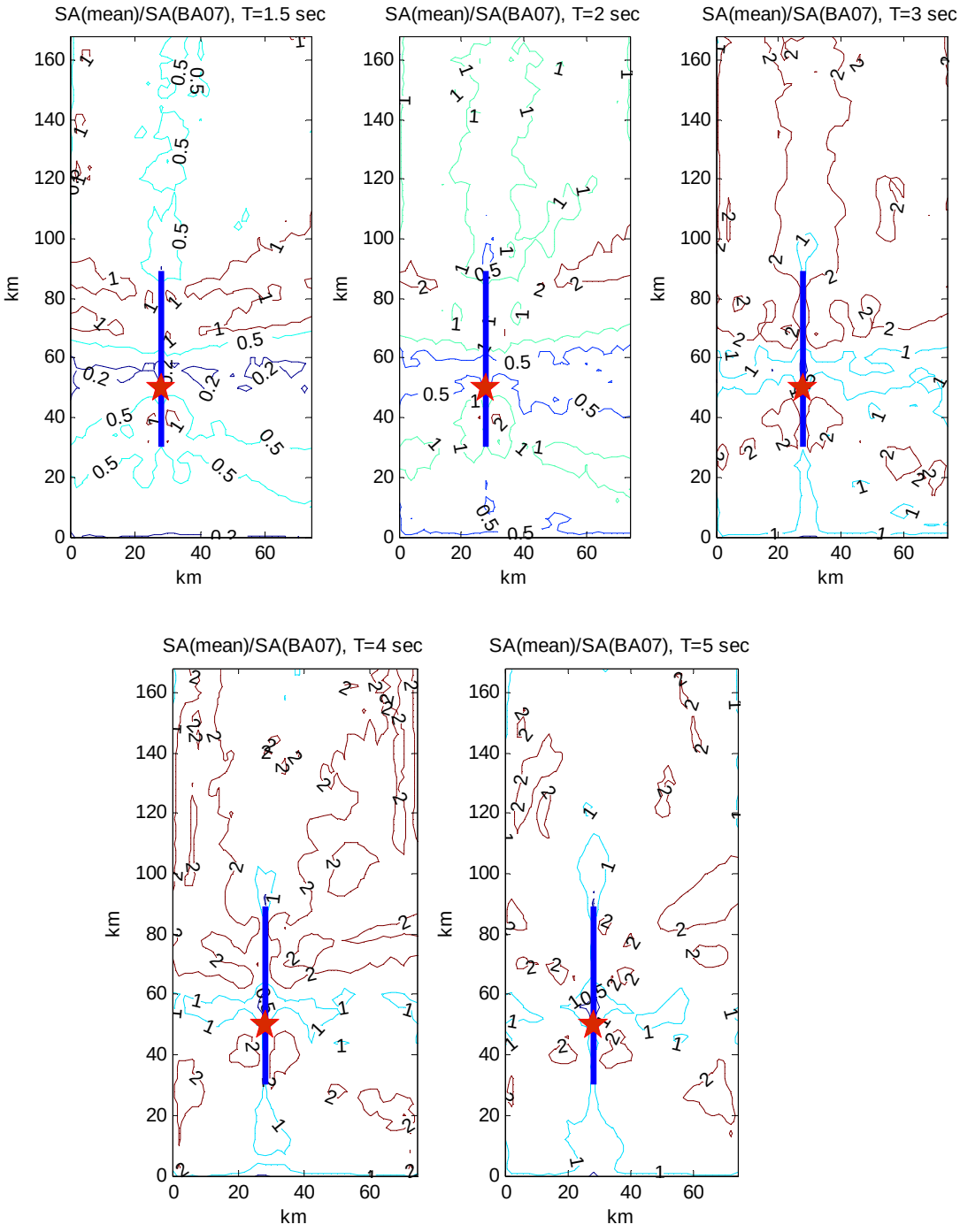

Figure 5.50. Simulated spectral accelerations over (σ = 1) spectral accelerations obtained from the Boore and Atkinson (2006) empirical prediction equation for the 1995 Kobe earthquake. Slip model of Zeng and Anderson (2000).

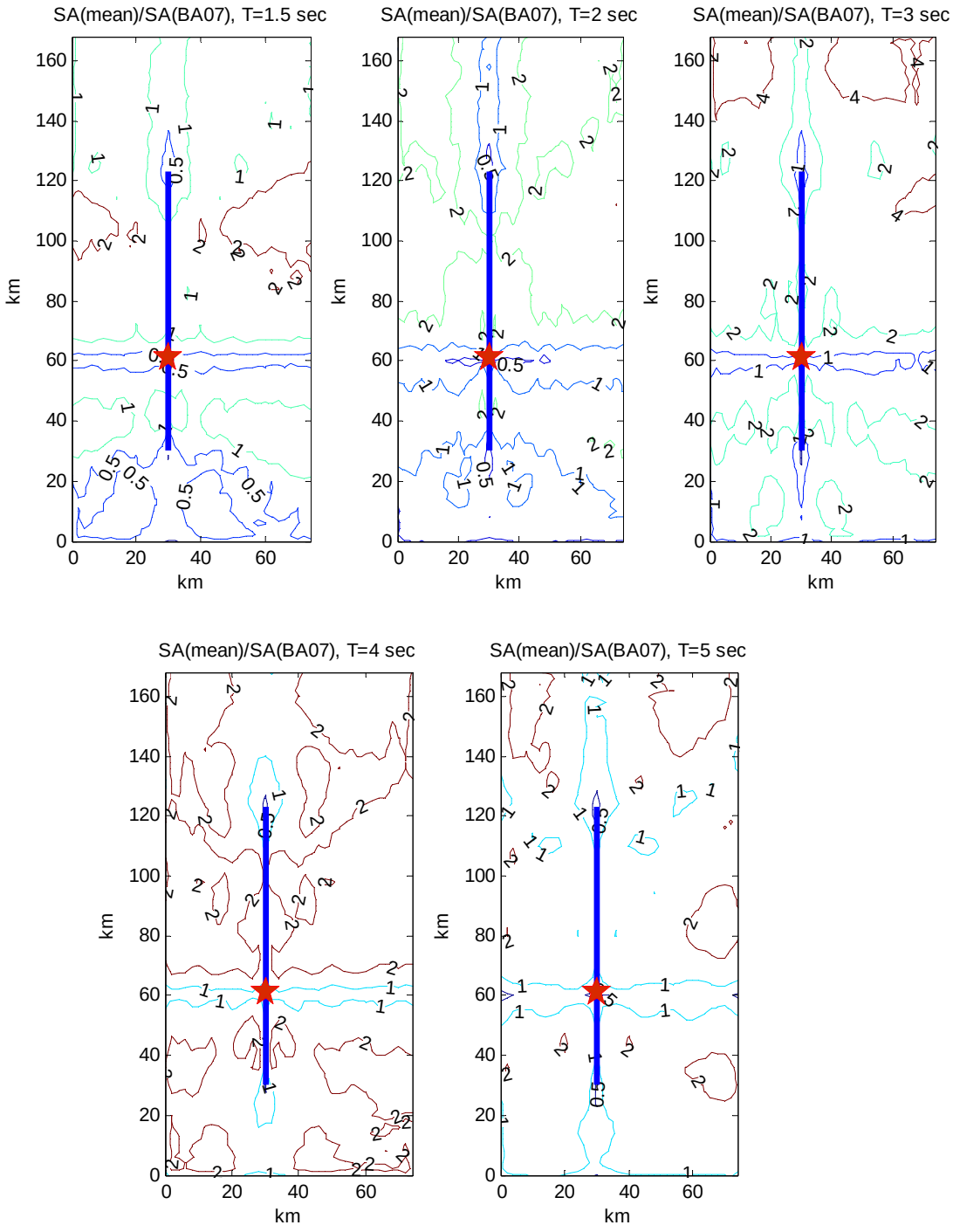

Figure 5.51. Simulated spectral accelerations over (σ = 1) spectral accelerations obtained from the Boore and Atkinson (2006) empirical prediction equation for the 1999 Kocaeli earthquake. Slip model of Yagi and Kikuchi (2000).

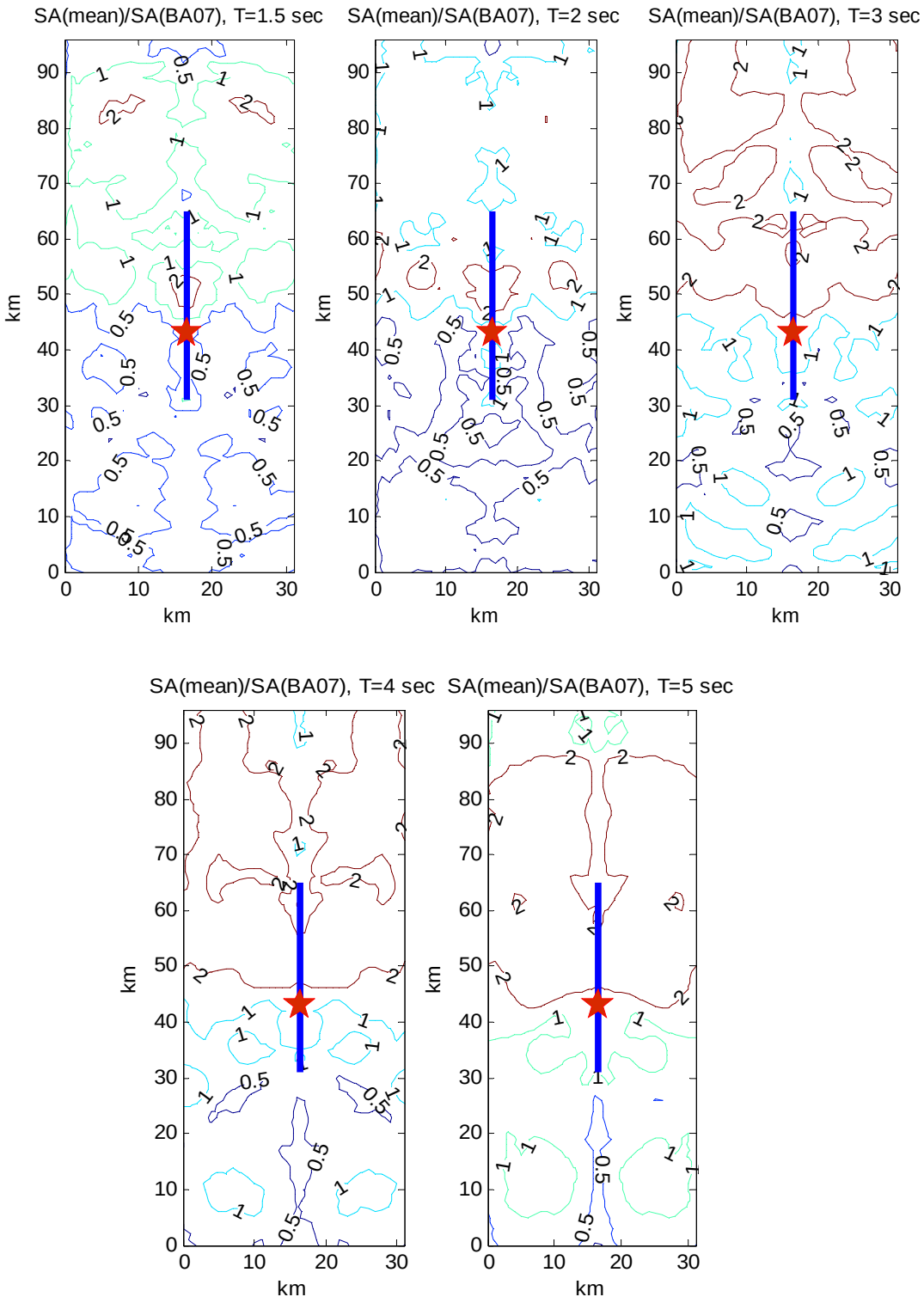

Figure 5.52. Simulated spectral accelerations over ($\sigma = 0$) spectral accelerations obtained from the Boore and Atkinson (2006) empirical prediction equation for the 2000 Tottori earthquake. Slip model of Sekiguchi *et al*. (2003).

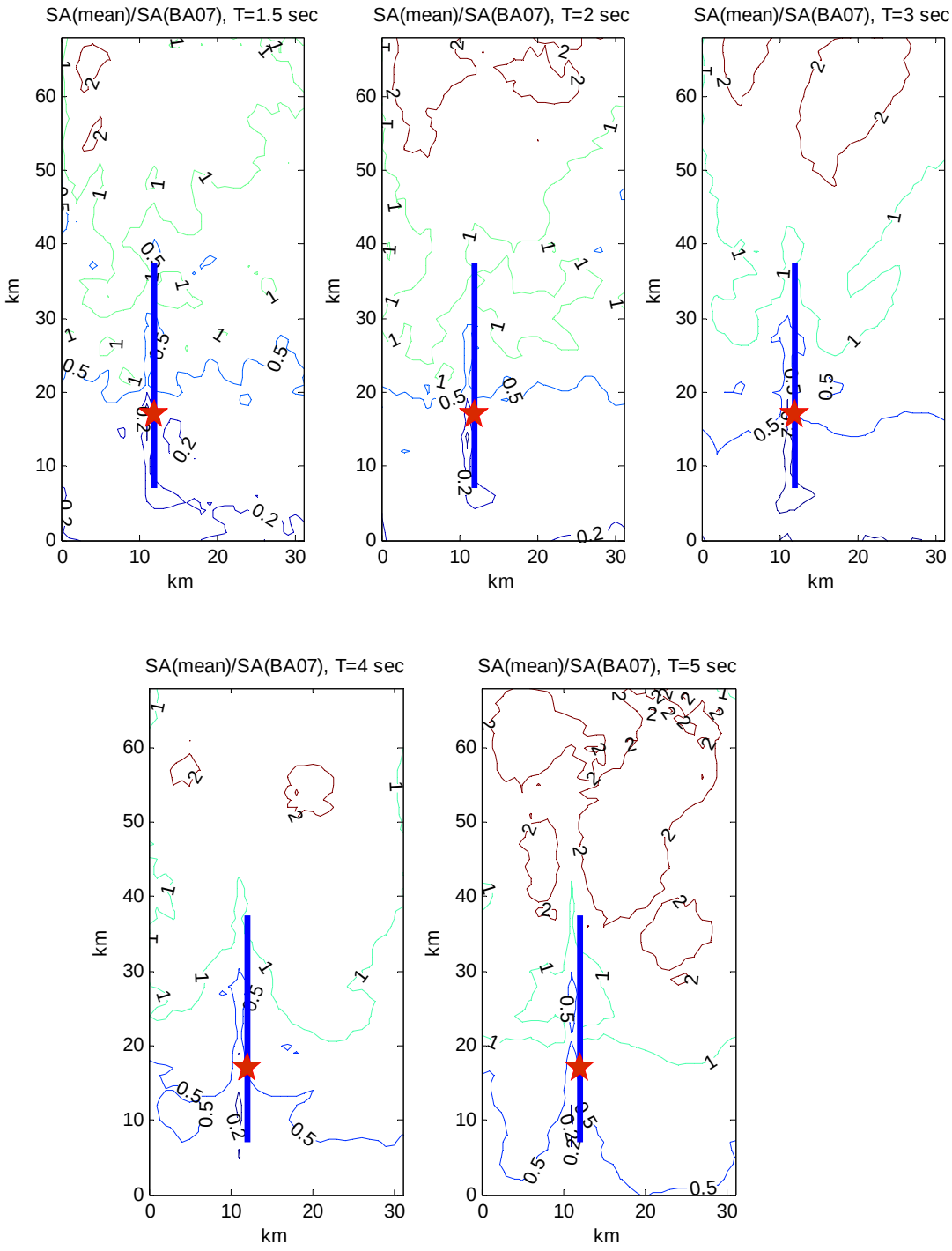

Figure 5.53. Simulated spectral accelerations over ($\sigma = 0$) spectral accelerations obtained from the Boore and Atkinson (2006) empirical prediction equation for the 2004 Parkfield earthquake. Slip model of Ji *et al.* (2005).

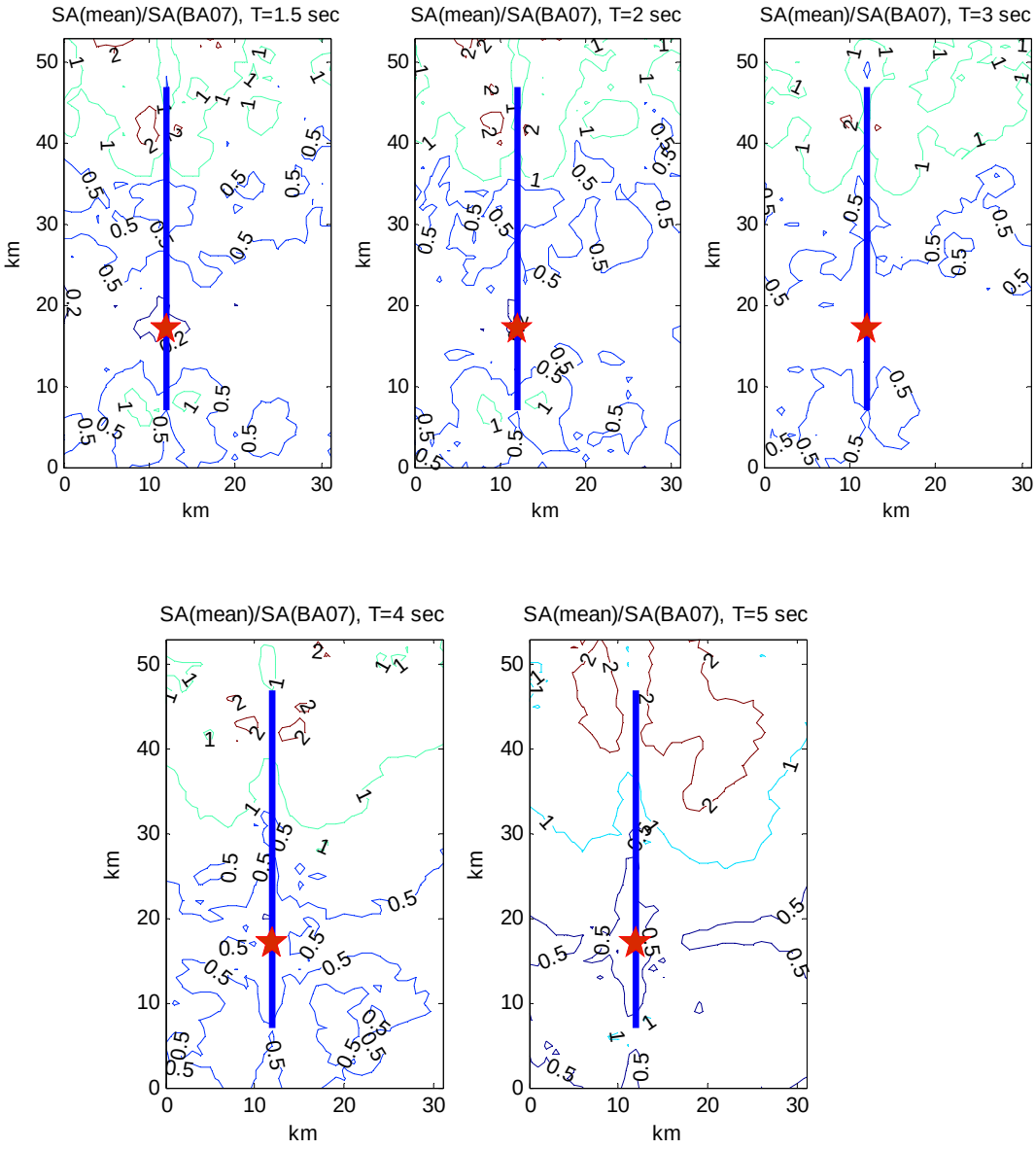

Figure 5.54. Simulated spectral accelerations over (σ = 0) spectral accelerations obtained from the Boore and Atkinson (2006) empirical prediction equation for the 2004 Parkfield earthquake. Slip model of Liu *et al.* (2006).

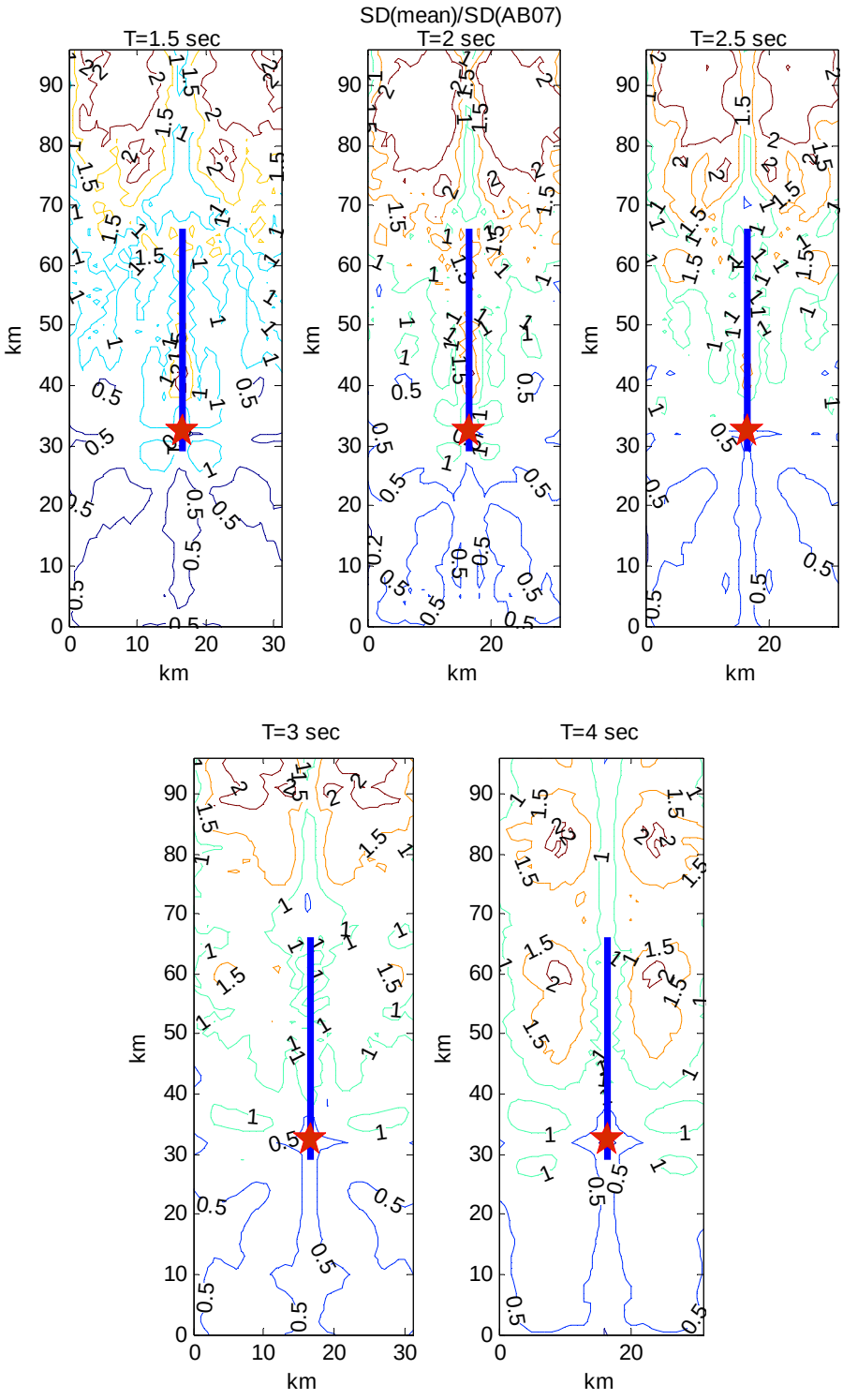

Figure 5.55. Simulated spectral displacements over median (σ = -0.5) spectral displacements obtained from the Akkar and Bommer (2007) empirical prediction equation for the 1979 Imperial Valley earthquake. Slip model of Archuleta (1984).

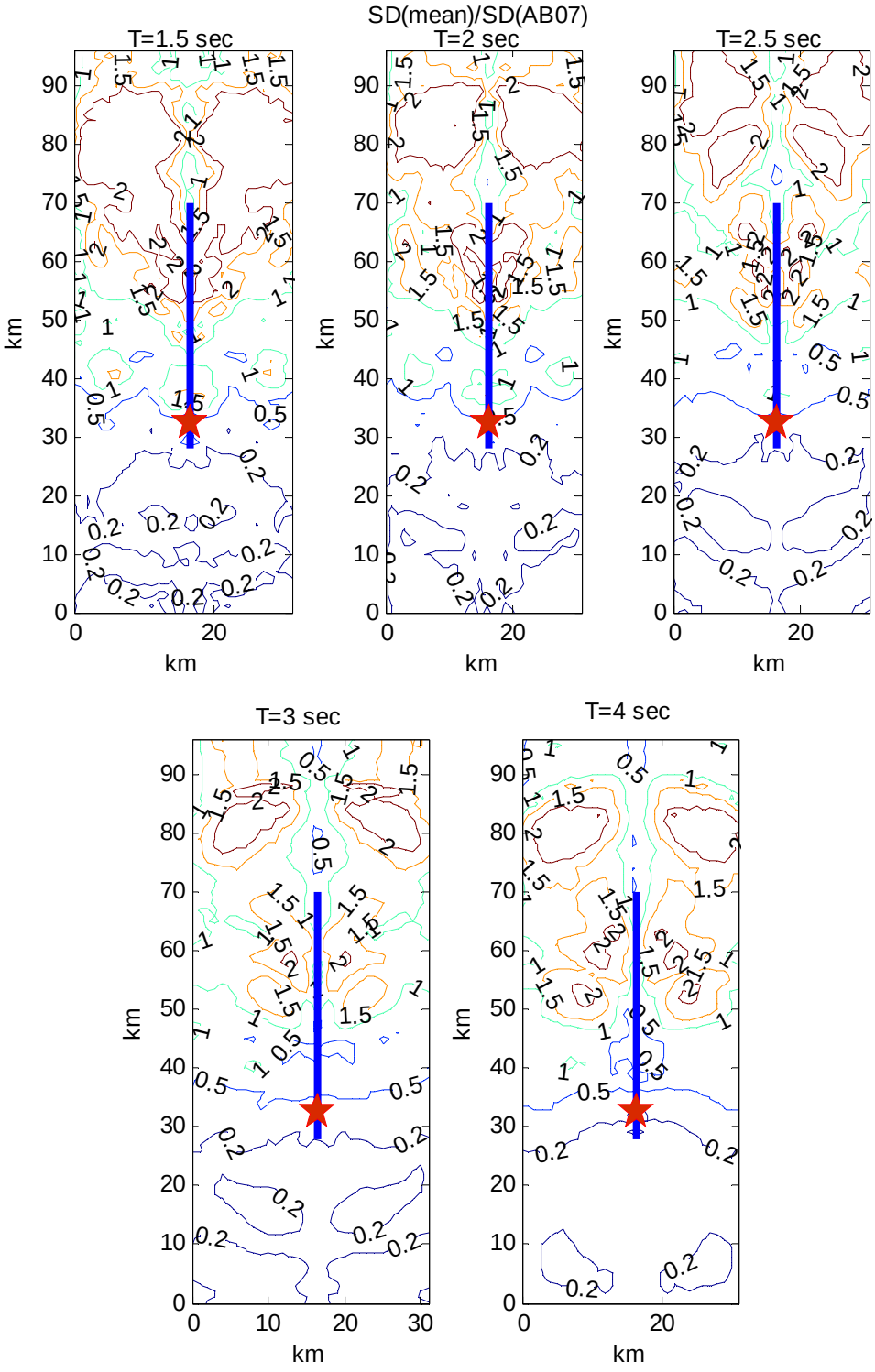

Figure 5.56. Simulated spectral displacements over median spectral displacements obtained from the Akkar and Bommer (2007) empirical prediction equation for the 1979 Imperial Valley earthquake. Slip model of Zeng and Anderson (2000).

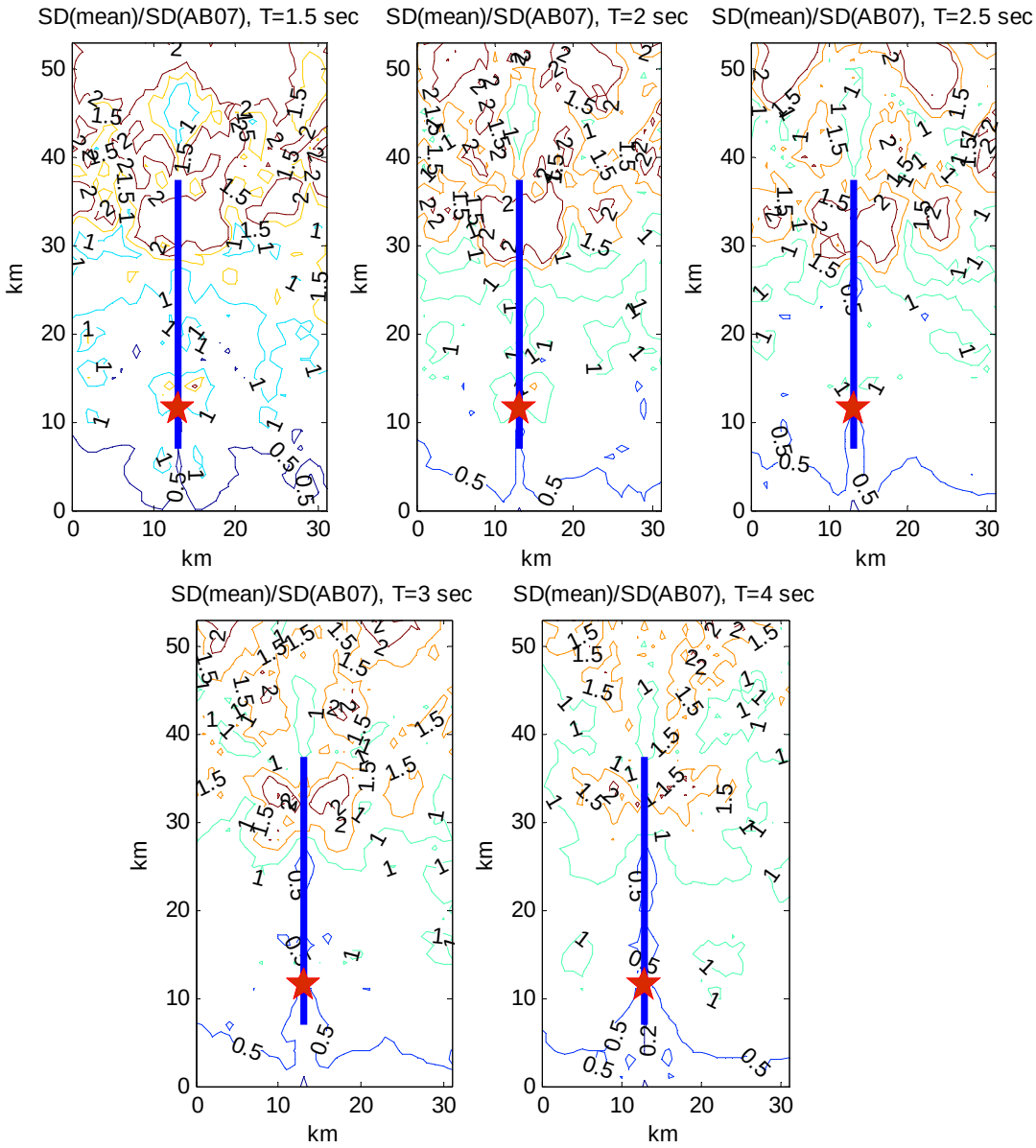

Figure 5.57. Simulated spectral displacements over median (σ = 0) spectral displacements obtained from the Akkar and Bommer (2007) empirical prediction equation for the 1984 Morgan Hill earthquake. Slip model of Beroza and Spudich (1988).

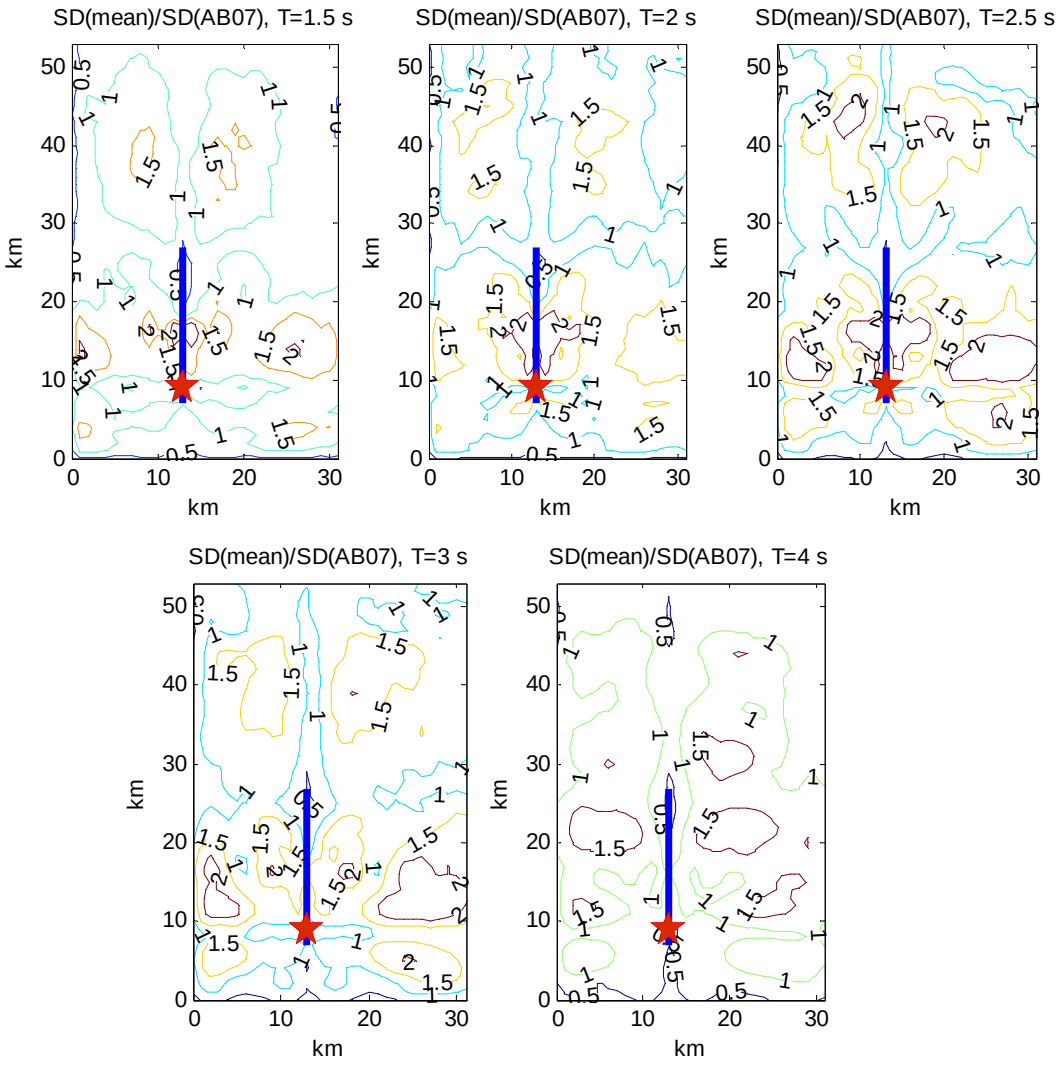

Figure 5.58. Simulated spectral displacements over (σ = 0.5) spectral displacements obtained from the Akkar and Bommer (2007) empirical prediction equation for the 1987 Supersition Hills earthquake. Slip model of Wald *et al.* (1990).

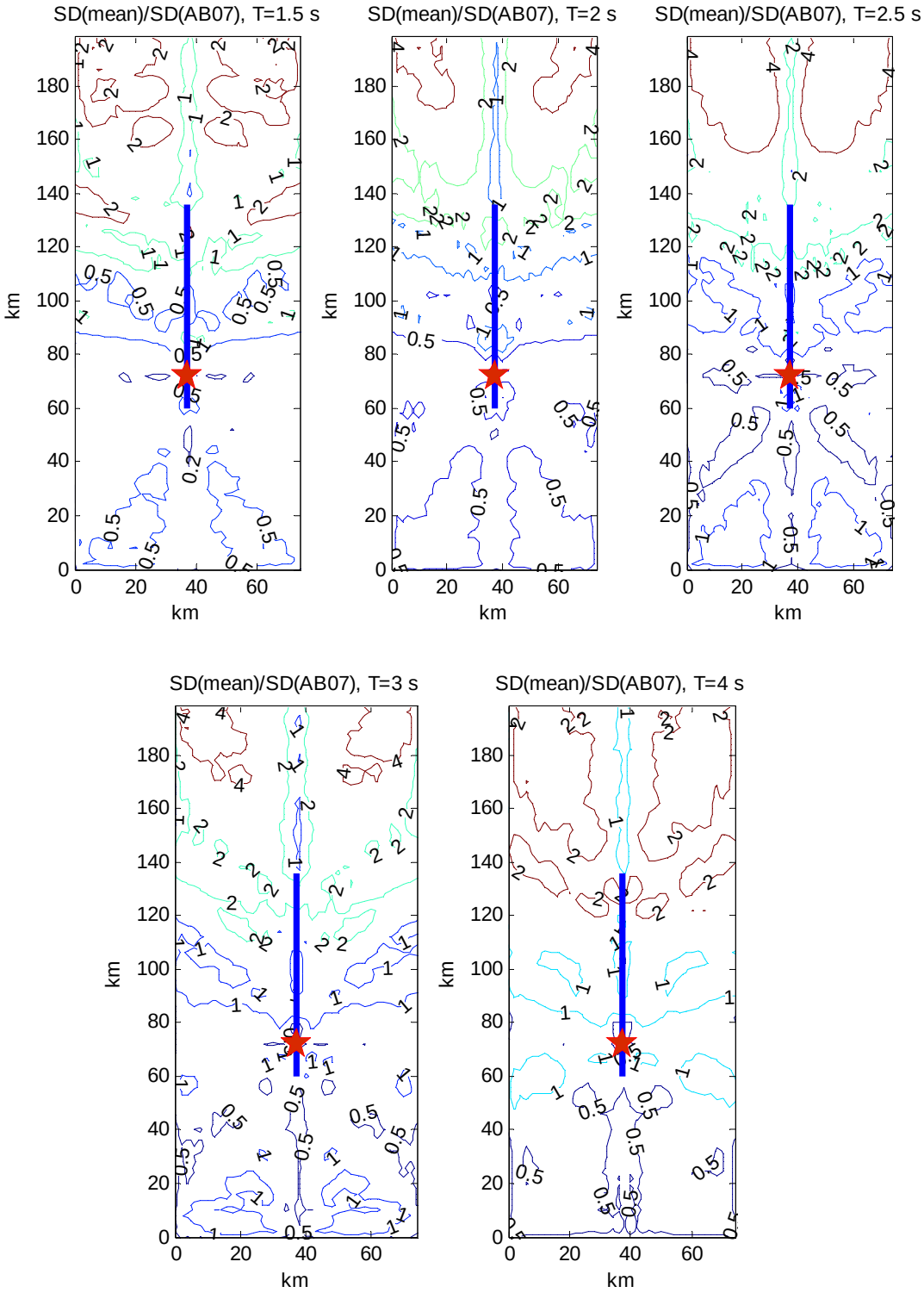

Figure 5.59. Simulated spectral displacements over (σ = 1) spectral displacements obtained from the Akkar and Bommer (2007) empirical prediction equation for the 1992 Landers earthquake. Slip model of Zeng and Anderson (2000).

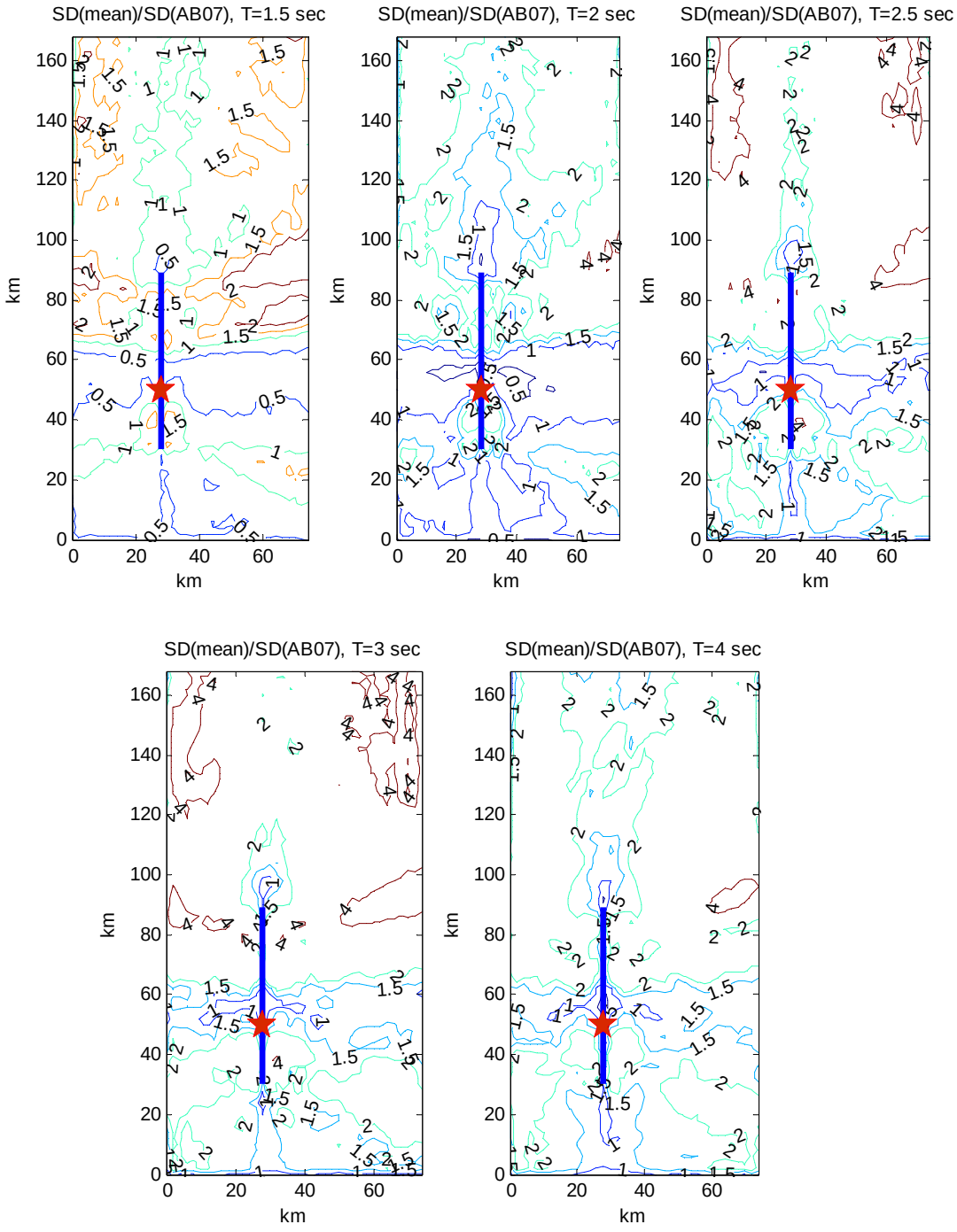

Figure 5.60. Simulated spectral displacements over ($\sigma = 0$) spectral displacements obtained from the Akkar and Bommer (2007) empirical prediction equation for the 1995 Kobe earthquake. Slip model of Zeng and Anderson (2000).

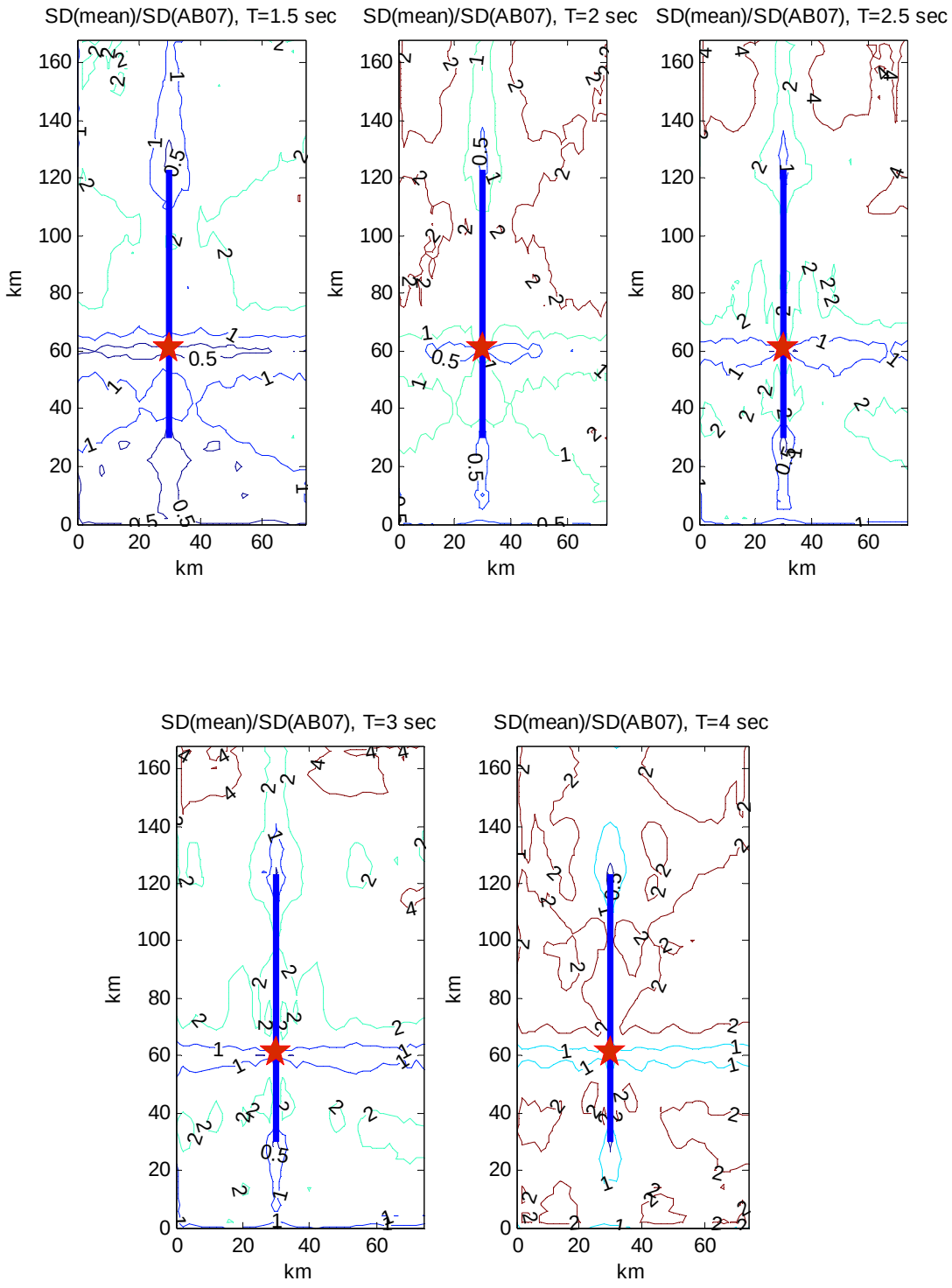

Figure 5.61. Simulated spectral displacements over ($\sigma = 1$) spectral displacements obtained from the Akkar and Bommer (2007) empirical prediction equation for the 1999 Kocaeli earthquake. Slip model of Yagi and Kikuchi (2000).

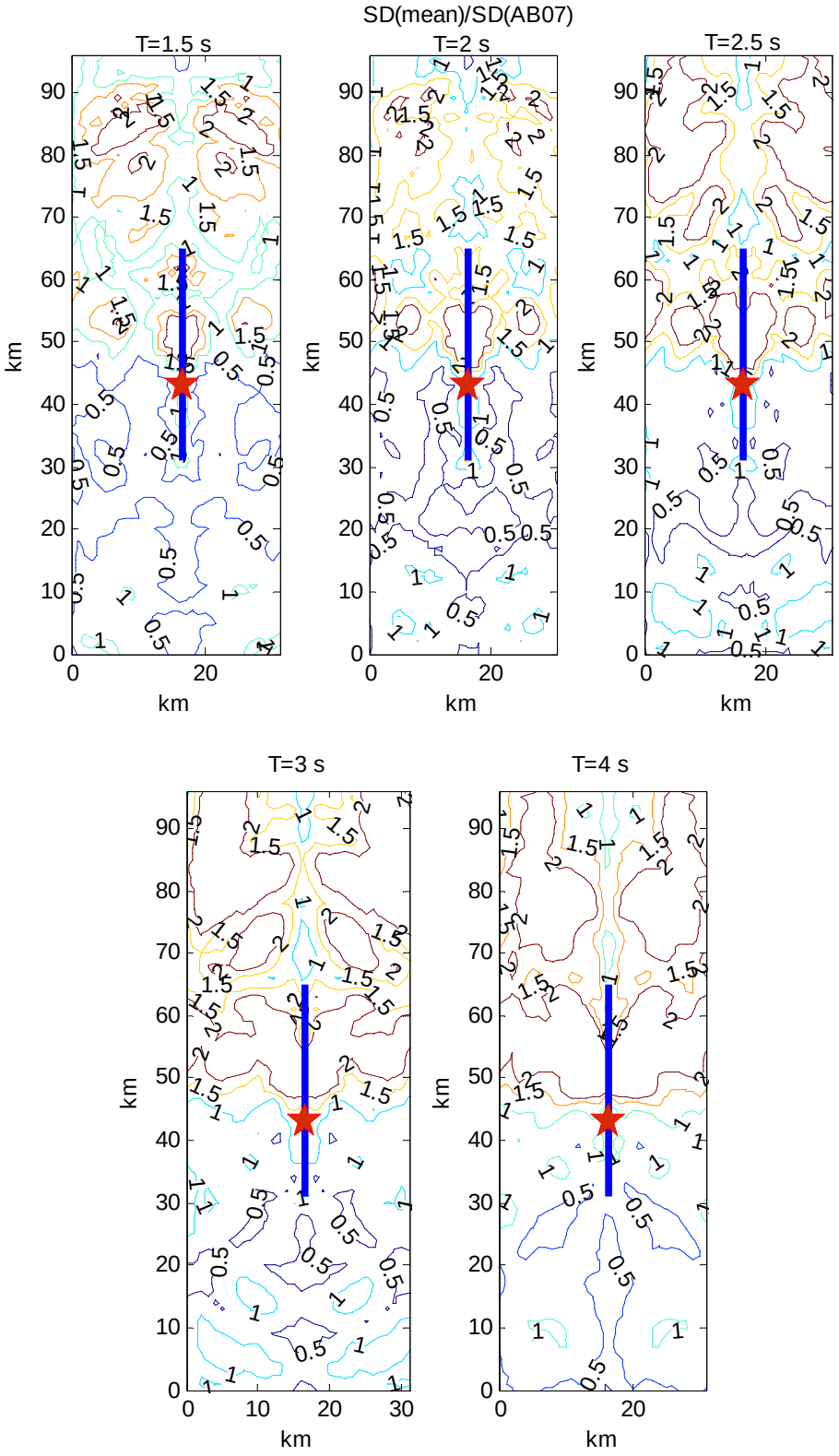

Figure 5.62. Simulated spectral displacements over (σ = -0.5) spectral displacements obtained from the Akkar and Bommer (2007) empirical prediction equation for the 2000 Tottori earthquake. Slip model of Sekiguchi *et al*, (2003).

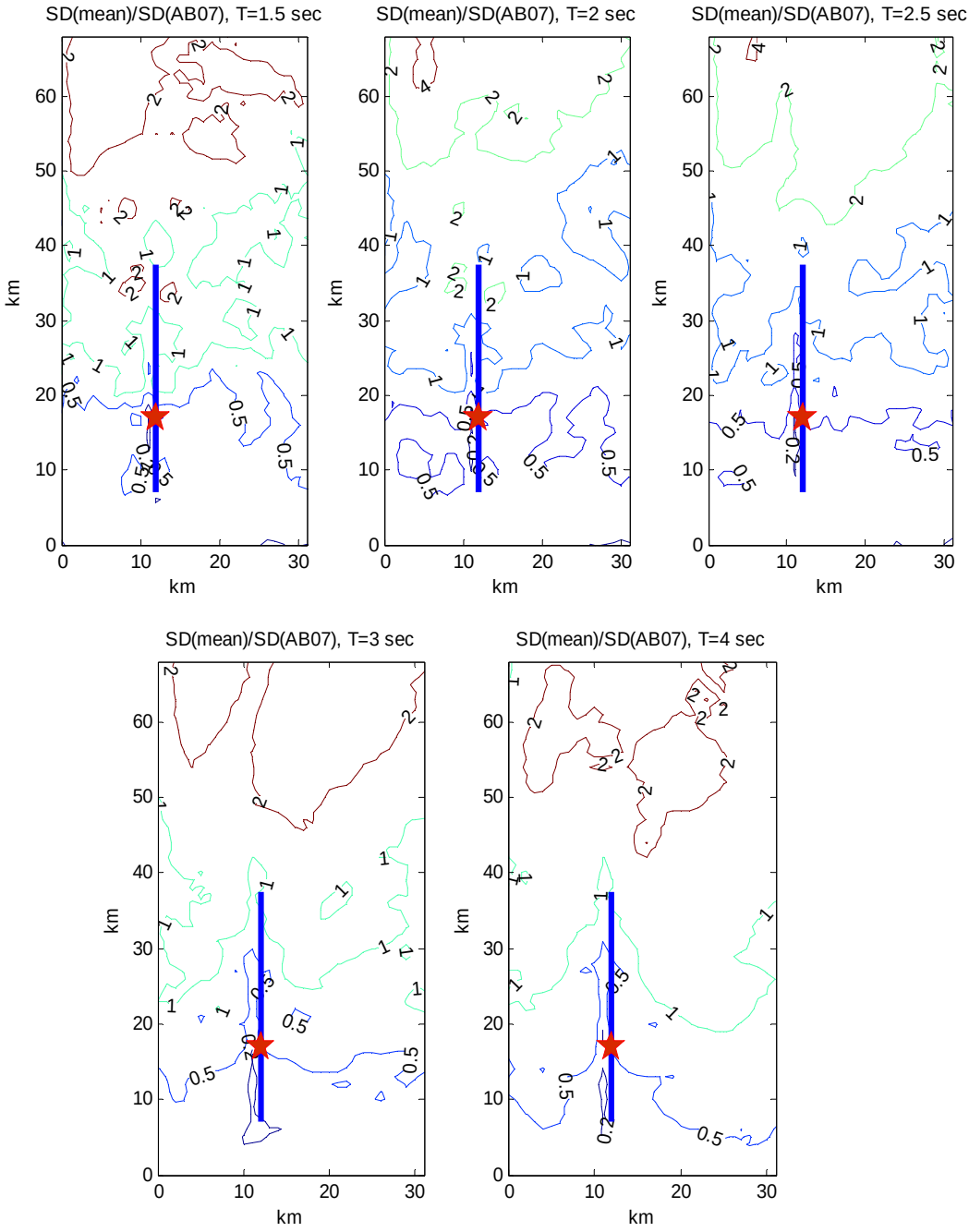

Figure 5.63. Simulated spectral displacements over (σ = -0.5) spectral displacements obtained from the Akkar and Bommer (2007) empirical prediction equation for the 2004 Parkfield earthquake. Slip model of Ji *et al.* (2005).

5.3. Results for the directivity effects and discussion

Both the results of the parametric set up described in Section 5.1 and the simulations carried out with source parameters of real earthquakes is described in Section 5.2, have been analyzed in terms of resulting surface ground motion distributions of various amplitudes and ratios to derive some characteristics of near source ground motions. Following the examples set by previous studies (e.g. Somerville *et al.*, 1997; Somerville, 2003), the results have been analyzed in terms of three parameters: the fault normal to average horizontal spectral acceleration ratio, the variation of the average horizontal spectral acceleration and displacement and the duration of the near fault directivity pulse. The spectral accelerations and displacements have been computed for periods of 1.5 s and higher as the upper frequency bound of the simulations have been set to 0.8 Hz (1.25 s).

5.3.1. The spatial variation of the fault normal to average horizontal spectral acceleration ratio

For the strike-slip events, fault normal to the geometric mean of the horizontal component ratios (FN / Mean ratio) followed the same pattern regardless of the earthquake magnitude, slip distribution. This pattern is characterized by a narrow zone of ratio = 2 around the fault which widens beyond the fault extremities. A zone of ratio = 0.5 is observed in a region perpendicular to the fault and passing through the hypocenter is also observed. This behavior is empirically evidenced in the 2004 Parkfield earthquake recordings of the Goldhill array. This zone indicating larger fault parallel spectral amplitudes becomes narrower as the period of the spectral accelerations increases. Almost a V-shape region of ratio contours of 1 and 1.5 intersecting at the epicenter are visible in all simulations.

A simple form can be proposed as a model for the distribution of the spatial variation of the fault normal to average horizontal spectral acceleration ratio. The standard pattern for strike-slip ruptures and the associated parameters (α_1, α_2, α_3, α_4 and D) are presented in Figure 5.64. Comparison of the FN / Mean distributions of the parametric study given in Figure 5.13, Figure 5.15 and Figure 5.16 and those resulting from the variable slip models

reveal that the this pattern is not sensitive to the constant slip amplitude but the rupture velocity, rise time and slip distribution on the rupture plane have a larger effect on the distribution pattern. The results for all slip models and the distinct periods for which spectral calculations were performed were statistically treated to obtain possible ranges of these parameters. The parameter set obtained for the base case (Case 1b) of the benchmark study (Section 5. 1) are presented in Table 5.5 for the periods of 2.0, 3.0, 4.0 and 5.0 s. The forward directivity zone is enlarged with period for ratios of 0.5 and 1.0 and 1.5. The R = 2.0 zone remains the same for all periods.

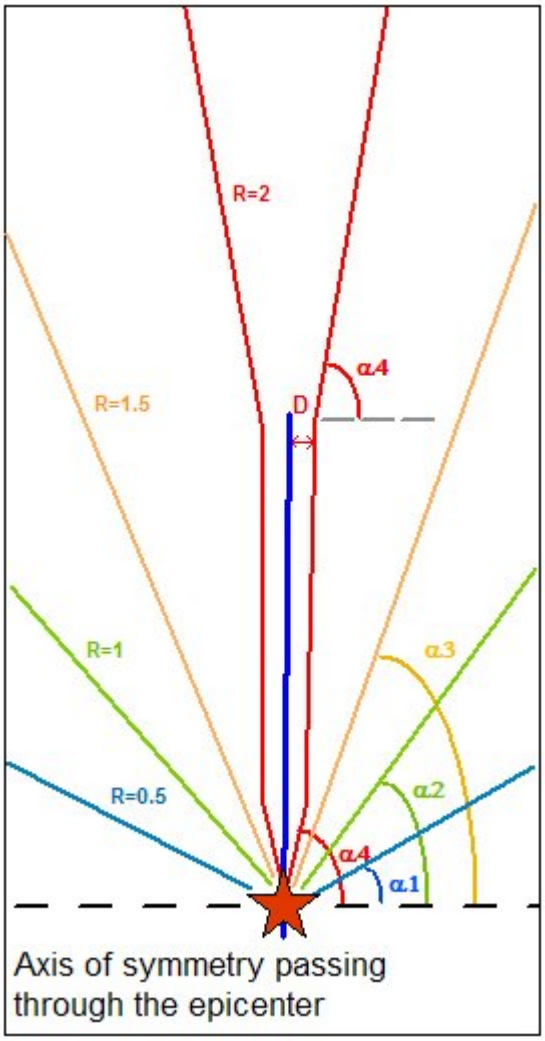

Figure 5.64. The generalized form of the fault normal to average spectral acceleration ratios for strike-slip earthquakes. The blue line represents the fault trace and the red star is the epicenter.

Table 5.5. Parameters to define the standard shape of the fault normal to average spectral acceleration ratio (based on case 1b)

	Period			
	2 s	3 s	4 s	5 s
α1	20°	10°	10°	10°
α2	55°	55°	40°	40°
α3	70°	70°	65°	65°
α4	85°	85°	85°	85°
D	2.5 km	2.5 km	2.5 km	2.5 km

Although rise time, rupture velocity and slip distribution on the fault plane generate variations in the parameters defining the standard shape of the directivity layout, angular parameters obtained from various slip models remained within ±5° of the results presented in Table 5.6. The width of the R = 2 zone around the fault has a variability of ±1 km. It is believed that for engineering purposes, the layout described in Figure 5.65 and Table 5.5 can be used to differentiate the amplitude of the fault normal component from mean values in near source regions.

For the dip-slip ruptures only fault normal to mean spectral acceleration ratios are considered. In all three cases simulated in this study, V-shaped zones of ratio =2 are observed at both ends of the fault in the slip direction. Again V-shaped zones of ratio =1.5 intersect at the epicenter. This implies that forward directivity conditions occur at both ends of the fault in the direction parallel to slip. Fault normal to mean acceleration ratios approach to 1 in the direction perpendicular to slip. In contrast to the strike-slip case, the FN / Mean ratios never fall below 1.0, a finding that should also be checked against recorded data. The generalized shape of the FN / Mean ratios derived from these observations is presented in Figure 5.65. However, the number of dip–slip simulations were not sufficient to derive any parametric form for the associated FN / Mean ratios.

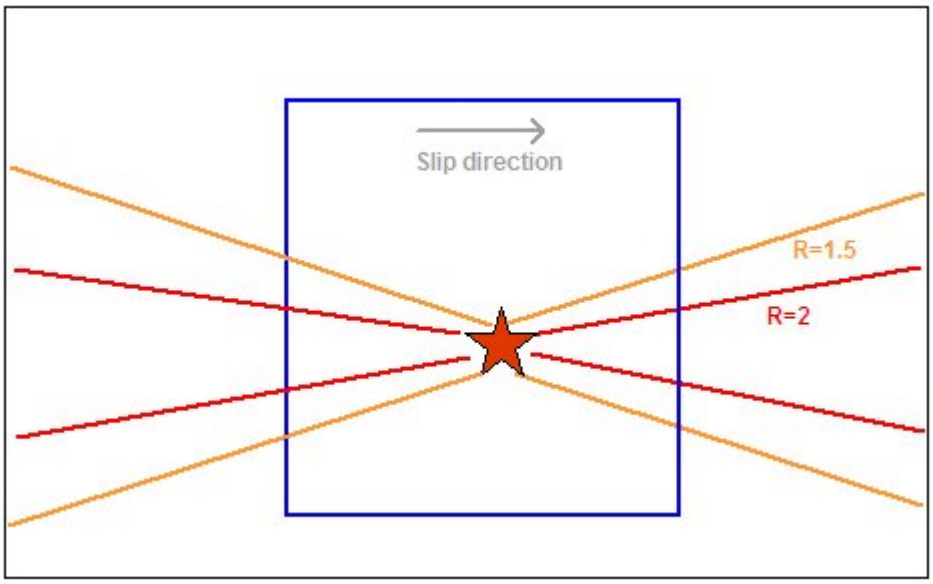

Figure 5.65. The generalized form of the fault normal to average spectral acceleration ratios for dip-slip earthquakes. The blue rectangle represents the ground surface projection of the fault and the red star is the epicenter.

The comparison of the results obtained for the spatial variation of the fault normal to average horizontal spectral acceleration ratio with the models presented in Somerville *et al.* (1997) are presented in Figure 5.66. The results obtained in the present study have some different features from the empirical study of Somerville *et al.* (1997). The simulation results indicate that the directivity affects a much larger zone and yields higher fault normal to average ratios in the near field. Furthermore, the contours resulting from this study are open ended, indicating that the changes in FN/Mean ratios are valid for large distances along the fault, whereas the Somerville *et al.* (1997) contours are closed at some distances from the fault. Since the Somerville *et al.* (1997) study, there has been a substantial increase in the near field strong motion data form earthquakes such as Kocaeli, 1999, Chi Chi, 1999 and Parkfiled 2004. In the M_w 6.0 Parkfield earthquake that can be cited as a moderate size event, the fault normal components of the Fault Zone array (Figure 3.1) were about twice of their horizontal counterparts. This suggests that the re-evaluation of previous empirical models model will probably yield higher ratios. Another reason for the differences in the ratios might be that in the low frequency range (less than 0.5 Hz) the simulation has a significant reliability when compared to empirical data that are very sensitive to the details of data processing and instrument characteristics in this frequency

range. Based on the NGA data also including recordings from the aforementioned recent earthquakes Campbell and Bozorgnia (2007) computed, the variation of strike-normal and strike-parallel horizontal components to their mean for oscillator periods ranging from 0.01 s to 10 s averaging them over all magnitudes and distances. Their results indicate maximum values of strike normal to geometric mean ratios of 1.7 to 6.9 for oscillator periods of 1.0 s to 10 s respectively. The authors emphasize the fact that source directivity effects become important especially at small distances, large magnitudes and long periods and that long-period fault normal spectral accelerations can be more than a factor of two higher than for a site located in the forward directivity region. But in any case herewith a comparison of the current results with new empirical data remains to be seen.

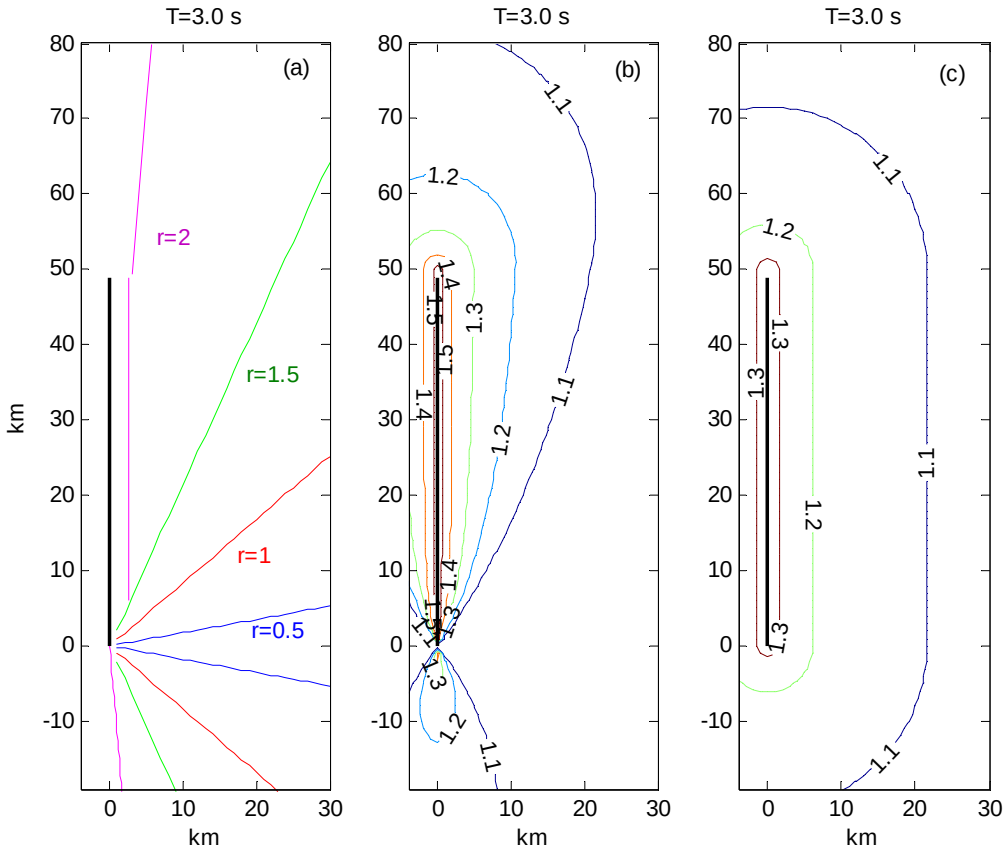

Figure 5.66. Spatial variation of the fault normal to average horizontal spectral acceleration ratio: (a) results obtained in this study, (b) empirical model developed by Somerville et al (1997) including $Xcos\theta$ dependence, (c) empirical model developed by Somerville et al (1997) excluding $Xcos\theta$ dependence. The black line represents the fault. The epicenter is located at the lower end of the fault.

5.3.2. Variation of the average horizontal spectral acceleration and displacement

To evaluate the variation of the average horizontal spectral acceleration in the near source region the simulated spectral accelerations and displacements have been compared with those obtained from empirical ground motion prediction equations. Three distinct zones are revealed from these comparisons. First in the region around the fault and close the hypocenter simulated and empirical average horizontal values are comparable and yield a zone of no directivity with a ratio = 1. Second zone is in the forward directivity region, where spectral accelerations obtained from simulations are clearly higher (in the order of 200 per cent to 400 per cent in the period range of 1.5 to 5 s) than those obtained from the ground motion prediction equations. And in case of unilateral ruptures the third zone is located in the backward directivity region where the simulated amplitudes are lower than the empirical values (in the order of 50 per cent to 20 per cent in the period range of 1.5 to 5 s). In the cases of Kobe 1995, Kocaeli 1999 and Tottori 2000 earthquakes where the epicenter is not located at one end of the rupture, but closer to its center, forward directivity effects are observed at both ends of the fault. These results indicate that in any case, for sites in the near source region if empirical ground motion prediction models are employed, they have to be adjusted for directivity effects.

One difficulty that we faced in obtaining the variation of the average horizontal spectral acceleration in the near source region was associated with the definition of average ground motion distribution without directivity effects. Somerville *et al.* (1997) use the median values obtained from the empirical prediction model of Abrahamson and Silva (1997) as average and the residuals as representative of directivity. Since we use simulated ground motion, several definitions of average can be used (such as median or a certain percentile of prediction equation of preference) resulting in up to 50 per cent variation of the ratios representing directivity. A more rational definition of average ground motion in different simulation cases would be a case specific estimation of the ground motion attenuation using an area including far field and than computing the ratios using the near field simulations versus this average model.

5.3.3. Magnitude Scaling of the Near Fault Directivity Pulse

The near source fault normal velocity pulses obtained from the simulation of eight strike-slip earthquakes have been plotted in Figure 5.67. The associated peak velocities and pulse durations are presented in Table 5.6.

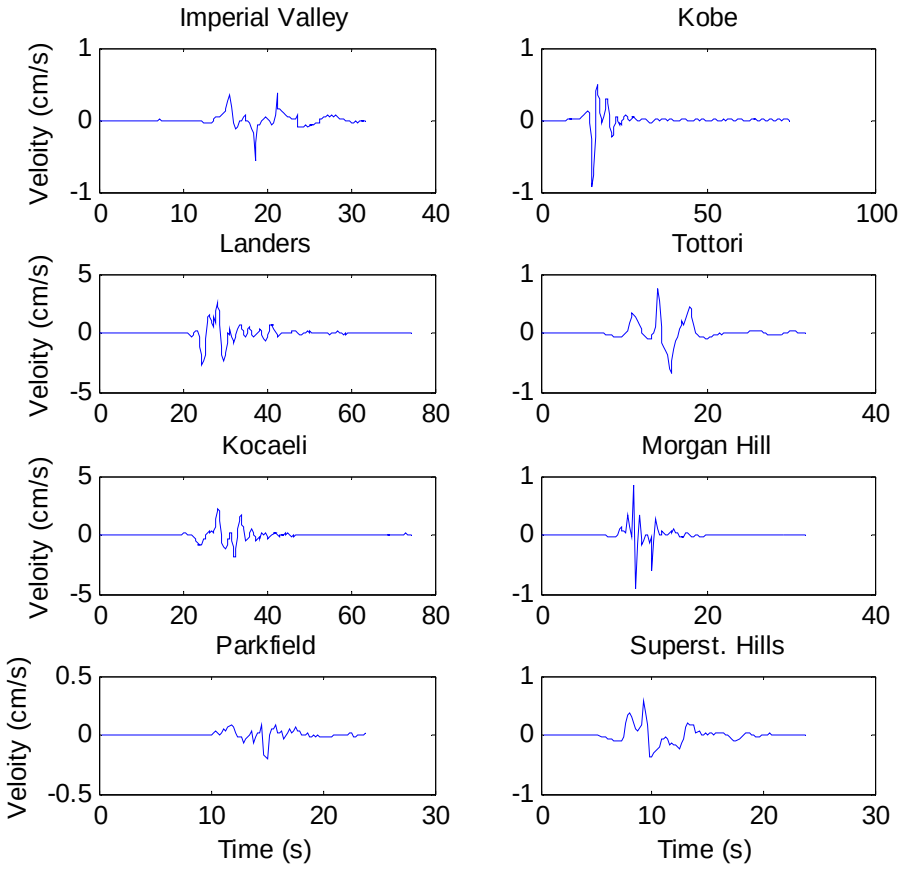

Figure 5.67. Near source fault normal velocity pulses obtained from the simulations of eight strike-slip earthquakes

Table 5.6. Width of the forward rupture directivity pulse

Earthqauke	Magnitude (M_w)	Peak velocity (m/s)	Width of the velocity pulse (s)
Imprerial Valley 1979	6.5	0.57	2.1
Morgan Hill 1984	6.3	0.93	0.7
Superstition Hillls 1987	6.5	0.57	2.8
Landers 1992	7.3	2.65	3.5
Kobe 1995	7.0	0.93	3.3
Kocaeli 1999	7.4	2.26	4.2
Tottori 2000	6.8	0.76	2.9
Parkfield 2004	6.0	0.2	1.1

The velocity pulse widths obtained in this study follow the same trend but plot a little higher than the relationship between the pulse period and magnitude proposed by Somerville (2003) (Figure 5.68). A relationship derived from the obtained results would have the following form:

$$\log_{10} T_{Dir} = 0.46 M_w - 2.75 \tag{5.1}$$

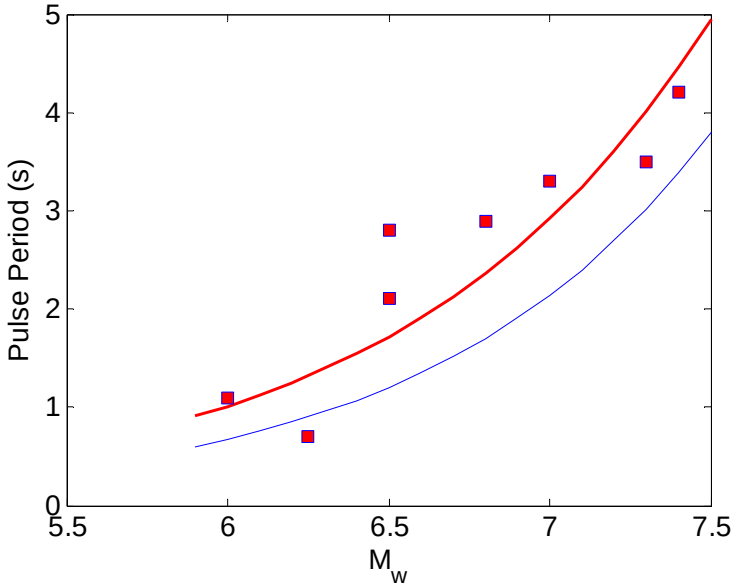

Figure 5.68. Width of the near source fault normal velocity pulses obtained in this study and the relationship suggested by Somerville (2003). The blue curve is the empirical relationship proposed by Somerville (2003). The red curve is based on the results of this study.

6. SUMMARY OF FINDINGS

This chapter will summarize the results associated with the simulation of strong ground motion with the finite difference method employed in this thesis and give perspectives for future work.

The tool used in the analytical studies covered in this thesis is the 3D Finite Difference kinematic simulation code initially developed by Olsen (1994) in its scalar version, subsequently revised by Madariaga *et al.* (1998) with the introduction of appropriate boundary conditions, rewritten and parallelized by Madariaga and Stoclet in 2002 – 2003 and modified by Frisenda and Madariaga in 2005 to perform variable slip finite source computations. Based on the staggered-grid finite-difference method developed by Madariaga (1976), the 3DFD code efficiently computes the wave propagation generated by finite ruptures in heterogeneous earth media.

The most important contribution of this thesis is that it single-handedly provides a systematic and comprehensive examination of deterministic earthquake simulation using finite differences at hand of a number of different events and from the view of a series of engineering problems. Specifically it presents a comparison of the 3DFD code with other simulation approaches using test cases designed to different levels of complexity; it reports on the effects of different source parameters, such as slip model, rise time, rupture velocity and the effect of crustal model on the distribution of ground motion. It also dwells on the use of finite differences in understanding earthquake engineering problems the most important ones being the spatial dependence of directivity, spectral accelerations and spectral displacements. Magnitude dependence of the duration of forward directivity pulse was also investigated.

Different aspects of the simulation code were elaborated in Chapter 2. To demonstrate the computational power of the FD3D code, a simple example was designed. A uniform strike slip rupture was modeled for three different velocity models; half-space, a horizontally layered earth structure and a three dimensional basin structure. The surface wave field for the homogenous model is very simple, with the typical fault parallel fling

and fault normal double pulses. The wave field for the layered model shows clear evidence of shock waves, the plane wave fronts emanating at an angle from the rupture front in the V_x and V_z components. These waves appear because the rupture propagates at depth with a higher rupture speed than the shear wave speed in the shallow layer. Hence it is very easy to mistakenly think that ruptures are super-shear when observing them on the surface. The apparent super-shear shock waves only appear in the shallow layer. When a 3-D earth-model that includes a basin is introduced, the wave-field on the surface is distorted with strong amplification along the basin. In the V_x and V_z components Rayleigh waves are generated inside the basin by the interaction between the rupture front and the 3D velocity structure. The complexity of these Rayleigh waves is neatly observed in cross-sections. In the seismograms located in the basin large ringing waves (surface waves) can clearly be seen. As shown by TeraShake simulations of the Los Angeles basin, these waves are the most important sources of strong ground motion at intermediate frequencies of the order a fraction of a Hertz. In the Marmara Sea basin, they have characteristic frequencies of about 3 s. Further work will be needed to exploit these interesting results.

The 3D Finite Difference code results were compared with the analytical method of Luco and Anderson (1983) and the Discrete Wavenumber Method for an extended source of Bouchon (2003) using the example provided in Anderson and Luco (1983, a and b) for strike-slip and dip-slip mechanisms. All three methods gave comparable results in the waveforms, amplitudes and durations of the ground motion. Some differences are however observed in amplitudes and waveforms. The reader is referred to Section 2.4 for further details.

In Chapter 3, a comprehensive simulation of the 2004 Parkfield earthquake is presented. By examining the 48 stations' recorded and simulated time histories we can conclude that the goodness of fit is very sensitive to the slip model used. S- wave radiation from the fault plane in the forward directivity region dominates the goodness of fit of the simulations as the fault normal components are more satisfactorily simulated than the fault parallel components in that region where the slip distribution from the entire rupture plane contributes to the ground motion. Fault parallel components are best simulated close to the epicentral region since in that region radiation from only one asperity dominates the ground motion. Simulation is generally less satisfactory in the immediate vicinity of the

fault where the fault-trapped waves dominate the ground motions. Simulation of the vertical components can be considered satisfactory given the fact that very low or even no weights were assigned to them during the inversion process. Improvement of the goodness of fit was achieved through modifications of various parameters such as slip model, source time function, rise time and crustal velocity structure. It should however be noted that the improvement is mostly achieved in the frequency range higher than 0.4 Hz.

A significant portion of this thesis is devoted to the investigation of spatial and frequency domain distribution of engineering ground motion parameters. Recent developments achieved in understanding of directivity phenomenon and associated parameters such as fault normal versus fault parallel ground motions, the duration of forward directivity pulse and methods to incorporate directivity effects in empirical ground motion prediction models are summarized in Chapter 4.

In Chapter 5, the phenomena covered in Chapter 4 are modeled. Two approaches have been used to model rupture directivity effects. First a parametric study was conducted to study the effects of various rupture parameters on the peak ground and spectral amplitudes generated by a uniform slip on a finite fault. Secondly, based on available slip models of recent earthquakes, simulations have been conducted to assess the directivity effects generated by more realistic source parameter distributions. Resulting spectral acceleration and displacement distributions at periods of 1.5 s, 2 s, 2.5 s, 3 s, 4 s and 5 s have been analyzed in terms of fault normal to geometric mean of the two horizontal components obtained from simulations as well as simulated over empirical average (based on empirical ground motion prediction equations without directivity) amplitudes to assess the near source effects based on magnitude, distance and period of vibration.

A simple form is proposed for the distribution of the spatial variation of the fault normal to average horizontal spectral acceleration ratio for strike-slip ruptures. The pattern is characterized with a narrow zone of ratio = 2 around the fault which widens beyond the fault extremities. A zone of ratio = 0.5 is observed in a region perpendicular to the fault and passing through the hypocenter is also observed. This behavior is empirically evidenced in the 2004 Parkfield earthquake recordings of the Goldhill array. This zone indicating larger fault parallel spectral amplitudes becomes narrower as the period of the

spectral accelerations increases. Almost a V-shape regions of ratio contours of 1 and 1.5 intersecting at the epicenter are visible in all simulations. For the dip-slip ruptures V-shaped zones of ratio =2 are observed at both ends of the fault in the slip direction. Again V-shaped zones of ratio =1.5 intersect at the epicenter. This implies that forward directivity conditions occur at both ends of the fault in the direction parallel to slip. Fault normal to mean acceleration ratios approaches to 1 in the direction perpendicular to slip. In contrast to the strike-slip case, the FN / Mean ratios never fall below 1.0, a finding that should also be checked against recorded data. A generalized shape of the FN / Mean ratios derived from these observations is presented. However the number of dip–slip simulations were not sufficient to derive any parametric form for the associated FN / Mean ratios.

By a better definition and modeling of average directivity included ground motion the spatial dependence of directivity can be more realistically incorporated in earthquake hazard assessments.

In the frequency range of interest of long period structures my results obtained from simple source models using uniform slip models and are equally satisfactory as those obtained from more elaborate models that involve a complex source. Therefore a systematic analysis of simple source models may yield reliable and realistic results in the evaluation of spatial distribution of parameters in the interest of earthquake engineering.

REFERENCES

Aagaard, B. T. and T. H. Heaton, 2004, "Near–Source Ground Motions from Simulations of Substained Intersonic and Supersonic Fault Ruptures", *Bulletin of Seismological Society of America*, Vol. 94, No. 6, pp. 2064–2078.

Abrahamson, N. A., 2000, "Effects of Rupture Directivity on Probabilistic Seismic Hazard Analysis", *Proceedings of the. Sixth International Conference on Seismic Zonation,* Palm Springs, CA. November 12-15, 2000.

Abrahamson, N.A. and W.J. Silva, 1997, "Empirical Response Spectral Attenuation Relations for Shallow Crustal Earthquakes", *Seismological Research Letters*, Vol. 68, No.1, pp. 94-127.

Aki, K., and P. G. Richards, 1980, *Quantitative Seismology: Theory and Methods*, W. H. Freeman, New York.

Akkar S and J.J. Bommer, 2007, "Prediction of Elastic Displacement Response Spectra in Europe and the Middle East", *Earthquake Engineering and Structural Dynamic,* Vol. 36, pp. 1275-1301.

Akkar S and J.J. Bommer, 2007b, "Empirical Prediction Equations for Peak Ground Velocity Derived from Strong-Motion Records from Europe and the Middle East", *Bulletin of the Seismological Society of America,* Vol. 97, No.2, pp. 511-530.

Alavi, B. and H. Krawinkler, 2000, "Design Considerations for Near-Fault Ground Motions, *Proceedings of the U.S. – Japan Workshop on the Effects of Near-Fault Earthquake Shaking*, San Francisco, March 20-21.

Anderson, J.G. and E. Luco, 1983a, "Parametric Study of Near-Field Ground Motions for a Strike-Slip Dislocation Model", *Bulletin of Seismological Society of America*, Vol. 73, No. 1, pp. 23-43.

Anderson, J.G. and E. Luco, 1983b, "Parametric Study of Near-Field Ground Motions for Oblique-Slip and Dip-Slip Dislocation Model", *Bulletin of Seismological Society of America*, Vol. 73, No. 1, pp. 45-57.

Andrews, D. J., 1976, "Rupture Propagation with Finite Stress in Antiplane Strain", *Journal of Geophysical Research*, Vol. 81, pp. 3575-3582.

Archuleta, R. J. and S. H. Hartzell, 1981, "Effects of Fault Finiteness on Near-Source Ground Motion", *Bulletin of Seismological Society of America,* Vol. 71, No. 2, pp. 939-957.

Archuleta, R.J., 1984 "A Faulting Model for the 1979 Imperial Valley Earthquake", *Journal of Geophysical Research*. Vol. 89, No. 6, pp. 4559-4585.

Beroza, G. C. and P. Spudich, 1988, "Linearized Inversion for Fault Rupture Behavior: Application to the 1984 Morgan Hill, California, Earthquake", *Journal of Geophysical Research*, Vol. 93, pp. 6275-6296.

Boore, D.M. and G M. Atkinson, 2006, "Boore- Atkinson NGA Emprical Ground Motion Model for the Average Horizontal component of PGA, PGV and SA at Spectral Periods of 0.1, 0.2, 1.0, and 3 seconds", Interim Report for USGS Review.

Bouchon, M., 2003, "A Review of the Discrete Wavenumber Method", *Pure and Applied Geophysics*, Vol. 160, pp. 445-465.

Bouchon, M. and K. Aki, 1977, "Discrete Wave-Number Representation of Seismic-Source Wave Fields", *Bulletin of Seismological Society of America*, Vol. 67, No. 2, pp. 259-277.

Borcherdt, R.D., M.J. S. Johnston, G. Glassmoyer, and C. Dietel, 2006, "Recordings of the 2004 Parkfield Earthquake on the General Earthquake Observation System Array: Implications for Earthquake Precursors, Fault Rupture, and Coseismic Strain Changes" *Bulletin of Seismological Society of America,* Vol. 96, No. 4B, pp. S73-S89.

Brocher, T. M., 2005, "Empirical Relations between Elastic Wavespeeds and Density in the Earth's Crust", *Bulletin of Seismological Society of America*, Vol. 95, No. 6, pp. 2081-2092.

Brune, J. N., 1970, "Tectonic Stress and the Spectra of Seismic Shear Waves from Earthquakes", *Journal of Geophysical Research*, Vol. 75, No. 26, pp. 4997-5009.

Burridge, R. and L. Knopoff, 1964, "Body Force Equivalents for Seismic Dislocations", *Bulletin of Seismological Society of America*, Vol. 54, No. 6A, pp. 1875-1888.

Campbell, K. W. and Y. Bozorgnia, 2006, "Campbell- Bozorgnia NGA Empirical Ground Motion Model for the Average Horizontal Component of PGA, PGV and SA at selected Spectral Periods Ranging from 0.01-10.0 seconds", Interim Report for USGS Review.

Campbell, K. W. and Y. Bozorgnia, 2007, "Campbell- Bozorgnia NGA Ground Motion Relations for the Geometric Mean Horizontal Component of Peak and Spectral Ground Motion Parameters", Pacific Earthquake Engineering Research Center Report for USGS.

Chiou, B. S. J. and R. R. Youngs, 2006, "Chiou and Youngs PEER-NGA Emprical Ground Motion Model for the Average Horizontal Component of Peak Acceleration

and Pseudo- Spectral acceleration for Spectral Periods of 0.01 to 10 seconds ” Interim Report for USGS Review.

Cornell, A., 1968, “Engineering Seismic Risk Analysis”, *Bulletin of Seismological Society of Americ*a, Vol. 58, No. 5, pp. 1583-1606.

Courant, R., K. Friedrichs and H. Lewy, 1928, “Über die partiellen Differenzengleichungen der mathematischen Physik”, *Mathematische Annalen*, Vol. 100, No. 1, pp. 32–74.

Das, S., and K. Aki , 1977, “A Numerical Study of Two-Dimensional Spontaneous Rupture Propagation”, *Geophysical Journal of the Royal Astronomical Society*, Vol. 50, pp. 643–668.

Durukal, E., A. S. Gunduz, B. Sanli, M. Sorensen, S. Richwalski, K. Sesetyan, K Atakan, R. Madariaga, R. A. Wang, 2006, ‘Benchmarking’ Exercise On The Performance Of Kinematic Ground Motion Simulation Codes, *European Geosciences Union General Assembly 2006, Vienna, Austria, 3-7 April 2006* , CD Volume Of Abstracts, EGU06-A-10043; Poster-0349.

Eberhart-Phillips, D., and A. J. Michael, 1993, “Three-Dimensional Velocity Structure, Seismicity and Fault Structure in the Parkfield Region, Central California”, *Journal of Geophysical Research,* Vol. 8, pp. 15737-15758.

Erdik M. and E. Durukal, 2002, “Simulation Modelling of Strong Ground Motion”, in *Earthquake Engineering Handbook*, W-F. Chen and C. Scawthorn, editors, CRC Press.

Gutenberg, B. and C. F. Richter, 1944, “Frequency of Earthquakes in California”, *Bulletin of Seismological Society of Americ*a, Vol. 34, No. 1, pp. 185-188.

Hartzell, S., C. Langer, and C. Mendoza, 1994, "Rupture Histories of Eastern North American Earthquakes", *Bulletin of the Seismological Society of America*, Vol. 85 No. 6, pp. 1703-1724.

Hartzell, S., P. Liu, and C. Mendoza, 1996, "The 1994 Northridge, California, Earthquake; Investigation of Rupture Velocity, Risetime, and High-Frequency Radiation", *Journal of Geophysical Research, B, Solid Earth and Planets,* Vol. 101, No. 9, pp. 20091-20108.

Hartzell, S.H., and C. Mendoza, 1991, "Application of an Iterative Least-Squares Waveform Inversion of Strong Motion and Teleseismic Records to the 1978 Tabas, Iran, earthquake", *Bulletin of Seismological Society of America*, Vol. 81, No.2, pp. 305-331.

Haskell, N.A., 1964, "Total Energy and Energy Spectral Density of Elastic Wave Radiation from Propagating Faults", *Bulletin of Seismological Society of America,* Vol. 54, No. 6, pp. 1811-1841.

Ji, C., 2004,. "Slip History, the 2004 (M_w 5.9) Parkfield Earthquake (Single- Plane Model), www.gps.caltech.edu/ jichen/parkfield/parkfield.htm/ (last accessed July 2006).

Ji, C., K. Choi, K. M. Larson, N. King and K. W. Hudnut, 2005, "Co-seismic slip history of the 2004 Parkfield , California earthquake" http://neic.usgs.gov/neis/eq_depot/2004/eq_041226/neic_slav_ff.html.

Kostrov, B. and S. Das, 1989, *Principles of Earthquake Source Mechanics,* Cambridge University Press, New York.

Kramer, S., 1996, *Geotechnical Earthquake Engineering,* International series in Civil Engineering and Engineering Mechanics, Prentice-Hall, New Jersey.

Levander, A. R., 1988, "Fourth-Order Finite-Difference P-SV Seismograms", *Geophysics* Vol. 53, No. 11, pp. 1425–1436.

Liu, P. S. Custodio and R. J. Archuleta, 2006, "Kinematic Inversion of the 2004 M_w 6.0 Parkfield Earthquake Including an Approximation to Site Effects", *Bulletin of Seismological Society of America*, Vol. 96, No. 4b, pp. S143-S158.

Luco, E. and J. G. Anderson, 1983, "Steady-State Response of an Elastic Half-Space to a Moving Dislocation of Finite Width", *Bulletin of Seismological Society of America*, Vol. 73, No. 1, pp. 1-22.

Madariaga, R., 1976, "Dynamics of an Expending Circular Fault", *Bulletin of Seismological Society of America,* Vol. 66, No. 3, pp. 639-666.

Madariaga, R., 1978, "The Dynamic Field of Haskell's Rectangular Dislocation Fault Model", *Bulletin of Seismological Society of America*, Vol. 68, No. 4, pp. 869-887.

Madariaga, R. and K. B. Olsen, 2002, "Earthquake Dynamics" in *International Handbook of Earthquake Engineering and Seismology,* Part A, 81 A, part 12, Editors W. Lee, H. Kanamori, P. Jennings and C. Kisslinger, Elsevier Science Ltd. , USA.

Madariaga, R., K. B. Olsen and R. Archuleta, 1998, "Modeling Dynamic Rupture in a 3D Earthquake Fault Model", *Bulletin of Seismological Society of America*, Vol. 88, No. 5, pp. 1182-1197.

McJunkin, R. D., and A. F. Shakal, 1983, "The Parkfield Strong-Motion Array, California" *Geology*, Vol. 36, pp. 27-34.

Mikumo, T. and T. Miyatake, 1979, "Earthquake Sequences on a Frictional Fault Model with Non-Uniform Strength and Relaxation Times", *Geophysical Journal of the Royal Astronomical Society*, Vol. 59, pp. 497-522.

Mindevalli O. Y.and B. J. Mitchell, 1989, "Crustal Structure and Possible Anisotropy in Turkey from Seismic Surface Wave Dispersion", *Geophysical Journal International,* Vol. 98, pp. 93–106.

Miyatake, T., 1980, "Numerical Simulations of Earthquake Source Process by a Three-Dimensional Crack Model. Part I. Rupture Process" *Journal of the Physics of the Earth,* Vol. 28, pp. 565-598.

NEHRP, 1997, "Recommended Provisions for Seismic Regulations for New Buildings and Other Structures, FEMA-303", Prepared by the Building Seismic Safety Council for the Federal Emergency Management Agency, Washington, DC.

Olsen K. B., R. Madariaga and R. Archuleta, 1997, "Three-Dimensioanal Dynamic Simulation of the 1992 Landers Earthquake" *Scienc*e Vol. 278, pp. 834-838.

Olsen, K. B, 1994, *Simulation of Three-Dimensional Wave Propagation in the Salt Lake Basin*, PhD thesis, University of Utah, Salt Lake City.

Olsen, K. B., 2000, "Site Amplification in the Los Angeles Basin from 3D Modeling of Ground Motion" *Bulletin of Seismological Society of America*, Vol. 90, No. 1, pp. S77-S94.

Olsen, K. B. and R. J. Archuleta, 1996, "Three-Dimensional Simulation of Earthquakes on the Los Angeles Fault System", *Bulletin of Seismological Society of America.,* Vol. 86, pp. 575-596.

Olsen, K. B., R. J. Archuleta and J. R. Matarese, 1995," Three-Dimensional Simulation of a Magnitude 7.75 Earthquake on the San Andreas Fault", *Science*, Vol. 270, pp. 1628-1632.

Olsen, K. B., S. M. Day, J. B. Minster, Y. Cui, A. Chourasia, M. Faerman, R. Moore, P. Maechling, and T. Jordan, 2006, "Strong Shaking in Los Angeles Expected from Southern San Andreas Earthquake", *Geophysical Research Letters*, Vol. 33, Citation no. L07305, 2006; doi. 10.1029/2005GL025472

Pitarka, A. and K. Irikura, 1996, "Modeling 3-D Surface Topography by Finite-Difference Method: the Kobe JMA Station Site Case Study", *Geophysical Research Letters*, Vol. 23, pp. 2723-2732.

Rodriguez-Marek, A., 2000, *Near fault seismic site response*, Ph.D. Thesis, Civil Engineering, University of California, Berkeley.

Scholtz C., 1989, *The Mechanics of Earthquake and Faulting*, Cambridge U Press, New York.

Sekiguchi, H., K. Irikura, T. Iwata, Y. Kakehi, and M. Hoshiba, 1996, "Minute Locating of Faulting beneath Kobe and the Waveform Inversion of the Source Process During the 1995 Hyogo-ken Nanbu, Japan, Earthquake Using Strong Ground Motion Records", *Journal of Physics of the Earth*, Vol. 44, No. 5, pp. 473-487.

Shakal, A., V. Graizer, M. Huang, R. Borcherdt, H. Haddadi, K. Lin, C. Stephens, and P. Roffers, 2005, "Preliminary Analysis of Strong-motion Recordings from the 28 September 2004 Parkfield, California Earthquake", *Seismological Research Letters*, Vol. 76, No. 1, pp. 27-39.

Shakal, A., H. Haddadi, V. Graizer, K. Lin, and M. Huang, 2006, "Some Key Features of the Strong-Motion Data from the M_w 6.0 Parkfield, California, Earthquake of 28

September 2004", *Bulletin of Seismological Society of America,* Vol. 96, No. 4b, pp. S90-S118.

Somerville, P. G., 1998, "Development of an Improved Ground Motion Representation for Near Fault Ground Motions", SMIP 98, Seminar on Utilization of Strong Motion Data, Oakland, CA.

Somerville, P. G., 2003, "Characterizing Near-Fault Ground motions for the Design and Evaluation of Bridges", *Report to the Pacific Earthquake Engineering Research Center (PEER,* http://www.peertestbeds.net/ucs.htm.

Somerville, P. G., N. F. Smith, R. W. Graves, and N. A. Abrahamson, 1997, "Modification of Empirical Strong Ground Motion Attenuation Relations to Include the Amplitude and Duration Effects of Rupture Directivity", *Seismological Research Letters*, Vol. 68, No. 1, pp. 199-222.

Stewart, J., S. Chiou, J. Bray, R. Graves, P. Somerville, and N. Abrahamson, 2001, "Ground Motion Evaluation Procedures for Performance-Based Design", *PEER Report 2001/09, Pacific Earthquake Engineering Research Center*, College of Engineering, University of California, Berkeley.

Thurber, C., H. Zhang, F. Waldhauser, J. Hardebeck, A. Michaels, and D. Eberhart-Phillips, 2006. "Three-Dimensional Compressional Wavespeed Model, Earthquake Relocations, and Focal Mechanisms for the Parkfield, California Region", *Bulletin of Seismological Society of America,* Vol. 96, No. 4B, pp. S38-S49.

Thurber, C., S. Roecker, K. Roberts, M. Gold, L. Powell, and K. Rittger, 2003, "Earthquake Locations and Three-Dimensional Fault Zone Structure along the Creeping Section of the San Andreas Fault near Parkfield, CA: Preparing for SAFOD", *Geophysical Research Letters*, Vol. 30, No. 3, 10.1029/2002GL016004.

UBC, 1997, *Uniform Building Code*, International Code Council, USA.

Virieux, J., 1986, "P-SV Wave-Propagation in Heterogeneous Media: Velocity-Stress Finite-Difference Method", *Geophysics*, Vol. 51, pp. 889-901.

Virieux, J. and R. Madariaga, 1982, "Dynamic Faulting Studied by a Finite Difference Method", *Bulletin of Seismological Society of Americ*a, Vol. 72, No. 2, pp. 345-369.

Wald, D.J., D.V. Helmberger, and S.H. Hartzell, 1990, "Rupture Process of the 1987 Superstition Hills Earthquake from the Inversion of Strong-Motion Data", *Bulletin of Seismological Society of Americ*a, Vol. 80, No. 5, pp. 1079-1098.

Wells, D. and K. Coppersmith, 1994, "New Empirical Relationships among Magnitude, Rupture Length, Rupture Width, Rupture Area and Surface Displacement", *Bulletin of Seismological Society of Americ*a, Vol. 84 No. 4, pp. 974-1002.

Yagi, Y. and M. Kikuchi, 2000, "Source Rupture Process of the Kocaeli, Turkey, Earthquake of August 17, 1999, Obtained by Joint Inversion of Near-Field Data and Teleseismic Data" , *Geophysical Research Letters*, Vol. 27, pp. 1969-1972.

Zeng, Y. H., and J. G. Anderson, 2000, "Evaluation of Numerical Procedures for Simulating Near-Fault Long-Period Ground Motions using Zeng Method", Report No. 2000/01, Pacific Earthquake Engineering Research Center.

Zhang, H., and C. H. Thurber, 2003, "Double-Difference Tomography: the Method and its Application to the Hayward fault, California", *Bulletin of Seismological Society of Americ*a, Vol. 93, No. 5, pp. 1875-1889.

APPENDIX A: PROGRAM INPUT FILES FOR SELECTED MODELS

A1. Input files for the models presented in Section 2.2

- **Input files for the homogeneous earth structure case**

Input.dat

```
 4000 NT      = # of timesteps
  261 nx      = number of steps in x direction
  201 ny      = number of steps in y direction
   80 nz      = number of steps in z direction
 250 DH       = spatial step (meters)
0.01 DT       = time step (seconds)
  90. STR     = strike of fault
  90. DIP     = dip of fault
   0. RAKE        = rake of fault
 1.0 SLIP     = slip of fault
  70 NXSC     = x nodal position for point source
  76 NYSC     = y nodal position for point source
  38 NZSC     = z nodal position for point source
  79 NDEPTH       = depth at which we plot snapshots
  71 IXPOS       = position of the vertical cross section along y
                 (nxsc)
  77 IYPOS       = position of the vertical cross section along x
                 (nysc)
   1 NBGX          = first x node to contain surface receivers
 261 NEDX          = last x node to contain surface receivers
   1 NSKPX         = skip of nodes containing x receivers
   1 NBGY          = first y node to contain surface receivers
 201 NEDY          = last y node to contain surface receivers
   1 NSKPY         = skip of nodes containing y receivers
   1 NBGZ          = first y node to contain surface receivers
  80 NEDZ          = last y node to contain surface receivers
   1 NSKPZ         = skip of nodes containing y receivers
  50 NTISKP   = time skip of seismograms
  35 NDAMP         = size of nodal region for exp damping
   0 IFRE          = =0 flat, <>0 irregular free surface
   0 NSV         = =0 no checkpt, >0 checkpt every nsv step
  2   nholes    = # of stations
  205, 110         = x and y coordinates of the first station
  220, 60          = x and y coordinates of the second station
```

asper2 : Input file to generate the source

```
2900              = rupture velocity (m/s)
250           = spatial step (m)
0.01              = time step (s)
1500              = number of time steps to generate the source
30000         = fault length (m)
10000         = fault width (m)
15000             = x position of the hypocenter (m), not considered
                for the Haskell type source
5000              = y position of the hypocenter (m), not considered
                for the Haskell type source
```

```
0.30             = sigma of the source time function
1.3500000e+000   = slip
```

Makemodel.run

```
#!/bin/bash

../src/mkmodel <<ENS > mkmodel.out
261 201 80       = dimensions of the simulation grid
6800 3900 3300       = Vp (m/s), Vs (m/s), density (kg/m3)

ENS

echo fin
```

This program creates the binary file *structure.dat* read by FD3D.

- **Input files for the horizontally layered earth structure case**

Input.dat and *asper2* are the same as the previous model.

Makemodel.run

```
#!/bin/bash

../src/mkmodel <<ENS > mkmodel.out
261 201 80       = dimensions of the simulation grid
6800 3900 3300       = Vp (m/s), Vs (m/s), density (kg/m3) of the
                   halfspace
2                = Number of layers
5800 3400 2700 64 12 = Vp (m/s), Vs (m/s), density (kg/m3),
                        z coordinate from bottom of the lowest layer
                        in grid spacing (dh) units, thickness of the
                        layer in grid spacing (dh) units
3500 2200 2000 76 4     = the same as the previous line for the
                        second layer

ENS

echo fin
```

- **Input files for the 3D earth structure case**

Input.dat and *asper2* are the same as the previous model.

The binary file *structure.dat* is created in 3D outside the program.

A2. Input files for the models presented in Sections 2.4 and 5.1

- **Input files for the base case (case 1b)**

The model being created in the previous version of the program FD3D, the input files are slightly different and higher in number.

mpi_input.dat

```
680      = number of nodes in x direction
440      = number of nodes in y direction
160      = number of nodes in z direction
1        = number of processors in x direction
1        = number of processors in y direction
4        = number of processors in z direction
```

input.dat

```
8000 NT               = # of timesteps
 250 DH               = spatial step (meters)
0.008 DT              = time step (seconds)
0.2 DOMP              = dominant period of source (in sec)
159   NDEPTH          = depth at which we plot snapshots
  1 NBGX              = first x node to contain surface receivers
680  NEDX             = last x node to contain surface receivers
  1 NSKPX            = skip of nodes containing x receivers
  1 NBGY             = first y node to contain surface receivers
440 NEDY             = last y node to contain surface receivers
  1 NSKPY            = skip of nodes containing y receivers
  1 NBGZ             = first y node to contain surface receivers
160 NEDZ             = last y node to contain surface receivers
  1 NSKPZ            = skip of nodes containing y receivers
 50 NTISKP           = time skip of seismograms
 35 NDAMP            = size of nodal region for exp damping
  0 IFRE             = =0 flat, <>0 irregular free surface
  0 NSV              = =0 no checkpt, >0 checkpt every nsv step
 45 nholes           = # of stations
 40, 124          = x and y coordinates of first station
 .....            = x and y coordinates of the following stations
```

crack.dat

```
 90. STR           = strike of fault
 90. DIP           = dip of fault
180. RAKE          = rake of fault
1.0 SLIP           = slip of fault (not used, slip is read from the
                     file asper2)
260 NXSC           = x nodal position for point source
120 NYSC           = y nodal position for point source
 76 NZSC           = z nodal position for point source
```

asper2 : Input file to generate the source

```
3000            = rupture velocity (m/s)
250          = spatial step (m)
0.008        = time step (s)
```

```
3800            = number of time steps to generate the source
40000       = fault length (m)
20000       = fault width (m)
500             = x position of the hypocenter (m)
500             = y position of the hypocenter (m)
0.25            = sigma of the source time function
1.5000000e+000  = slip
```

make_model.run

```
#!/bin/bash

../src/mkmodel <<ENS > mkmodel.out
680 440 160
8000 4600 3340
4
6200 3600 2800 32 60
5800 3400 2700 92 52
3500 2200 2000 144 14
1700 1000 1700 158 2

ENS

echo fin
```

APPENDIX B: EMPIRICAL GROUND MOTION PREDICTION EQUATIONS

B1. Boore and Atkinson (2006) Model

Boore and Atkinson (2006) model presents ground motion prediction equations for a particular measure of the horizontal-component as a function of earthquake mechanism, distance from source to site, local average shear-wave velocity, and fault type. Equations derived by empirical regression of the PEER NGA strong motion database are presented for peak ground acceleration (PGA), peak ground velocity (PGV), and 5 per cent-damped pseudo-absolute-acceleration spectra (PSA) at periods between 0.01 s and 10 s. 1574 records from 58 mainshocks in the distance range from 0 km to 400 km are used in the analysis. The number of available data decreased as period increased.

The equation for predicting ground motions is presented as follows:

$$In(Y) = F_M(M) + F_D(R_{JB} + M) + F_S(V_{S30}, R_{JB}, M) + \varepsilon\sigma_T \qquad \text{(B1.1)}$$

In this equation Y is the ground motion parameter to be predicted., F_M, F_D and F_S represent the magnitude scaling, distance function and site amplification, respectively. M is moment magnitude, R_{JB} is the Joyner-Boore distance (defined as the closest distance to the surface projection of the fault, which is approximately equal to the epicentral distance for events of **M**<6), and V_{S30} is the time-averaged shear-wave velocity over the top 30 m of the site. The predictive variables are M, R_{JB} , and V_{S30} ;

The distance function is given by:

$$F_D(R_{JB}, M) = \left[c_1 + c_2(M - M_{ref})\right]\ln\left(R/R_{ref}\right) + c_3(R - R_{ref}) \qquad \text{(B1.2)}$$

where

$$R = \sqrt{R_{JB}^2 + h^2} \qquad \text{(B1.3)}$$

and c_1, c_2, c_3, M_{ref}, R_{ref}, and h are the coefficients to be determined in the analysis.

The magnitude scaling is given by

(a) $M \le M_h$

$$F_M(M) = e_1 U + e_2 SS + e_3 NS + e_4 RS + e_5 (M - M_h) + e_6 (M - M_h)^2 \qquad \text{(B1.4)}$$

(b) $M > M_h$

$$F_M(M) = e_1 U + e_2 SS + e_3 NS + e_4 RS + e_7 (M - M_h) \qquad \text{(B1.5)}$$

where *U, SS, NS* and *RS* are dummy variables used to specify the fault type as given in Table B.1 (unspecified, strike-slip, normal- slip, and reverse-slip, respectively), and M_h is the "hinge magnitude" for the shape of the magnitude scaling.

Table B.1. Values of dummy variables for different fault types.

Fault Type	U	SS	NS	RS
unspecified	1	0	0	0
Strike-slip	0	1	0	0
normal	0	0	1	0
thrust/reverse	0	0	0	1

The site function is given by:

$$F_S = F_{LIN} + F_{NL} \qquad \text{(B1.6)}$$

where F_{LIN} and F_{NL} are the linear and nonlinear terms, respectively. Note that for the reference velocity of 760 m/s, 0 $F_{LIN} = F_{NL} = F_S = 0$. Thus the soil amplifications are specified relative to motions that would be recorded on a B/C boundary site conditions.

The regression coefficients are tabulated in Table B.2 through Table B.4 for various structural periods. 5 per cent damped acceleration response spectra obtained for $M_w = 6.0$ and rock site conditions at various source distances are presented in Figure B. 1.

Table B.2. Regression coefficients for the BA06 model

Period (s)	c1	c2	c3	H	Mref	Rref
PGV	-0.8737	0.1006	-0.00334	2.54	4.5	1
PGA	-0.6605	0.1197	-0.01151	1.35	4.5	1
0.01	-0.6622	0.12	-0.01151	1.35	4.5	1
0.02	-0.666	0.1228	-0.01151	1.35	4.5	1
0.03	-0.6901	0.1283	-0.01151	1.35	4.5	1
0.05	-0.717	0.1317	-0.01151	1.35	4.5	1
0.075	-0.7205	0.1237	-0.01151	1.55	4.5	1
0.1	-0.7081	0.1117	-0.01151	1.68	4.5	1
0.15	-0.6961	0.09884	-0.01113	1.86	4.5	1
0.2	-0.583	0.04273	-0.00952	1.98	4.5	1
0.25	-0.5726	0.02977	-0.00837	2.07	4.5	1
0.3	-0.5543	0.01955	-0.0075	2.14	4.5	1
0.4	-0.6443	0.04394	-0.00626	2.24	4.5	1
0.5	-0.6914	0.0608	-0.0054	2.32	4.5	1
0.75	-0.7408	0.07518	-0.00409	2.46	4.5	1
1	-0.8183	0.1027	-0.00334	2.54	4.5	1
1.5	-0.8303	0.09793	-0.00255	2.66	4.5	1
2	-0.8285	0.09432	-0.00217	2.73	4.5	1
3	-0.7844	0.07282	-0.00191	2.83	4.5	1
4	-0.6854	0.03758	-0.00191	2.89	4.5	1
5	-0.5096	-0.02391	-0.00191	2.93	4.5	1
7.5	-0.3724	-0.06568	-0.00191	3	4.5	1
10	-0.09824	-0.138	-0.00191	3.04	4.5	1

Table B.3. Regression coefficients for the BA06 model (cont.)

Period (s)	e1	e2	e3	e4	e5	e6	e7	Mh
PGV	5.00121	5.04727	4.63188	5.0821	0.18322	-0.12736	0	8.5
PGA	-0.53804	-0.5035	-0.75472	-0.5097	0.28805	-0.10164	0	6.75
0.01	-0.52883	-0.49429	-0.74551	-0.49966	0.28897	-0.10019	0	6.75
0.02	-0.52192	-0.48508	-0.73906	-0.48895	0.25144	-0.11006	0	6.75
0.03	-0.45285	-0.41831	-0.66722	-0.42229	0.17976	-0.12858	0	6.75
0.05	-0.28476	-0.25022	-0.48462	-0.26092	0.06369	-0.15752	0	6.75
0.075	0.00767	0.04912	-0.20578	0.02706	0.0117	-0.17051	0	6.75
0.1	0.20109	0.23102	0.03058	0.22193	0.04697	-0.15948	0	6.75
0.15	0.46128	0.48661	0.30185	0.49328	0.1799	-0.14539	0	6.75
0.2	0.5718	0.59253	0.4086	0.61472	0.52729	-0.12964	0.00102	6.75
0.25	0.51884	0.53496	0.3388	0.57747	0.6088	-0.13843	0.08607	6.75
0.3	0.43825	0.44516	0.25356	0.5199	0.64472	-0.15694	0.10601	6.75
0.4	0.3922	0.40602	0.21398	0.4608	0.7861	-0.07843	0.02262	6.75
0.5	0.18957	0.19878	0.00967	0.26337	0.76837	-0.09054	0	6.75
0.75	-0.21338	-0.19496	-0.49176	-0.10813	0.75179	-0.14053	0.10302	6.75
1	-0.46896	-0.43443	-0.78465	-0.3933	0.6788	-0.18257	0.05393	6.75
1.5	-0.86271	-0.79593	-1.20902	-0.88085	0.70689	-0.2595	0.19082	6.75
2	-1.22652	-1.15514	-1.57697	-1.27669	0.77989	-0.29657	0.29888	6.75
3	-1.82979	-1.7469	-2.22584	-1.91814	0.77966	-0.45384	0.67466	6.75
4	-2.24656	-2.15906	-2.58228	-2.38168	1.24961	-0.35874	0.79508	6.75
5	-1.28408	-1.2127	-1.50904	-1.41093	0.14271	-0.39006	0	8.5
7.5	-1.43145	-1.31632	-1.81022	-1.59217	0.52407	-0.37578	0	8.5
10	-2.15446	-2.16137	0	-2.14635	0.40387	-0.48492	0	8.5

Table B.4. Standard deviations

Period (s)	σ	τ_u	$\sigma_{\tau U}$	τ_M	$\sigma_{\tau M}$
PGV	0.5	0.286	0.576	0.256	0.56
PGA	0.502	0.265	0.566	0.26	0.564
0.01	0.502	0.267	0.569	0.262	0.566
0.02	0.502	0.267	0.569	0.262	0.566
0.03	0.507	0.276	0.578	0.274	0.576
0.05	0.516	0.286	0.589	0.286	0.589
0.075	0.513	0.322	0.606	0.32	0.606
0.1	0.52	0.313	0.608	0.318	0.608
0.15	0.518	0.288	0.592	0.29	0.594
0.2	0.523	0.283	0.596	0.288	0.596
0.25	0.527	0.267	0.592	0.267	0.592
0.3	0.546	0.272	0.608	0.269	0.608
0.4	0.541	0.267	0.603	0.267	0.603
0.5	0.555	0.265	0.615	0.265	0.615
0.75	0.571	0.311	0.649	0.299	0.645
1	0.573	0.318	0.654	0.302	0.647
1.5	0.566	0.382	0.684	0.373	0.679
2	0.58	0.398	0.702	0.389	0.7
3	0.566	0.41	0.7	0.401	0.695
4	0.583	0.394	0.702	0.385	0.698
5	0.601	0.414	0.73	0.437	0.744
7.5	0.626	0.465	0.781	0.477	0.787
10	0.645	0.355	0.735	0.477	0.801

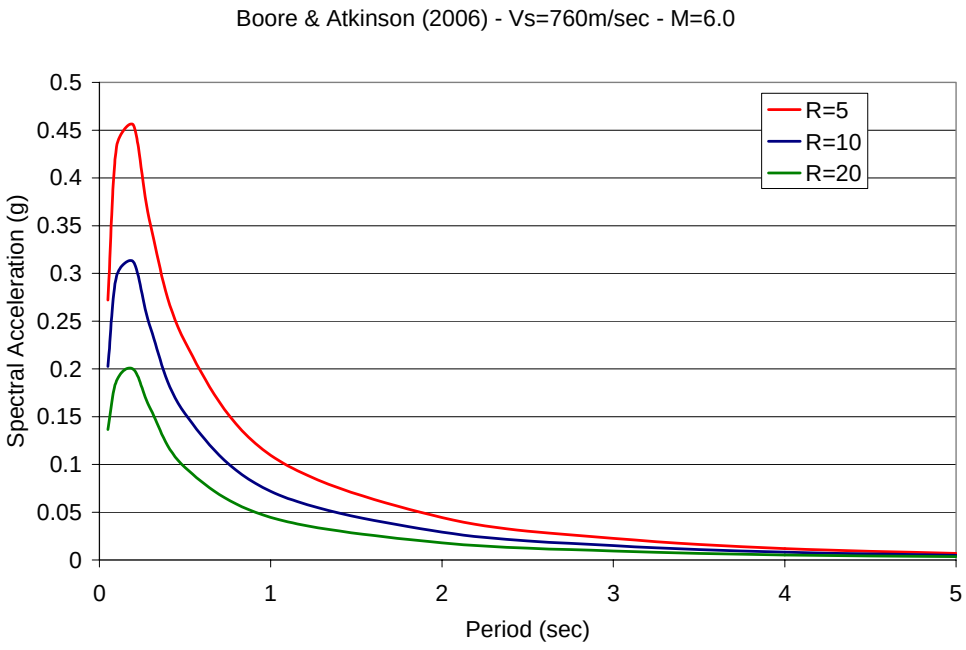

Figure B. 1. Median 5 per cent damped acceleration response spectra obtained from Boore and Atkinson (2006) model for an M_w = 6.0 earthquake.

B2. Akkar and Bommer (2007) Model

Displacement-based seismic design and assessment of structures require the reliable definition of displacement spectra for a wide range of periods and damping levels. Akkar and Bommer (2007) have developed attenuation relationships for spectral displacement, to predict displacement response ordinates for damping rations of 2, 5, 10, 20 and 30 per cent of the critical damping and for response periods up to 4 s.

The equations can be applied to predict the geometric mean displacement and pseudo-acceleration spectra for earthquakes with moment magnitudes (**M**) between 5 and 7.6, and for distances up to 100 km. The functional form selected for the equation is the same as that used by Akkar and Bommer (2007b) for the prediction of PGV. The equation that predicts the geometric mean of spectral displacement has the following form:

$$\log\left[SD(T,\xi)\right] = b_1 + b_2 M + b_3 M^2 + (b_4 + b_5 M)\log\sqrt{R_{jb}^2 + b_6^2} + b_7 S_S + b_8 S_A + b_9 F_N + b_{10} F_R \quad \text{(B2.1)}$$

where M is moment magnitude, R_{JB} is the Joyner-Boore distance in kilometers, S_S and S_A are binary variables taking values of 1 for soft and stiff soil sites, respectively (and zero otherwise), and F_N and F_R are similarly derived for normal and reverse faulting earthquakes. The coefficients b_1-b_{10} were estimated using a maximum likelihood one stage regression, as described in Akkar and Bommer (2007b).

The regression coefficients for the periods of 1.5, 2.0, 2.5, 3.0 and 4.0 s for 5 per cent damped displacement response spectra used in this study are tabulated in Table B.5 and Table B.6, respectively. 5 per cent damped displacement response spectra obtained for M_w = 6.0 and rock site conditions at various source distances are presented in Figure B. 2.

Table B.5. Regression coefficients b_1–b_{10} for 5 per cent-damped spectral ordinates

Period	b1	b2	b3	b4	b5	B6	b7	b8	b9	b10
1.5	−6.724	2.205	−0.143	−1.857	0.146	5.189	0.373	0.164	0.011	0.041
2	−8.352	2.693	−0.175	−1.617	0.101	6.274	0.327	0.146	−0.008	0.01
2.5	−8.903	2.871	−0.190	−1.622	0.116	5.16	0.298	0.119	−0.026	−0.009
3	−7.899	2.496	−0.158	−1.584	0.125	3.528	0.268	0.089	−0.025	−0.021
4	−10.965	3.303	−0.209	−1.279	0.091	2.694	0.244	0.054	0.039	−0.084

Table B.6. Standard deviation (σ_1 and σ_2 denote the intra- and inter-event standard deviations, respectively).

Period	σ1	σ2
1.5	0.936-0.107M	0.427-0.049M
2	0.723-0.073M	0.398-0.040M
2.5	0.817-0.088M	0.462-0.050M
3	0.877-0.096M	0.481-0.052M
4	1.464-0.179M	0.768-0.094M

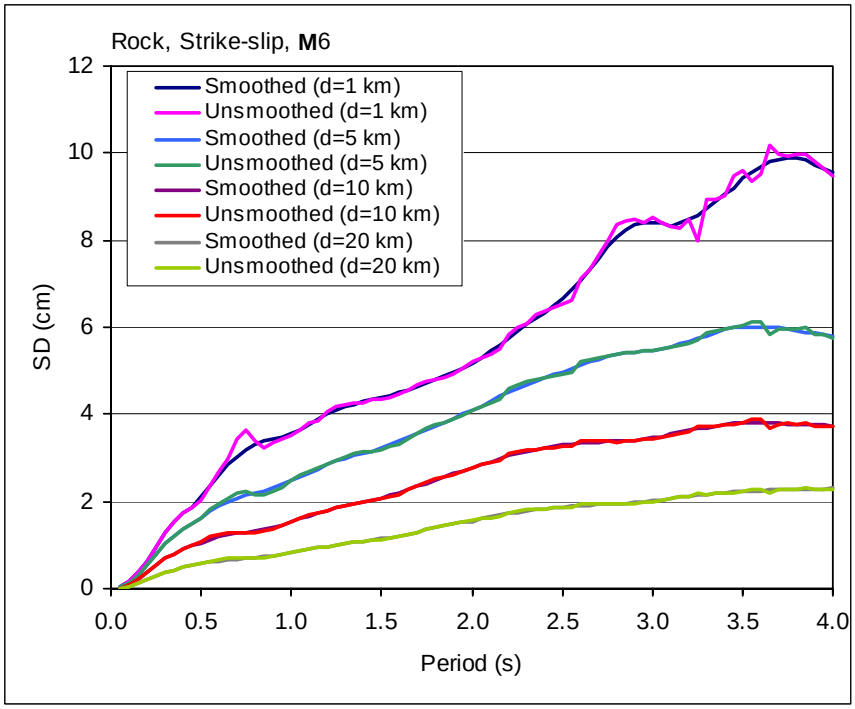

Figure B. 2. 5 per cent damped median displacement response spectra obtained from Akkar and Bommer (2007) model for an M_w = 6.0 earthquake.

B3. Regression Coefficients for the Somerville *et al.* (1997) Directivity Model

The coefficients for the spectral variation of average horizontal spectral acceleration, for the spatial variation of duration and for the strike normal to average horizontal response spectral ratios as given by Somerville *et al.* (1997) are presented in Table B. 7 through Table B. 10.

Table B. 7. Coefficients for spectral variation of average horizontal spectral acceleration

Period (s)	C_1	C_2	σ	τ	Total error	Smoothed Total Error
Strike – slip						
0.6	0.000	0.000	0.751	0.123	0.761	0.78
0.75	-0.084	0.185	0.791	0.170	0.809	0.78
1.0	-0.192	0.423	0.756	0.243	0.794	0.78
1.5	-0.344	0.759	0.804	0.185	0.825	0.78
2.0	-0.452	0.998	0.778	0.156	0.793	0.78
3.0	-0.605	1.333	0.774	0.001	0.774	0.78
4.0	-0.713	1.571	0.718	0.104	0.726	0.78
5.0	-0.797	1.757	0.741	0.154	0.757	0.78
Dip – slip						
0.6	0.000	0.000	0.514	0.000	0.514	0.50
0.75	-0.045	0.008	0.549	0.000	0.549	0.53
1.0	-0.104	0.178	0.540	-0.001	0.540	0.57
1.5	-0.186	0.318	0.568	0.169	0.593	0.62
2.0	-0.245	0.418	0.602	0.260	0.655	0.66
3.0	-0.327	0.559	0.690	0.211	0.721	0.71
4.0	-0.386	0.659	0.616	0.360	0.713	0.75
5.0	-0.431	0.737	0.634	0.522	0.822	0.78

Table B. 8. Coefficients for the spatial variation of duration

C_1	C_2	σ	τ	Total error
Strike – slip				
0.414	-1.043	0.436	0.343	0.555
Dip – slip				
0.722	-1.289	0.363	0.202	0.415

Table B. 9. Coefficients of the strike normal to average horizontal response spectral ratio excluding dependence on the angles θ or Φ

Period (s)	C_1	C_2	C_3	σ	τ	Total error	Smoothed Total Error
0.5	0.000	0.000	0.000	0.217	0.000	0.217	0.224
0.6	0.048	-0.012	0.000	0.234	0.019	0.234	0.231
0.7	0.079	-0.019	0.000	0.238	0.041	0.242	0.236
0.75	0.093	-0.022	0.000	0.241	-0.024	0.242	0.238
0.8	0.108	-0.026	0.000	0.245	0.037	0.248	0.239
0.9	0.124	-0.030	0.000	0.261	0.044	0.265	0.242
1.0	0.139	-0.033	0.000	0.268	0.047	0.272	0.243
1.5	0.192	-0.046	0.000	0.231	0.065	0.239	0.247
2.0	0.231	-0.055	0.005	0.237	0.072	0.248	0.249
2.5	0.270	-0.065	0.011	0.225	0.066	0.235	0.249
3.0	0.304	-0.075	0.025	0.238	0.063	0.246	0.250
3.5	0.331	-0.084	0.046	0.240	0.075	0.251	0.250
4.0	0.351	-0.096	0.063	0.241	0.083	0.255	0.250
4.5	0.362	-0.098	0.081	0.234	0.088	0.250	0.250
5.0	0.369	-0.103	0.093	0.235	0.093	0.252	0.250
6.0	0.375	-0.113	0.106	0.242	0.080	0.255	0.250

Table B. 10. Coefficients of the strike normal to average horizontal response spectral ratio including dependence on the angles θ or Φ

Period (s)	C_1	C_2	C_3	σ	τ	Total error	Smoothed Total Error
0.5	0.000	0.000	0.000	0.226	0.000	0.226	0.25
0.6	0.027	-0.0069	0.000	0.240	0.000	0.240	0.25
0.7	0.050	-0.0127	0.000	0.250	0.045	0.254	0.25
0.75	061	-0.0155	0.000	0.252	0.001	0.252	0.25
0.8	070	-0.0178	0.000	0.257	0.043	0.261	0.25
0.9	088	-0.0220	0.000	0.279	0.067	0.287	0.25
1.0	104	-0.0255	0.000	0.282	0.065	0.290	0.25
1.5	164	-0.0490	0.034	0.224	0.103	0.246	0.25
2.0	207	-0.0613	0.059	0.237	0.082	0.250	0.25
2.5	280	-0.0816	0.078	0.218	0.063	0.227	0.25
3.0	353	-0.1007	0.093	0.242	0.042	0.246	0.25
3.5	415	-0.1172	0.106	0.236	0.039	0.239	0.25
4.0	456	-0.1282	0.118	0.239	0.054	0.245	0.25
4.5	462	-0.1307	0.128	0.244	0.072	0.254	0.25
5.0	450	-0.1269	0.137	0.245	0.068	0.254	0.25
6.0	424	-0.1223	0.152	0.244	0.039	0.247	0.25